DESIGN AND SYNTHESIS OF CHIRAL CYCLOMETALATED OXAZOLINE-BASED GOLD(III) COMPLEXES FOR ASYMMETRIC CATALYSIS AND SUPRAMOLECULAR ASSEMBLY IN AQUEOUS MEDIA

CHAN KWOK HEUNG ARIES

PhD

The Hong Kong Polytechnic University

2025

Initial Submission for Examination Purpose

The Hong Kong Polytechnic University

Department of Food Science and Nutrition

Design and Synthesis of Chiral Cyclometalated Oxazoline-based Gold(III)

Complexes for Asymmetric Catalysis and Supramolecular Assembly in

Aqueous Media

Chan Kwok Heung Aries

A thesis submitted in partial fulfilment of

the requirements for the degree of

Doctor of Philosophy

August 2024

CERTIFICATE OF ORIGINALITY

I hereby declare that this thesis is my own work and that, to the best of my knowledge and belief, it reproduces no material previously published or written, nor material which has been accepted for the award of any other degree or diploma, except where due acknowledgement has been made in the text.

_____

Chan Kwok Heung Aries

Abstract

Gold catalysis exhibited exceptional reactivity, great selectivity, and high functional group compatibility in a variety of organic transformations, which has been developed rapidly in recent decades. Compared to the extensively studied asymmetric gold(I) catalysis, the development of asymmetric gold(III) catalysis is still in its infancy. Several pioneering works have highlighted the potential of using chiral gold(III) complexes as effective catalysts in enantioselective transformations. In spite of these advances, literature examples with enantioselectivity above 90% ee are limited. Therefore, the development of new chiral gold(III) complexes is of significant interest to achieve high enantioselectivity in asymmetric gold catalysis. On the other hand, amphiphilic design of gold(III) complexes was independently reported showing the self-assembling abilities of the cyclometalated gold(III) complexes and was highly responsive to slight changes in molecular structure and resulting supramolecular nanostructures. However, compared with the well-developed organic amphiphiles, the luminescent properties, cytocompatibilities and chiral supramolecular assembly of gold(III) amphiphile systems are yet unknown.

In chapter 1, the scientific background of homogeneous gold catalysis, chemistry of gold(I) and gold(III) complexes, development of asymmetric catalysis and our previous works on development of gold(III) complexes were introduced. In addition, the introduction of supramolecular chemistry and luminescent properties of self-assembled metal complexes were described.

In chapter 2, a new synthetic strategy for the development of optically pure C,O-chelated oxazoline-based BINOL/gold(III) complexes through diastereomeric resolution was

reported. Using inexpensive enantiopure BINOL as the chiral resolving agent, the diastereomers of the chiral BINOL/gold(III) complexes could be easily resolved and purified through simple filtration in high yield. Moreover, the gram scale optical resolution of enantiopure chiral gold(III) dichloride complexes was established. Besides, the gold(III)-mediated chiral resolution of BINOL derivatives was demonstrated to afford optically active BINOLs in good to excellent yields (overall 77 – 96%) with high optical purity up to 99% ee. In addition, the catalytic activity of this new class of C,O-chelated oxazoline-based BINOL/gold(III) complexes was examined which achieved asymmetric carboalkoxylation of *ortho*-alkynylbenzaldehydes in excellent enantioselectivity up to 99% ee.

In chapter 3, an advanced supramolecular assembly system of luminescent amphiphilic C^N-chelated alkynyl gold(III) complexes with biocompatibility in aqueous media was demonstrated. The amphiphilic nature of the gold(III) complexes arising from the hydrophilic charged quaternary ammonium ion connected with the hydrophobic cyclometalated gold(III) core by an alkyl-linker improved the aqueous solubility. The alkynyl ligands as the strong σ-donor greatly enhanced the ambient luminescent properties of these gold(III) amphiphiles. Moreover, these gold(III) amphiphiles self-assembled into nanostructures in aqueous media showing high aspect ratio. The reversible supramolecular assembly transformation was observed by changing the packing parameters through counterion exchange process. Cytocompatibilities of gold(III) amphiphiles in aqueous media was studied showing limited cytotoxicity at low concentration.

In chapter 4, the first example of the chiral cyclometalated gold(III) amphiphile (GA) was demonstrated with supramolecular assembly in aqueous media. The amphiphilicity of the chiral oxazoline gold(III) complex arise from connected the hydrophobic gold(III) core to a hydrophilic charged quaternary ammonium ion with an alkyl-linker which improved the aqueous solubility. The chirality was transferred from the chiral oxazoline moiety to the resulting supramolecular nanostructures. The counterion induced supramolecular transformations were demonstrated by the addition of D-, L-, or racemic-camphorsulfonates. Cytocompatibility of GA in aqueous media was shown with limited cytotoxicity.

Publications Arising from the Thesis

Chapter 2: <u>Chan, A. K.-H.</u>; O, W.-Y.; Jiang, J.-J.; Cui, J.-F.; Wong, M.-K. Consecutive Chirality Transfer: Efficient Synthesis of Chiral C,O-Chelated BINOL/Gold(III) Complexes for Asymmetric Catalysis and Chiral Resolution of Disubstituted BINOLs. *Chemical Science* **2024**, *15*, 16733–16742.

Chapter 3: Chau, M.-H.; <u>Chan, A. K.-H.</u>; Ren, Y.; Jiang, J.-J.; Wong, M.-K.; Leung, F. K.-C. Aqueous supramolecular assemblies of luminescent cyclometalated gold (III) amphiphiles with biocompatibility. *Journal of Organometallic Chemistry* **2023**, *999*, 122827.

Chapter 4: <u>Chan, A. K.-H.</u>; Chau, M.-H.; Ren, Y.; Jiang, J.-J.; Wong, M.-K.; Leung, F. K.-C. Controlled Supramolecular Assemblies of Chiral Cyclometalated Gold (III) Amphiphiles in Aqueous Media. *ChemPlusChem* **2024**, *89*, e202300316.

Acknowledgements

Finally, I am eternally indebted to my family for their unwavering love, encouragement and understanding during my academic journey.

Table of Contents

X

List of Figures

Chapter 2 Development of Chiral C,O-Chelated BINOL/Gold(III) Complexes for Asymmetric Catalysis

Chapter 3 Aqueous Supramolecular Assemblies of Luminescent Cyclometalated Gold(III) Amphiphiles with Biocompatibility

Chapter 4 Controlled Supramolecular Assemblies of Chiral Cyclometalated Gold(III) Amphiphiles in Aqueous Media

List of Tables

XXII

List of Abbreviations

δ	Chemical shift (NMR)
MS	Mass spectrometry
NMR	Nuclear magnetic resonance spectroscopy
CD	Circular dichroism
TEM	Transmission electron microscopy
DLS	Dynamic Light Scattering
UV-Vis	UV-Visible
HPLC	High-performance liquid chromatography
CAC	Critical aggregation concentration
equiv.	Equivalent
h	Hour
rt	Room temperature
ee	Enantiomeric excess
R	Generalized alkyl or aryl group
Me	Methyl
Et	Ethyl
n-Bu	*n*-butyl
i-Pr	isopropyl
t-Bu	*t*-butyl
Ar	Aryl
Ph	Phenyl
Ts	Tosyl

NHC	N-heterocyclic carbenes
DCM	Dichloromethane
$CHCl_3$	Chloroform
THF	Tetrahydrofuran
DMF	Dimethylformamide
MeOH	Methanol
EtOH	Ethanol
Et_2O	Diethyl ether
EA	Ethyl acetate
GA	Gold(III) Amphiphiles

Chapter 1 Introduction

1.1 History of Homogeneous Gold Catalysis

Gold has been widely used in jewelry, arts, bullion and coinage for several thousands of years due to its tempting bright yellow color and unusual stability against air and moisture. Despite the ubiquity of metallic gold in public culture, it was traditionally considered as catalytically inactive and underestimated for a long time until the accidental discovery of catalytic active gold nanoparticles in 1980s.[1] In 2000, homogeneous gold catalysis was initiated by Hashmi *et al.* and, since that, has received remarkable attention with widespread applications in organic transformations.[2]

Only limited literature of homogeneous gold catalysis can be found before 21st century. The discovery of homogenous gold catalysis can be traced back to the first notable example of gold(I) catalyzed asymmetric aldol reaction reported by Ito and Hayashi *et al.* in 1986.[3] The next major breakthrough was made by Fukuda and Utimoto in 1991 that demonstrated the nucleophilic addition reaction of alkynes using gold(III) salts to produce ketones, ketals, or cyclic imines, which set up the basis for the majority of the following developments of homogeneous gold catalysis.[4] In 1998, Teles *et al.* reported the highly efficient gold(I) catalyzed ketalization of alkynes with excellent turnover number (TONs) and turnover frequency (TOFs).[5]

In the beginning of 21st century, a crucial step for homogeneous gold catalysis was initiated by Hashmi *et al.* who reported the intramolecular addition of alcohols to alkynes, and intermolecular addition of arenes onto allenes and alkenes in 2000.[6] The other major discovery made in 2000 from the same group was cycloisomerization of furan-ynes using gold(III) catalysts.[7] Started from 2003, several research groups extended the potential of

homogeneous gold catalysis in organic synthesis based on these successful initial results. The reactivities of gold catalysts towards a variety of organic transformations were subsequently discovered and extensively attracted the interest of organic synthetic chemists.[8] A "gold rush" has been witnessed that the remarkable number of studies and review articles that have emerged since 2006, showing gold salts and complexes as the powerful catalysts for efficient and selective organic transformations.[9]

1.2 Chemistry of Gold

Gold, as a group 11 metal, exhibits exceptional stability in its elemental state. Despite its elemental form, various oxidation states ranging from -1 to +5 are accessible. Among them, gold species with the oxidation states of 0, +1 and +3 are mainly applied in chemistry. Gold(I) compounds with d^{10} electron configuration show the linear coordination geometry with two coordination sites. Gold(III) compounds, similar to other d^8 heavy transition metal ions, display a square-planar coordination geometry that shows distinctly different reactivity to gold(I) compounds.

Gold(I) and gold(III) catalysts have been demonstrated as strong carbophilic Lewis acid that is capable to activate carbon-carbon π-bonds including alkenes, alkynes, and allenes towards nucleophilic addition, allowing the formation of carbon-carbon, carbon-nitrogen, carbon-oxygen, carbon-sulfur bonds, as shown in Figure 1.1.[2c] Among them, alkynes are the best substrates for homogeneous gold catalysis which dominate the majority of gold catalyzed transformations in the literature.[9] Since gold(III) species are unstable towards reduction, their applications in organic transformations are much less then gold(I) species. Compared to other Group 11 metals, cationic gold(I) species exhibit

a superior Lewis acidity for organic transformations, providing selective activation of carbon-carbon π-bonds under soft reaction conditions with remarkably high functional group tolerance,[9i, 10] which attribute to relativistic effects.[11]
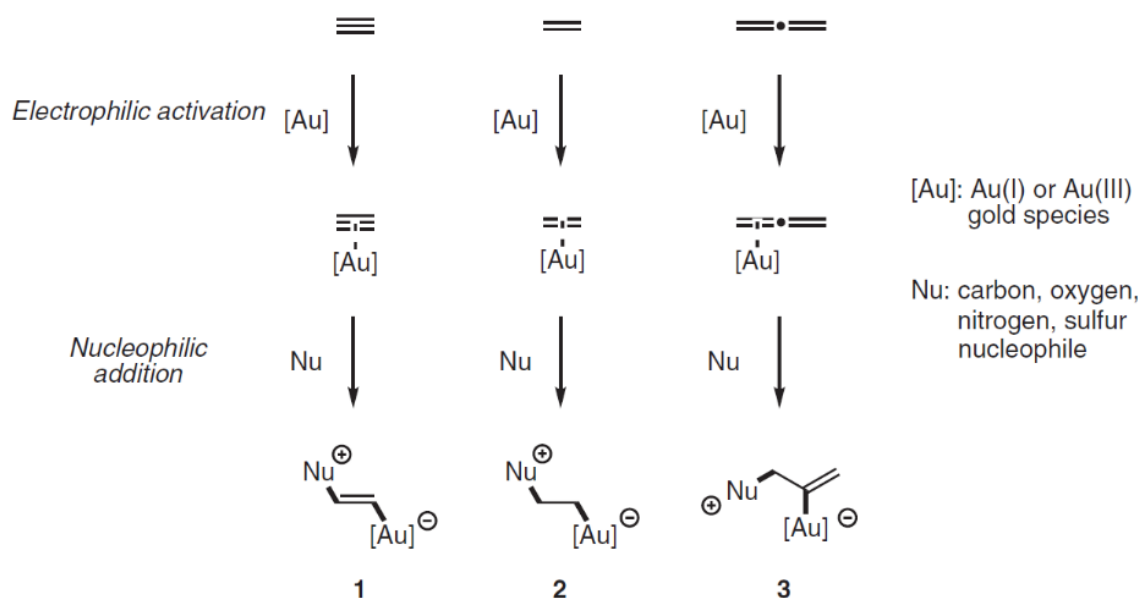
Figure 1.1 Activation of C-C multiple bonds by gold species towards nucleophilic addition.[2c]

1.2.1   Relativistic Effects

Relativistic effects are the important factor affecting the electronic structure of heavy elements as well as the post-lanthanide elements, especially for gold having the most "relativistic" as compared to other elements along the row in periodic table (Group 1 to Group 18), as shown in Figure 1.2.[12] In chemistry, relativistic effects associate with all electrons moving close to a heavy nucleus. A heavy nucleus, containing a large number of protons, has a very high nuclear charge that largely attracted the closer electrons leading to high-speed approaching to speed of light. When the speed of particles

(including electrons) approach to the speed of light, their mass will increase, which called "relativistic mass" and can be expressed mathematically by the equation $m = m_o / \sqrt{1 - (\frac{v}{c})^2}$, where m refers to relativistic mass, m_0 as non-relativistic mass, v as velocity, and c as speed of light. For those elements with atomic number $Z > 70$, the speed of their 6s electron becomes not negligible leading to a significant increase of relativistic mass, but less important for electrons in p or d orbitals. Since Bohr radius of s orbital decreases as the mass of electrons increases, the 6s orbital contraction occurs. The contraction of these orbitals leads to the strong shielding effect on nuclear attraction, resulting in expansion and destabilization of 5d orbital.[11-13] A well-known example explaining the relativistic effects on the 6th row elements is the comparison between silver and gold, which are the 5th and 6th row elements respectively in the same Group of periodic table. Based on the calculation of orbital energies of Ag and Au with the absence of relativity, the non-relativistic 4d and 5s orbital energies of Ag are close to the non-relativistic 5d and 6s orbital energies of Au, while they are significantly different in the presence of relativity.[14]
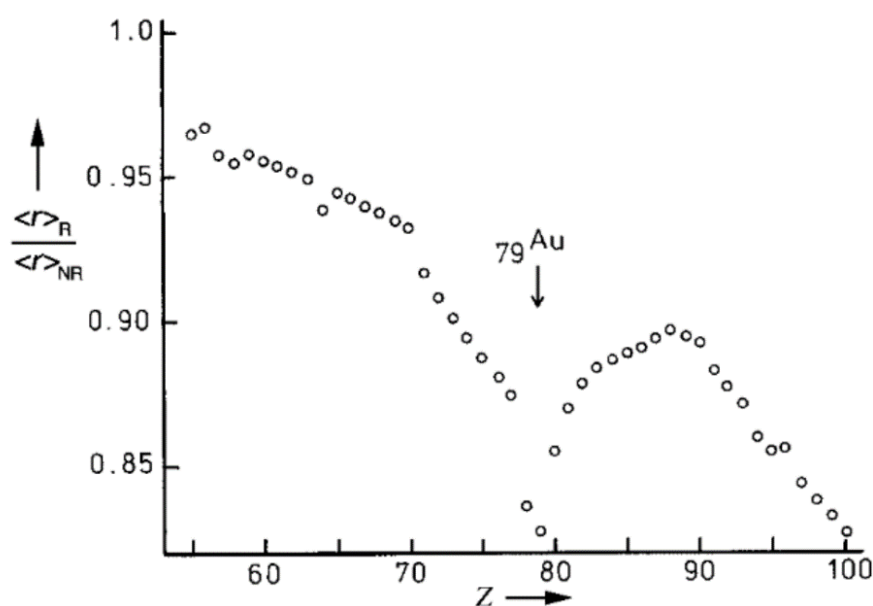
Figure 1.2 The ratio of relativistic (<r>R) and nonrelativistic (<r>NR) 6s-shell radii of the elements bearing Z = 55 – 100.[12]

1.2.2 Gold(I) Chemistry

Gold(I) complexes were commonly synthesized in the form of L-Au-Cl, where L are frequently encountered phosphine and carbene ligands, and sometimes phosphite and phosphoramidite. This gold(I) chloride complexes are the pre-catalysts which are not active for catalysis without the use of activator. Silver salts are commonly used as co-catalyst to *in-situ* generate the catalytically active form, cationic gold(I) species [LAu]$^+$ as shown in Figure 1.3.[2c] For gold(I) species, as a consequence of the relativistic effects, the contracted 6s orbital as well as the lowest unoccupied molecular orbital (LUMO) is relatively low. This low-lying LUMO of gold(I) species therefore provides strong Lewis acidity. In addition, due to the greater shielding effect from the electrons in the contracted s and p orbitals, the 5d orbital is expanded leading to a weaker nuclear attraction and higher degree of delocalization. The activated form, cationic gold(I) species [LAu]$^+$ therefore diffuse positive charge over the expanded large orbital, making [LAu]$^+$ as a

"soft" Lewis acid with high carbophilicity towards "soft" π-bonds. The contraction of $6s$ orbital also affects the L-Au(I) bond in which the covalent radius of gold(I) species is much shorter than that of silver(I) species. On the other hand, the aurophilicity, gold(I) species tending to interact with the neighboring gold(I) centers to give multi-metallic aggregates, is also a consequence of relativistic effect.[11-13, 15]
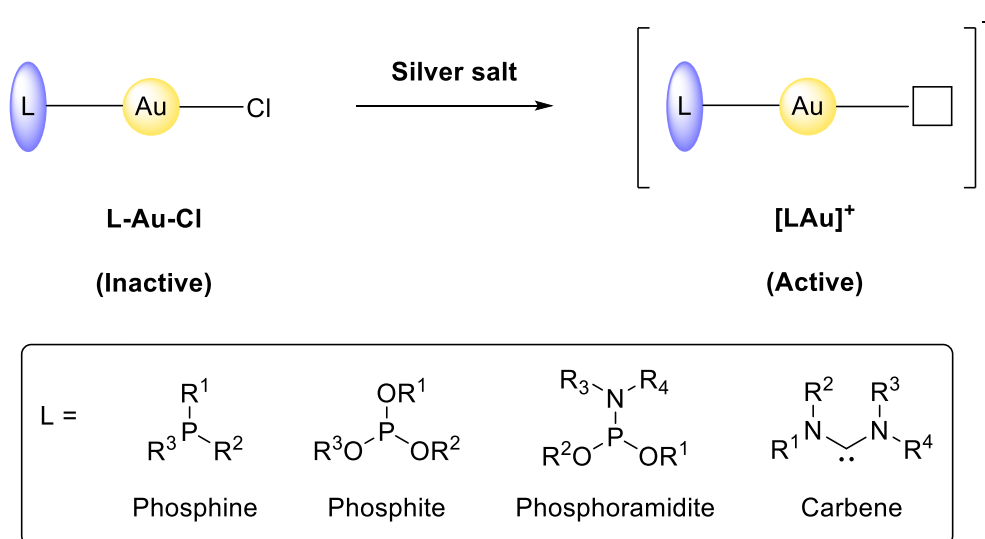
Figure 1.3 Activation of gold(I) chloride complex L-Au-Cl.

1.2.3   Gold(III) Chemistry

For gold(III) species, the relativistic effects are less important as the relativistic L-Au(III) bond length contractions is not obvious. Compared to the significantly different covalent radius between Ag^I/Au^I pair, silver(III) and gold(III) have very similar covalent radius.[16] This reduced relativistic effects on gold(III) species is also observed as the aurophilicity is almost absent.[17] Compared to the "soft" carbophilic gold(I) species favoring "soft" atom like P and S, gold(III) species bearing high positive charge is more

electrophilic and relatively "hard" which bind to "hard" atom like O and F, showing higher oxophilicity in nature.

Homogenous gold catalysis has a short developmental history compared to the well-studied platinum, a neighbor metal in periodic table. Due to the similar catalytic process, the gold-mediated reaction mechanism was often referred to the well-known platinum- or palladium- catalyzed reaction mechanism.[18] Despite the similar reactivities in some of the reactions, they have significantly different redox potentials. The redox potentials of Au^{III}/Au^0 (1.52 V), Au^I/Au^0 (1.83 V), and Au^{III}/Au^I (1.36 V) are much more positive than Pt^{II}/Pt^0 (1.19 V) and Pd^{II}/Pd^0 (0.91 V) under standard conditions, meaning that gold(III) species is unstable towards reduction as compared to platinum(II) and palladium(II).[19] This instability of gold(III) species therefore leads to the challenges in the development of stable and reactive gold(III) complexes, as compared to the extensively studied homogenous gold(I) catalysis. To modify the redox potentials of gold(III) species, the selection of ligands plays a prominent role in stabilizing the gold(III) complexes against reduction. Particularly, chelating bidentate and pincer tridentate ligands are mostly used as stabilizing ligand in gold(III) chemistry.[20] To date, numerous well-defined gold(III) complexes have been developed for homogeneous gold(III) catalysis.[9r]

1.3 Asymmetric Gold Catalysis

Over the past two decades, homogeneous gold catalysis has been rapidly developed owing to the exceptional Lewis acidity of gold complexes for activation of carbon-carbon π-bonds towards nucleophilic addition.[9, 21] This unique reactivity of gold apart from other transition metal arises from the soft carbophilic nature, which establishes the promising

contender for transition metal catalysis. Despite the plethora of homogeneous gold-catalyzed organic transformations have been reported, this upward trend did not extend to enantioselective version. Although the first example of homogeneous gold catalysis was a highly enantioselective organic transformation reported in 1980s, the initial development of asymmetric catalysis was slow.[3] In the first decade of the 21st century, "gold rush" started leading to the tremendous growth in the field, but the examples of enantioselective gold catalysis were still limited due to the linear geometry of gold(I) complexes.[11, 13a, 22] In asymmetric transition metal catalysis, chiral ligand is of critical importance for transferring chiral information to the incoming substrate bound to the metal center. However, as shown in Figure 1.4, the linear geometry of gold(I) complexes positioned the chiral ligand and substrate on opposite sides of the metal center, rendering the inherent difficulties of chiral induction. Given the followed outer-sphere nucleophilic addition occurred at the back of the substrate, the transformation of chiral information from ligand to the reactive center would be even more difficult, making high challenges to achieve enantioselective gold(I) catalysis. As a result, simple chiral ligands are not suitable for gold(I) catalysis since they usually provide poor chiral induction. The rational ligand design is therefore inevitable to tackle this problem.
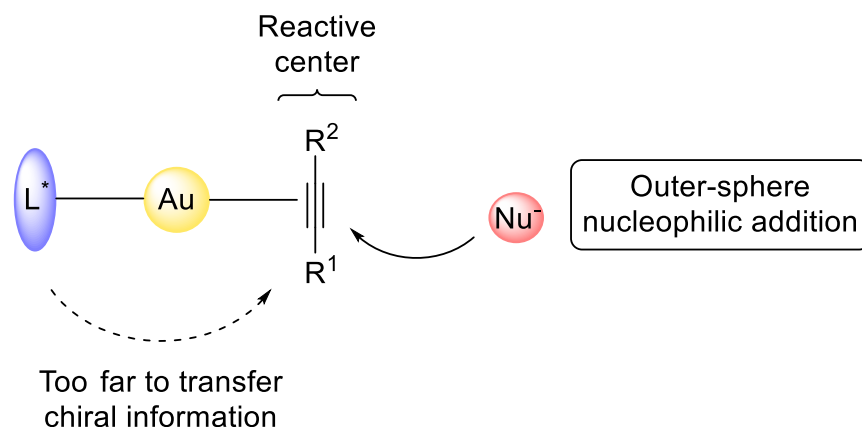
Figure 1.4 Chiral induction by gold(I) catalysis.

1.3.1 Asymmetric Gold(I) Catalysis

In the past few years, several strategies of novel chiral phosphine and carbene ligands for chiral gold(I) complexes have been developed to achieve enantioselective gold(I) catalysis.[23] There are mainly four systems achieving high enantioselectivity, including axially chiral digold complexes, bulky chiral ligand or helical ligands, chiral counterions, and merging gold with organocatalysts as shown in Figure 1.5.[24] Binuclear gold catalysis is one of the most powerful strategies achieving high enantioselectivity. Since gold(I) complexes favor linear coordinating mode, the use of chiral diphosphine ligand, a powerful ancillary ligand to induce chiral environmental, may tend to adopt the binuclear chiral gold complexes providing a second phosphine gold center, which is important for chiral induction.[23g] Chiral bulky monophosphine ligands or helical ligands, are also employed for asymmetric gold(I) catalysis providing good enantioselectivity.[25] Nevertheless, considering the difficulties to construct a chiral induction space, dinuclear gold(I) catalysts demonstrate more controllable enantioselectivity in most of the cases.[24j] The use of achiral cationic gold(I) catalysts coupled with chiral counterion is an

alternative strategy to achieve high enantioselectivity. The more-coordinating anions, such as benzoates and tosylate, were shown to have positive effects on the late-stage gold catalytic cycle as well as the protodeauration stage to control the chemo-, regio, or stereoselectivity.[24i] Moreover, merging gold with organocatalysis is a promising strategy in gold-catalyzed asymmetric transformations. Although asymmetric organocatalysis has shown to participate in a broad range of enantioselective transformations, extending to new chemistry areas is difficult due to the challenges in the activation of inactive chemical bonds. In contrast, metal complexes are frequently used to activate a wide range of inactive chemical bonds, especially for those chemically inert bonds (e.g. C-H bond). By merging gold metal complexes and chiral organocatalysts, an alternative strategy combining the advantages of the two catalysts is achieved to create new asymmetric transformations.[24g]
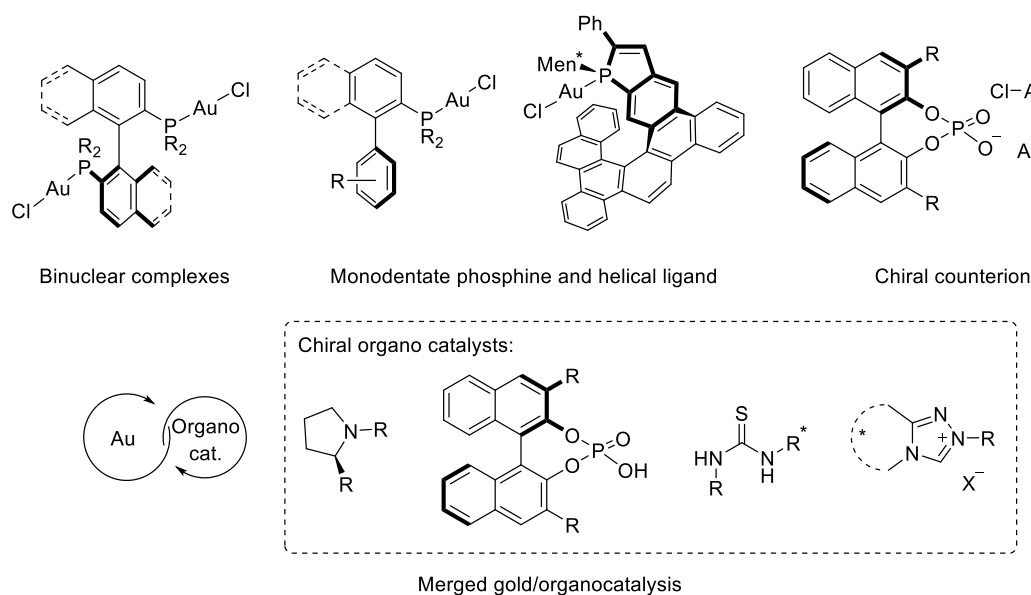
Figure 1.5 Enantioselective gold(I) catalysis strategies.

1.3.2   Asymmetric Gold(III) Catalysis

Gold(III) complexes adopting square planar geometry, similar to the known chiral platinum(II) and palladium(II) complexes, are very appealing to overcome the limitations of linear gold(I) complexes in asymmetric catalysis. The chiral ligands in square planar manner are placed in close proximity to reactive site, allowing high efficiency and controllable in chiral induction (Figure 1.6). However, the development of asymmetric gold(III) catalysis is still in their infancy as compared to the extensively studied asymmetric gold(I) catalysis.[26] The high oxidation potential of gold(III) species is prone to reduction under catalytic conditions which is less stable than gold(I) complexes and other d^8 transition metal complexes, limiting the development of stable and reactive gold(III) complexes.[27] Incorporating the electron-rich ligands, such as tertiary amine, to the gold(III) center may lead to destabilization and undergo reduction, while the less electron-rich ligands like Schiff base and N-heterocyclic carbenes (NHC) provide stability to gold(III) complexes.[9r, 20, 28] However, highly stable complexes reflect poor catalytic activity. It is difficult to strike a proper balance between stability and activity. Nevertheless, more than hundred well-defined chiral gold(III) complexes have been reported since 2005 and showed that chelating ligands play the significantly important role in stability and activity. A few examples demonstrated the ability of chiral gold(III) complexes to achieve high enantioselective catalysis.[27b]
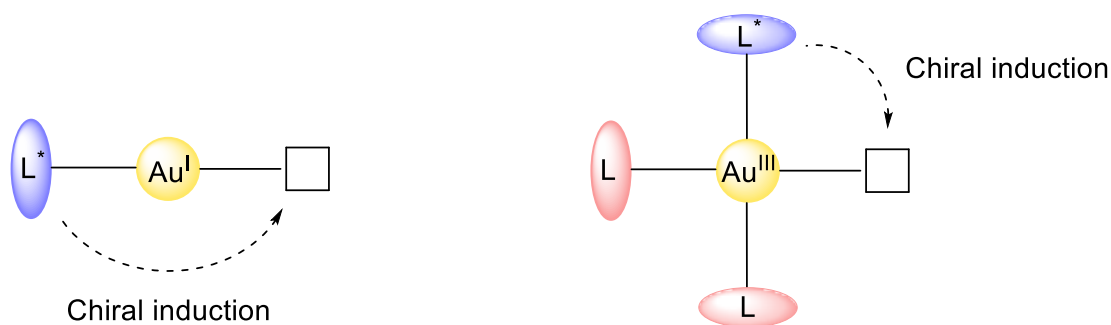
Figure 1.6 Chiral induction of gold(I) and gold(III) complexes.

In 2015, Toste *et al.* reported a novel NHC-gold(III) complex which was stabilized by chelating with a biphenyl ligand.[29] The chloro ligand of this stable complex is able to be activated using silver salt to *in situ* generate a vacant site available for substrate binding. From the structural point of view, the chloride group is much closer to the NHC ligand as compared to the conventional linear NHC-gold(I) chloride complex, which shows the potential in chiral induction with the use of chiral ligand (Scheme 1.1a). In 2017, the chiral version of NHC-biphenyl gold(III) complexes were designed by the same group which was able to catalyze an enantioselective cycloisomerization of 1,5-enynes providing the reaction product bicyclohexences with high enantioselectivities up to 90% ee and s-factor up to 48 (Scheme 1.1b).[30] This cycloisomerization is the enantioconvergent kinetic resolution of racemic 1,5-enynes, meaning that the remaining starting material 1,5-enyne after reaction was enantioenriched.
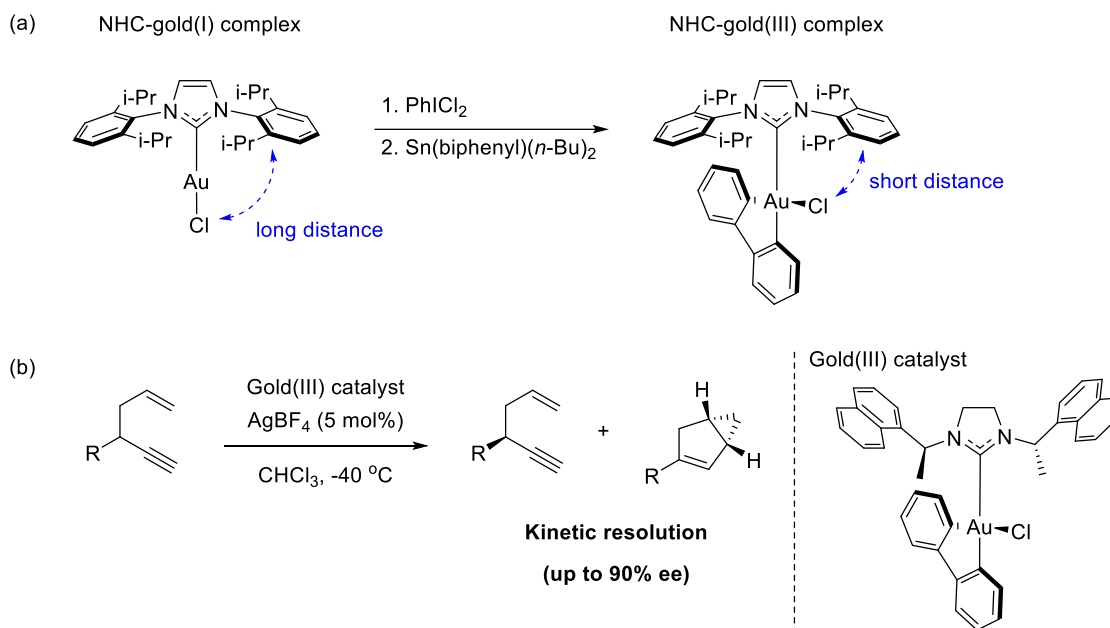
Scheme 1.1 (a) Synthesis of NHC-biphenyl gold(III) complex; **(b)** gold(III) catalyzed enantioconvergent kinetic resolution of 1,5-enynes.

In 2020, Toste's group adopted a new chiral NHC-biphenyl gold(III) complexes with imidazolium- and triazolium- ligands which enabled the enantioselective γ,δ Diels–Alder reaction between cyclopentadienes and 2,4-dienals.[31] The initial attempt of using the NHC-gold(III) complexes with C_2 symmetric imidazolium ligand afforded low enantioselectivity. Later on, the unsymmetric version of NHC-gold(III) complexes with triazolium ligands incorporating a morpholine scaffold was further developed (Scheme 1.2a). The computational studies were conducted and the result revealed that the enhancement in chiral induction was attributed to the stabilization of lowest energy transition by two attractive non-covalent π-π interactions between substrate and ligand (Scheme 1.2b). The use of gold(III) complex bearing a 2-chloro-naphthyl substituent afforded the reaction product with excellent enantioselectivity 98% ee.

(a)
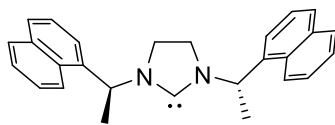
C_2-imidazolium ligand

C_1-triazolium ligand

(b)

Gold(III) catalyst (10 mol%)
AgNTf$_2$ (10 mol%)

PhCF3/MeNO2 (4:1)
r.t., 5-21 h
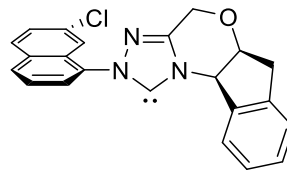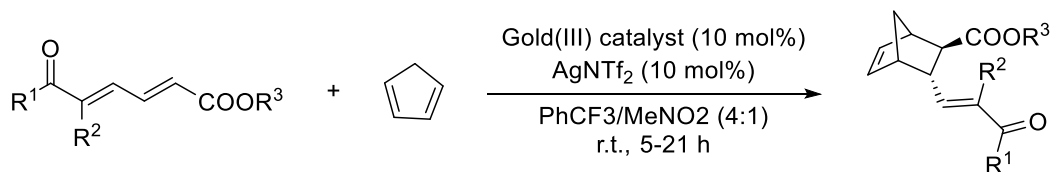
up to 87% yield
up to 98% ee

Gold(III) catalyst
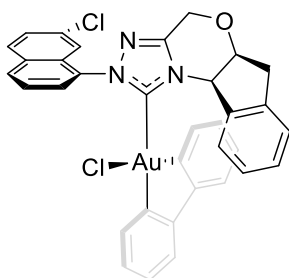
π-π interactions
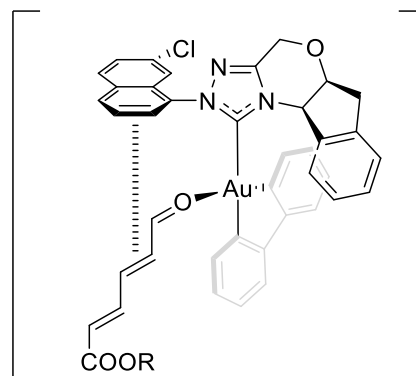
Scheme 1.2 (a) Chiral imidazolium- and triazolium- ligands; **(b)** Gold(III)

catalyzed enantioselective Diels-Alder reaction.

1.4 Our Previous Works on the Development of Gold(III) Complexes

In 2009, our group reported a class of square planar cyclometalated C,N-chelated gold(III) complexes using typical ligands as shown in Figure 1.7. These gold(III) complexes could catalyze the three-coupling reactions of aldehydes, amines and alkynes.[32]

Au(C^N)Cl₂

[Au(salen)]PF₆

Au(C^N^C)Cl

[Au(TPP)]Cl
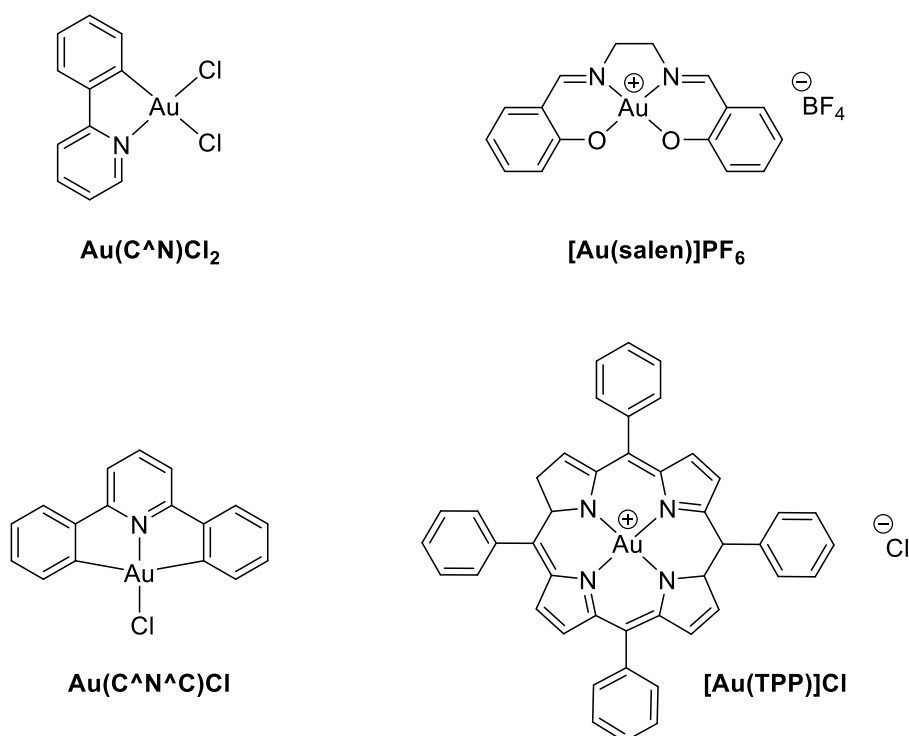
Figure 1.7 Square planar cyclometalated C,N-chelated gold(III) complexes.

In 2013, our group reported two bis-cyclometalated C,N-chelated gold(III) complexes using 2-phenylquionline ligand and 3-phenylisoquinoline ligand respectively (Scheme 1.3a).[33] Compared to the conventional square planar gold(III) complexes, the bis(2-phenylquionline)gold(III) complex exhibited a distorted square planar geometry with a dihedral angel of 43˚, possibly due to the steric repulsion between two quionline moieties (Scheme 1.3b). These two gold(III) complexes could the catalyze propargylamine formation through the three-coupling reaction. Notably, the bis(2-

phenylquionline)gold(III) complex with the distorted square planar geometry showed significantly higher catalytic activities than the bis(3-phenylisoquinoline)gold(III) complex.

(a)

Bis(2-phenylquinoline)gold(III) complex   Bis(3-phenylisoquinoline)gold(III) complex

(b)
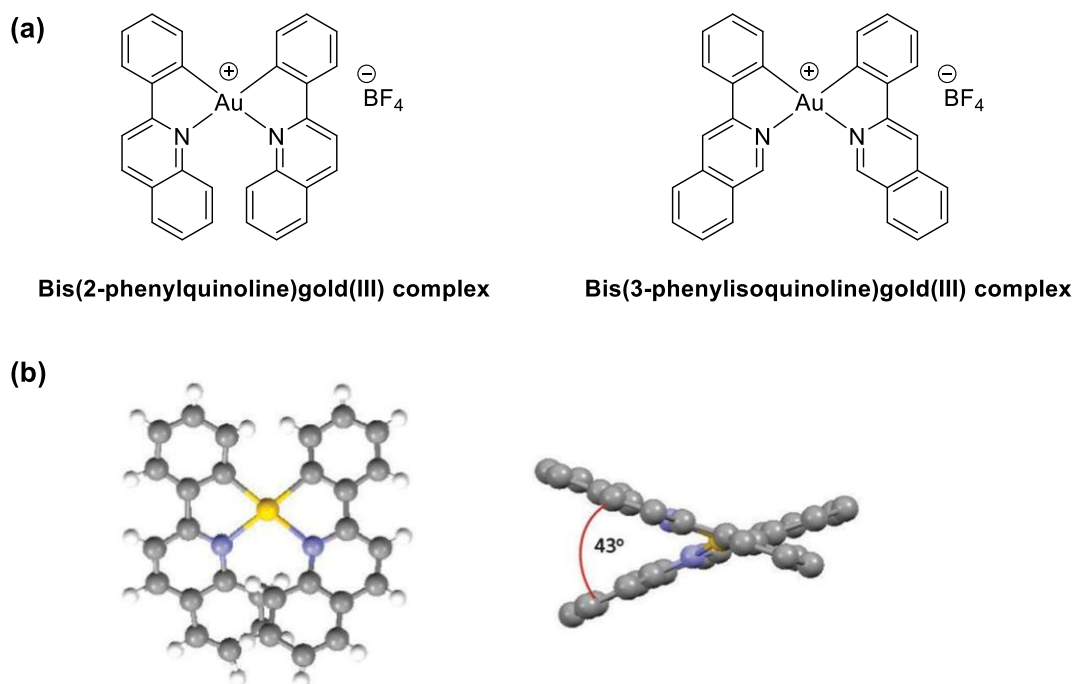
Scheme 1.3 (a) Bis-cyclometalated C,N-chelated gold(III) complexes; **(b)** Crystal structure of the bis(2-phenylquinoline)gold(III) complex.

In 2017, our group reported the synthesis of oxazoline-based C,N-chelated cyclometalated gold(III) dichloride complexes.[34] By substituted the two chloro ligands to a BINOL ligand, a series of C,N-chelated cyclometalated gold(III) complexes were developed. Interestingly, instead of the conventional O,O'-chelation mode, the unique C,O-chelation mode attributed to the enol-keto tautomerization of the BINOL ligand was observed. The BINOL ligand underwent axial-to-central chirality transfer to generate the novel C,O-chelated oxazoline-based BINOL/gold(III) complexes. Notably, as compared to the original gold(III) dichloride precursor, this kind of BINOL/gold(III) complexes

offered high stability against air, moisture and light, which could be stored under ambient conditions. Following the synthetic protocol, around 50 of these stable C,O-chelated BINOL/gold(III) complexes could be readily prepared using a variety of C,N-chelated gold(III) dichloride precursors matching with 3,3'- and 6,6'-disubstituted BINOL ligands (Scheme 1.4a). The performance in asymmetric catalysis was examined using a chiral oxazoline-based BINOL/gold(III) complex, in which the enantioselective carboalkoxylation of *ortho*-ethnylbenzaldehyde was achieved in the presence of methanol and camporsulfonic acid, affording 3-alkoxy indanones as the reaction product with moderate yield and enantioselectivity (52% yield, 41% ee) (Scheme 1.4b). In this work, despite the moderate enantioselectivity, this result was a very early example showing the potential of rationally designed stable gold(III) complexes in asymmetric catalysis.
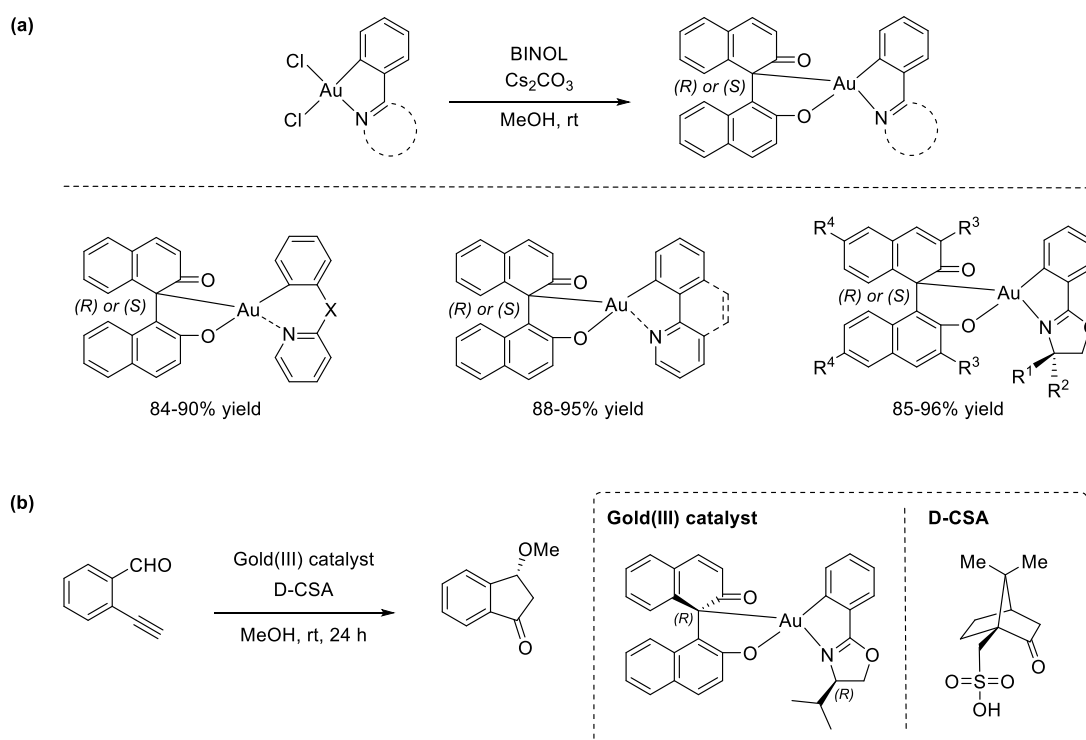
Scheme 1.4 (a) Synthesis of C,O-chelated oxazoline-based BINOL/gold(III) complexes; **(b)** gold(III) catalyzed enantioselective carboalkoxylation of *ortho*-ethnylbenzaldehyde.

On the basis of the previous results, in 2019, our group reported another class of chiral gold(III) complexes using similar synthetic protocol but replacing BINOL ligand with 4,4'-biphenol ligand.[35] Unlike BINOL ligand, O,O'-chelation mode was observed due to the absence of tautomerization and a variety of chiral O,O'-chelated biphenol oxazoline-based gold(III) catalysts were successfully synthesized. To study the ligand effect on the reaction enantioselectivity, asymmetric carboalkoxylations was performed using a series of chiral C,O- and O,O'-chelated oxazoline-based gold(III) catalysts (Scheme 1.5a). The results indicated that BINOL or biphenol ligands contributed a little effect to the reaction enantioselectivity. In contrast, a wide range of enantioselectivity between 19% and 90% ee was obtained through modifying the steric bulkiness of the chiral oxazoline group, revealing that the enantioselectivity was significantly affected by the oxazoline ligand. The reaction product 3-methoxyindanone with the highest enantioselectivity (90% ee) was achieved using the biphenol/gold(III) complex with a 1,3,5-trimethylphenyl substituent on the oxazoline moiety.

A mechanistic study was performed for study of the enantiodetermining step. We proposed that the presence of sulfonic acid may cause the photodeauration with only one oxygen of the biphenol ligand. Due to higher *trans*-effect of carbon than nitrogen, the Au-O bond *trans* to Au-C bond was weaker than that *trans* to Au-N bond. The vacant site was therefore placed in close proximity to the chiral oxazoline moiety that enhance the chiral induction. For the mechanism of the carboalkoxylation reaction, the alkyne group of the substrate was first activated by gold(III) catalyst followed by intramolecular nucleophilic addition. The cyclic acetal intermediate then underwent Petasis-Ferrier rearrangement to generate oxonium ion and the following 5-exo-trig cyclization was proposed to be the enantiodetermining step. The less sterically hindered transition state

of the intramolecular nucleophilic addition onto the oxonium intermediate afforded the major product enantiomer (Scheme 1.5b).

Toste and our group showcased the potential application of chiral gold(III) catalysts in enantioselective transformations. However, despite these advances, the enantioselectivity was rarely achieved exceeding 90% ee in most of the cases.[26, 27b] Therefore, it is of ongoing interest in developing new chiral gold(III) complexes in the pursuit of highly enantioselective asymmetric gold catalysis.
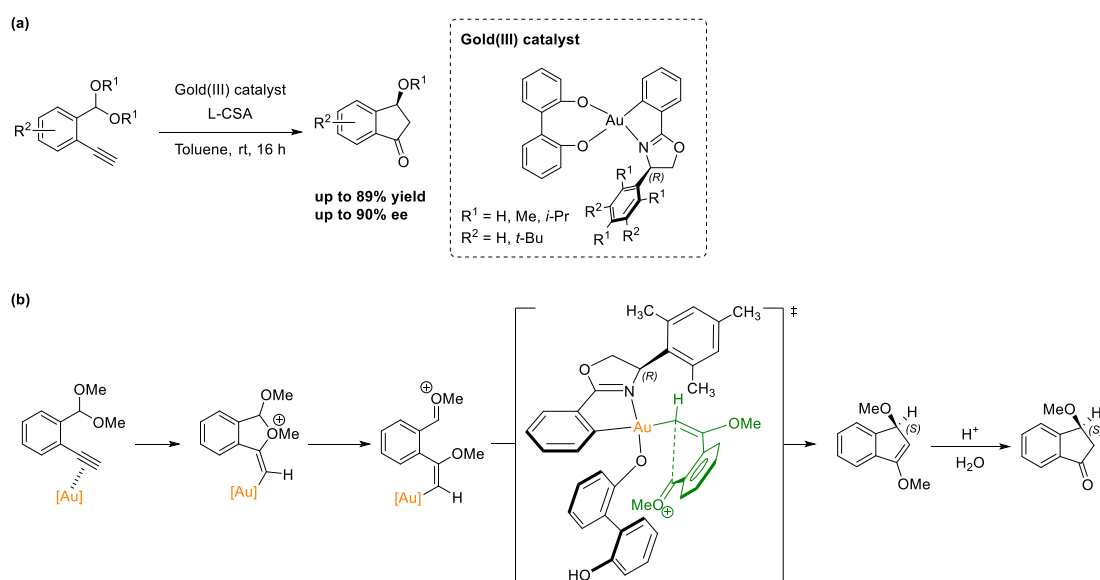
Scheme 1.5 (a) Chiral biphenol oxazoline gold(III) catalyzed carboalkoxylation of alkynes; **(b)** Reaction mechanism and the enantiodetermining step.

1.5 Supramolecular Chemistry

Supramolecular chemistry, also known as "chemistry beyond the molecule", is the study of spontaneous association of molecules into spatially ordered structures, which was driven by non-covalent interactions including hydrogen bonding, metal coordination,

hydrophobic effects, van der Waals forces, π−π interactions, and electrostatic interactions, instead of conventional covalent bonds.[36] Among these non-covalent interactions, hydrogen bonding arising from the electronic attraction between hydrogen atoms and electronegative atoms, has nowadays emerged as a fundamental tool in field of supramolecular chemistry. The term "supramolecular chemistry" was firstly described by Jean-Marie Lehn in the 1970s.[37] At that time, although supramolecular chemistry was focused on the study of non-covalent molecular interactions, the scientists in this field was awarded in the Nobel prize in Chemistry in 1987. The achievement promoted the field of supramolecular chemistry as a well-accepted chemical disciplines with further development into a scope of another research fields, such as biological science, materials science, polymer chemistry, organic chemistry, physical chemistry, inorganic chemistry.[38] After around 50 years growing of the field, supramolecular chemistry is now exploring into widespread applications of scientific areas including molecular machines, molecular sensors, nanoreactors, chemical catalysis, and drug delivery systems.

1.5.1   Amphiphilic Self-Assembly

Amphiphilic molecule is one of the most important candidates in field of supramolecular chemistry, which exhibits the spontaneous self-assembly to construct well-organized structures by non-covalent interactions.[39] This self-assembly process offers a powerful strategy for the development of novel nanomaterials with diverse scientific applications.[40] Self-assembly always presents in nature including the biomolecules like proteins and lipids organized into a complex biological system associated with exclusive cellular functions, which demonstrated the elegance and efficiency of self-assembly. Inspired by the biological system originated from self-

assembly, the study of amphiphilic self-assembly for mimicking the biological system has extensively attracted researchers to create biomimetic systems and drive advancements in nanotechnology. This opened new avenues in bionanotechnology applications by the study of regulating assembly-disassembly of amphiphilic structures through external stimuli. Thus, it is crucial to have a comprehensive understanding of amphiphilic self-assembly in order to take advance in nanotechnology as well as developing innovative molecular building blocks.[41]

Amphiphiles, including naturally occurring and synthetically derived molecules, contain both distinct hydrophilic polar head moiety (water-compatible group) and hydrophobic tail moiety (water-insoluble group), which is a property that drives their assembly into diverse nanostructures. For conventional amphiphiles, the hydrophobic moiety typically consists of a long hydrocarbon chain (either saturated or unsaturated), while the hydrophilic moiety can be either nonionic with no formal charge, or ionic carrying a net positive/negative charge. Nonionic amphiphiles often feature polyhydroxyl or polyether units as their hydrophilic components. A common class of nonionic amphiphiles generally consists of a hydrophilic poly(ethylene oxide) chain attached with a hydrophobic alkyl chain, which is frequently used in cleaning applications. Anionic amphiphiles commonly consist of a negative charge head group (carboxylate, phosphate or sulphonate) with a positively charge counterion (sodium or ammonium ions). These anionic amphiphiles are widely employed in soaps and detergents. On the contrary, cationic amphiphiles feature a positively charged head group (quaternary ammonium) and a negatively charged counterion (halide ion). Zwitterionic amphiphiles, e.g. vesicle-forming phospholipid, contain both covalently linked positive and negative charges within their headgroups. The amphoteric nature of zwitterions allows them to maintain

the anionic behavior at high pH and cationic behavior at low pH. Common examples of non-ionic, anionic, cationic and zwitterionic amphiphiles are shown in Figure 1.8.[42]
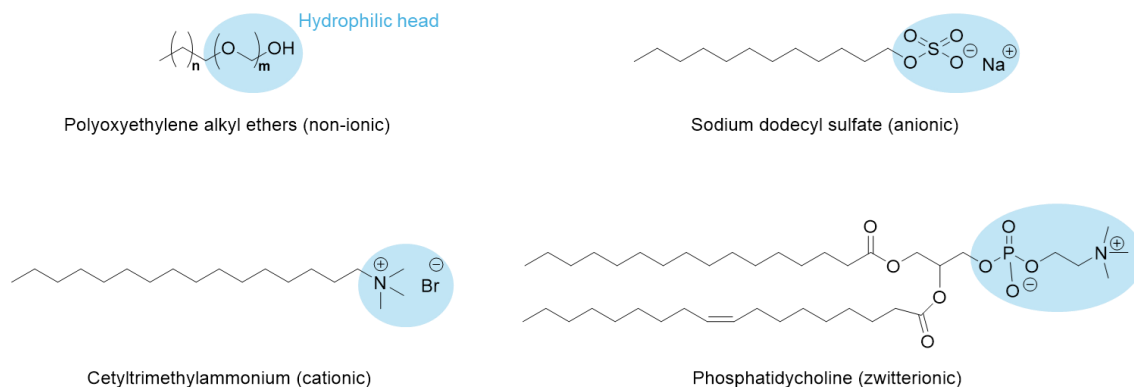
Figure 1.8 Common examples of non-ionic, anionic, cationic and zwitterionic amphiphiles.

The amphiphiles possessing both hydrophilic and lipophilic moieties, exhibit distinct interfacial behaviors in water. The polar hydrophilic head groups favorably interact with polar solvents, like water, while the nonpolar lipophilic tails tend to minimize the contact with the polar environment and migrate towards the interface. This behavior disrupts the interfacial cohesion leading to a microphase separation. In this case, self-assemblies of amphiphiles occur since the lipophilic tails tend to be sequestered from the polar solvent, forming micelles-like aggregates. Amphiphiles are usually called as surfactants due to their distinct ability to reduce interfacial tension. As such, these important properties of amphiphiles lead to widespread applications as detergents, emulsifiers, wetting and foaming agents.[43]
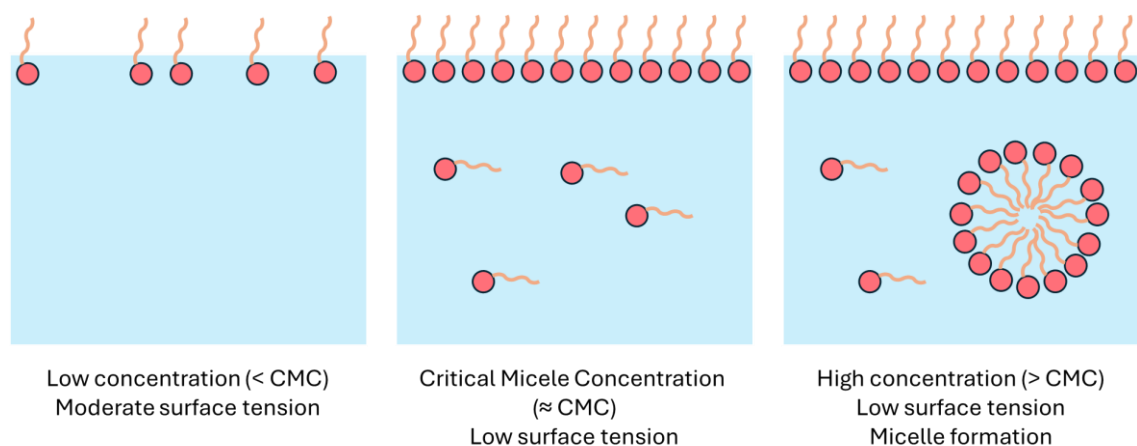
Figure 1.9 Micelle formation according to the concentration.

Micelles, self-assembled aggregates of amphiphilic molecules in solution, are formed when their concentration reaching above a specific concentration threshold known as the critical micelle concentration (CMC) (Figure 1.9). In aqueous solutions, normal micelles exhibit a core-shell structure: hydrophilic polar or ionic headgroups form the outer shell in contact with water, while the hydrophobic nonpolar tails sequestered in the interior. Conversely, amphiphiles can form reverse micelles in nonpolar organic media, where the polar headgroups constitute the core and the tails extending into the solvent. Spherical micelles are one of the most common forms of micelles, while other morphologies including bilayers, ellipsoids, and cylinders, are also observed. In some cases, micelles can grow into elongated structures, resembling long-chain polymers. Furthermore, amphiphiles can assemble into extended flat sheets lacking a close structure, which called lamellae structure. Amphiphiles are also able to form a closed bilayer structures called vesicles, which enclosing an aqueous core within a bilayer membrane. The hydrophilic head groups facing the outer aqueous solution and internal aqueous core, while the hydrophobic tails sandwiched between the two layers of hydrophilic heads. A schematic representation of different self-assembled structures is shown in Figure 1.10.[44]
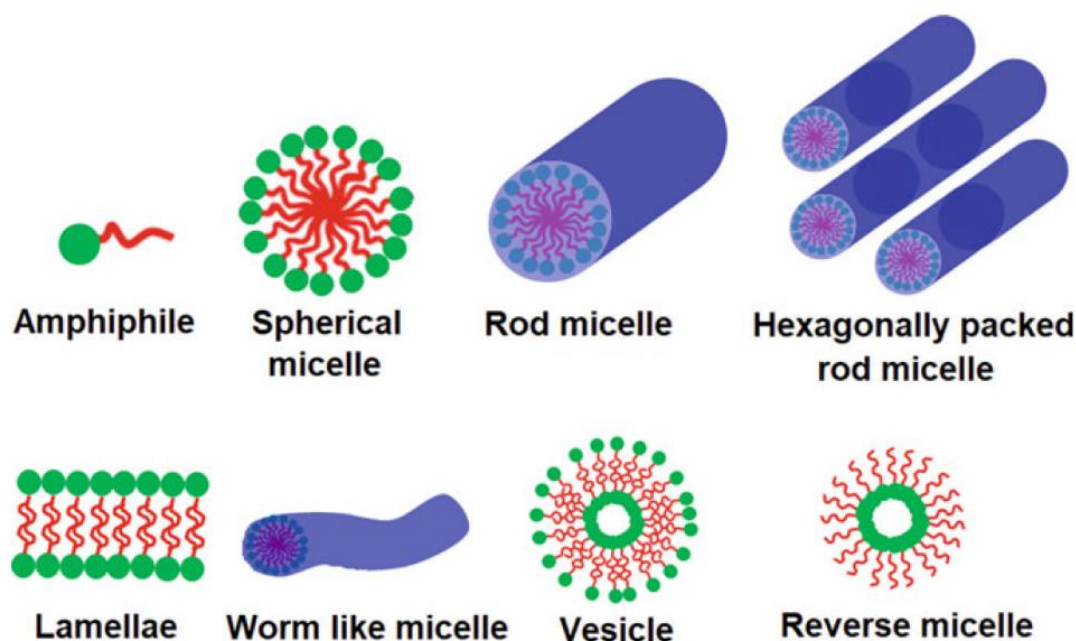
Figure 1.10 Schematic representation of different self-assembled structures of amphiphiles.[44]

1.5.2 Critical Packing Parameters

The formation of these self-assembled structures is governed by critical packing parameters. An initial estimate of aggregate morphology can be made using the critical packing parameter (C_{pp}), which is expressed mathematically by $C_{pp} = V_0/A_{mic}l_c$, where V_0 represents the volume of the hydrophobic tails within the aggregate core, A_{mic} is regarded as the area of the hydrophobic/hydrophilic interface, and l_c refers to the hydrophobic chain length.[45] The aggregate structure changes as the C_{pp} value increases: spherical ($C_{pp} \leq 1/3$), cylindrical ($1/3 \leq C_{pp} \leq 1/2$), and lamellar ($C_{pp} = 1$). Vesicles, a closed bilayer structures, are typically formed with the range of $1/2 \leq C_{pp} \leq 1$. For C_{pp} values exceeding 1, the aggregate structure can be changed to inverse micelles, in which the hydrophobic tails extend outward from centrally aggregated head groups surrounding

a water core.[43a] Figure 1.11 shows the predicted aggregate structures according to C_{pp} value. It is important to aware that C_{pp} value prediction for amphiphile aggregate morphology could be more challenging with more complex structures due to the complex interplay of intermolecular interactions and synergistic effects.
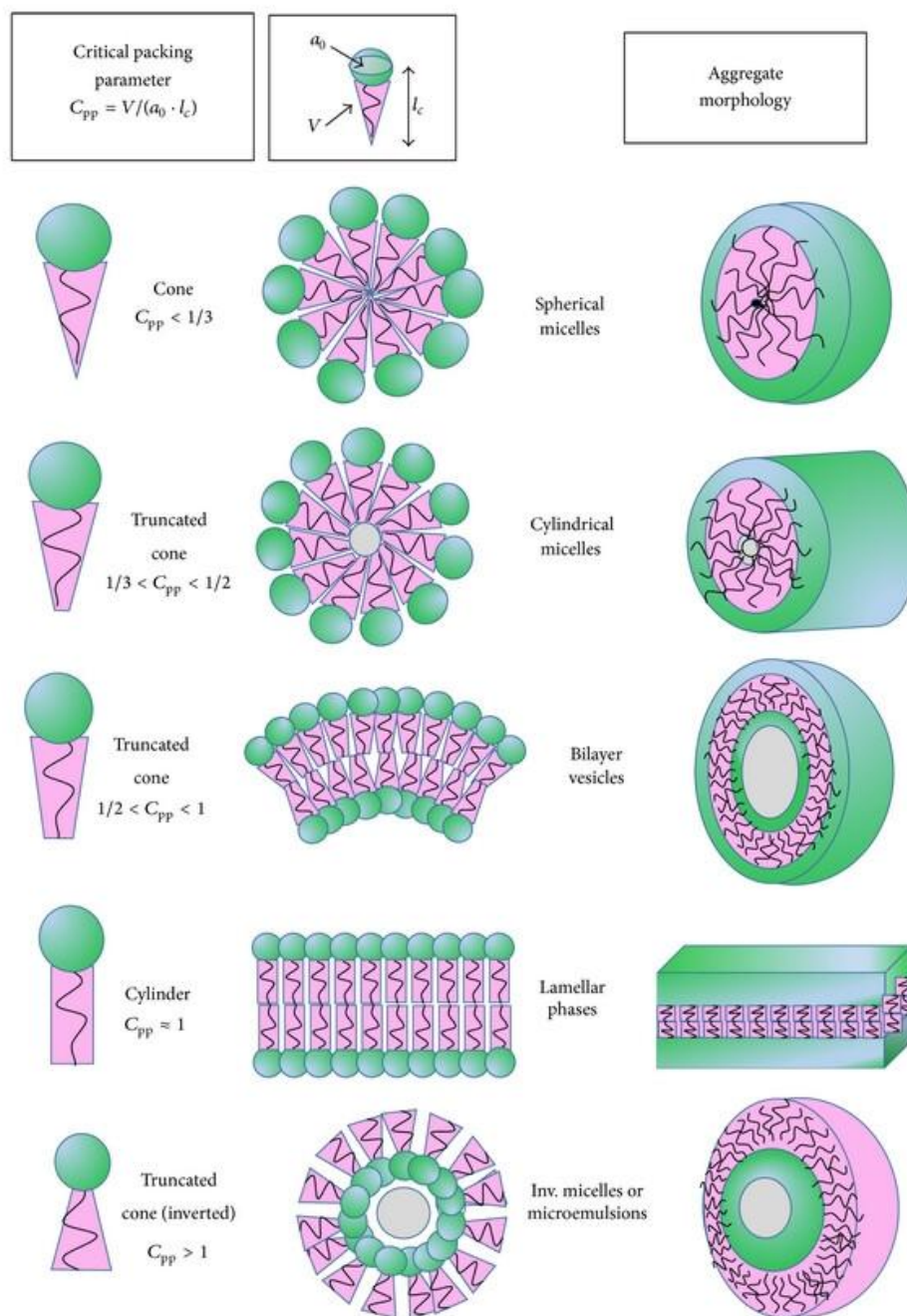
Figure 1.11 Predicted aggregate structures according to Cpp value.[42]

1.5.3 Amphiphilic Metal Complexes

Metal-ligand amphiphiles (or called metallosurfactants), initially developed since 1989, have gained recognition as a viable approach to conventional organic amphiphiles, offering the extensive structural diversity in metal-ligand complexes and the flexibility of ligand design. Similar to conventional surfactants, metallosurfactants can assemble into a variety of morphologies, such as micelles, vesicles, reverse vesicles, bilayers and disks, in which the aggregating behavior is affected by the interaction between lipophilic regions, hydrophilic headgroups, and specific metal-ligand interactions.[46] Importantly, the coordination between metal ions and surfactant molecule can change the molecular geometry and ionic charge of the amphiphile, leading to significant changes in aggregate structure. Furthermore, the location of metal ions within a surfactant significantly affects its properties and potential applications. Metallosurfactants can be categorized into three distinct types according to the position of the metal ion: (1) the metal ion with its primary coordination sphere serves as a hydrophilic head group, associated with a long hydrophobic tail,[47] (2) the metal ion conversely embeds within the hydrophobic group of the surfactant molecule,[48] and (3) the metal ion serves as the counterion weakly bonded to the ionic surfactant molecule,[49] as shown in Figure 1.12. This strategic positioning of metal ions provides a tunable feature of metallosurfactants.

(1)

Hydrophilic head

M

Metal ion

(2)

M

(3)

[⌃⌄⌃⌄⌃⌄ ⬭]⁺ [M]⁻
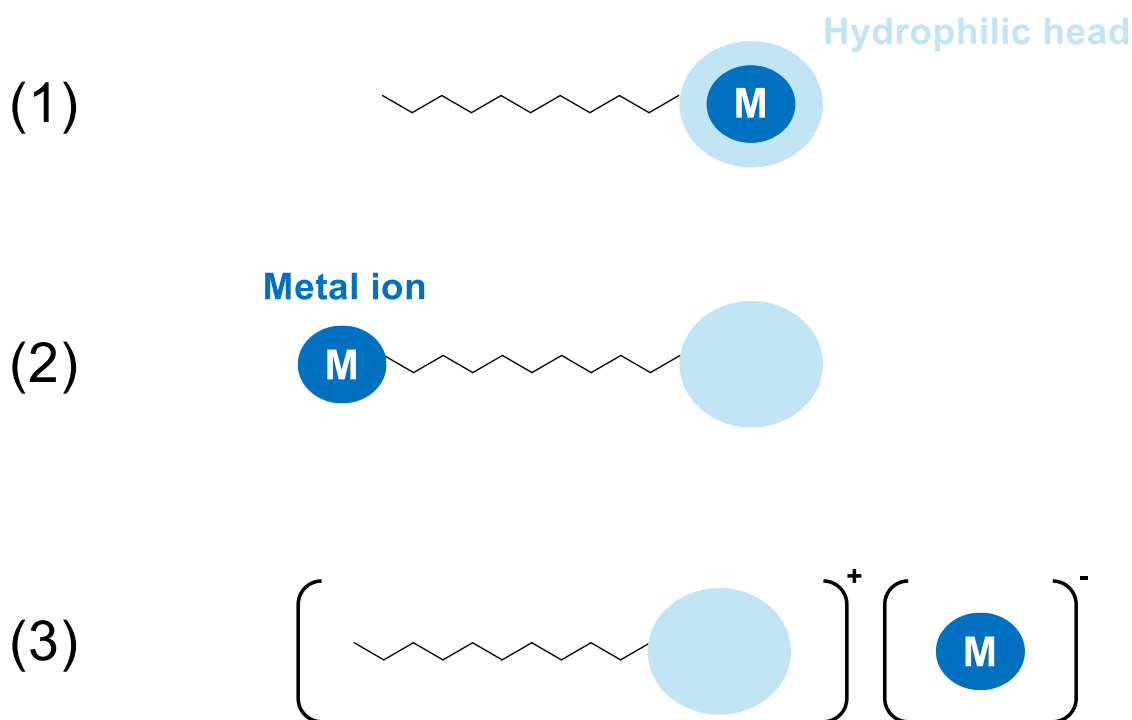
Figure 1.12 Three distinct types of metallosurfactants.

1.5.4   Properties of Metallosurfactants

Metallosurfactants have attracted substantial research interest due to their unique position bridging the fields of organometallic chemistry and surface science. Transition metal ions, as d- or f-block elements, have been known to exhibit unique chemical and physical properties. By incorporating a transition metal as a structural component, the surfactant molecules can be functionalized by sharing the unique properties from transition metal, such as oxidation states, catalytic ability, distinct colors, magnetism, and pH sensitivity.[50] Combining the intrinsic surface activity, metallosurfactants allow catalytic, redox, magnetic properties and pH sensitivities localized at the air-water interface.

1.5.5 Amphiphilic Gold(III) Complexes

Metallosurfactants have been found with a wide range of applications including the use as catalysts,[51] components of electronic materials,[52] medicinal agents,[53] and precursors for nanoparticle fabrication.[54] However, amphiphilic gold(III) complexes remain scarcely explored, with the first examples appearing only in 2016.

In 2016, Che *et al.* reported the first example of gold(III) complexes-based amphiphile.[55] Different to conventional amphiphile design, this amphiphilic gold(III) complex with a hydrophobic head and hydrophilic tail consisted of a fluorene modified C^N^C pincer ligand and a long poly(ethylene glycol) chain respectively to confer water solubility. The amphiphilic nature of the complex facilitated self-assembly into nanoscale micelles (Scheme 1.6), which exhibited a long-live emissive triplet excited state. This excited state property was successfully exploited for the generation of singlet oxygen via photoinduced energy transfer. *In vitro* studies demonstrated that the gold(III) amphiphile exhibited favourable biocompatibility, stability, and phototoxicity profiles. Notably, the self-assembling properties of the gold(III) amphiphile was shown to promote enhanced permeability and retention (EPR) effects, highlighting its potential for in *vivo* anticancer applications. In 2019, the same group reported supramolecular assemblies of the tridentate C^N^C-chelated gold(III) complexes controlled kinetically in a solution of acetonitrile and water.[56]
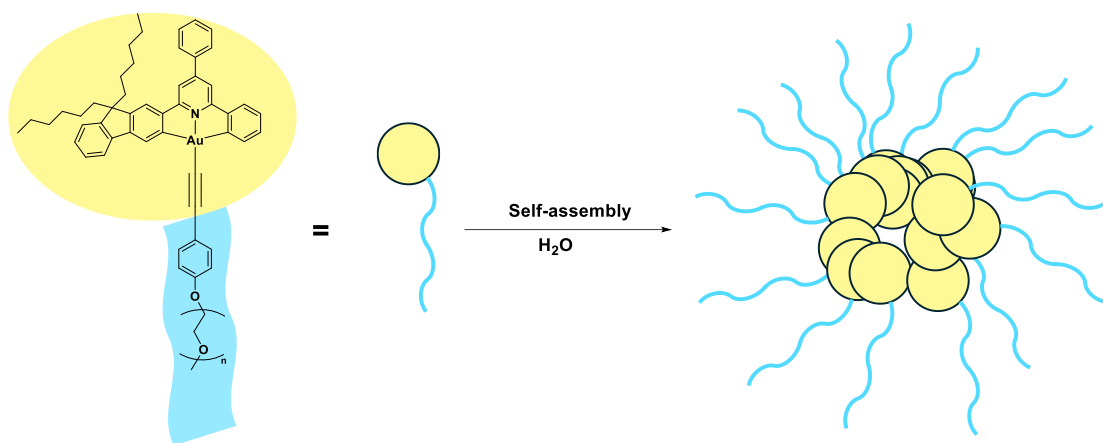
Scheme 1.6 Gold(III) amphiphile self-assembled to micelle in water.

In 2022, our group has developed a cyclometalated gold(III) amphiphile with supramolecular assembly in aqueous media.[57] The amphiphilicity of the complexes arised from the hydrophobic C,N-chelated phenylpyridine gold(III) dichloride core and the hydrophilic quaternary ammonium ion linked to the ligand by a long alky chain. Notably, the gold(III) amphiphile exhibited high aqueous solubility without implementing the poly(ethylene glycol) (PEG) moiety to increase hydrophilicity and no co-solvent system was required. In addition, the nanostructure of the gold(III) amphiphile in aqueous media could be finely tuned by counterion exchange affecting the supramolecular assembly, leading to a reversible supramolecular transformation (Scheme 1.7).
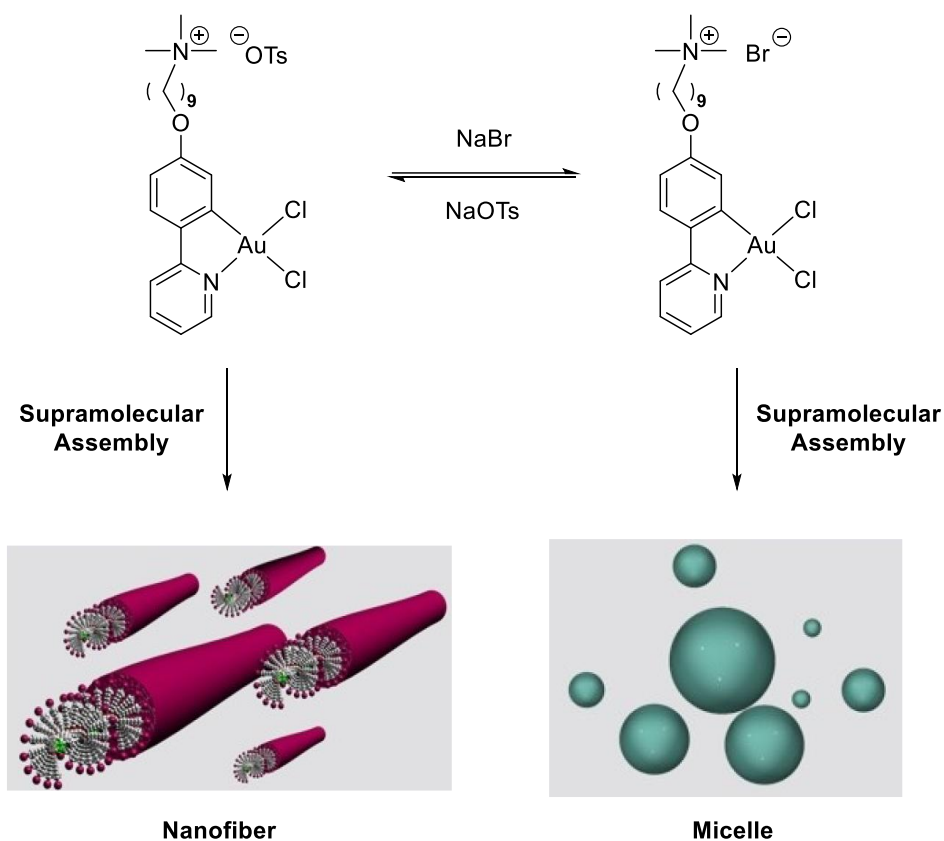
Scheme 1.7 Controllable supramolecular assemblies of cyclometalated gold(III) amphiphile.[57]

1.6 Luminescent Self-Assembled Transition Metal Complexes

1.6.1 Photophysical and Photochemical Properties of Transition Metal Complexes

The study of the photophysical and photochemical properties of transition metal complexes is of significant important due to their potential use as luminophors in organic light-emitting diodes (OLED).[58] Compared to the nonmetallic organic light emitters usually only generate fluoresces, transition metals have intense heavy atom effect as well as spin-orbit coupling that enhance intersystem crossing transitions to generate

luminescence from triplet excited states. The unique properties of transition metal, as d-block elements, having diverse oxidation states, electronic configurations, various choice of ligands allow numerous types of photoemissive electron transitions, such as metal-to-ligand charge transfers (MLCT), ligand-to-metal charge transfers (LMCT), ligand-to-ligand charge transfers (LLCT), and intraligand charge transfers (ILCT).[59] Among the transition metals, the photophysical and photochemical properties of the d^6 metal complexes (e.g., Re(I), Ru(II), Os(II), and Ir(III)) and d^8 metal complexes (e.g., Pt(II), Pd(II), and Au(III)) have been extensively studied due to their strong luminescent properties.[60]

Compared to the isoelectronic d^8 transition metals, including iridium(III) and platinum(II), which are known to exhibit rich luminescence, the luminescent gold(III) complexes are much less explored. This is probably attributed to the presence of non-emissive low-lying d-d ligand field states energetically close to the potentially emissive electron transitions, such as ILCT and MLCT, resulting in quenching of the luminescence excited states. Introduction of σ-donor ligands into the gold(III) center is now a common strategy to render the gold(III) complexes with luminescence properties at room temperature.[20, 61] The strong σ-donor ligands are responsible for increasing the ligand field strength as well as raising the energy of d-d ligand field states to enhance the luminescent properties. Cyclometalated alkynylgold(III) complexes have become the most common light-emitting gold(III) complexes which exhibit high thermal stability and strong luminescence in different media at ambient temperatures.[65]

1.6.1 Self-assembled Transition Metal Complexes with Luminescent Properties

Self-assembled transition metal complexes, combining with their photophysical and photochemical properties has become an important class of luminescent self-assemblies.[62] Transition metal complexes with their versatility in coordination modes enable the vast structural diversity and flexibility in molecular design. In addition to the non-covalent interactions (i.e. hydrogen bonding, metal coordination, hydrophobic effects, van der Waals forces, $\pi-\pi$ interactions and electrostatic interactions), the unique metal-metal interaction of transition metal has also been found to assist the supramolecular self-assembly. The luminescent properties of transition metal complexes are significantly influenced by the nature of both the transition metal center and the coordinating ligands. Together with the modification of ligand for manipulating the noncovalent interaction and fine-tuning the hydrophilicity and hydrophobicity, the interesting strategies of supramolecular self-assemblies in various structure and morphology can be designed.[63] Self-assembled transition metal complexes emerged with their luminescent properties offer a wide range of applications including chemosensing, biolabeling, molecular imaging,[64] fabrication phosphorescent OLEDs,[65] and photodynamic therapy.[60, 66]

1.6.2 Luminescent Gold(III) Amphiphiles

Gold(III) complexes show relatively low propensity of luminescence,[61a, 67] and gold(III)-gold(III) interaction is rarely observed,[68] which have limited the design and synthesis of luminescent self-assembled gold(III) complexes. The majority of examples

focused on discrete gold(III) complexes.[61a, 67, 69] Nevertheless, handful examples of luminescent gold(III) self-assembled complexes have been reported.

In 2019, Yam reported a new class of tridentate C^N^C chelated cyclometalated alkynylgold(III) complexes containing a cationic -CH$_2$NMe$_3^+$ group as hydrophilic moiety, together with the hydrophobic chains attached to the ligand that introduced amphiphilicity.[70] The X-ray crystallography indicated that the presence of π-π interaction between the complexes and the hydrophobic-hydrophobic interaction assisted the self-assembly process (Figure 1.13). One of the gold(III) amphiphiles was self-assembled in both polar solvent and non-polar solvent to generate nanofibers and nanorods respectively. The nanostructures were altered by the slightly change of the alkynyl ligand that possibly due to difference in molecular shape.
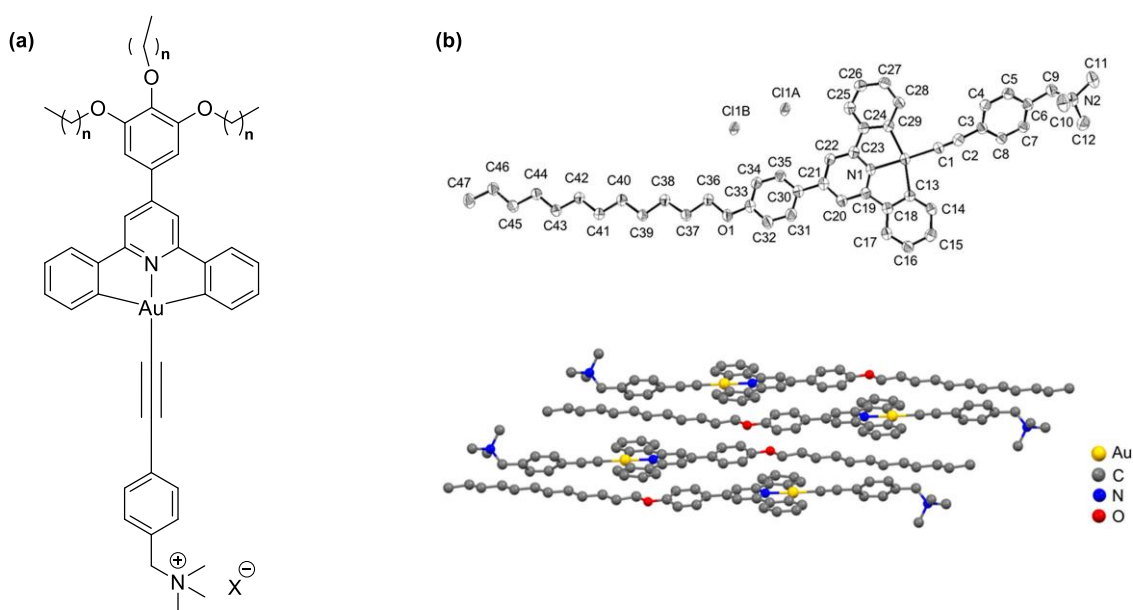
Figure 1.13 (a) Structure of amphiphilic alkynylgold(III) amphiphile **(b)** X-ray crystal packing diagram.[70]

1.7 Aims and Objectives

Gold catalysis exhibited the exceptional reactivity, great selectivity, and high functional group compatibility in a variety of organic transformations, which has been developed rapidly in recent decades. While asymmetric gold(I) catalysis has been extensively investigated, research into asymmetric gold(III) catalysis remains relatively underdeveloped. Nevertheless, several pioneering studies have highlighted the potential of chiral gold(III) complexes as efficient catalysts for enantioselective transformations. Despite of these advances, literature examples with enantioselectivity above 90% ee are limited. Therefore, the development of novel chiral gold(III) complexes continue to be of significant interest for enhancing enantioselectivity in asymmetric gold catalysis.

Throughout the years, our group has developed a series of chiral C,O- and O,O'-chelated cyclometalated gold(III) complexes, successfully applied to the enantioselective carboalkoxylation of 2-ethynylbenzaldehyde and its corresponding acetal derivative, achieving enantioselectivities of 41% and 90% ee, respectively. Our research has revealed a strong correlation between the steric bulkiness of the chiral oxazoline group of the gold(III) complex and the degree of chiral induction. However, the large-scale synthesis of chiral oxazoline ligands has been hampered by the need for expensive chiral starting materials and a time-consuming chiral preparative HPLC process. Therefore, establishing a more accessible synthetic route is crucial for further exploring the catalytic potential of these chiral gold(III) complexes in asymmetric transformations. This thesis explored the use of novel oxazoline-based gold(III) complexes in asymmetric carboalkoxylation of *ortho*-alkynylbenzaldehydes. The study focused on evaluating the catalytic activity of these complexes and developing a viable synthetic strategy for their preparation.

Besides, gold complexes have also been studied for the applications in bioconjugation strategies and optoelectronic materials due to the exceptional water stability. Amphiphilic design of gold(III) complexes were independently reported showing the self-assembling abilities of the cyclometalated gold(III) complexes. These cyclometalated gold(III) amphiphiles have been shown to be highly responsive to slight changes in molecular structure and resulting supramolecular nanostructures. In previous research, we have established the reversible modulation of supramolecular transformations of cyclometalated gold(III) amphiphiles in aqueous media, which achieved through the counterion exchange process. Compared to the well-developed organic amphiphiles, the chiral supramolecular assembly of gold(III) amphiphile systems is yet unknown. In this thesis, the new chiral cyclometalated gold(III) amphiphile was developed for supramolecular assembling in aqueous media.

Chapter 2 Development of Chiral C,O-Chelated Oxazoline-based BINOL/Gold(III) Complexes for Asymmetric Catalysis

2.1 Introduction

Over the years, our research group has developed various classes of chiral cyclometalated gold(III) complexes via coupling reactions between aromatic diol ligands and gold(III) dichloride precursors for enantioselective synthesis (Scheme 2.1a). In 2017, we reported a series of 1,1'-bi-2-naphthol (BINOL) derived C,O-chelated chiral oxazoline gold(III) complexes which was able to catalyze carboalkoxylation of 2-ethnylbenzaldehyde achieving 41% ee.[34] In 2019, our group developed a series of O,O'-chelated chiral oxazoline-based gold(III) catalysts derived from 4,4'-biphenol, which effectively catalyzed the enantioselective carboalkoxylation of the acetal derivative of 2-ethynylbenzaldehyde, achieving high enantioselectivity of up to 90% ee.[35] Despite the good performance in catalysis, the preparation of the chiral oxazoline gold(III) dichloride precursor relies on the expensive chiral resources, including either the use of chiral amino alcohols as the starting materials, or the enantiomeric separation of the racemic oxazoline compound (Scheme 2.1b). Both synthetic routes present significant limitations for large-scale production due to the high cost of chiral reagents and the labor-intensive, time-consuming preparative HPLC purification processes that require expensive HPLC-grade solvents. Hence, the development of simple approach to this class of cyclometalated chiral gold(III) complexes is important to explore their potential in asymmetric catalysis.

36

(a)

Angew. Chem. Int. Ed.,
2017, *56*, 3074.

Org. Lett., **2019**, *21*, 6289.

(b) **(1) Use of chiral preparative HPLC**

(2) Use of chiral building blocks
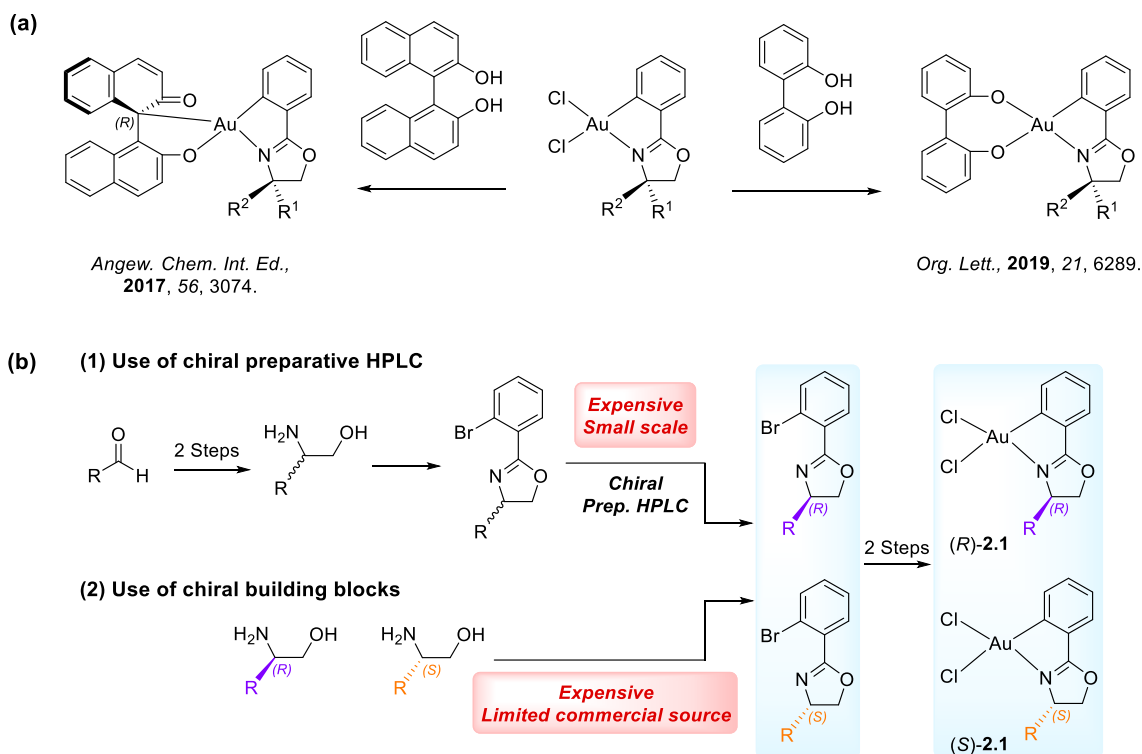
Scheme 2.1 **(a)** Synthesis of chiral cycometalated gold(III) complexes from gold(III) dichloride precursors; **(b)** previous reported preparation of chiral oxazoline ligands.

Considering the potential utility of enantiopure BINOL derivatives in chiral resolution, we envisioned that combining enantiomerically pure BINOL with racemic gold(III) dichloride complexes bearing sterically bulky substituents could offer a novel synthetic strategy to obtain optically pure C,O-chelated oxazoline-based BINOL/gold(III) catalysts for enantioselective transformations. In this chapter, we reported an efficient synthetic route to prepare optically pure C,O-chelated oxazoline-based BINOL/gold(III) complexes via diastereomeric resolution. Treatment of racemic oxazoline-based gold(III) dichloride complexes (*rac*)-**2.1a** with enantiomerically pure BINOL **2.2a**, an inexpensive chiral source, in the presence of Cs_2CO_3 in MeOH, afforded a mixture of diastereomeric gold(III) complexes. Remarkably, these diastereomers could be readily resolved by simple precipitation and filtration due to their distinct solubilities in MeOH, yielding

optically pure BINOL/gold(III) complexes **2.3a** in good yields. Furthermore, subsequent acid treatment enabled the isolation of enantiopure chiral oxazoline-based gold(III) dichloride complexes (*S*)-**2.1a** in good yields. Employing enantiopure (*S*)-**2.1a** as a chiral resolving agent allowed the efficient resolution of racemic BINOL derivatives, providing optically active BINOLs in good to excellent yields (overall 77 – 96%) with high optical purity of up to 99% ee. Additionally, the application of these newly synthesized chiral C,O-chelated oxazoline-based BINOL/gold(III) complexes as catalysts in the asymmetric carboalkoxylation of *ortho*-alkynylbenzaldehydes resulted in excellent enantioselectivities of up to 99% ee.

2.2   Results and Discussion

2.2.1   Synthesis of Optically Pure C,O-Chelated Oxazoline-based BINOL/Gold(III) Complexes from Racemic Gold(III) Dichloride Complexes by Diastereomeric Resolution using Chiral BINOL

1,1'-Binaphthalene-2,2'-diol (BINOL) and its derivatives constitute an important class of chiral compounds characterized by their distinctive axial chirality, and have been extensively investigated as O,O'-ligands in asymmetric catalysis.[71] Numerous methodologies have been developed for the chiral resolution of racemic BINOL, including enzymatic resolution, kinetic resolution, and chemical resolution via the formation of diastereomeric salts utilizing chiral auxiliaries.[72] In contrast, the reverse approach, employing enantiopure BINOL derivatives for the enantioselective resolution of racemic compounds, has been scarcely reported. Existing literature examples are limited to the enantioselective recognition of ammonium ions by enantiopure BINOL derivatives, resulting in the formation of chiral ammonium cations.[73] Notably, the

application of enantiopure BINOLs for the chiral resolution of racemic gold(III) complexes through the separation of corresponding diastereomeric complexes remains unexplored. Considering the potential utility of enantiopure BINOLs in chiral resolutions, we envisioned that combining enantiopure BINOL with racemic gold(III) dichloride complexes could offer a novel synthetic strategy achieving optically pure C,O-chelated oxazoline-based BINOL/gold(III) catalysts for enantioselective transformations.

Our investigation commenced with the reaction between chiral BINOL and an oxazoline-based gold(III) dichloride complex bearing a 2,4,6-trimethylphenyl substituent (Scheme 2.2). Treatment of the racemic oxazoline-based gold(III) dichloride complexes (*rac*)-**2.1a** with enantiomerically pure BINOL (*S*)-**2.2a** in the presence of Cs_2CO_3 in MeOH for 1 h resulted in the formation of a diastereomeric mixture of gold(III) complexes. Notably, the diastereomers (*R,R*)- and (*R,S*)-**2.3a** exhibited distinct solubility in MeOH. Diastereomer (*R,S*)-**2.3a** displayed high solubility, whereas (*R,R*)-**2.3a** exhibited limited solubility. Due to its poor solubility, (*R,R*)-**2.3a** readily precipitated from the reaction mixture and was isolated by filtration, followed by washing with MeOH and H_2O, affording the optically pure product in 43% yield. Subsequently, purification of the filtrate via flash column chromatography provided optically pure (*R,S*)-**2.3a** in 42% yield. The synthesized C,O-chelated oxazoline-based gold(III) complexes were characterized by ^{1}H NMR, ^{13}C NMR, HRMS and circular dichroism spectroscopy. The molecular structure of (*R,R*)-**2.3a** was confirmed by X-ray crystallographic analysis (CCDC 2355500). Consistent with our previous findings on C,O-chelated oxazoline-based BINOL/gold(III) complexes, axial-to-central chirality transfer was observed upon coordination of the O,O'-bidentate BINOL ligand to the oxazoline-based gold(III) complex, leading to the formation of the corresponding C,O-chelated gold(III) complexes.

The C,O-chelation mode involving the gold(III) center was confirmed by ^{13}C NMR spectroscopy, which revealed a characteristic carbonyl signal at approximately $\delta \approx 201$ ppm.
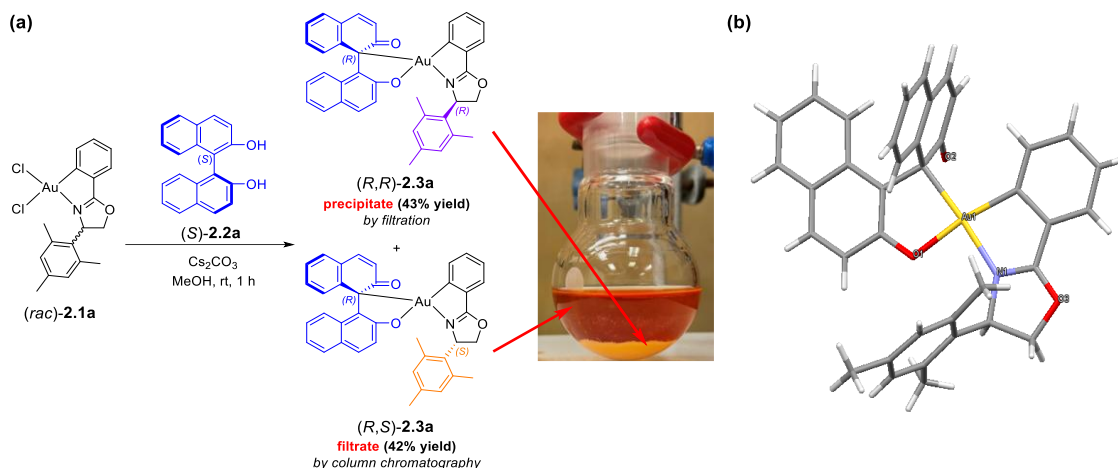
Scheme 2.2 (a) Synthesis of optically pure C,O-chelated gold(III) complexes by diastereomeric resolution using enantiopure BINOL (*S*)-**2.2a**; (b) X-ray crystal structure of (*R,R*)-**2.3a**.

To evaluate the efficiency of chiral resolution for (*rac*)-**2.1a**, we conducted the BINOL ligand substitution reaction of (*R,R*)-**2.3a** to regenerate (*R*)-**2.1a**. (*R,R*)-**2.3a** was dissolved in a mixed solvent of dichloromethane and methanol (DCM/MeOH), followed by treatment with 6 N HCl for 1 min. An immediate color change from red to colorless was clearly observed (Scheme S2.3). The reaction mixture was dried and purified by flash column chromatography, affording the enantiopure BINOL ligand (*S*)-**2.2a** and the oxazoline-based gold(III) dichloride complex (*R*)-**2.1a** in excellent yields of 95% and 91%, respectively. Importantly, the recovered (*S*)-**2.2a** maintained its optical purity (>99.5% ee) upon the central-to-axial chirality transfer after the acid treatment. These results indicated that the enantiopure BINOL ligand could be efficiently recovered without loss of optical purity throughout the entire process.

The successful preparation of optically pure C,O-chelated BINOL/gold(III) complexes from racemic gold(III) precursors and the subsequent regeneration of enantiomerically pure (*R*)-**2.1a** demonstrated the efficacy of employing enantiopure BINOL as a resolving agent for racemic complex **2.1a**. To further elucidate this novel synthetic strategy, we investigated the role of BINOL in differentiating the enantiomers through ^{1}H NMR spectroscopic analysis. Examination of the crude reaction mixture by ^{1}H NMR spectroscopy revealed clearly resolved peaks corresponding to the BINOL/gold(III) diastereomers, allowing straightforward determination of a diastereomeric ratio (dr) of 1:1. Following filtration, the precipitated diastereomer (*R,R*)-**2.3a** exhibited a diastereomeric purity exceeding 99:1, whereas the filtrate-contained diastereomer (*R,S*)-**2.3a** exhibited a dr of 72:28, as determined by ^{1}H NMR spectroscopy (Scheme 2.3). Given that the stereochemistry of the oxazoline ligand remains intact throughout the reaction, the enantiomeric excess (ee) of the chiral gold(III) dichloride complex **2.1a** obtained after the acid treatment directly correlated with the observed diastereomeric ratio of the resolved BINOL/gold(III) complexes (Scheme 2.3). These findings indicated that the BINOL ligand effectively functioned as a chiral resolving agent for (*rac*)-**2.1a**, facilitating clear differentiation of diastereomers via ^{1}H NMR spectroscopy. This distinctive resolving capability of chiral BINOL toward complex **2.1a** provided a significant advantage, enabling direct resolution of racemic gold(III) complexes. Typically, determination of the enantiomeric purity of chiral gold(III) catalysts via chiral HPLC is problematic due to the inherent instability of gold(III) complexes towards reduction, which may lead to the formation of gold nanoparticles and subsequent damage to costly chiral HPLC columns. In contrast, employing BINOL as a chiral resolving agent

allowed the facile assessment of optical purity for gold(III) catalysts through simple ^{1}H NMR analysis, circumventing the need for expensive chiral HPLC methods.
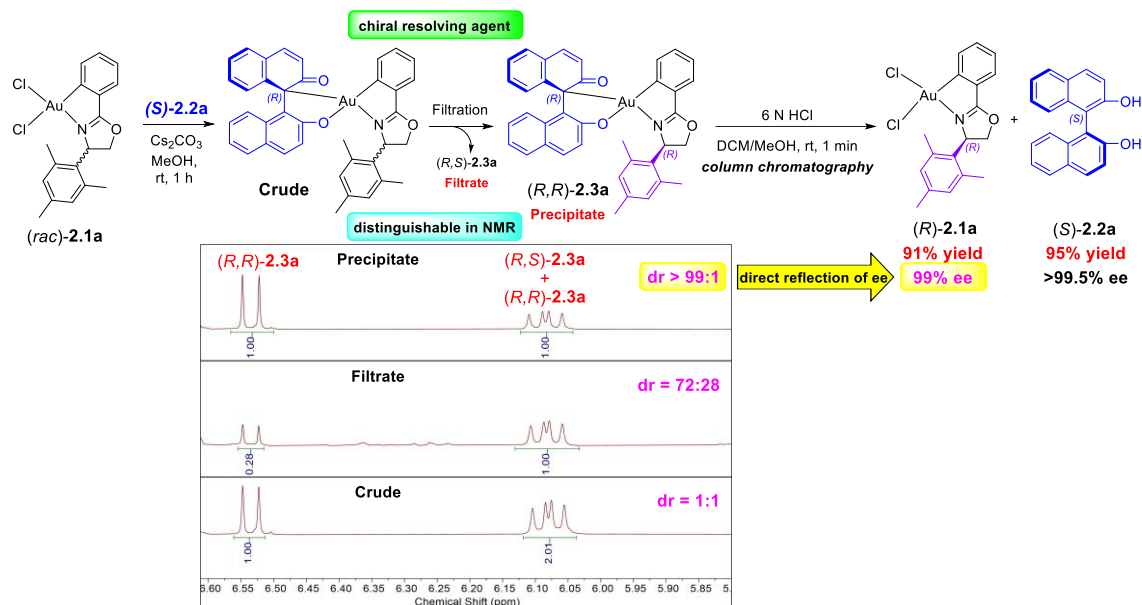
Scheme 2.3 ^{1}H NMR analysis for diastereomeric resolution of (*R*)-**2.1a** using BINOL (*S*)-**2.2a** as chiral resolving agent.

2.2.2   Column-Free Chiral Resolution of (*rac*)-2.1a in Gram Scale to Obtain Optically Pure Gold(III) Complexes 2.1a and 2.3a

A chromatography-free method was developed for the efficient chiral resolution of the racemic gold(III) complex (*rac*)-**2.1a**, enabling access to its optically pure form (*R*)- and (*S*)-**2.1a**, and the BINOL/gold(III) complexes **2.3a** (Scheme 2.4). Initially, **2.3a** were synthesized by reacting (*rac*)-**2.1a** (1.0 g, 1.878 mmol) with (*S*)-**2.2a** (590 mg, 2.066 mmol). Following filtration, diastereomers (*R*,*R*)-**2.3a** and (*R*,*S*)-**2.3a** were separately isolated, exhibiting diastereomeric ratios (dr) of >99:1 and 72:28 respectively as determined by ^{1}H NMR spectroscopy. Subsequently, treatment of (*R*,*R*)-**2.3a** with 6 N HCl for 1 min, followed by concentration and precipitation from methanol, afforded enantiomerically pure (*R*)-**2.1a** in 99% ee. Similarly, acid treatment of (*R*,*S*)-**2.3a** yielded

42

(*S*)-**2.1a** with 44% ee. To further enhance the optical purity of (*S*)-**2.1a**, the partially resolved (*S*)-**2.1a** (44% ee) was reacted with (*R*)-**2.2a** under standard coupling conditions, providing diastereomers (*S,S*)-**2.3a** and (*S,R*)-**2.3a** with diastereomeric ratios of 99:1 and 78:22, respectively. Subsequent acid-mediated dissociation of (*S,S*)-**2.3a** yielded enantiopure (*S*)-**2.1a** with 98% ee. As a result, this procedure provided the enantiopure gold(III) dichloride complexes (*R*)- and (*S*)-**2.1a** in a combined yield of 70%, without the need for chromatographic purification. The BINOL ligands (*S*)- and (*R*)-**2.2a** employed in this process could be recovered by column chromatography with yields exceeding 95% and maintaining their original optical purity. With the enantiomerically pure gold(III) dichloride complexes (*R*)- and (*S*)-**2.1a** readily available, the corresponding diastereomeric gold(III) complexes (*S,R*)- and (*R,S*)-**2.3a** could be synthesized in high optical purity through coupling reactions with the appropriate BINOL ligands.

Overall, a highly efficient methodology for the synthesis of chiral BINOL/gold(III) complexes with exceptional chirality transfer efficiency has been developed. Utilizing cost-effective enantiopure BINOL **2.2a** as a chiral resolving agent, the diastereomeric forms of BINOL/gold(III) complexes **2.3a** were effectively separated through simple filtration, achieving diastereomeric ratios exceeding 99:1 without requiring chromatographic purification. Subsequent acid treatment of the resolved complexes afforded enantiopure gold(III) dichloride **2.1a** in high yields, while simultaneously enabling excellent recovery of the BINOL resolving agent with preserved optical purity for recyclable applications. Gold(III) dichloride complexes represented essential intermediates that could be utilized in asymmetric catalytic reactions or as precursors for the synthesis of chiral oxazoline-based gold(III) catalysts. This straightforward and efficient methodology enabled the facile preparation of a diverse range of chiral gold(III)

dichloride derivatives, providing a robust platform for the design and synthesis of structurally diverse chiral gold(III) complexes.
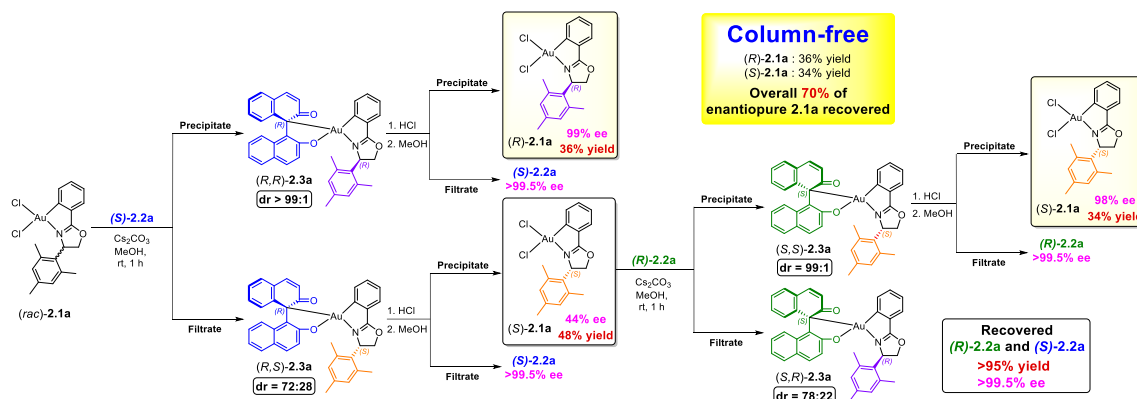
Scheme 2.4 A column-free process for chiral resolution of *(rac)*-**2.1a** to successively obtain optically pure gold(III) complexes **2.1a** and **2.3a**.

2.2.3 Chiral Resolution of Racemic BINOL Derivatives Enabled by Enantiopure Oxazoline-based Gold(III) Dichloride Complexes

Axially chiral biaryls, such as BINOL and its derivatives representing a prototypical structure with axial chirality, have found extensive applications in asymmetric catalysis.[71a-c, 74] The substitution pattern of BINOL significantly influenced both the steric and chiral environments, particularly in organocatalysts derived from bulky 3,3′-disubstituted BINOL motifs, which are capable of achieving high enantioselectivity.[74-75] Therefore, the development of enantiopure substituted BINOL derivatives has garnered significant interest. Various strategies have been explored for this purpose, including asymmetric oxidative coupling reactions, modifications of the enantiopure BINOL scaffold, chiral resolution, enzymatic hydrolysis/esterification, and central-to-axial chirality transformations.[71a, 72a-g, 76] While numerous methods have been established for the chiral resolution of simple BINOLs, efficient approaches for accessing enantiopure BINOL derivatives remain limited. Most reported methods focus on the chiral resolution

of BINOL derivatives substituted at the 4- to 7-positions, while the studies addressing the substituents at the 3-position are relatively scarce.[72a-g]

Previous studies have demonstrated the utility of chiral gold(III) complexes in the optical resolution of 1,16-dihydroxytetraphenylene (DHTP).[77] However, this reported strategy was limited to a benzyl-substituted chiral oxazoline gold(III) complex, while the phenyl-, isopropyl-, or *tert*-butyl-substituted analogs proved ineffective. These findings suggested a strong correlation between the substituent on the chiral oxazoline ligand and the formation of C,O-chelated gold(III) complexes, particularly impacting their solubility. It was hypothesized that the differential solubility of the diastereomers (*R,R*)- and (*R,S*)-**2.3a** stemmed from the 2,4,6-trimethylphenyl group on the oxazoline ligand. Building upon the successful diastereomeric resolution strategy employed in the synthesis of **2.3a**, it is postulated that the enantiopure gold(III) dichloride complex **2.1a** could serve as a versatile chiral resolving agent for a broader range of racemic BINOL derivatives.

The chiral resolving agent (*S*)-**2.1a** was employed to resolve several 3,3'-disubstituted BINOL derivatives (Scheme 2.5). The reaction of enantiopure (*S*)-**2.1a** with racemic BINOL **2.2b**, bearing 4-(2-naphthyl)phenyl substituents at the 3,3'-positions, was conducted in the presence of Cs_2CO_3 and MeOH for 1 h, yielding a crude mixture of diastereomeric BINOL/gold(III) complexes **2.3b**. The diastereomeric pair, (*R,S*)- and (*S,S*)-**2.3b**, was resolved using a hexane/acetone solvent system and separated via simple filtration. The filtration residue and filtrate were independently treated with 6 N HCl, followed by column chromatographic purification. This afforded (*R*)- and (*S*)-**2.2b** in excellent overall yield (96% based on 1 equivalent of racemic **2.2b**) and high

enantiomeric purity (96% and 99% ee, respectively). The chiral resolving agent, (*S*)-**2.1a**, was recovered in 95% yield after the resolution process.
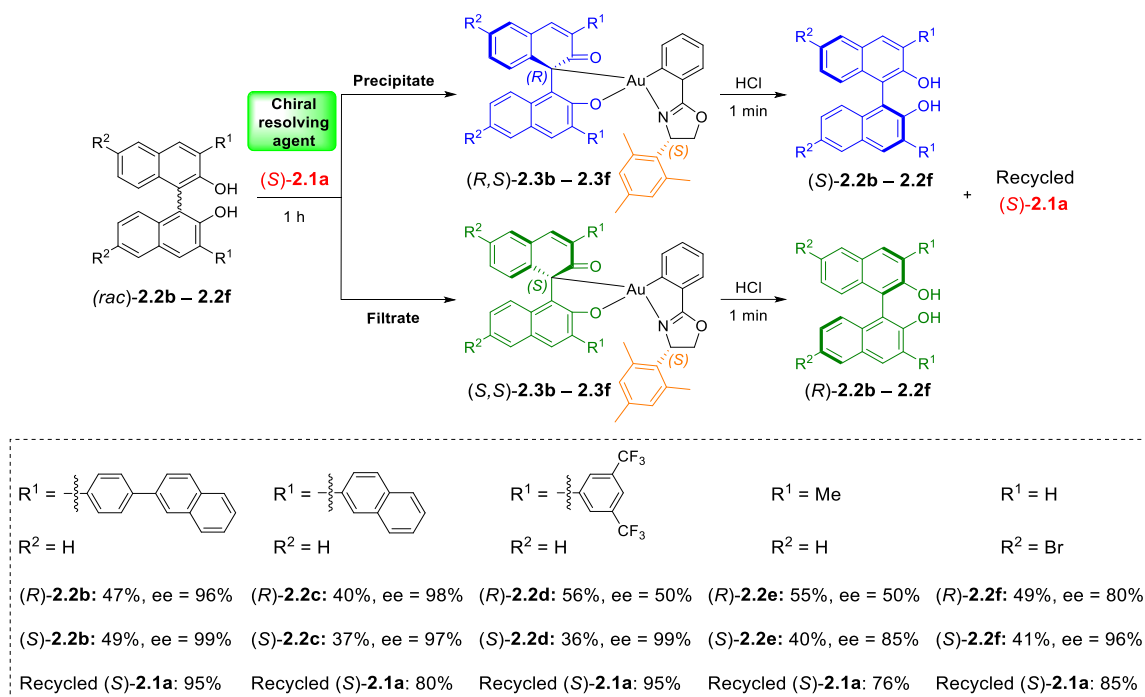
Scheme 2.5 Chiral resolution of BINOL derivatives using (*S*)-**2.1a**.

Employing a modified solvent system, we successfully resolved 3,3'-disubstituted BINOL derivatives **2.2c** - **2.2e**, featuring 2-naphthyl, 3,5-bis(trifluoromethyl)phenyl, and methyl substituents, respectively (see details in Experimental Section). Optically pure (*S*)-**2.2c**, (*S*)-**2.2d**, and (*S*)-**2.2e** were isolated in 36 – 40% yields (relative to one equivalent of racemic **2.2**) and with excellent enantiomeric excesses (85 – 99% ee). The corresponding enantiomers, (*R*)-**2.2c**, (*R*)-**2.2d**, and (*R*)-**2.2e**, were obtained in 40-56% yields and with 50 – 98% ee. The chiral resolving capability of (*S*)-**2.1a** was further demonstrated with 6,6'-disubstituted BINOL. (*rac*)-**2.2f** was resolved, yielding (*R*)- and (*S*)-**2.2f** in a combined 90% yield, with 80% ee and 96% ee respectively. These findings indicated that the differential solubility of the diastereomeric pairs (*R*, *S*)- and (*S*, *S*)-**2.3** is significantly affected by the substituents on the BINOL framework. Notably, BINOL

46

derivatives **2.2b** and **2.2c**, possessing bulky 4-(2-naphthyl)phenyl and 2-naphthyl groups at the 3,3'-positions, respectively, afforded high optical purity for both *R* and *S* enantiomers. The chiral resolving agent (*S*)-**2.1a** was recovered in 76 – 95% yield. To our knowledge, this represented the first example of chiral resolution of disubstituted BINOL derivatives utilizing enantiopure gold(III) dichloride complexes.

In short, a novel approach for the gold(III)-mediated chiral resolution of racemic disubstituted BINOL derivatives has been developed. This method offered a significantly reduced reaction time (approximately 1 h) compared to previously reported chemical resolution methods for BINOL derivatives, which typically require overnight or even multi-day procedures. The efficiency of this strategy is further highlighted by the excellent recovery of both the resolved chiral BINOLs (overall 77 – 96%) and the gold(III) complex (*S*)-**2.1a** (76 – 95%).

Notably, the chirality transfer process proceeded consecutively: initially from enantiopure BINOL **2.2a** to the gold(III) complex **2.1a**, and subsequently to the target BINOL derivatives **2.2b** – **2.2f**. This sequential chirality transfer was rapid, facile, and exhibited excellent enantioselectivity and yields. The method facilitated the convenient preparation of enantiopure BINOL derivatives, valuable chiral building blocks for the synthesis of diverse chiral ligands and organocatalysts. Furthermore, new optically pure C,O-chelated BINOL/gold(III) complexes **2.3b** – **2.3f** could be readily accessed. This novel methodology is anticipated to stimulate further advancements in the development of new chiral BINOL/gold(III) complexes.

2.2.4 Catalytic Activity of the Sterically Hindered Chiral C,O-Chelated BINOL/Gold(III) Complexes

Previous investigations into C,O-chelated oxazoline-based BINOL/gold(III) complexes revealed that the complex bearing an isopropyl substituent on the oxazoline ligand exhibited asymmetric catalytic activity, achieving 41% ee.[34] Subsequent studies on chiral O,O'-chelated cyclometalated gold(III) catalysts demonstrated a strong correlation between the steric bulk of substituents on the chiral oxazoline ligands and the enantioselectivity of the catalytic products.[35] To further study this correlation, we investigated the influence of ligand modification on reaction enantioselectivity. Consistent with our previously established design for chiral oxazoline ligands, enantiopure BINOL (*S*)-**2.2a** was reacted with chiral gold(III) dichloride complexes incorporating various bulky substituents on the chiral oxazoline ligands. This afforded chiral C,O-chelated oxazoline-based BINOL/gold(III) complexes (*R,R*)-**2.3g**, (*R,S*)-**2.3h**, (*R,R*)-**2.3i**, and (*R,R*)-**2.3j** in 78-85% yields (see details in Experiment Section).

The catalytic activity of these newly synthesized chiral catalysts was evaluated in the carboalkoxylation of *ortho*-alkynylbenzaldehydes. Given the facile preparation and purification of gold(III) complex (*R,R*)-**2.3a** via simple filtration, it was selected as the catalyst for reaction condition optimization (Table 2.1). 2-Ethynylbenzaldehyde **2.4a** served as the model substrate. In the absence of activator, the catalyst exhibited no activity (entry 1). Initial optimization studies employed 5 mol% catalyst and varied the acid activator (2.5 mol%). Acetic acid was ineffective, yielding no desired product (entry 2). *p*-Toluenesulfonic acid (TsOH), L-camphorsulfonic acid (L-CSA), and D-camphorsulfonic acid (D-CSA) afforded the desired product **2.5a** in 38 – 54% yield and 75-89% ee (entries 3-5). Chiral phosphoric acids bearing bulky aryl 3,3'-disubstituents

resulted in either low yields (entries 6-8, 16 – 27%) or no product formation (entry 9), despite exhibiting high enantioselectivities (entries 6-8, 75 – 90% ee). D-CSA was identified as the most effective acid, affording **2.5a** in 47% yield and 89% ee (entry 5), and was therefore selected for subsequent investigations.

The influence of acid loading on enantioselectivity was investigated by varying the catalyst:acid ratio from 4:1 to 1:5 (Table 2.1, entries 10-13). A catalyst:acid ratio of 4:1 (1.25 mol% D-CSA) resulted in low yield but high enantioselectivity (6% yield, 80% ee) (entry 10). Increasing the D-CSA loading to 2.5 mol%, 5 mol%, and 7.5 mol% improved both product yields and enantioselectivities to 45 – 50% and 83 – 89% ee, respectively (entries 5, 11-12). However, a further increase to a 1:5 catalyst:acid ratio (25 mol% D-CSA) led to a significant decrease in both yield and enantioselectivity (14% yield, 77% ee) (entry 13). Maintaining the catalyst:acid ratio at 2:1, which afforded the highest enantioselectivity (89% ee), the effect of catalyst loading was also examined (entries 14-15). Reducing the catalyst loading to 2.5 mol% resulted in a decrease in both yield and enantioselectivity (22% yield, 80% ee) (entry 14). Conversely, increasing the catalyst loading to 10 mol% did not improve either yield or enantioselectivity (37% yield, 88% ee) (entry 15). These results indicated that D-CSA loading had a moderate effect on enantioselectivity but a substantial impact on product yield. The optimal conditions, providing the highest enantioselectivity (89% ee, entry 5), were determined to be 5 mol% catalyst and 2.5 mol% D-CSA, maintaining a 2:1 catalyst:acid ratio. These conditions were selected for subsequent studies.

Table 2. 1 Screening of reaction conditions.[a]

Entry	Acid	Catalyst loading (mol %)	Acid loading (mol %)	Catalyst/ acid ratio	Yield (%) [b]	ee (%) [c]
1	/	5	0	/	n.d.	/
2	AcOH	5	2.5	2:1	n.d.	/
3	TsOH	5	2.5	2:1	54	75
4	L-CSA	5	2.5	2:1	38	80
5	**D-CSA**	**5**	**2.5**	**2:1**	**47**	**89**

6	BINOL-PO₂H-1	5	2.5	2:1	22	75
7	BINOL-PO₂H-2	5	2.5	2:1	27	90
8	BINOL-PO₂H-3	5	2.5	2:1	16	80
9	BINOL-PO₂H-4	5	2.5	2:1	n.d.	/
10	D-CSA	5	1.25	4:1	6	80
11	D-CSA	5	5	1:1	45	85
12	D-CSA	5	7.5	1:1.5	50	83
13	D-CSA	5	25	1:5	14	77
14	D-CSA	2.5	1.25	2:1	22	80
15	D-CSA	10	5	2:1	37	88

[a] Reaction conditions: 0.2 mmol of substrate **2.4a**, 2 mL of MeOH. [b] Isolated yield. [c] Determined by chiral HPLC.

To elucidate the reaction progress and product formation, a kinetic profile study of the carboalkoxylation of **2.4a** was conducted using ^{1}H NMR analysis (Scheme 2.6). The ^{1}H NMR spectrum of a mixture of **2.4a** and D-CSA (2.5 mol%) in CD$_3$OD revealed that **2.4a** was almost completely converted (<1% remaining) to its corresponding acetal form,

2.4a', which was the predominant species (>99%) (Scheme 2.6a). Notably, only 11% of **2.4a'** was observed in CDCl₃, suggesting that **2.4a'** was generated *in situ* in CD₃OD in the presence of D-CSA. Assuming complete conversion of **2.4a** to **2.4a'**, **2.4a'** was normalized to 100% yield at t = 0 for the kinetic profile. Upon addition of catalyst (*R*,*R*)-**2.3a**, the consumption of **2.4a'** and the formation of product **2.5a** were monitored over time. The results indicated that **2.4a'** was nearly completely consumed within 4 hours. A competing reaction, which was the formation of the hydration product **2.6a**, limited the yield of **2.5a** (Scheme 2.6b). Kinetic studies for other substrates are detailed in the Experimental Section.
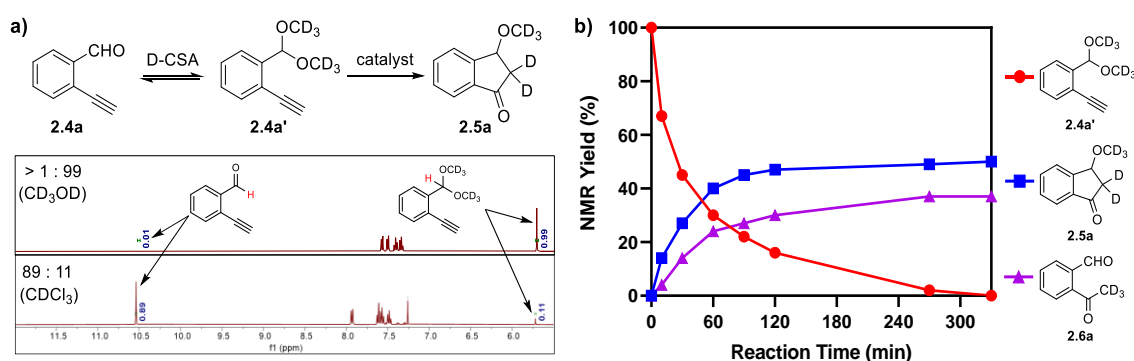
Scheme 2.6 (a) *In situ* generation of **2.4a'**; **(b)** Kinetic profile study of carboalkyoxylation of **2.4a**.

Having established the optimized reaction conditions, the influence of the ligand on product enantioselectivity was investigated (Table 2.2). Initially, the four enantiomers/diastereomers of the catalyst, (*R*,*R*)-, (*R*,*S*)-, (*S*,*R*)-, and (*S*,*S*)-**2.3a** (5 mol%), were employed with D-CSA (2.5 mol%) at room temperature. The desired products were obtained with high enantioselectivity (89% ee, -88% ee, 80% ee, and -89% ee, respectively) (entries 1-4). Notably, gold(III) complexes (*R*,*R*)- and (*R*,*S*)-**2.3a**, possessing opposite configurations at the oxazoline moiety, yielded products with similar

but opposite enantiomeric excess values (89% ee and -88% ee, respectively) (entries 1-2). A similar trend of opposing chiral induction was observed with (*S*,*R*)-**2.3a** and (*S*,*S*)-**2.3a**, which afforded 80% ee and -89% ee, respectively (entries 3-4). These findings suggest that the chiral induction in the reaction is predominantly governed by the chirality of the oxazoline ligand within the gold(III) catalysts, while the configuration of the BINOL ligand exerts a minimal influence on enantioselectivity. Thin-layer chromatography (TLC) analysis indicated complete consumption of substrate **4a** after 16 hours of stirring with all four catalyst enantiomers/diastereomers, resulting in product yields ranging from 25% to 47% (entries 1-4). To further elucidate the structural effects of the BINOL moiety, a series of gold(III) catalysts (*R*,*S*)-**2.3b**, (*S*,*S*)-**2.3b**, (*R*,*S*)-**2.3c**, (*S*,*S*)-**2.3c**, (*R*,*S*)-**2.3d**, and (*R*,*S*)-**2.3f**, which derived from chiral resolution of racemic BINOL derivatives with high diastereomeric ratios, were investigated (Table 2.2, entries 5-10). Compared to (*R*,*S*)- and (*S*,*S*)-**2.3a**, these catalysts exhibited relatively lower activity. Specifically, (*R*,*S*)-**2.3d** induced a rapid color change in the reaction mixture within 10 minutes under the optimized conditions, yielding product **2.5a** with 38% yield and -83% ee (entry 9). To enhance catalyst activation, the acid loading was increased for the remaining catalysts (entries 5-8 and 10). With an increased D-CSA loading of 10 mol% and an extended reaction time of 40 h, (*R*,*S*)-**2.3b** found to be the least reactive catalyst, resulting in low conversion and affording the product with low yield and ee (11% yield and 35% ee) (entry 5). This diminished reactivity may be attributed to the extremely poor solubility of (*R*,*S*)-**2.3b** in MeOH. Complete conversions were observed using catalysts (*S*,*S*)-**2.3b**, (*R*,*S*)-**2.3c**, (*S*,*S*)-**2.3c**, and (*R*,*S*)-**2.3f** in the presence of 5 mol% D-CSA, providing product **2.5a** with moderate yields and high enantiomeric excesses (27 – 45% yield, -75 to -90% ee) (entries 6-8 and 10). With the exception of the unreactive

(*R*,*S*)-**2.3b**, these results further supported that the substituents and configuration of the BINOL moiety exert a minimal influence on the enantioselectivity of the reaction. However, they demonstrate a significant impact on the activation process of the catalysts.

Table 2.2 Study of ligand configuration effect on enantioselectivity.[a]
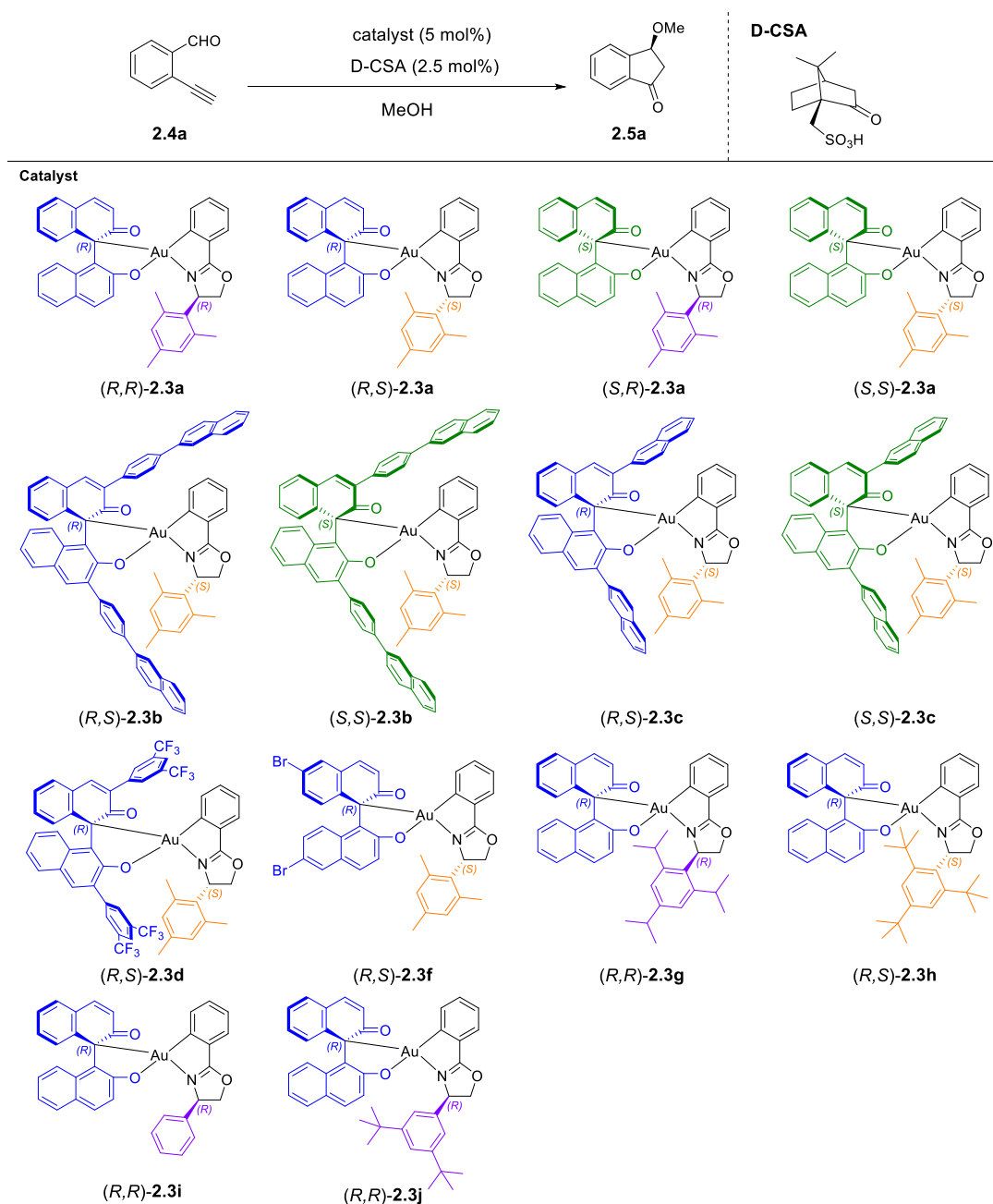
Entry	Catalyst	Temp (°C)	Reaction Time (h)	Yield (%) [b]	ee (%) [c]
1	(*R,R*)-**2.3a**	r.t.	16	47	89
2	(*R,S*)-**2.3a**	r.t.	16	37	-88
3	(*S,R*)-**2.3a**	r.t.	16	25	80
4	(*S,S*)-**2.3a**	r.t.	16	41	-89
5 [d]	(*R,S*)-**2.3b**	r.t.	40	11	-35
6 [e]	(*S,S*)-**2.3b**	r.t.	16	43	-87
7 [e]	(*R,S*)-**2.3c**	r.t.	16	43	-89
8 [e]	(*S,S*)-**2.3c**	r.t.	16	35	-90
9	(*R,S*)-**2.3d**	r.t.	16	38	-83
10 [e]	(*R,S*)-**2.3f**	r.t.	16	27	-75
11	(*R,R*)-**2.3g**	r.t.	16	34	92
12	(*R,S*)-**2.3h**	r.t.	16	32	-40
13	(*R,R*)-**2.3i**	r.t.	16	46	13
14	(*R,R*)-**2.3j**	r.t.	16	21	9
15	(*R,R*)-**2.3a**	4	16	49	92
16	(*R,R*)-**2.3a**	-20	40	36	96
17	(*R*,S)-**2.3a**	-20	40	30	-96

[a] Reaction conditions: 5 mol% of different catalysts, 2.5 mol% of D-CSA, 0.2 mmol of substrate **2.4a**, 2 mL of MeOH. [b] Isolated yield. [c] Determined by chiral HPLC. [d] 10 mol% of D-CSA. [e] 5 mol% of D-CSA.
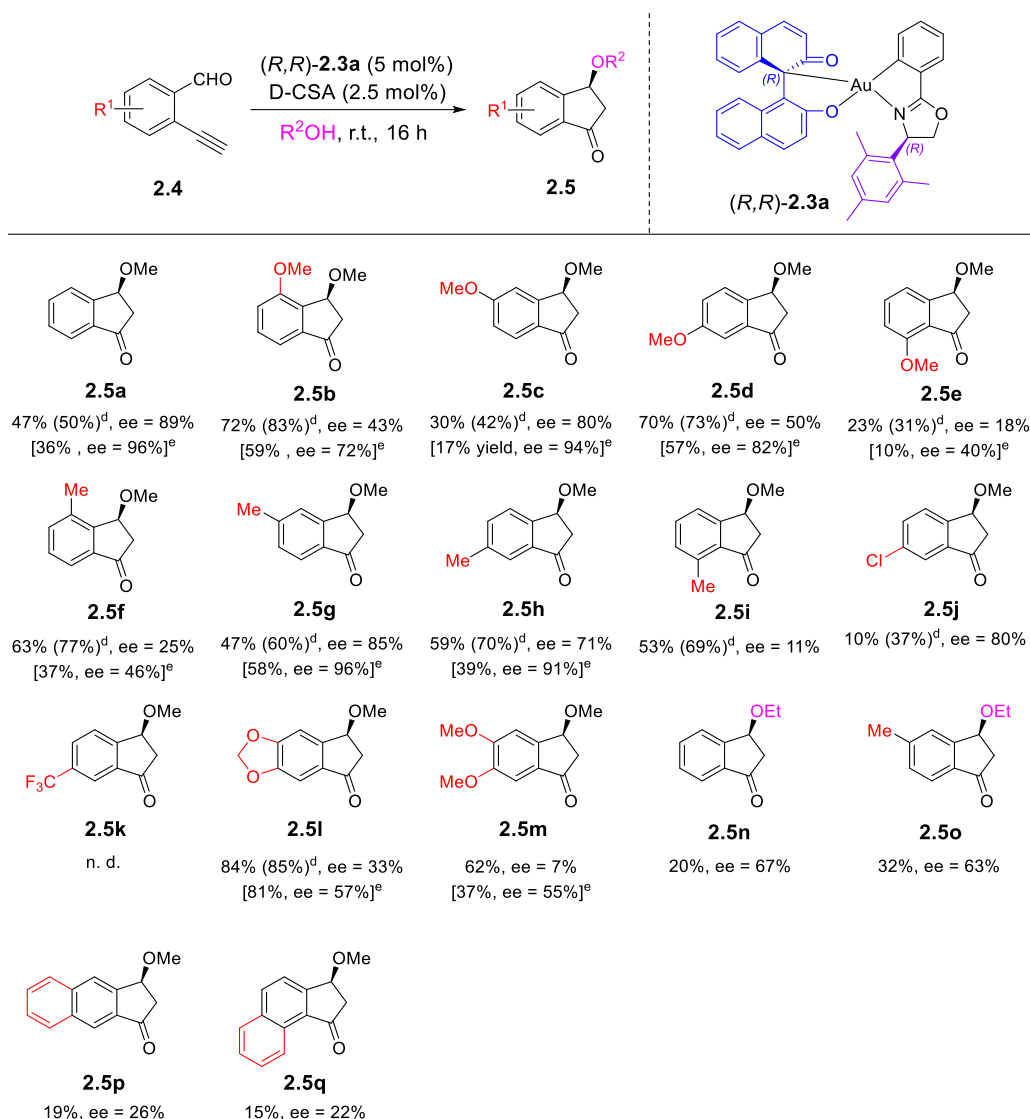
Given that the configuration of the oxazoline ligand dictated the direction of the product's optical rotation (Table 2.2, entries 1-4), the steric influence of the oxazoline

moiety on enantioselectivity was further investigated by modifying the substituents on the aryl group attached to the chiral oxazoline ring (entries 11-14). Increasing the steric bulk of the *ortho-* and *para-*substituents on the aryl group of the oxazoline moiety, catalyst (*R,R*)-**2.3g**, featuring a 2,4,6-triisopropylphenyl group, afforded an enhanced enantioselectivity of 92% ee under the optimized conditions (entry 11). In contrast, while (*R,S*)-**2.3a** provided -88% ee, (*R,S*)-**2.3h**, possessing a bulkier *tert*-butyl substituent, significantly diminished the enantioselectivity to -40% ee (entry 12). (*R,S*)-**2.3i**, with a simple phenyl group on the oxazoline moiety, yielded a low enantioselectivity of 13% ee (entry 13). These findings suggested that chiral induction could be enhanced by increasing the steric bulk of the substituents on the aryl group. However, the enantioselectivity plateaus, and could even decrease, with exceptionally bulky substituents. Furthermore, the steric effect of the *meta*-substituent on the aryl group was also investigated. Catalyst (*R,R*)-**2.3j**, bearing a *tert*-butyl substituent in the *meta*-position, yielded a poor enantioselectivity of 9% ee (entry 14), comparable to the 13% ee observed with (*R,R*)-**2.3i** bearing simple phenyl ring (entry 13). This result suggests that the *meta*-substituents are likely too distant to interact effectively with the incoming substrate during the enantiodetermining step of the reaction. Given that subtle changes in the *ortho*-substituent significantly impacted enantioselectivity (entries 1 and 11-12), the *ortho*-substituent of the aryl group is likely a key component influencing the enantioselectivity. Subsequently, the effect of temperature on enantioselectivity was examined using catalyst (*R,R*)-**2.3a** under the optimized conditions (entries 15-16). Cooling the reaction to 4 °C resulted in a similar yield, but with a slight improvement in enantioselectivity (49% yield, 92% ee) (entry 15). Further reducing the reaction temperature to -20 °C led to incomplete conversion of substrate **2.4a** after 16 hours, as observed by TLC, attributable to the

lowered reaction temperature. Extending the reaction time to 40 hours afforded the desired product **2.5a** with 36% yield and 96% ee (entry 16). Employing catalyst (*R,S*)-**2.3a** for the reaction at -20 °C also resulted in enhanced enantioselectivity of -96% ee (entry 17), demonstrating the temperature-dependent nature of the product's enantioselectivity.

Given the high catalytic activity of (*R,R*)-**2.3a** in the carboalkoxylation of **2.4a**, it was selected as the catalyst for investigating the substrate scope (Table 2.3). Under the optimized conditions, the carboalkoxylation of mono-substituted 2-ethynylbenzaldehydes **2.4b** – **2.4i** bearing electron-donating groups was performed, affording the corresponding products **2.5b** – **2.5i** with isolated yields of 23 – 72% and of 11 – 85% ee. These results were consistent with NMR yield analysis, which indicated good yields up to 83% (yields in parentheses). The broad range of ee values indicated that enantioselectivity was significantly influenced by the position of the substituents on the substrates. Products **2.5b**, **2.5e**, **2.5f**, and **2.5i**, with substituents at the 3- and 6-positions, were obtained with low enantioselectivity (11 – 43% ee). Lowering the reaction temperature to -20 °C led to an increase in enantioselectivity, affording the products with up to 72% ee. Conversely, products **2.5c**, **2.5d**, **2.5g**, and **2.5h**, with substituents at the 4- and 5-positions, were obtained with moderate to high enantioselectivity (50 – 85% ee) under optimized conditions, and excellent enantioselectivity (82 – 96% ee) at a reaction temperature of -20 °C. These findings suggested that substituents adjacent to the aldehyde and ethynyl groups of the substrates significantly diminished the enantiomeric excesses of the products, whereas *para*-substituents yielded relatively higher ee values. Based on the observation that 4-substituted products generally afforded relatively higher yields and enantioselectivities, substrates **2.4j** – **2.4k**, bearing electron-withdrawing groups at the

Table 2.3 Substrate scope of asymmetric carboalkoxylation catalyzed by (*R,R*)-**2.3a**.[a-c]

2.5a
47% (50%)[d], ee = 89%
[36% , ee = 96%][e]

2.5b
72% (83%)[d], ee = 43%
[59% , ee = 72%][e]

2.5c
30% (42%)[d], ee = 80%
[17% yield, ee = 94%][e]

2.5d
70% (73%)[d], ee = 50%
[57%, ee = 82%][e]

2.5e
23% (31%)[d], ee = 18%
[10%, ee = 40%][e]

2.5f
63% (77%)[d], ee = 25%
[37%, ee = 46%][e]

2.5g
47% (60%)[d], ee = 85%
[58%, ee = 96%][e]

2.5h
59% (70%)[d], ee = 71%
[39%, ee = 91%][e]

2.5i
53% (69%)[d], ee = 11%

2.5j
10% (37%)[d], ee = 80%

2.5k
n. d.

2.5l
84% (85%)[d], ee = 33%
[81%, ee = 57%][e]

2.5m
62%, ee = 7%
[37%, ee = 55%][e]

2.5n
20%, ee = 67%

2.5o
32%, ee = 63%

2.5p
19%, ee = 26%

2.5q
15%, ee = 22%
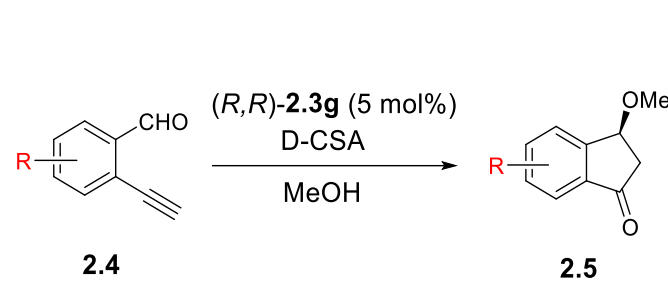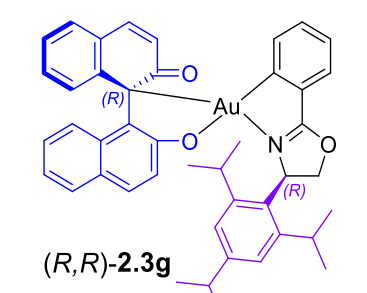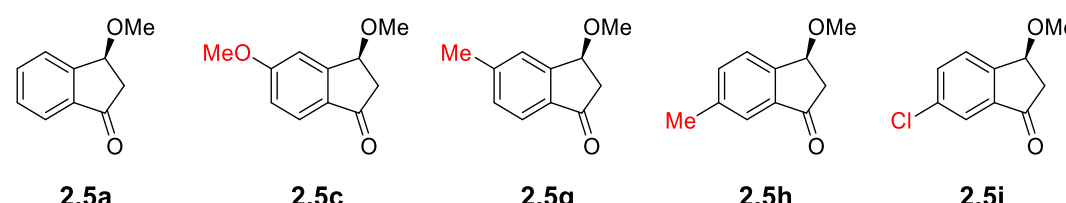
[a] Reaction conditions: 5 mol% of (*R,R*)-**2.3a**, 2.5 mol% of D-CSA, 0.2 mmol of different substrates, 2 mL of R²OH. [b] Isolated yield. [c] %ee of products were determined by chiral HPLC. [d] Yields determined by ¹H NMR spectroscopy with 1,3,5-trimethoxybenzene as an internal standard. [e] - 20 °C, 40 h.

4-position, were investigated. Product **2.5j** was obtained in low yield (10%) but with high enantioselectivity (80% ee), while product **2.5k** was not detected. This indicates that the presence of an electron-withdrawing group on the substrate significantly impacted the

reaction outcome. Disubstituted substrates **2.4l** and **2.4m** were also examined, yielding

moderate yields and poor enantioselectivities (62 – 84% yield, 7 – 33% ee). When ethanol

(EtOH) was employed as the solvent, the corresponding products **2.5n** and **2.5o** were

obtained with low yields and moderate enantioselectivities (20 – 32% yield, 63 – 67%

ee). Finally, *ortho*-ethynylnaphthaldehyde substrates **2.4p** and **2.4q** were subjected to the

catalytic conditions, resulting in poor yields and enantioselectivities (15 – 19% yield, 22

– 26% ee).

Encouraged by the aforementioned results, we investigated the use of (*R*,*R*)-**2.3g** as

a catalyst to further enhance enantioselectivity. Due to the lower catalytic activity of

(*R*,*R*)-**2.3g** in the carboalkoxylation reaction, a select group of substrates (**2.4a**, **2.4c**, **2.4g**,

2.4h, and **2.4j**) were chosen to evaluate its performance (Table 2.4). Initially, the reaction

of **2.4a** was conducted using 5 mol% of (*R*,*R*)-**2.3g** and 2.5 mol% of D-CSA at -20 °C;

however, the desired product was not determined (entry 1). Increasing the acid loading to

5 mol% resulted in the formation of product **2.5a** with an excellent enantioselectivity of

99% ee (entry 2). Under these modified conditions, products **2.5c**, **2.5g**, and **2.5h** were

obtained in low to moderate yields but with excellent enantioselectivities (16 – 52% yield,

92 – 99% ee, entries 3-5). In contrast, product **2.5j**, bearing an electron-withdrawing

group, was not determined (entry 6). Performing the reaction of substrate **2.4j** at room

temperature yielded the product in low yield but excellent enantioselectivity (17% yield

and 92% ee, entry 7). These results suggest that the oxazoline ligand of the gold(III)

catalyst, possessing a bulkier isopropyl substituent on the aryl ring, may lead to decreased

product yields but improved enantioselectivity.

Table 2.4 Substrate scope of asymmetric carboalkoxylation catalzed by (*R,R*)-**2.3g**.[a-c]

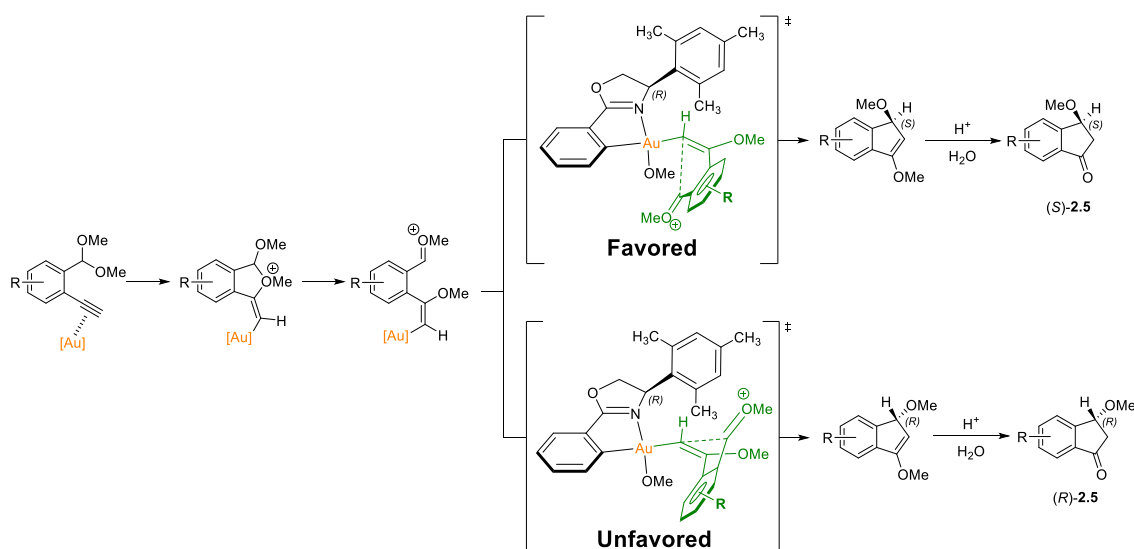| Entry	Product	D-CSA (mol %)	Temp (°C)	Reaction time (h)	Yield (%)[b]	ee (%)[c]
1	**2.5a**	2.5	-20	72	n.d.	/
2	**2.5a**	5	-20	72	12	99
3	**2.5c**	5	-20	72	16	97
4	**2.5g**	5	-20	72	52	99
5	**2.5h**	5	-20	72	43	92
6	**2.5j**	5	-20	72	n.d.	/
7	**2.5j**	5	rt	16	17	92

[a] Reaction conditions: 5 mol% of (*R,R*)-**2.3g**, 0.2 mmol of different substrates, 2 mL of MeOH. [b] Isolated yield. [c] Determined by chiral HPLC.

Scheme 2.7 Reaction mechanism of carboalkoxylation of *ortho*-ethynylbenzaldehyde

The mechanism of the carboalkoxylation reaction, previously investigated using density functional theory calculations,[78] proposed an initial activation of the substrate's alkyne group by the gold(III) catalyst, followed by intramolecular nucleophilic addition. The resulting cyclic acetal intermediates then undergo a Petasis-Ferrier rearrangement, generating an oxonium ion [-CH=(OMe)$^+$]. The subsequent 5-*exo-trig* cyclization is proposed to be the enantio-determining step. Two transition states within this enantio-determining step ultimately led to the formation of the enantiomeric products, (*S*)-**2.5** and (*R*)-**2.5**, respectively (Scheme 2.8b). Based on the experimental results, the BINOL ligand appears to exert a limited influence on enantioselectivity, suggesting that it may not be directly involved in the enantio-determining step. Conversely, the solvent likely participated in the transition state, as a change from MeOH to EtOH significantly diminished enantioselectivity. Furthermore, the substrate scope screening revealed a substantial impact of substrate substituents on enantioselectivity. This is potentially attributable to steric interactions between the substituents of the substrates and the bulky

chiral oxazoline moiety within the favored transition state, leading to a reduction in enantioselectivity.

In our previous work, we demonstrated the use of chiral C,O-chelated and O,O'-chelated cyclometalated gold(III) complexes for the enantioselective carboalkoxylation of 2-ethynylbenzaldehyde and its acetal derivative (yielding 41% and 90% ee, respectively),[34-35] in which the study focused on the development of more sterically hindered C,O-chelated cyclometalated gold(III) complexes. This was achieved by modifying the substituents on the aryl group attached to the chiral oxazoline moiety. By varying the steric bulk and position of these substituents, the enantioselectivity was increased from 9% to 92%, demonstrating the high sensitivity of enantioselectivity to structural modifications of the chiral ligands. Further optimization through a reduction in reaction temperature led to an enhancement of enantioselectivity, reaching up to 99% ee (Scheme 2.7). These findings underscore the considerable potential of chiral gold(III) complexes as effective catalysts in asymmetric synthesis.
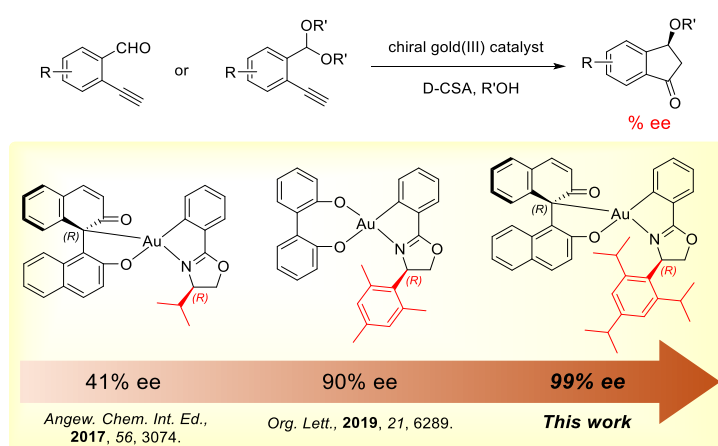
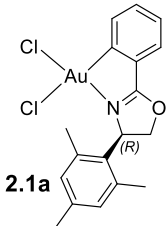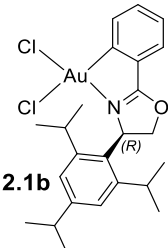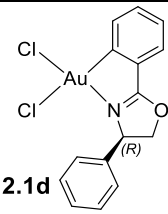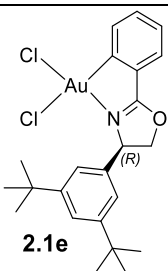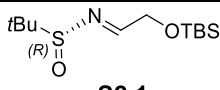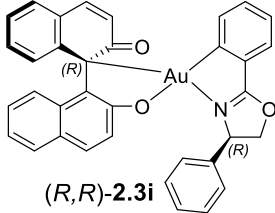**Scheme 2.8** Summary of our research on asymmetric gold(III) catalysis.

2.3 Conclusion

In summary, this work introduced a novel methodology for the preparation of optically pure C,O-chelated, oxazoline-based BINOL/gold(III) complexes via a diastereomeric resolution strategy. A facile, efficient, and column chromatography-free method was developed for the gram-scale chiral resolution of racemic, oxazoline-based gold(III) dichloride complexes, facilitated by a successful BINOL ligand substitution process. Concurrently, the resolved enantiopure gold(III) dichloride complexes demonstrated the capability to act as chiral resolving agents for disubstituted BINOL derivatives. These findings provided new opportunities for the development of chiral gold(III) complexes and gold(III)-mediated chiral resolution of BINOL derivatives. A consecutive chirality transfer process was successfully demonstrated, wherein chiral information was initially transferred from the inexpensive chiral source, BINOL, to the high-value gold(III) complexes, and ultimately to BINOL derivatives. Furthermore, the catalytic activity of this new class of C,O-chelated, oxazoline-based BINOL/gold(III) complexes was investigated in the asymmetric carboalkoxylation of *ortho*-alkynylbenzaldehydes, affording products with excellent enantioselectivity (up to 99% ee). It is anticipated that this work will broaden the applications of chiral gold(III) chemistry across various research fields.
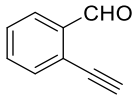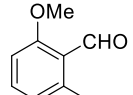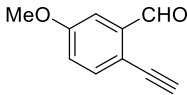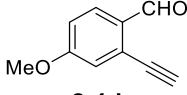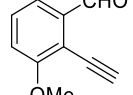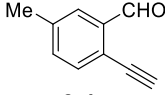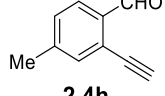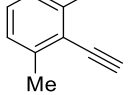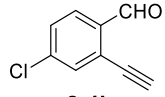
2.4 Experimental Section

2.4.1 General Procedures

All reagents were acquired from commercial suppliers and utilized without further purification. Flash column chromatography was performed with silica gel 60 (230-400 mesh ASTM). Thin-layer chromatography employed on precoated silica gel 60 F254 plates. ^{1}H and ^{13}C NMR spectra were obtained on a Bruker DPX-400 or DPX-600 spectrometer with TMS serving as the internal standard. ^{1}H NMR data are presented as chemical shift (δ, ppm), multiplicity (s = singlet; brs = broad singlet; d = doublet; dd = double doublet; t = triplet; td = triple doublet; tt = triple triplet; q = quartet; qd = quadruple doublet, m = multiplet), coupling constant (Hz), integration. ^{13}C NMR data are presented as chemical shift (δ, ppm). High-resolution mass spectra (HR-MS) were acquired on an Agilent 6540 UHD Accurate-Mass Q-TOF LC/MS system employing ESI ionization. X-ray crystallographic analysis for small molecule structural determination was carried out using a Bruker D8 Venture single crystal X-ray diffractometer. Previously reported compounds were characterized by comparing their ^{1}H and/or ^{13}C NMR spectra to the published data. Chiral phase high performance liquid chromatography (HPLC) was performed on Waters Alliance 2695 Separations Module with 2998 Photodiode Array (PDA) Detector using CHIRALPAK® and CHIRALCEL® columns (5µm, 4.6 mm x 250 mm).

2.4.2 Literature References

Structure	Reference
2.1a	J.-J. Jiang, J.-F. Cui, B. Yang, Y. Ning, N. C.-H. Lai, M.-K. Wong, *Org. Lett.*, **2019**, *21*, 6289 – 6294.
2.1b	J.-J. Jiang, J.-F. Cui, B. Yang, Y. Ning, N. C.-H. Lai, M.-K. Wong, *Org. Lett.*, **2019**, *21*, 6289 – 6294.
2.1d	J.-J. Jiang, J.-F. Cui, B. Yang, Y. Ning, N. C.-H. Lai, M.-K. Wong, *Org. Lett.*, **2019**, *21*, 6289 – 6294.
2.1e	J.-J. Jiang, J.-F. Cui, B. Yang, Y. Ning, N. C.-H. Lai, M.-K. Wong, *Org. Lett.*, **2019**, *21*, 6289 – 6294.
S2.1	J. C. Barrow, P. L. Ngo, J. M. Pellicore, H. G Selnick, P. G. Nantermet, *Tetrahedron Lett.*, **2001**, *42*, 2051 – 2054.
(*R,R*)-**2.3i**	J.-F. Cui, H.-M. Ko, K.-P. Shing, J.-R. Deng, N. C.-H. Lai, M.-K. Wong, *Angew. Chem. Int. Ed.*, **2017**, *56*, 3074 – 3079.

65

2.4a	M. D. Acqua, D. Facoetti, G. Abbiati, E. Rossi, *Synthesis*, **2010**, *14*, 2367 – 2378.
2.4b	H. Luo, C. He, H. Jiang, S. Zhu, *Chin. J. Chem.*, **2020**, *38*, 1052 – 1056.
2.4c	Y. Ohta, Y. Kubota, T. Watabe, H. Chiba, S. Oishi, N. Fujii, H. Ohno, *J. Org. Chem.*, **2009**, *16*, 6299 – 6302.
2.4d	J. Kong, F. Zhang, C. Zhang, W. Chang, L. Liu, J. Li, *Molecular Catalysis*, **2022**, *530*, 112633.
2.4e	W. Debrouwer, R. A. J. Seigneur, T. S. A. Heugebaerta, C. V. Stevens, *Chem. Commun.,* **2015,** *51***,** 729 – 732.
2.4g	W. Debrouwer, R. A. J. Seigneur, T. S. A. Heugebaerta, C. V. Stevens, *Chem. Commun.,* **2015**, *51*, 729 – 732.
2.4h	Y. Ohta, Y. Kubota, T. Watabe, H. Chiba, S. Oishi, N. Fujii, H. Ohno, *J. Org. Chem.*, **2009**, *74*, 6299 – 6302.
2.4i	G. He, C.Wu, J. Zhou, Q. Yang, C. Zhang, Y. Zhou, H. Zhang, H. Liu, *J. Org. Chem.*, **2018**, *83*, 13356 − 13362.
2.4j	J. Nejedlý, M. Šámal, J. Rybáček, I. G. Sánchez, V. Houska, T. Warzecha, J.Vacek, L. Sieger, M. Buděšínský, L. Bednárová, P. Fiedler, I. Císařová, I. Starý*, I. G. Stará* *J. Org. Chem.*, **2020**, *85*, 248 – 276.

2.4k (structure: benzaldehyde with CHO, ethynyl, and F₃C substituents)	J.-R. Deng, N. C.-H. Lai, K. K.-Y. Kung, B. Yang, S.-F. Chung, A. S.-L. Leung, M.-C. Choi, Y.-C. Leung, M.-K Wong, *Commun. Chem.*, **2020**, *3*, 67.
2.4l (structure: methylenedioxy benzaldehyde with CHO and ethynyl)	Z. Cao, H. Zhang, X. Zhang, L. Zhang, X. Meng, G. Chen, X.-E. Zhao, X. Suna, J. You, *RSC Adv.*, **2015**, *5*, 103155 – 103158.
2.4m (structure: dimethoxy benzaldehyde with CHO and ethynyl)	Z. Cao, H. Zhang, X. Zhang, L. Zhang, X. Meng, G. Chen, X.-E. Zhao, X. Suna, J. You, *RSC Adv.*, **2015**, *5*, 103155 – 103158.
2.4p (structure: naphthalene with CHO and ethynyl)	P.-S. Chen, C.-L. Tai, C.-H. Chou, *Tetrahedron Lett.*, 1998, **39**, 7381–7384.
2.4q (structure: naphthalene with CHO and ethynyl)	J.-R. Deng, N. C.-H. Lai, K. K.-Y. Kung, B. Yang, S.-F. Chung, A. S.-L. Leung, M.-C. Choi, Y.-C. Leung, M.-K. Wong, *Commun. Chem.*, 2020, **3**.
2.5a (structure: indanone with OMe)	J.-J. Jiang, J.-F. Cui, B. Yang, Y. Ning, N. C.-H. Lai, M.-K. Wong, *Org. Lett.*, **2019**, *21*, 6289 – 6294.
2.5c (structure: MeO-substituted indanone with OMe)	J.-J. Jiang, J.-F. Cui, B. Yang, Y. Ning, N. C.-H. Lai, M.-K. Wong, *Org. Lett.*, **2019**, *21*, 6289 – 6294.
2.5g (structure: Me-substituted indanone with OMe)	J.-J. Jiang, J.-F. Cui, B. Yang, Y. Ning, N. C.-H. Lai, M.-K. Wong, *Org. Lett.*, **2019**, *21*, 6289 – 6294.

2.5h	J.-J. Jiang, J.-F. Cui, B. Yang, Y. Ning, N. C.-H. Lai, M.-K. Wong, *Org. Lett.*, **2019**, *21*, 6289 – 6294.
2.5l	Z. Cao, H. Zhang, X. Zhang, L. Zhang, X. Meng, G. Chen, X.-E. Zhao, X. Suna, J. You, *RSC Adv.*, **2015**, *5*, 103155 – 103158.
2.5m	Z. Cao, H. Zhang, X. Zhang, L. Zhang, X. Meng, G. Chen, X.-E. Zhao, X. Suna, J. You, *RSC Adv.*, **2015**, *5*, 103155 – 103158.
2.5n	J.-J. Jiang, J.-F. Cui, B. Yang, Y. Ning, N. C.-H. Lai, M.-K. Wong, *Org. Lett.*, **2019**, *21*, 6289 – 6294.
2.5q	W. Zi, F. D. Toste, *J. Am. Chem. Soc.*, 2013, **135**, 12600 – 12603.

2.4.3 Preparation of Gold(III) Dichloride Complexes 2.1a-2.1e
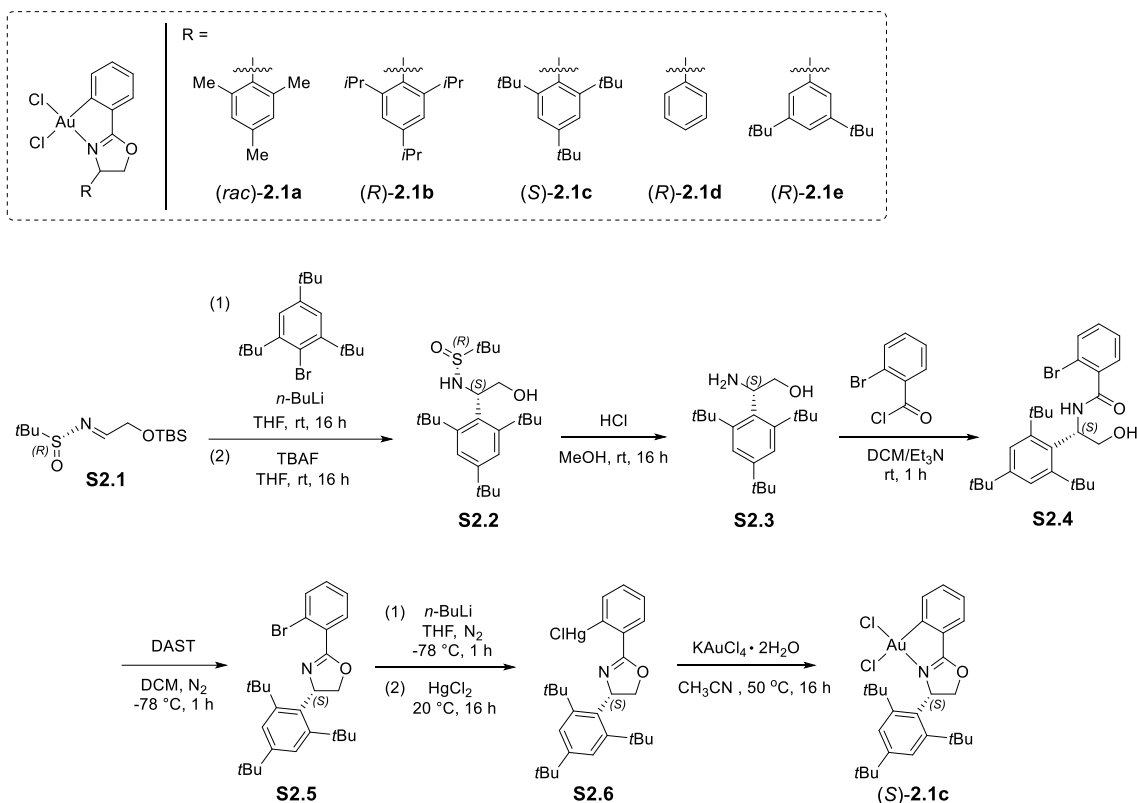
Scheme S2.1 Preparation of gold(III) dichloride complexes **2.1a**-**2.1e**.

The synthesis of compounds (*rac*)-**2.1a**, (*R*)-**2.1b**, (*R*)-**2.1d** and (*R*)-**2.1e** was accomplished and the characterization data was verified according to our previous publication.[79]

Compound **S2.1** was prepared and verified according to the literature characterization data.[35]

Compound **S2.2**: A solution of 2-bromo-1,3,5-tri-tert-butylbenzene (5.47 g, 16.8 mmol) in 90 mL anhydrous THF was cooled to 0 °C in N_2 environment. *n*-Butyllithium (*n*-BuLi, 1.6 M solution in hexane, 12.25 mL) was added dropwise to the solution and then warmed to room temperature. After stirring for 2 h, compound **S2.1** (3.89 g, 14 mmol) was

dissolved in 10 mL anhydrous THF and added dropwise into the solution. The reaction was stirred for further 16 h. The reaction was quenched with 30 mL sat. NH4Cl(aq) and extracted with ethyl acetate (50 mL × 3). The organic layer was dried with anhydrous MgSO4, concentrated, and purified by chromatographic column (hexane/EA) to yield a pale-yellow oil (2.32 g, 4.43 mmol, 32% yield). The oil was dissolved in 22 mL THF and added with tetra-n-butylammonium fluoride (TBAF, 1.0 M solution in THF, 5.27 mL) at 20°C for 16 h. The reaction was quenched with 30 mL water and extracted with ethyl acetate (20 mL × 3). The organic layer was dried with anhydrous MgSO4, concentrated, and purified by chromatographic column (hexane/DCM/EA) to yield the compound **S2.3** as a white solid (922 mg, 2.25 mmol, 51% yield).

Compound **S2.3**: Compound **S2.2** (865 mg, 2.11 mmol) was added into the solution containing 6 mL 12M HCl(aq) and 6 mL MeOH and stirred for 2 h at room temperature to afford the clear pale-yellow solution. The solution was adjusted to pH 12 at 0 °C, followed by the dilution with water, extraction with DCM (20 mL × 5), and washing with 30 mL brine. The organic layer was dried with anhydrous MgSO4, concentrated, and purified by chromatographic column (DCM/MeOH) to yield the compound **S2.3** as a white solid (638 mg, 2.08 mmol, 99% yield).

Compound **S2.4**: Compound **S2.3** (611 mg, 2 mmol) was dissolved in 2 mL DCM with 1 mL triethylamine (Et3N) and cooled to 0 °C followed by the dropwise addition of 2-bromobenzoyl chloride (483 mg, 2.2 mmol, 287 μL). The solution was warmed to room temperature and stirred for 1 h. The reaction was quenched with 10 mL water, extracted with ethyl acetate (10 mL × 3), and washed with 30 mL brine. The organic layer was dried with anhydrous MgSO4, concentrated, and purified by chromatographic column

(hexane/acetone) to yield the compound **S2.4** as a white solid (713 mg, 1.46 mmol, 73% yield).

Compound **S2.5**: Compound **S2.4** (691 g, 1.42 mmol) was dissolved in 10 mL dry DCM and cooled to to -78 °C under N_2. Diethylaminosulfur trifluoride (DAST, 251 mg, 1.56 mmol, 204 µL) was added dropwise, and the mixture was stirred for 1 hour. Potassium carbonate (K_2CO_3, 179 mg, 2.13 mmol) was added to the solution and warmed to room temperature and stirred for further 1 h. The reaction was quenched with the slowly added sat. $NaHCO_{3(aq)}$ until no bubble coming out, extracted with DCM (30 mL × 3), and washed with 30 mL brine. The organic layer was dried with anhydrous $MgSO_4$, concentrated, and purified by chromatographic column (hexane/EA) to yield the compound **S2.5** as a white solid (563 mg, 1.20 mmol, 84% yield).

Compound **S2.6**: Compound **S2.5** (471 g, 1 mmol) was dissolved in 5 mL anhydrous THF cooled to to -78 °C under N_2. *n*-butyllithium (*n*-BuLi, 1.6 M solution in hexane, 938 µL) was added dropwise to the solution and the mixture was stirred for 1 h. $HgCl_2$ (326 mg, 1.2 mmol) was add and the solution was warmed to room temperature and stirred for further 16 h. The reaction was quenched with water, filtered through celite, extracted with DCM (10 mL × 3), and washed with 30 mL brine. The organic layer was dried with anhydrous $MgSO_4$, concentrated, and purified by chromatographic column (hexane/DCM) to yield the compound **S2.6** as a white solid (333 mg, 0.532 mmol, 53% yield).

Compound (*S*)-**2.1c**: Compound **S2.6** (265 mg, 0.423 mmol) and $KAuCl_4·2H_2O$ (193 mg, 0.465 mmol) were added in 2 mL CH_3CN and was heated to 65 °C for 16 h. The reaction mixture was dried, resuspended in DCM, and filtered through celite. The filtrate was

concentrated and purified by chromatographic column (hexane/acetone) to yield the compound (*S*)-**2.1c** as a white solid (145 mg, 0.220 mmol, 52% yield).
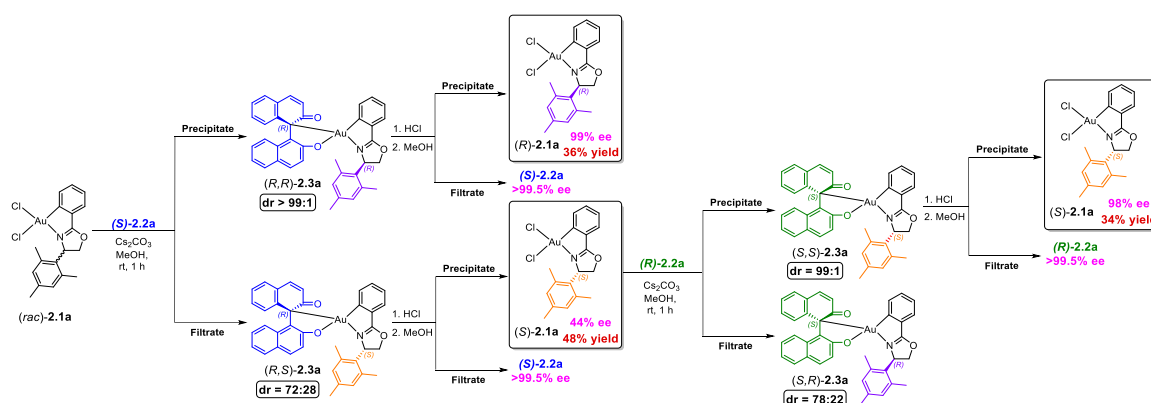
2.4.4 Column-Free Chiral Resolution Method for Preparation of Gold(III) Dichloride Complexes (*R*)-2.1a and (*S*)-2.1a

Scheme S2.2 Column-free chiral resolution of gold(III) dichloride complexes (*R*)-**2.1a** and (*S*)-**2.1a**.

Diastereomeric resolution: A mixture of racemic cyclometalated gold(III) complex (C^N)AuCl$_2$ (*rac*)-**2.1a** (1.0 g, 1.878 mmol, 1.0 equiv.), BINOL (*S*)-**2.2a** (590 mg, 2.066 mmol, 1.1 equiv.) and Cs$_2$CO$_3$ (1.34 g, 4.132 mmol, 2.2 equiv.) were added in 10 mL MeOH and stirred for 1 h at room temperature. Orange red precipitate mixed with a red solution was observed. The precipitate was collected by filtration which was then washed with methanol and dried under vacuum, yielding the C,O-chelated oxazoline-based BINOL/gold(III) complex (*R,R*)-**2.3a** with dr > 99:1 as orange red solid. Besides, The filtrate was processed by dilution with EA and washing with water. After concentrating the resulting solution under reduced pressure, hexane was added to precipitate the crude BINOL/gold(III) complex complex (*R,S*)-**2.3a** with dr = 72:28 as orange red solid.

Acid treatment: The obtained (*R,R*)-**2.3a** was dissolved in DCM/MeOH (1:1, 20 mL) resulting in a red solution. After addition of 6 N hydrochloric acid (0.94 mL, 5.634 mmol, 3 equiv.) at room temperature, the color of the solution immediately changed from red to colorless within 1 min. After removing the solvent under reduced pressure, a crude mixture of (*R*)-**2.1a** and (*S*)-**2.2a** was obtained. Methanol was added to this mixture for suspension, the precipitate was filtered to afford (*R*)-**2.1a** (99% ee) as white solid (360 mg, 0.676 mmol, 36% yield). Using the same method for (*R,S*)-**2.3a**, (*S*)-**2.1a** (44% ee) was obtained as white solid (480 mg, 0.902 mmol, 48% yield). Two filtrates were combined and purified by chromatographic column to recover the BINOL (*S*)-**2.2a** (560 mg, 1.962 mmol, 95% yield).
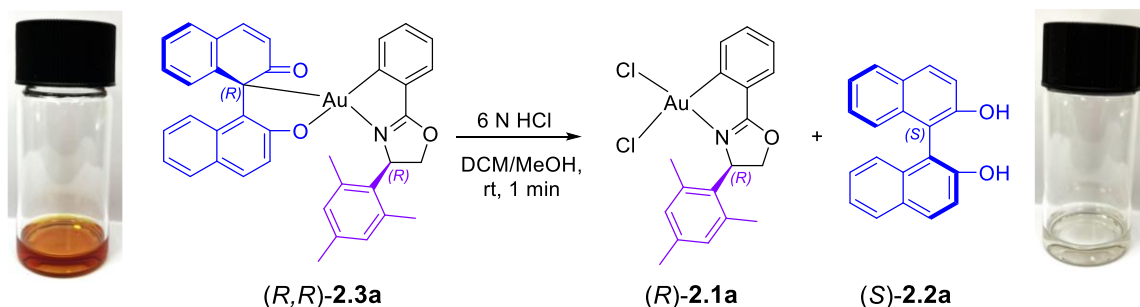
Scheme S2.3 Acid treatment of (*R,R*)-**2.3a** to give (*R*)-**2.1a** and (*S*)-**2.2a**.

Repeat the diastereomeric resolution method with (*S*)-**2.1a** (44% ee) by changing the resolving agent to (*R*)-**2.2a** (284 mg, 0.992 mmol, 1.1 equiv) to give (*S,S*)-**2.3a** (dr = 99:1) and crude (*S,R*)-**2.3a** (dr = 78:22). After acid treatment for (*S,S*)-**2.3a**, (*S*)-**2.1a** (98% ee) was obtained (280 mg, 0.638 mmol, 34% yield) and BINOL (*R*)-**2.2a** was recovered (272 mg, 0.952 mmol, 96% yield).
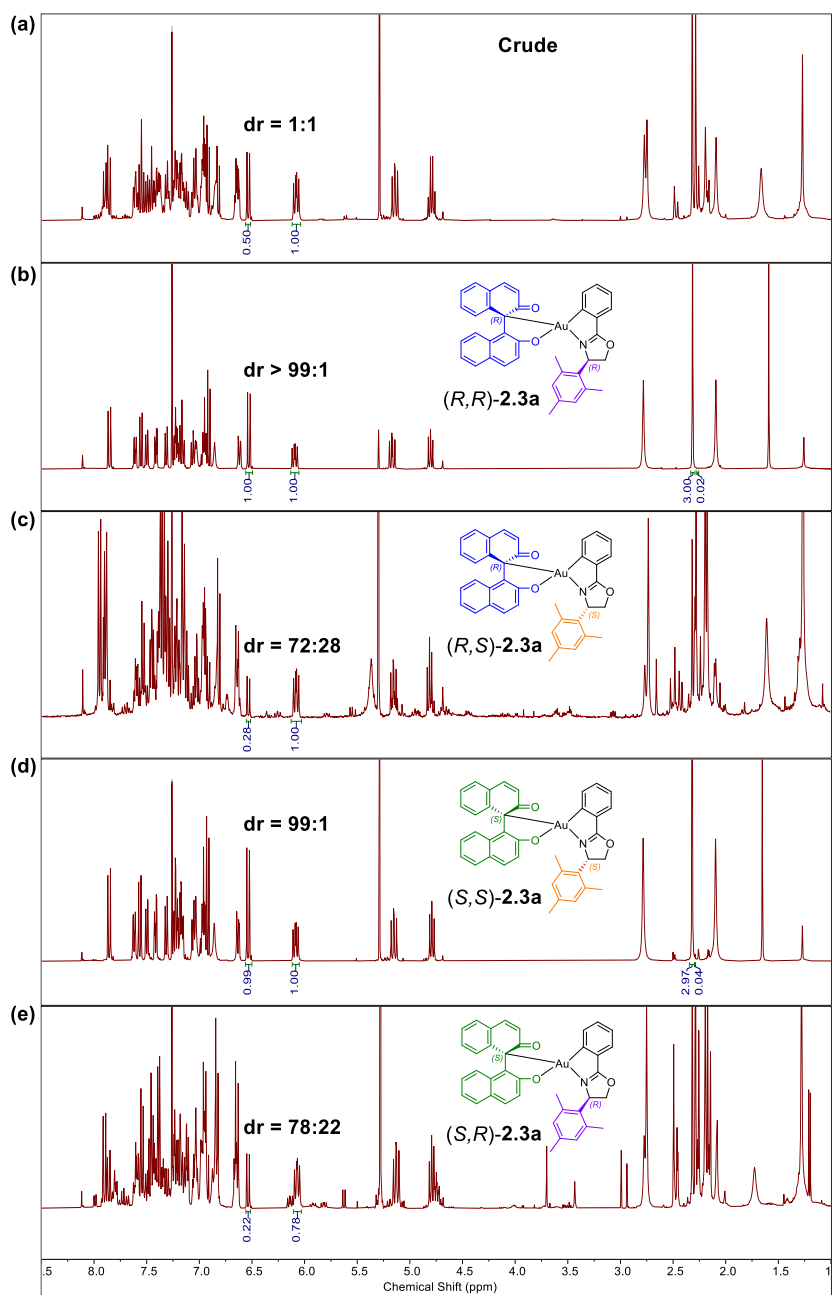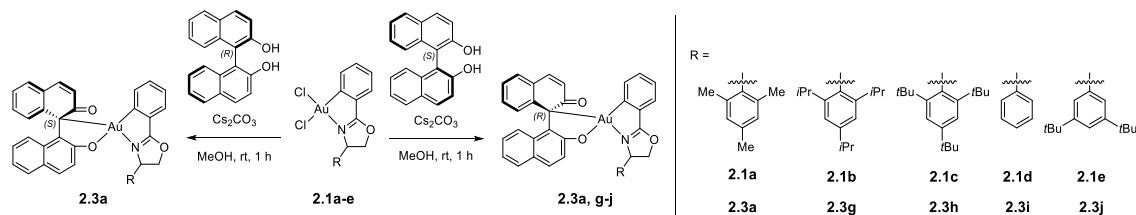
Figure S2.1 Determination of dr of **(a)** crude mixture of **2.3a**; **(b)** (*R*,*R*)-**2.3a**;

(c) (*R*,*S*)-**2.3a**; **(d)** (*S*,*S*)-**2.3a**; **(e)** (*S*,*R*)-**2.3a** by ^{1}H NMR analysis.

2.4.5 Preparation of BINOL/Gold(III) Complexes

Scheme S2.4 Preparation of BINOL/gold(III) complexes **2.3a**, **g-j**.

(*R,R*)-**2.3a** (602 mg, 0.808 mmol, 43% yield) and (*S,S*)-**2.3a** (504 mg, 0.676 mmol, 36% yield) can be prepared by the above diastereomeric resolution method using (*rac*)-**2.1a**.

(*R,S*)-**2.3a** and (*S,R*)-**2.3a** were synthesized using similar procedure: The enantiopure cyclometalated gold(III) complex, either (*S*)-**2.1a** or (*R*)-**2.1a** (22.0 mg, 0.0413 mmol, 1.1 equiv.), was reacted with the corresponding enantiomer of BINOL, (*S*)-**2.2a** or (*R*)-**2.2a** (10.8 mg, 0.0376 mmol, 1.0 equiv.), respectively, in the presence of Cs_2CO_3 (26.9 mg, 0.0826 mmol, 2.2 equiv.) in MeOH for 1 h at room temperature. After filtration through celite, the reaction mixture was diluted with EA and washed with water. The organic layer was concentrated and the product was precipitated by addition of hexane, affording the desired BINOL/gold(III) complex as orange-red solids (*R,S*)-**2.3a** (23.8 mg, 0.0320 mmol, 85% yield) and (*S,R*)-**2.3a** (25.2 mg, 0.0338 mmol, 90% yield) respectively.

(*R,R*)-**2.3g**, (*R,S*)-**2.3h**, (*R,R*)-**2.3i** and (*R,R*)-**2.3j**: The enantiopure cyclometalated gold(III) complex (C^N)AuCl$_2$ **2.1** (1.0 equiv.) was reacted with BINOL (*S*)-**2.2a** (1.1 equiv.) in the presence of Cs_2CO_3 (2.2 equiv.) in 2 mL MeOH for 1 h at room temperature. Orange red precipitate was formed in a suspension. The resulting precipitates were collected by filtration, washed with methanol, and dried under vacuum to afford the desired C,O-chelated cyclometalated BINOL/gold(III) complex (*R,R*)-**2.3g** (orange red

solid, 78 mg, 0.0935 mmol, 85% yield), (*R,S*)-**2.3h** (salmon orange solid, 20 mg, 0.0229

mmol, 78% yield), (*R,R*)-**2.3i** (orange solid, 237 mg, 0.337 mmol, 82% yield) and (*R,R*)-

2.3j (orange solid, 114 mg, 0.140 mmol, 82% yield).

2.4.6 Synthesis of C,O-Chelated BINOL/Gold(III) Complexes 2.3b-f and Resolution of BINOLs 2.2b-2.2f
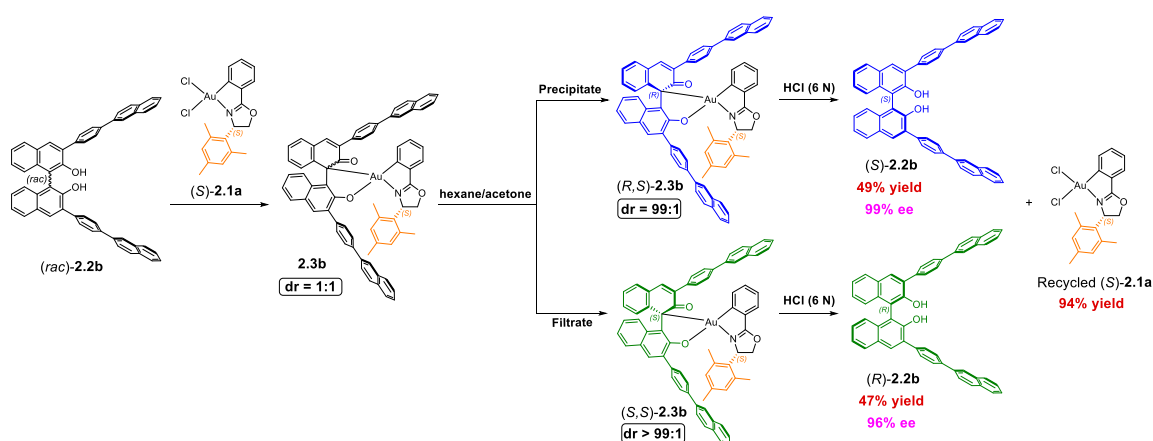
Scheme S2.5 Synthesis of BINOL/gold(III) complexes **2.3b** and resolution of BINOLs **2.2b**.

The enantiopure gold(III) complex (*S*)-**2.1** (22 mg, 0.0413 mmol, 1.1 equiv.) was reacted

with the racemic BINOL (*rac*)-**2.2b** (25.9 mg, 0.0375 mmol, 1.0 equiv.) in the presence

of Cs_2CO_3 (26.9 mg, 0.0827 mmol, 2.2 equiv.) in 2 mL MeOH for 1 h at room temperature.

Orange red precipitate was formed in a suspension. The resulting precipitates were

collected by filtration to afford the diastereomeric mixtures of **2.3b** with dr = 1:1. After

addition of hexane/acetone (1:1, 4 mL), orange red precipitate mixed with a red solution

was observed. The precipitate was collected to give BINOL/gold(III) complex (*R,S*)-**2.3b**

with dr = 99:1 as orange red solid (21.6 mg, 0.0187 mmol, 50% yield). Besides, The

filtrate was concentrated and the product was precipitated by addition of hexane,

affording the BINOL/gold(III) complex (*S,S*)-**2.3b** with dr > 99:1 as orange red solid (21.1 mg, 0.0184 mmol, 49% yield).

The obtained (*R,S*)-**2.3b** and (*S,S*)-**2.3b** was separately dissolved in DCM/MeOH (1:1, 2 mL). After addition of 6 N hydrochloric acid (19 μL, 0.0188 mmol, 3 equiv.) at room temperature, the color of the solution immediately changed from red to colorless within 1 min. The solution was concentrated and purified by chromatographic column (hexane/DCM) to afford BINOL (*S*)-**2.2b** (white solid, 12.7 mg, 0.0184 mmol, 49% yield, 99% ee), BINOL (*R*)-**2.2b** (white solid, 12.2 mg, 0.0176 mmol, 47% yield, 96% ee) and recovered (*S*)-**2.1a** (20.7 mg, 0.0388 mmol, 94% yield).
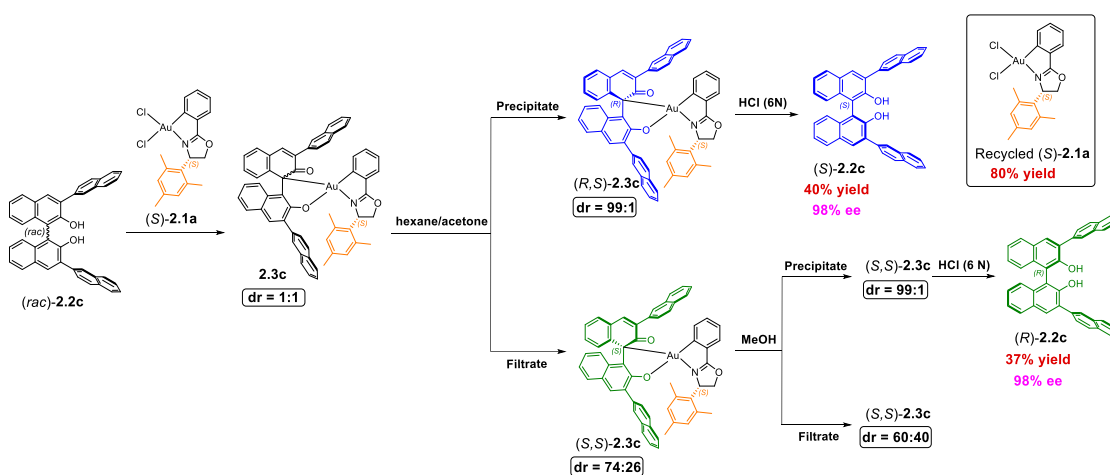

Scheme S2.6 Synthesis of BINOL/gold(III) complexes **2.3c** and resolution of BINOLs **2.2c**.

The enantiopure gold(III) complex (*S*)-**2.1** (22 mg, 0.0413 mmol, 1.1 equiv.) was reacted with the racemic BINOL (*rac*)-**2.2c** (20.2 mg, 0.0375 mmol, 1.0 equiv.) in the presence of Cs$_2$CO$_3$ (26.9 mg, 0.0827 mmol, 2.2 equiv.) in 2 mL MeOH for 1 h at room temperature. The solution was diluted with addition of DCM and washed with water. The organic layer was concentrated and dried to afford the diastereomeric mixtures of **2.3c** with dr = 1:1.

After addition of hexane/acetone (5:1, 12 mL), orange red precipitate mixed with a red solution was observed. The precipitate was collected to give BINOL/gold(III) complex (*R,S*)-**2.3c** with dr = 99:1 as orange red solid (15.7 mg, 0.0157 mmol, 42% yield). Besides, The filtrate was concentrated and the product was precipitated by addition of hexane, affording the crude BINOL/gold(III) complex (*S,S*)-**2.3c** with dr = 74:26 as orange red solid. MeOH (5 mL) was subsequently added to the obtained crude (*S,S*)-**2.3c**. Orange red precipitate mixed with pale yellow solution was observed. The precipitate was collected by filtration to give BINOL/gold(III) complex (*S,S*)-**2.3c** with dr = 99:1 as orange red solid (14.6 mg, 0.0146 mmol, 39% yield).

The obtained (*R,S*)-**2.3c** and (*S,S*)-**2.3c** was separately added in DCM/MeOH (1:1, 2 mL). After addition of 6 N hydrochloric acid (19 μL, 0.0188 mmol, 3 equiv.) at room temperature, the color of the solution immediately changed from red to colorless within 1 min. The solution was concentrated and purified by chromatographic column (hexane/DCM) to afford BINOL (*S*)-**2.2c** (white solid, 8.1 mg, 0.0150 mmol, 40% yield, 98% ee), BINOL (*R*)-**2.2c** (white solid, 7.5 mg, 0.0139 mmol, 37% yield, 98% ee) and recovered (*S*)-**2.1a** (17.6 mg, 0.0330 mmol, 80% yield).
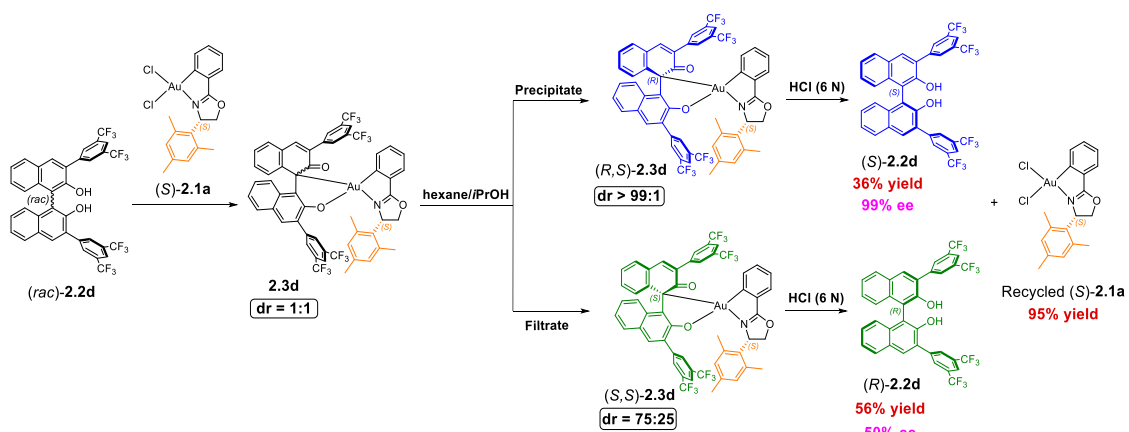

Scheme S2.7 Synthesis of BINOL/gold(III) complex **2.3d** and resolution of BINOLs **2.2d**.

The enantiopure gold(III) complex (*S*)-**2.1** (22 mg, 0.0413 mmol, 1.1 equiv.) was reacted with the racemic BINOL (*rac*)-**2.2d** (27.9 mg, 0.0375 mmol, 1.0 equiv.) in the presence of Cs$_2$CO$_3$ (26.9 mg, 0.0827 mmol, 2.2 equiv.) in 2 mL MeOH for 1 h at room temperature. The solution was diluted with addition of EA and washed with water. The organic layer was concentrated and dried to afford the diastereomeric mixtures of **2.3d** with dr = 1:1. After addition of hexane/*i*PrOH (9:1, 20 mL), yellow precipitate mixed with a red solution was observed. The precipitate was collected to give BINOL/gold(III) complex (*R,S*)-**2.3d** with dr > 99:1 as orange red solid (17.5 mg, 0.0150 mmol, 40% yield The filtrate was concentrated and the product was precipitated by addition of hexane, affording the crude BINOL/gold(III) complex (*S,S*)-**2.3d** with dr = 75:25 as yellow solid.

The obtained (*R,S*)-**2.3d** and crude (*S,S*)-**2.3d** was separately dissolved in EA/MeOH (1:1, 2 mL). After addition of 6 N hydrochloric acid (19 μL, 0.0188 mmol, 3 equiv.) at room temperature, the color of the solution immediately changed from red to colorless within 1 min. The solution was concentrated and purified by chromatographic column (hexane/DCM) to afford BINOL (*S*)-**2.2d** (white solid, 10.0 mg, 0.0135 mmol, 36% yield, 99% ee), BINOL (*R*)-**2.2d** (white solid, 15.6 mg, 0.0210 mmol, 56% yield, 50% ee) and recovered (*S*)-**2.1a** (20.9 mg, 0.0392 mmol, 95% yield).
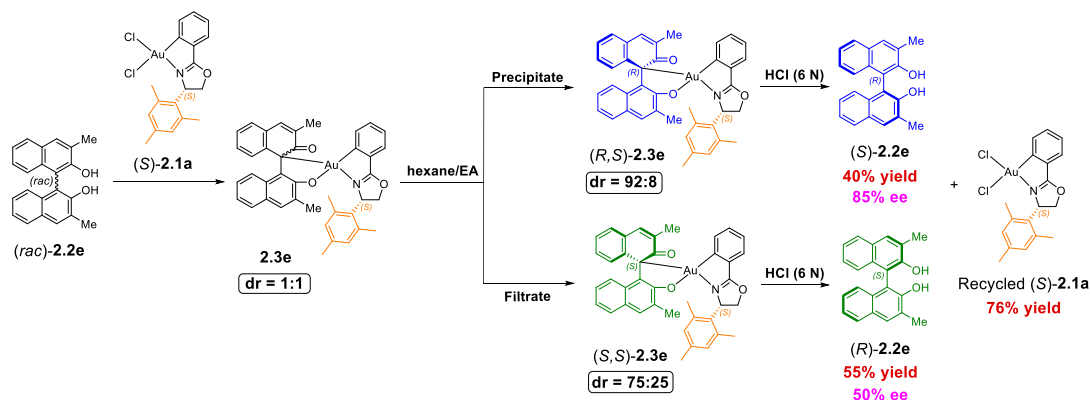
Scheme S2.8 Synthesis of BINOL/gold(III) complex **2.3e** and resolution of BINOLs **2.2e**.

The enantiopure gold(III) complex (*S*)-**2.1** (22 mg, 0.0413 mmol, 1.1 equiv.) was reacted with the racemic BINOL (*rac*)-**2.2e** (11.8 mg, 0.0375 mmol, 1.0 equiv.) in the presence of Cs$_2$CO$_3$ (26.9 mg, 0.0827 mmol, 2.2 equiv.) in 2 mL MeOH for 1 h at room temperature. The solution was diluted with addition of DCM and washed with water. The organic layer was concentrated and dried to afford the diastereomeric mixtures of **2.3e** with dr = 1:1. After addition of hexane/EA (2:1, 12 mL), orange red precipitate mixed with red solution was observed. The precipitate was collected to give BINOL/gold(III) complex (*R,S*)-**2.3e** with dr = 92:8 as orange red solid (12.2 mg, 0.0157 mmol, 42% yield). The filtrate was concentrated and the product was precipitated by addition of hexane, affording the crude BINOL/gold(III) complex (*S,S*)-**2.3e** with dr = 75:25 as orange red solid.

The obtained (*R,S*)-**2.3e** and crude (*S,S*)-**2.3e** was separately added in DCM/MeOH (1:1, 2 mL). After addition of 6 N hydrochloric acid (19 μL, 0.0188 mmol, 3 equiv.) at room temperature, the color of the solution immediately changed from red to colorless within 1 min. The solution was concentrated and purified by chromatographic column (hexane/DCM) to afford BINOL (*S*)-**2.2e** (white solid, 4.7 mg, 0.0150 mmol, 40% yield, 85% ee), BINOL (*R*)-**2.2e** (white solid, 6.5 mg, 0.0206 mmol, 55% yield, 50% ee) and recovered (*S*)-**2.1a** (16.7 mg, 0.0314 mmol, 76% yield).
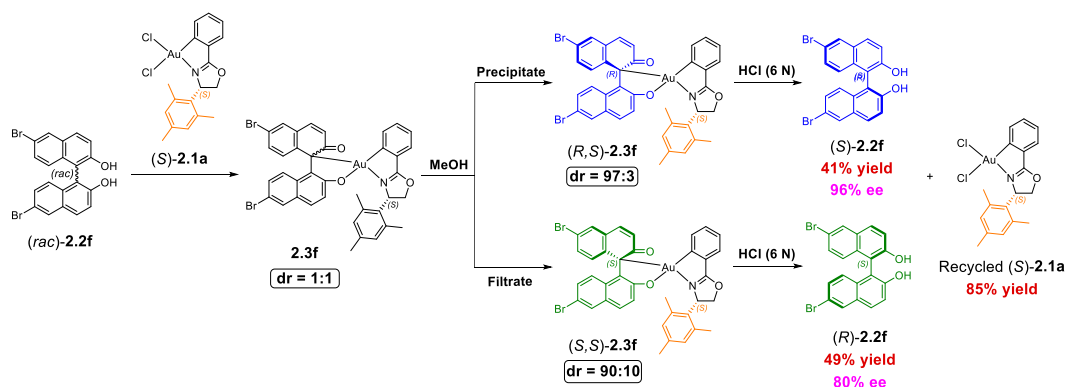
Scheme S2.9 Synthesis of BINOL/gold(III) complex **2.3f** and resolution of BINOLs **2.2f**.

The enantiopure gold(III) complex (S)-**2.1** (28 mg, 0.0525 mmol, 1.4 equiv.) was reacted with the racemic BINOL (rac)-**2.2f** (16.7 mg, 0.0375 mmol, 1.0 equiv.) in the presence of Cs_2CO_3 (34.2 mg, 0.105 mmol, 2.8 equiv.) in 1 mL MeOH for 1 h at room temperature. Orange red precipitate was formed in a suspension. The resulting precipitates were collected by filtration to afford the diastereomeric mixtures of **2.3f** with dr = 1:1. After addition of MeOH (10 mL), orange red precipitate mixed with red solution was observed. The precipitate was collected to give BINOL/gold(III) complex (R,S)-**2.3f** with dr = 97:3 as orange red solid (14.2 mg, 0.0157 mmol, 43% yield). The filtrate was concentrated and the product was precipitated by addition of hexane, affording the BINOL/gold(III) complex (S,S)-**2.3f** with dr = 90:10 as orange red solid (17.9 mg, 0.0199 mmol, 53% yield).

The obtained (R,S)-**2.3f** and (S,S)-**2.3f** was separately added in DCM/MeOH (1:1, 2 mL). After addition of 6 N hydrochloric acid (19 μL, 0.0188 mmol, 3 equiv.) at room temperature, the color of the solution immediately changed from red to colorless within 1 min. The solution was concentrated and purified by chromatographic column (hexane/DCM) to afford compound BINOL (S)-**2.2f** (white solid, 6.8 mg, 0.0154 mmol, 41% yield, 96% ee), BINOL (R)-**2.2f** (white solid, 8.2 mg, 0.0184 mmol, 49% yield, 80% ee) and recovered (S)-**2.1a** (23.8 mg, 0.0446 mmol, 85% yield).

2.4.7 ^{1}H NMR Analysis for Determination of Diastereometric Ratio of 2.3b-2.3f

In the ^{1}H NMR spectra, the protons on the oxazoline ring were used to determine the diastereometric ratio of **2.3b-2.3f** (Figure S2.2a).
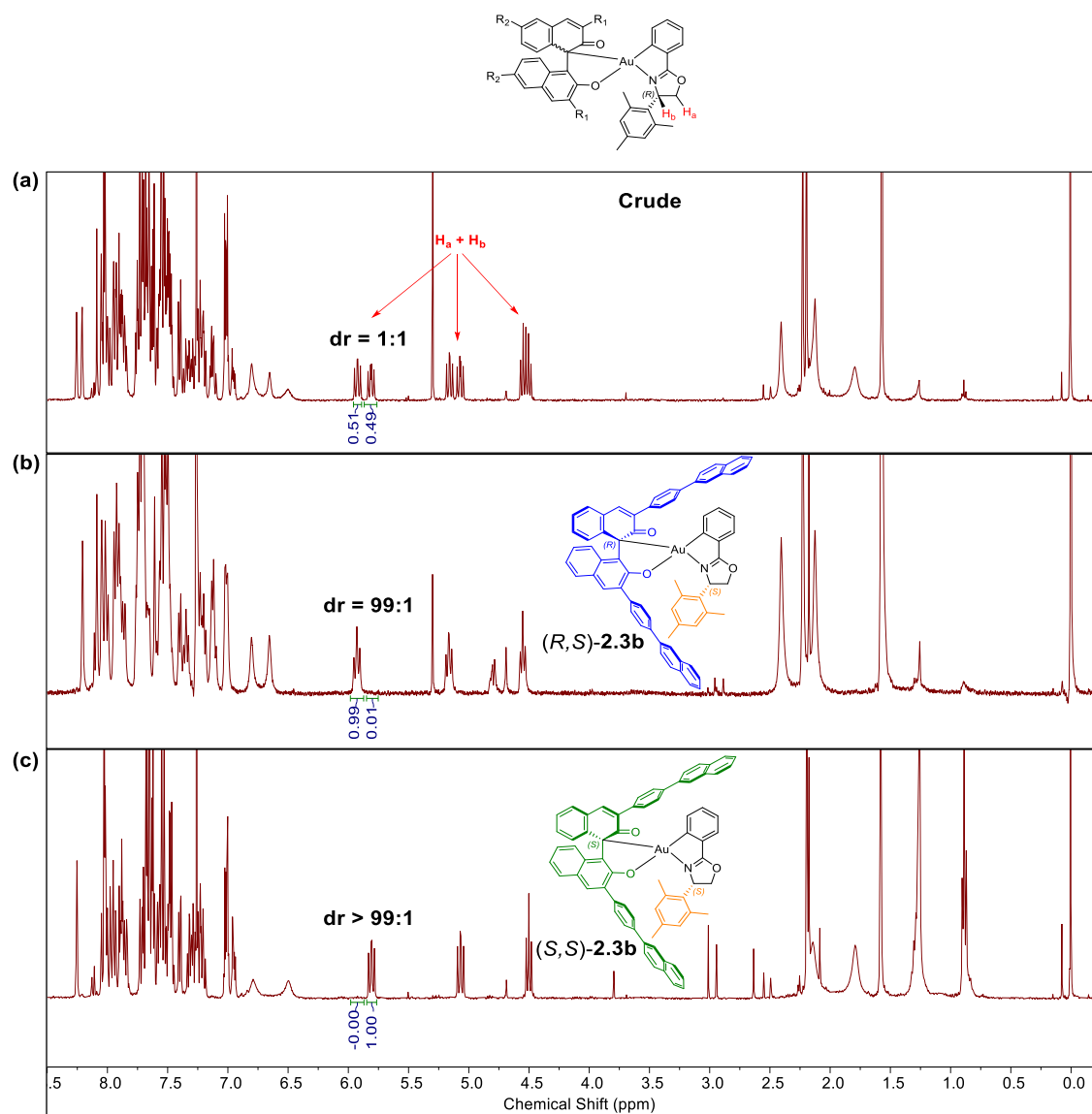
Figure S2.2 Determination of dr of **(a)** crude mixture of **2.3b**; **(b)** (*R,S*)-**2.3b**; **(c)** (*S,S*)-**2.3b** by ^{1}H NMR analysis.
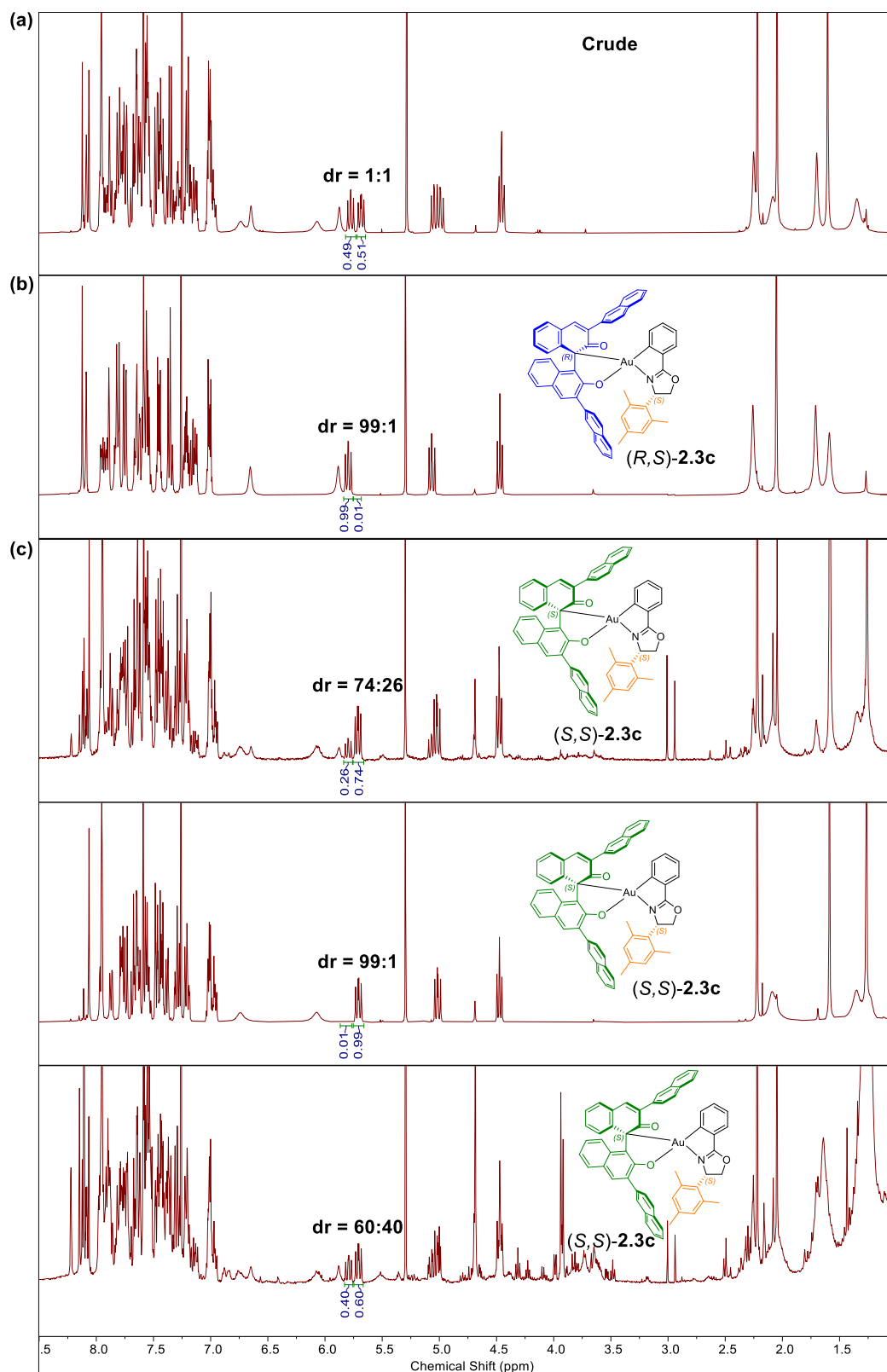
Figure S2.3 Determination of dr of **(a)** crude mixture of **2.3c**; **(b)** (*R*,*S*)-**2.3c**;

(c) (*S*,*S*)-**2.3c** by ^{1}H NMR analysis.
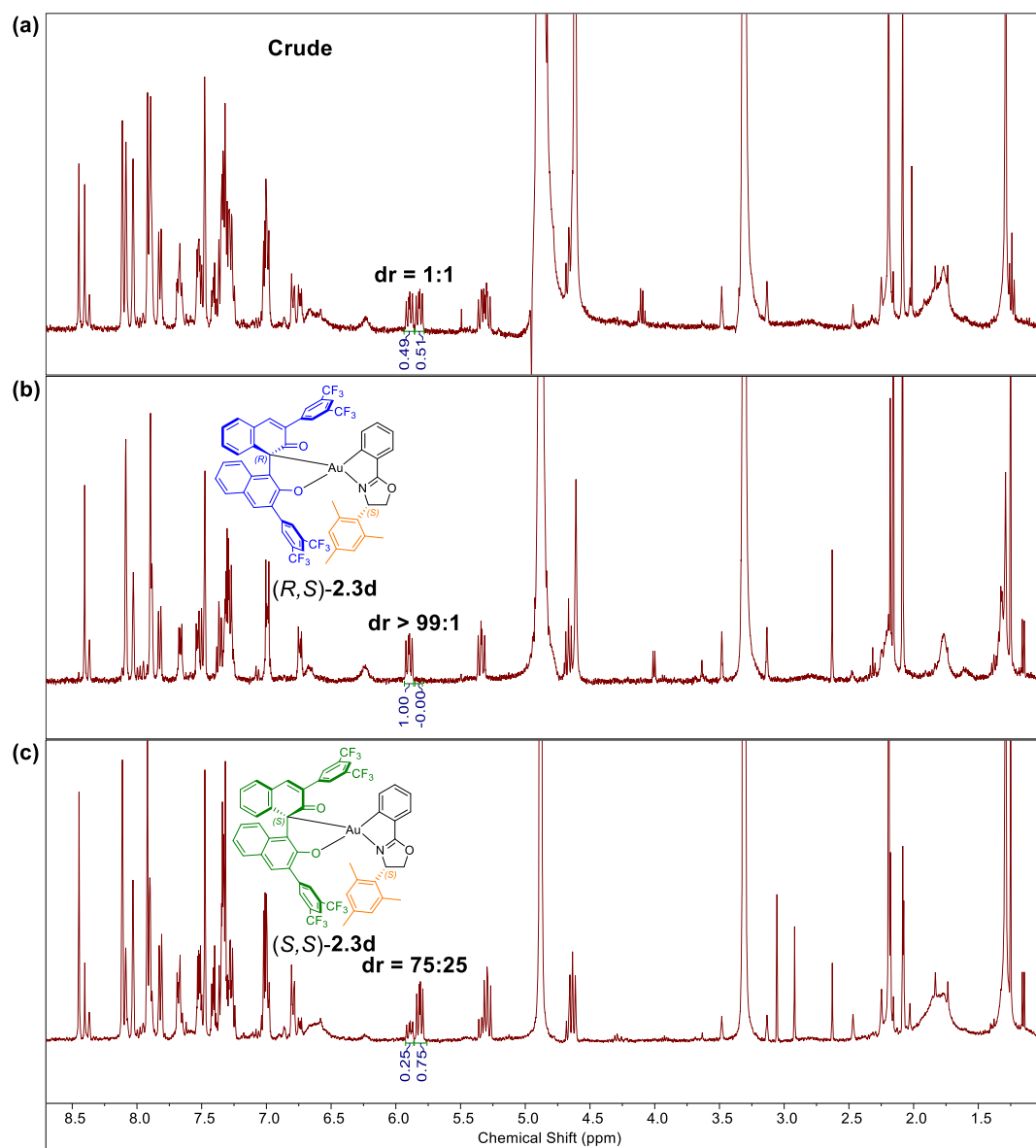
Figure S2.4 Determination of dr of **(a)** crude mixture of **2.3d**; **(b)** (*R*,*S*)-**2.3d**;

(c) (*S*,*S*)-**2.3d** by ^{1}H NMR analysis.

Figure S2.5 Determination of dr of **(a)** crude mixture of **2.3e**; **(b)** (*R*,*S*)-**2.3e**;

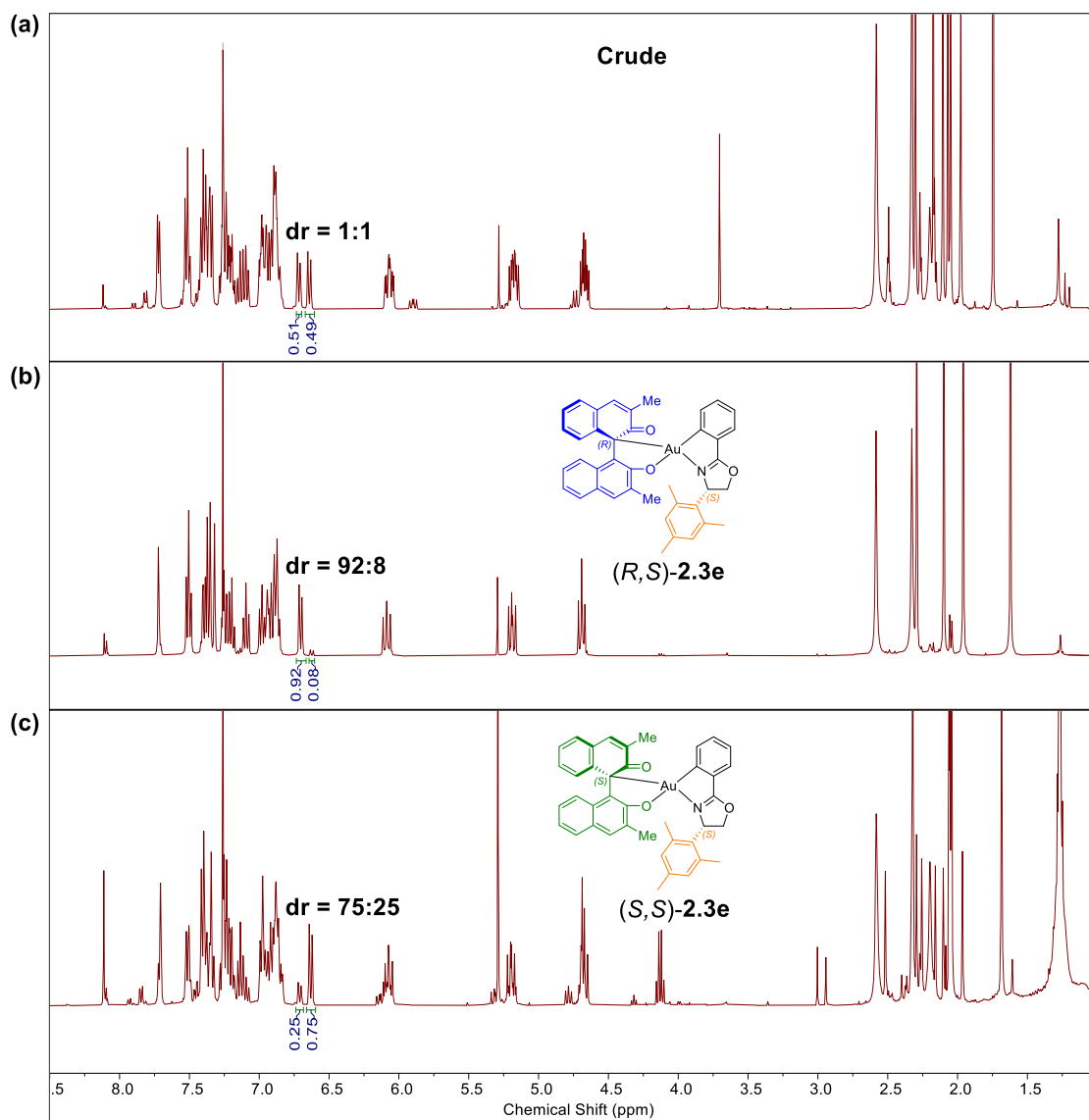**(c)** (*S*,*S*)-**2.3e** by ^{1}H NMR analysis.
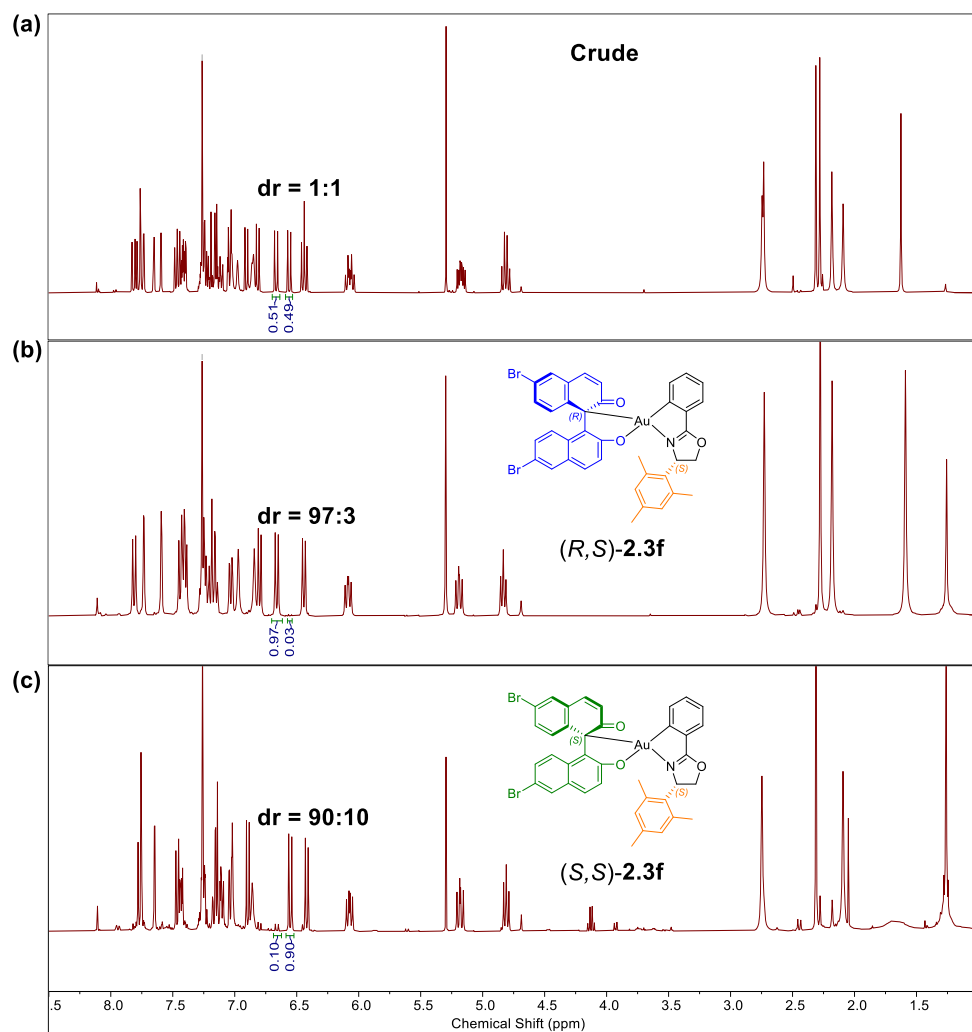
Figure S2.6 Determination of dr of **(a)** crude mixture of **2.3f**; **(b)** (*R*,*S*)-**2.3f**;

(c) (*S*,*S*)-**2.3f** by ^{1}H NMR analysis.

2.4.8 ^{1}H NMR Kinetic Study

Quantitative NMR Analysis: A 0.05 M solution of 1,3,5-trimethoxybenzene in CD$_3$OD was prepared as internal standard stock solution. The catalysis was performed under standard conditions except changing the solvent to CD$_3$OD. 10 μL of internal standard stock solution and 20 μL of reaction crude solution were transferred to 500 μL CD$_3$OD in an NMR tube for measurement.

Before the kinetic study of carboalkoxylation of substrate **2.4a** started, the ^{1}H NMR of the **2.4a** in CD$_3$OD was obtained. When dissolving in CD$_3$OD, a mixture of substrate **2.4a** and its hemiacetal form was present in the solvent with the ratio of 2:1 (Figure S2.7).
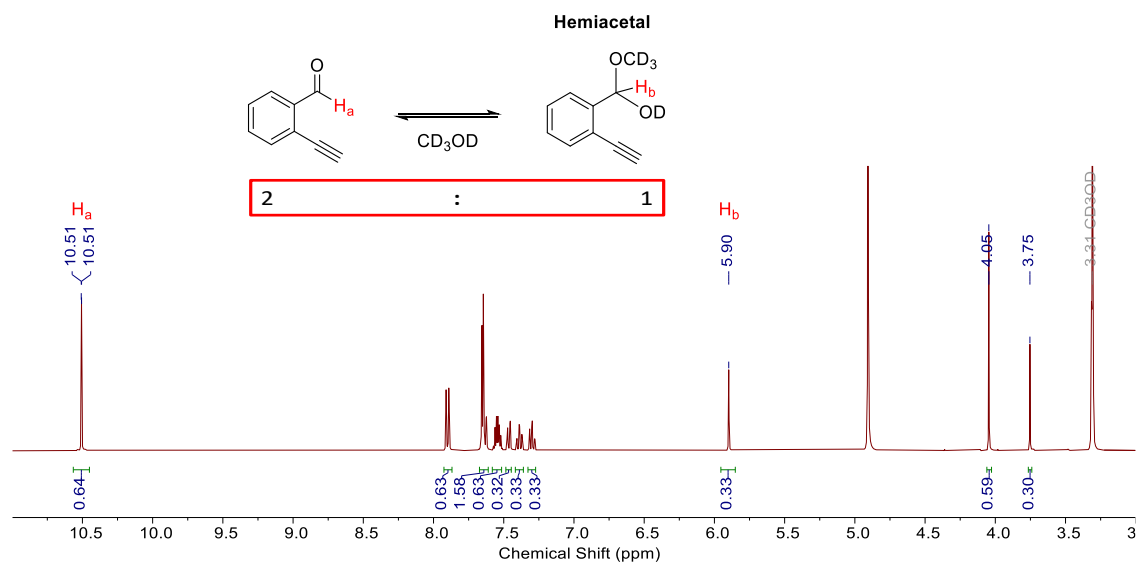
Figure S2.7 ^{1}H NMR of substrate **2.4a** in CD$_3$OD
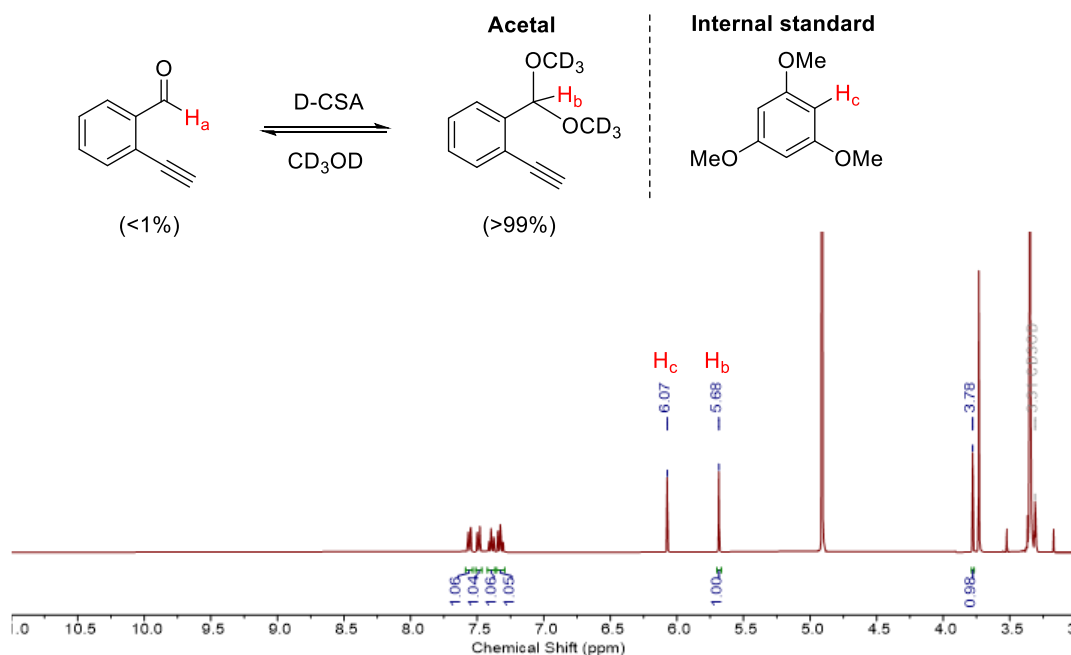
Figure S2.8 ^{1}H NMR of substrate **2.4a** with D-CSA and internal standard in CD$_3$OD

When dissolving in CD$_3$OD with 2.5 mol% D-CSA, all substrate **2.4a** was converted into acetal form (Figure S2.8). With the use of internal standard, the kinetic study could be conducted. It was assumed that all substrate **2.4a** was converted into acetal form at t = 0.
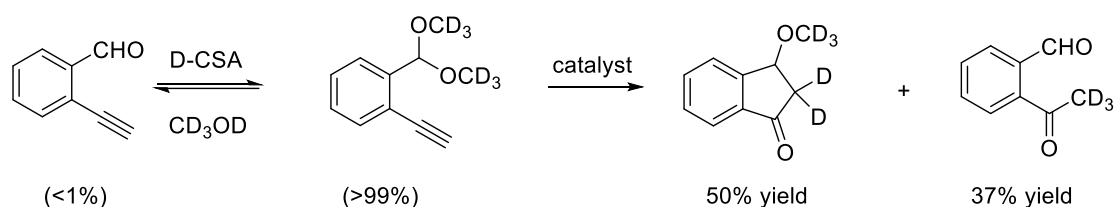
Table S2.1 Kinetic study of substrate **2.4a** under optimized conditions.[a]

Reaction time (min)	^{1}H NMR Yield (%)		
0	100	0	0

10	67	14	4
30	45	27	14
60	30	40	24
90	22	45	27
120	16	47	30
270	2	49	37
330	0	50	37

[a] Reaction conditions: Optimized condition, 2 mL CD$_3$OD as solvent.
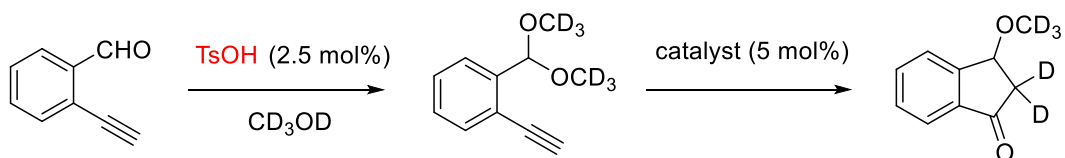
Table S2.2 Kinetic study of substrate **2.4a** using TsOH as acid.[a]

Reaction time (min)	¹H NMR Yield (%)		
0	100	0	0
75	41	33	24
120	13	47	40
170	5	50	43
270	0	54	48

[a] Reaction conditions: Optimized condition, 2 mL CD$_3$OD as solvent.
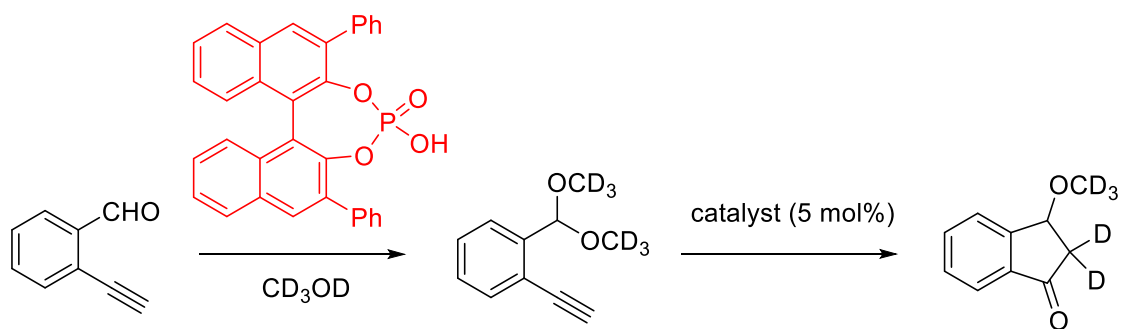
Table S2.3 Kinetic study of substrate **2.4a** using **BINOL-PO₂H-1** as acid.[a]

Reaction time (min)	¹H NMR Yield (%)		
0	100	0	0
75	77	10	8
110	58	16	11
170	56	19	17
270	47	22	21

[a] Reaction conditions: Optimized condition, 2 mL CD₃OD as solvent.
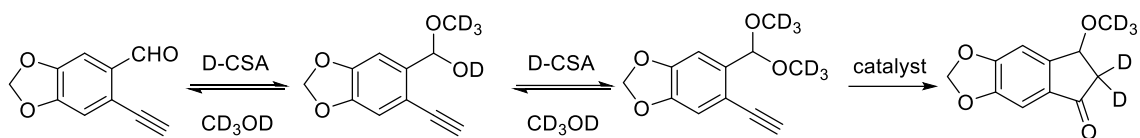
Table S2.4 Kinetic study of substrate **2.4l** under optimized conditions.[a]

Reaction time (min)	¹H NMR Yield (%)	
0	98	0
10	53	39
20	33	56
30	21	65
40	15	72
50	10	76
60	6	80
75	3	83
90	1	85
105	<1	85
120	0	85
150	0	85

[a] Reaction conditions: Optimized condition, 2 mL CD$_3$OD as solvent.
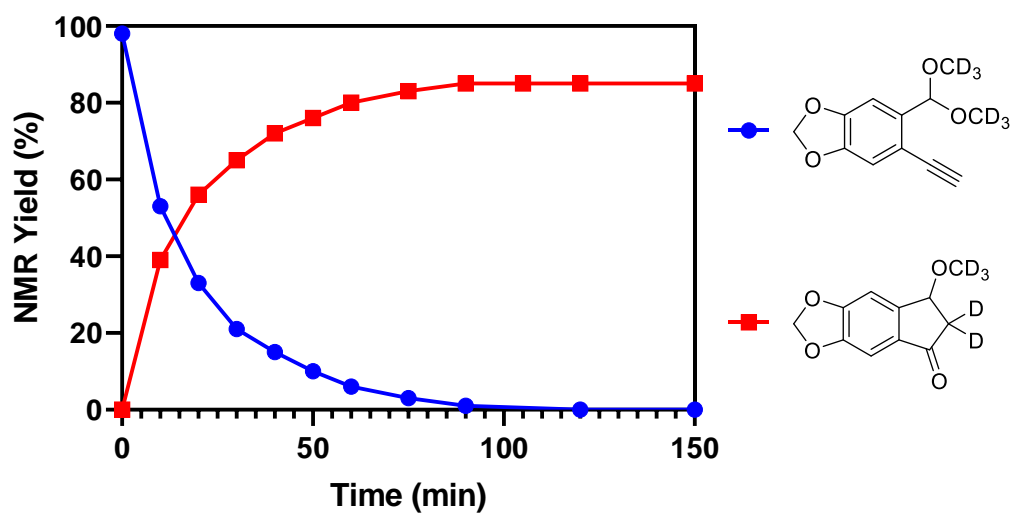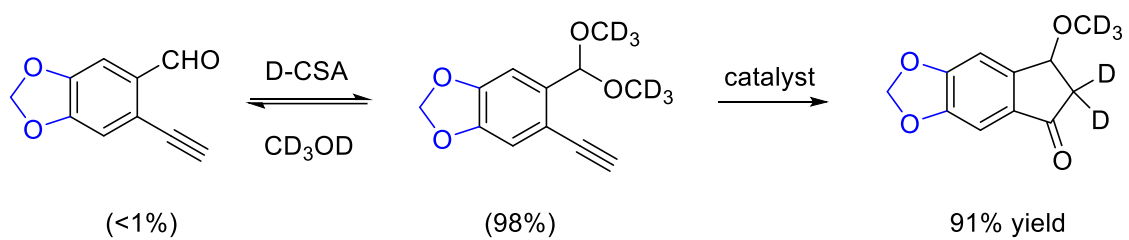
Figure S2.9 Kinetic profile of catalyzing substrate **2.4l**.
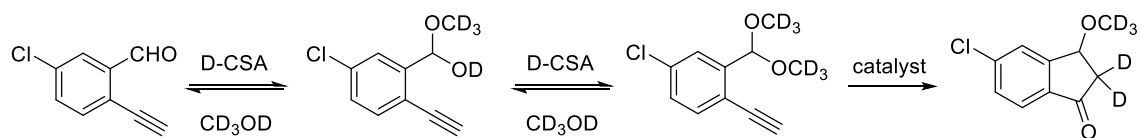
Table S2.5 Kinetic study of 5-Cl substituted substrate under optimized conditions.[a]

Reaction time (min)	¹H NMR Yield (%)		
0	51	0	0
8	70	<1	1
13	71	1	2
20	72	1	2
30	73	2	3
40	72	3	3
50	72	3	3
60	72	4	4
80	72	4	5
100	71	5	5
120	70	5	6
150	68	6	8
180	68	6	9
210	68	6	10

[a] Reaction conditions: Optimized condition, 2 mL CD$_3$OD as solvent.
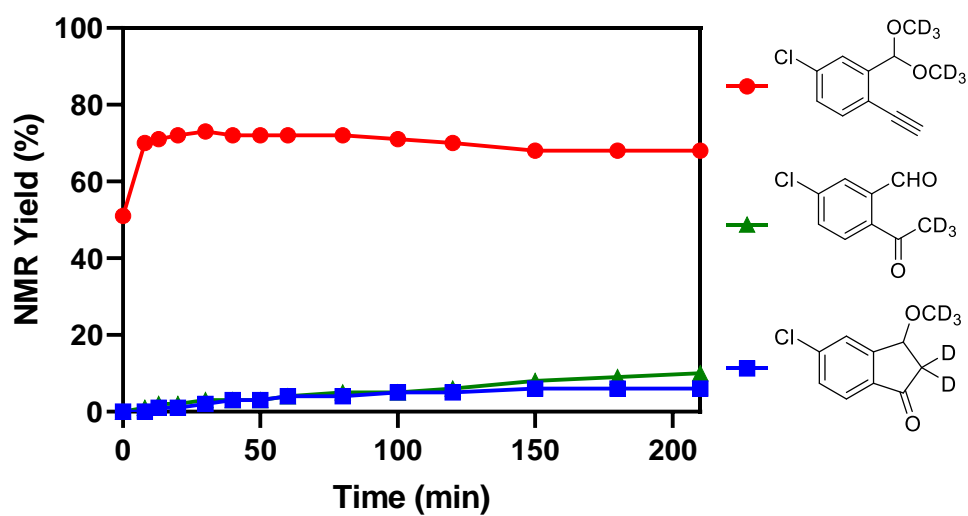
Figure S2.10 Kinetic profile of catalyzing 5-Cl substituted substrate.
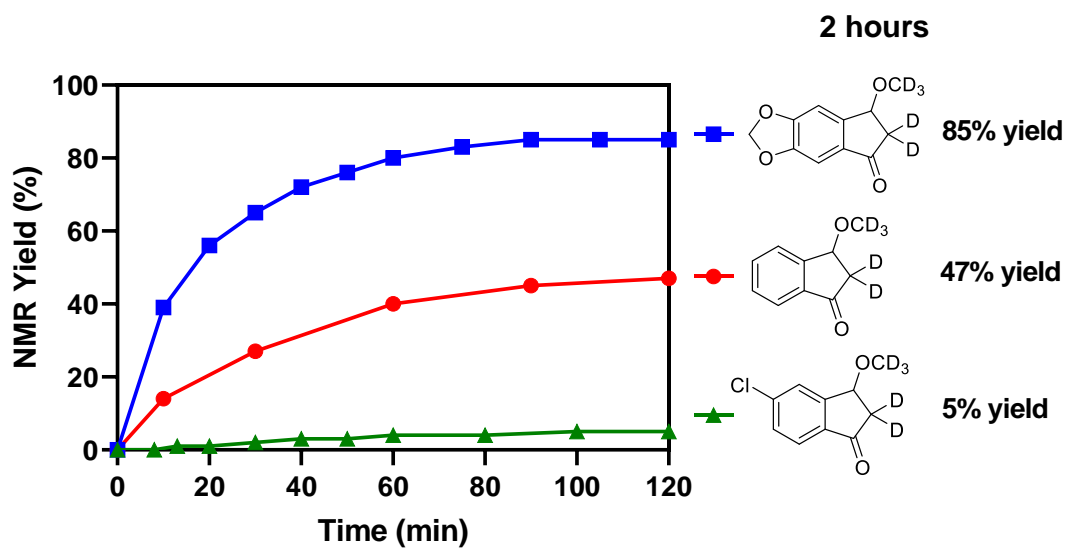
Figure S2.11 Summary of kinetic profile of catalyzing different substrates.
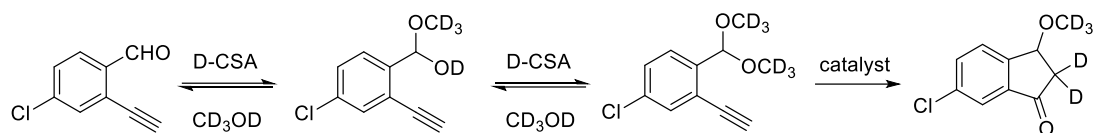
Table S2.6 Kinetic study of substrate **2.4j** under optimized conditions.[a]

Reaction time (min)	¹H NMR Yield (%)		
0	98	0	0
120	38	28	13
240	32	32	22
360	28	34	29

[a] Reaction conditions: Optimized condition, 2 mL CD₃OD as solvent.
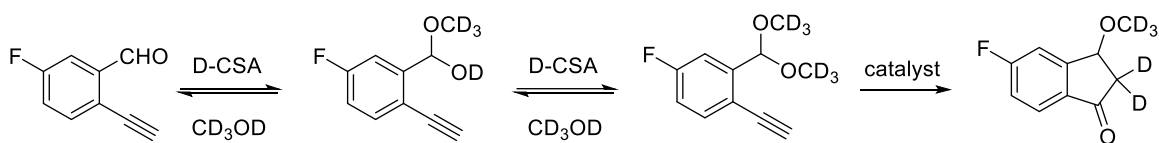
Table S2.7 Kinetic study of 5-F substituted substrate under optimized conditions.[a]

Reaction time (min)	¹H NMR Yield (%)		
0	85%	0%	0%
120	56%	11%	24%
240	49%	14%	32%
360	37%	16%	38%

[a] Reaction conditions: Optimized condition, 2 mL CD₃OD as solvent.
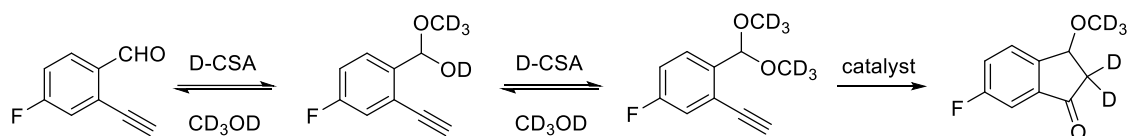
Table S2.8 Kinetic study of 4-F substituted substrate under optimized conditions.[a]

Reaction time (min)	^{1}H NMR Yield (%)		
0	>99	0	0
120	65	17	10
240	55	21	15
360	44	26	22

[a] Reaction conditions: Optimized condition, 2 mL CD_3OD as solvent.

Table S2.9 Kinetic study of 5-CF_3 substituted substrate under optimized conditions.[a]

Reaction time (min)	^{1}H NMR Yield (%)		
0	49	0	0
120	75	3	6
240	72	3	8
360	64	4	10

Table S2.10 ^{1}H NMR yield of the substate scope.[a]

(R,R)-**2a** (5 mol%)
D-CSA (2.5 mol%)

MeOH, r.t., 16 h

2.3 → **2.4**

(R,R)-**2.2a**

(83% yield)

(77% yield)

(42% yield)

(60% yield)

(22% yield)

(12% yield)

(<5% yield)

(73% yield)

(70% yield)

(35% yield)

(37% yield)

(5% yield)

(31% yield)

(69% yield)
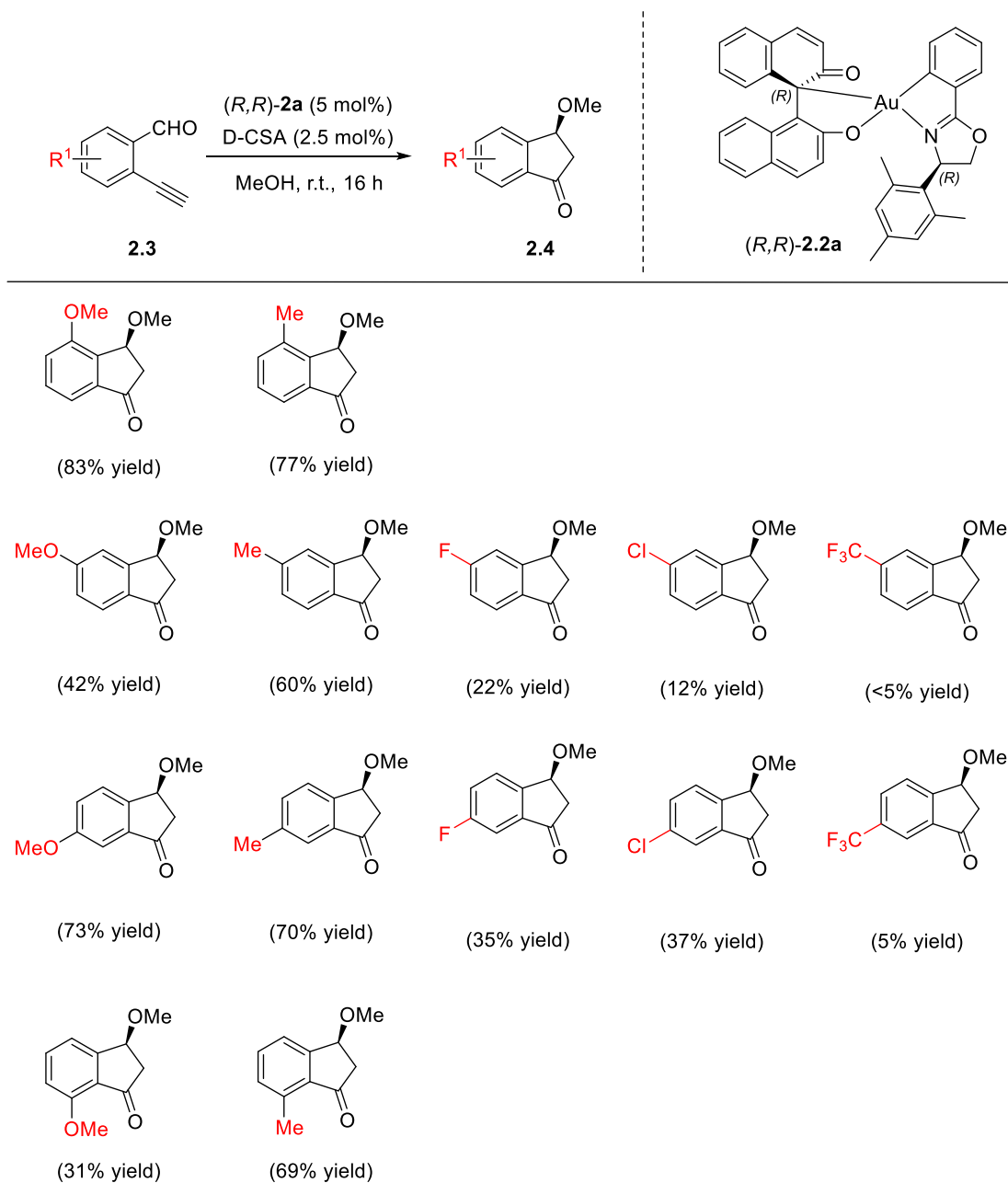
2.4.9   HPLC Analysis of Resolved BINOLs 2.2b-2.2f

(*rac*)-**2.2b**
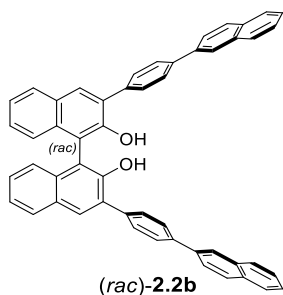
Chiralpak IC column,

55:45 hexane/isopropanol,

1 mL/min,

t_R = 10.1 min, 19.6 min,

ee = 0%.

	RT	Area	% Area	Height
1	10.068	3407855	49.57	72703
2	19.604	3467350	50.43	29070

(S)-**2.2b**
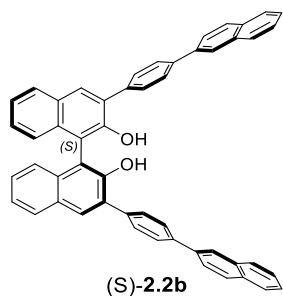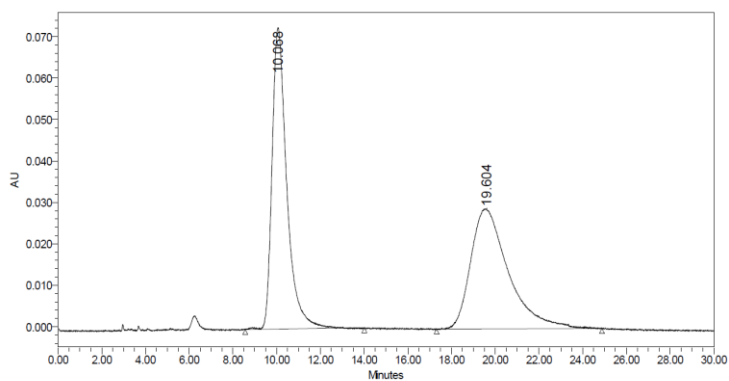
Chiralpak IC column,

55:45 hexane/isopropanol,

1 mL/min,

t_R = 10.1 min (major),

19.1 min (minor),

ee = 99%.

	RT	Area	% Area	Height
1	10.052	1402756	99.62	29687
2	19.090	5306	0.38	261

(*R*)-**2.2b**
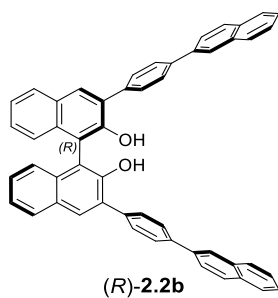
Chiralpak IC column,

55:45 hexane/isopropanol,

1 mL/min,

t_R = 10.7 min (minor),

21.2 min (major),

ee = 96%.

	RT	Area	% Area	Height
1	10.670	91573	1.77	2086
2	21.203	5088501	98.23	34982

(*rac*)-**2.2c**
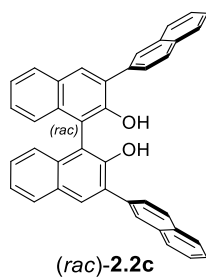
Chiralcel AD-H column,

55:45 hexane/isopropanol,

1 mL/min,

t_R = 13.2 min, 27.1 min,

ee = 0%.

	RT	Area	% Area	Height
1	13.221	5547564	49.86	60060
2	27.123	5578178	50.14	30224

(S)-**2.2c**
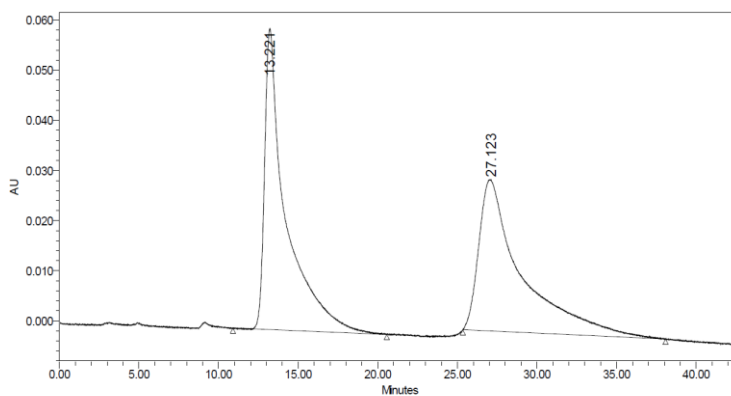
Chiralcel AD-H column,

55:45 hexane/isopropanol,

1 mL/min,

t_R = 13.1 min (minor),

26.6 min (major),

ee = 98%.
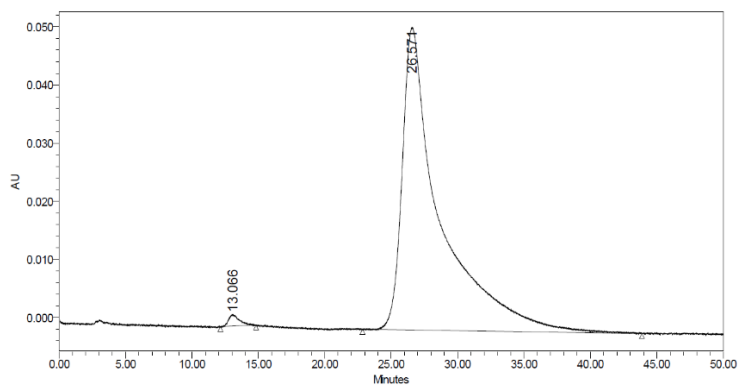
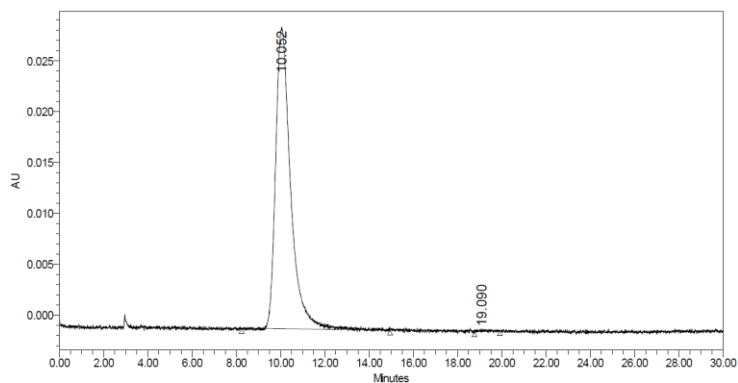|	RT	Area	% Area	Height
1	13.066	111180	1.07	2013
2	26.571	10291249	98.93	52032

(R)-**2.2c**
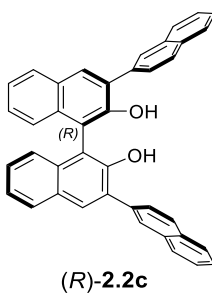
Chiralcel AD-H column,

55:45 hexane/isopropanol,

1 mL/min,

t_R = 13.0 min (major),

26.7 min (minor),

ee = 98%.
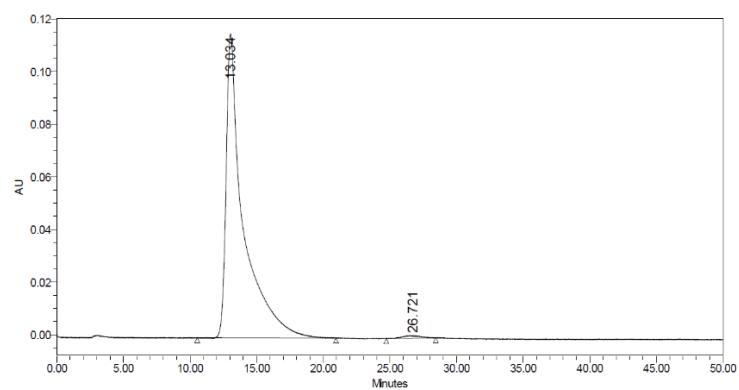
	RT	Area	% Area	Height
1	13.034	10292059	99.14	115506
2	26.721	89427	0.86	1036

(*rac*)-**2.2d**
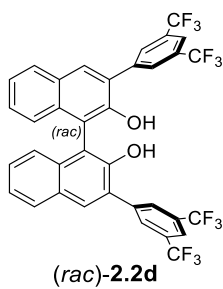
Chiralcel AD-H column,

99:1 hexane/isopropanol,

0.5 mL/min,

t_R = 7.0 min, 7.7 min,

ee = 0%.
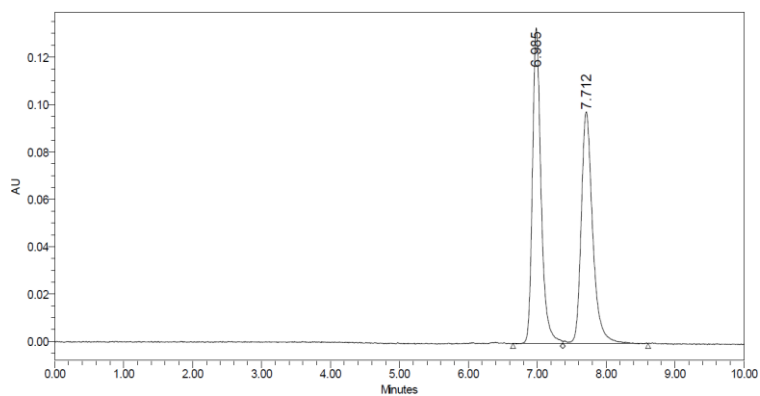
	RT	Area	% Area	Height
1	6.985	1155465	50.60	133081
2	7.712	1127890	49.40	97675

(*S*)-**2.2d**
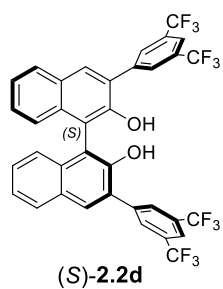
Chiralcel AD-H column,

99:1 hexane/isopropanol,

0.5 mL/min,

t_R = 6.8 min (major), 7.3 min (minor),

ee = 99%.
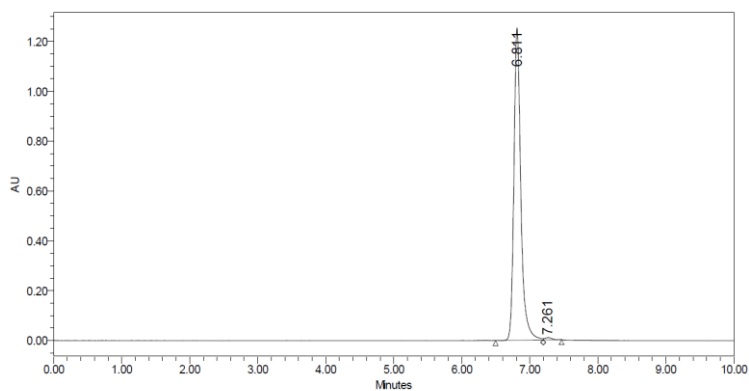
	RT	Area	% Area	Height
1	6.811	8838431	99.31	1252022
2	7.261	61777	0.69	8458

(*R*)-**2.2d**
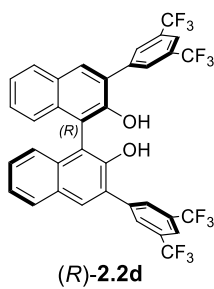
Chiralcel AD-H column,

99:1 hexane/isopropanol,

0.5 mL/min,

t_R = 6.8 min (minor),

7.2 min (major),

ee = 50%.
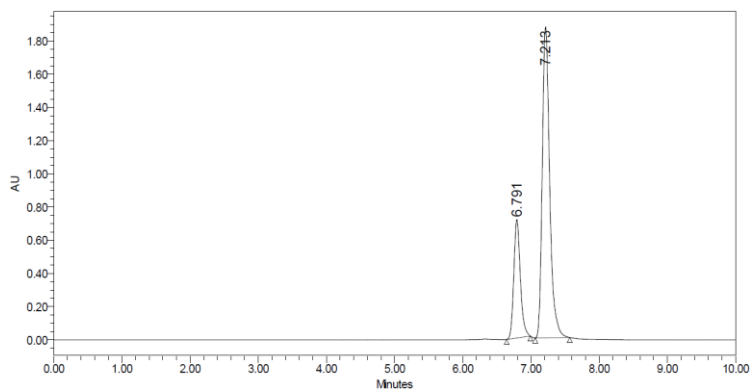
	RT	Area	% Area	Height
1	6.791	4722529	25.08	712671
2	7.213	14106097	74.92	1872273

(*rac*)-**2.2e**
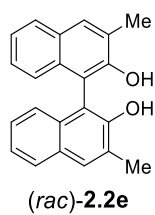
Chiralpak IC column,

98:2 hexane/isopropanol,

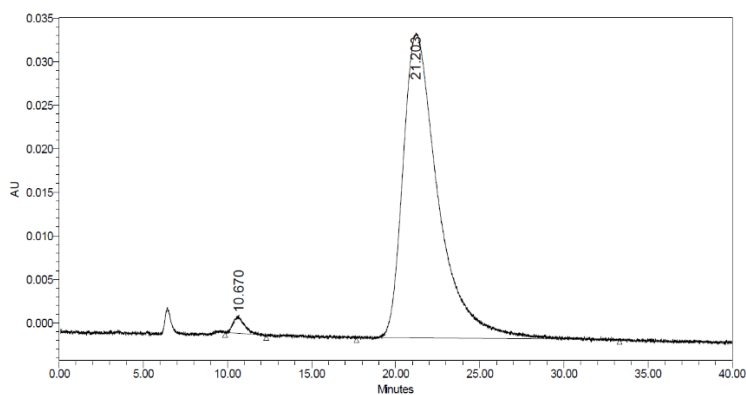1 mL/min,

t_R = 4.4 min, 4.9 min,

ee = 0%.
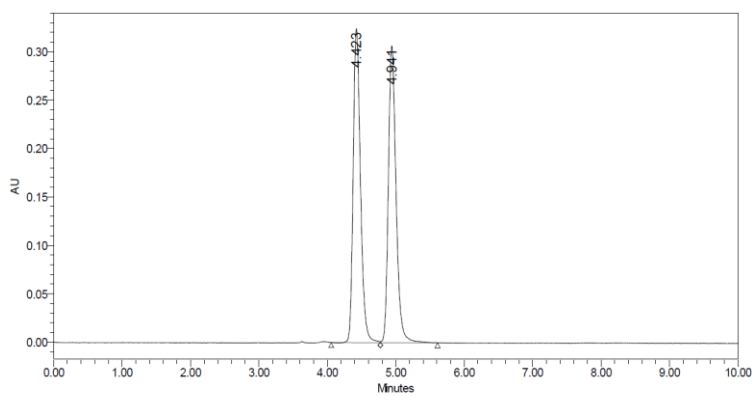
	RT	Area	% Area	Height
1	4.423	2396054	50.06	324145
2	4.941	2390388	49.94	306579

(S)-**2.2e**
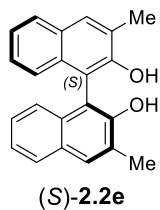
Chiralpak IC column,

98:2 hexane/isopropanol,

1 mL/min,

t_R = 4.4 min (minor),

4.9 min (major),

ee = 85%.

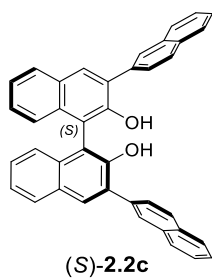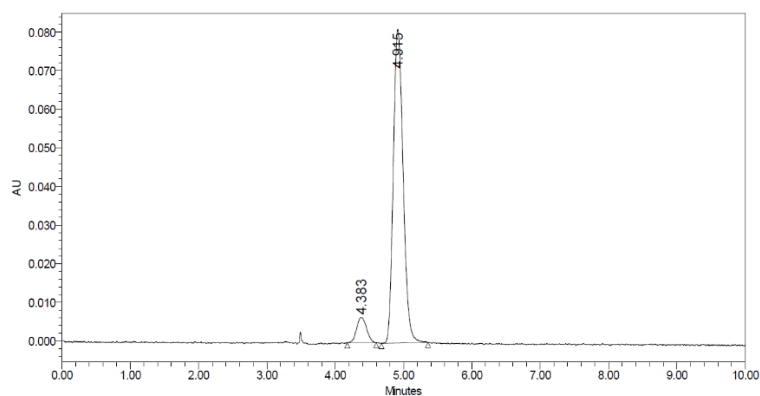|	RT	Area	% Area	Height
1	4.383	65677	7.49	6544
2	4.915	811170	92.51	81283

(R)-**2.2e**
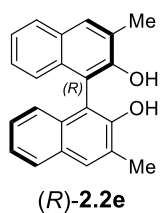
Chiralpak IC column,

98:2 hexane/isopropanol,

1 mL/min,

t_R = 4.4 min (major),

5.0 min (minor),

ee = 50%.
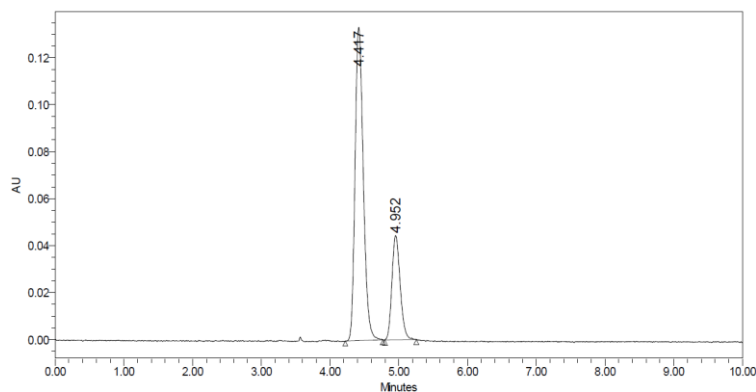
	RT	Area	% Area	Height
1	4.417	1108486	75.02	133269
2	4.952	369118	24.98	44338

(*rac*)-**2.2f**
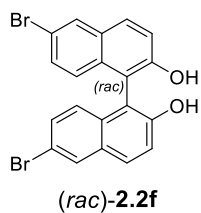
Chiralpak IC column,

95:5 hexane/isopropanol,

1 mL/min,

t_R = 7.7 min, 10.8 min,

ee = 0%.
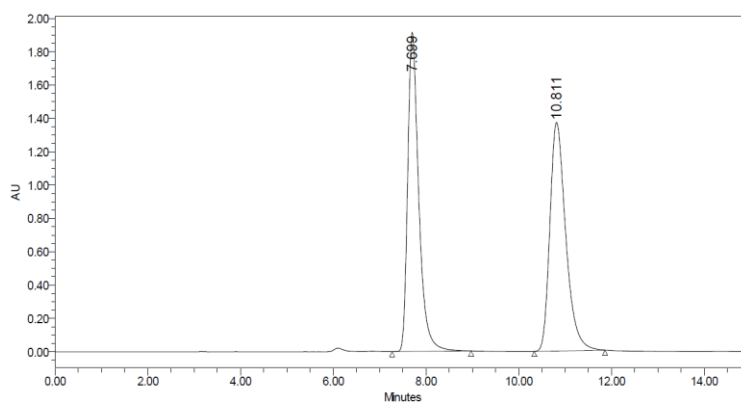
	RT	Area	% Area	Height
1	7.699	31596231	49.23	1914315
2	10.811	32588649	50.77	1370909

(*S*)-**2.2f**
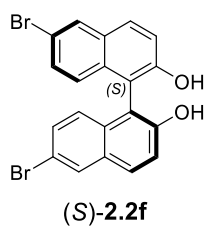
Chiralpak IC column,

95:5 hexane/isopropanol,

1 mL/min,

t_R = 7.7 min (minor),

10.8 min (major),

ee = 96%.
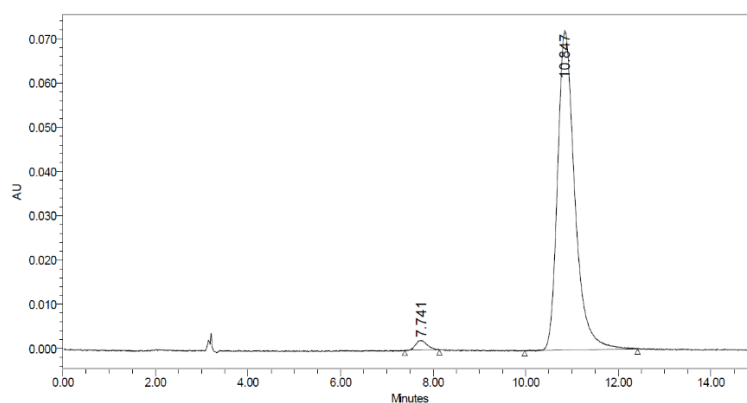
	RT	Area	% Area	Height
1	7.741	38545	2.03	2266
2	10.847	1863208	97.97	72205

(R)-2.2f
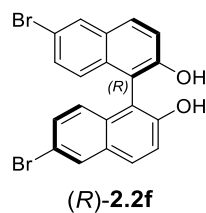
Chiralpak IC column,

95:5 hexane/isopropanol,

1 mL/min,

t_R = 7.7 min (major),

10.9 min (minor),

ee = 80%.
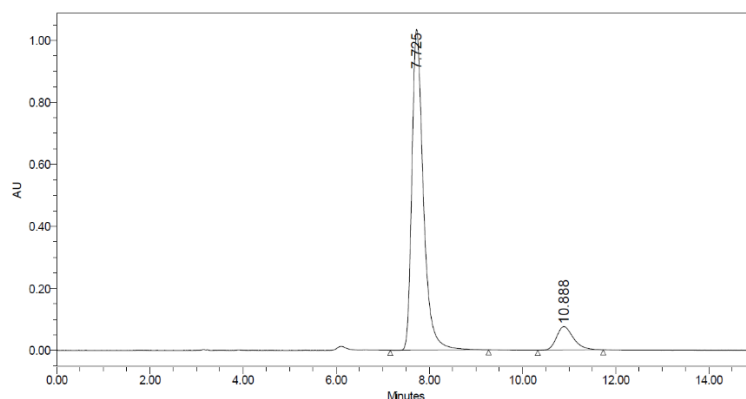
	RT	Area	% Area	Height
1	7.725	17699961	90.28	1035064
2	10.888	1904821	9.72	75778

2.4.10 Synthesis of Substrates 2.4a-2.4m
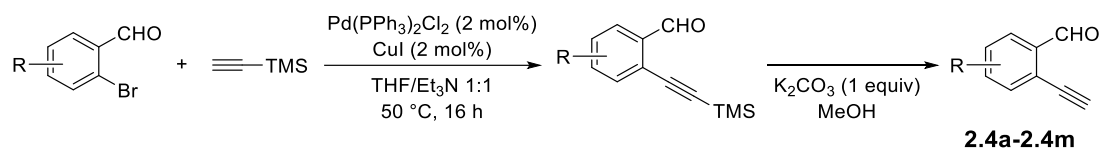
Scheme S2.10 Preparation of substrates **2.4a-2.4m**

Substrates **2.4a-2.4e, 2.4g-2.4m** was accomplished and the characterization data was verified according to our previous publication.[80] The synthesis of substrate **2.4f** was carried out as follows: a Sonogashira coupling of 2-bromo-6-methylbenzaldehyde (3 mmol, 1.0 equiv) with trimethylsilylacetylene (4.5 mmol, 1.5 equiv.) in 10 mL degegassed THF/Et$_3$N (1:1), catalyzed by Pd(PPh$_3$)$_2$Cl$_2$ (0.06 mmol, 0.02 equiv.) and CuI (0.06 mmol, 0.02 equiv.). The reaction was performed at 50 °C for 16 h. After filtration through celite, the filtrate was concentrated and purified by chromatographic column

(hexane/EA to afford the corresponding reaction intermediate (86% yield). The reaction intermediate was then subjected to deprotection of the trimethylsilyl group using K_2CO_3 (0.56 g, 2.58 mmol) in 10 mL MeOH at room temperature. Upon completion of the reaction, as indicated by thin-layer chromatography (TLC), water was added to the reaction mixture. The resulting residue was extracted with DCM and dried by anhydrous $MgSO_4$. The filtrate was concentrated and purified by chromatographic column (hexane/EA) to afford **2.4f** (pale yellow solid, 0.19 g, 1.34 mmol, 52% yield).

2.4.11 General Procedure for Gold(III) Complex (*R,R*)-2.3a Catalyzed Asymmetric Carboalkoxylation of *ortho*-Alkynylbenzaldehydes

The asymmetric carboalkoxylation affording **2.5a** is representative. A mixture of gold catalyst (*R,R*)-**2.2a** (0.010 mmol, 5 mol %), and D-camphorsulfonic acid (0.005 mmol, 2.5 mol %), and substrate **2.4a** (0.20 mmol) in 2 mL MeOH was stirred at room temperature for 16 h. The reaction mixture was concentrated and purified by chromatographic column (hexane/EA) to afford **5a** as pale yellow oil. This general procedure was applied to **2.5b-2.5m**. For **2.5n-2.5o**, MeOH was replaced by EtOH. Racemic samples were obtained with $KAuCl_4 \cdot 2H_2O$ as catalyst. Products **2.5a, 2.5c, 2.5g-2.5h, 2.5l-2.5m** were identified with reference to the characterization data in literatures.[79-80]

2.4.12   X-Ray Crystallography Data
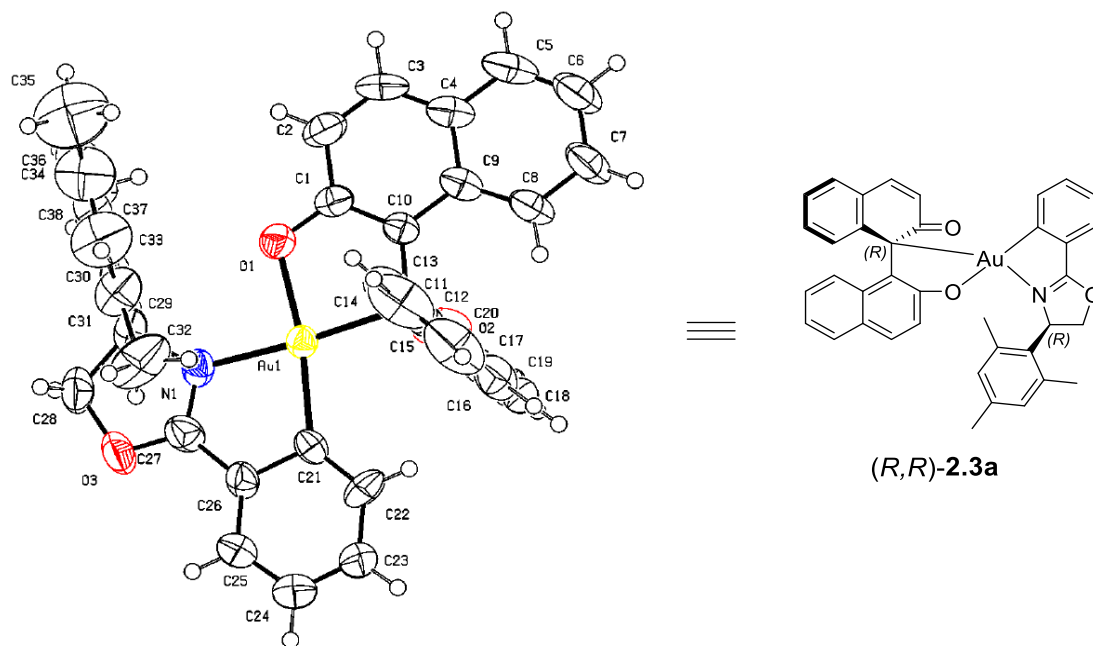
Figure S2.12 X-ray crystal structure of (*R*,*R*)-**2.3a**.

Table S2.11 Crystal data and structure refinement for (*R,R*)-**2.3a**.

Empirical formula	$C_{38}H_{30}AuNO_3$
Formula weight	745.60
Temperature/K	216(2)
Crystal system	orthorhombic
Space group	P212121
a/Å	10.4093(9)
b/Å	13.2093(12)
c/Å	23.861(2)
α/°	90
β/°	90
γ/°	90
Volume/Å^3	3280.9(5)
Z	4
ρcalcg/cm^3	1.510
μ/mm-1	4.520
F(000)	1472.0
Crystal size/mm3	$0.06 \times 0.04 \times 0.02$
Radiation	MoKα ($\lambda = 0.71073$)
2Θ range for data collection/°	4.27 to 55.944
Index ranges	$-13 \leq h \leq 13$, $-17 \leq k \leq 17$, $-31 \leq 1 \leq 31$
Reflections collected	54762
Independent reflections	7895 [$R_{int} = 0.1107$, $R_{sigma} = 0.0553$]
Data/restraints/parameters	7895/0/391
Goodness-of-fit on F^2	1.143
Final R indexes [I>=2σ (I)]	$R_1 = 0.0533$, w$R_2 = 0.1123$
Final R indexes [all data]	$R_1 = 0.0660$, w$R_2 = 0.1177$
Largest diff. peak/hole / e Å^{-3}	1.86/-4.17
Flack parameter	0.011(5)

Table S2.12 Fractional Atomic Coordinates ($\times 10^4$) and Equivalent Isotropic Displacement Parameters ($\text{Å}^2 \times 10^3$) for (*R,R*)-**2.3a**. U_{eq} is defined as 1/3 of the trace of the orthogonalised U_{IJ} tensor.

Atom	*x*	*y*	*z*	U(eq)
Au1	6833.2(5)	4622.0(3)	5296.9(2)	38.84(12)
C1	6196(13)	3996(11)	6381(5)	46(3)
C2	6113(16)	3371(13)	6859(7)	66(4)
C3	5352(19)	3660(14)	7295(6)	71(5)
C4	4629(16)	4537(13)	7275(5)	61(4)
C5	3810(20)	4812(16)	7718(7)	84(6)
C6	3050(30)	5649(14)	7687(7)	91(7)
C7	3110(20)	6278(12)	7220(6)	82(5)
C8	3921(17)	6048(12)	6790(6)	64(4)
C9	4710(14)	5189(10)	6798(5)	49(3)
C10	5504(13)	4887(9)	6344(5)	41(3)
C11	5661(11)	5546(8)	5816(5)	37(3)
C12	6419(14)	6490(9)	5942(6)	48(3)
C13	7521(18)	6465(14)	6229(7)	73(5)
C14	8260(30)	7299(18)	6346(8)	105(8)
C15	7830(30)	8218(18)	6165(10)	107(9)
C16	6660(30)	8302(12)	5887(8)	84(6)
C17	5960(19)	7416(11)	5760(6)	63(4)
C18	4770(20)	7482(14)	5484(7)	74(5)
C19	4020(16)	6680(15)	5348(8)	71(5)
C20	4390(13)	5649(10)	5520(5)	46(3)
C21	6902(13)	5411(10)	4560(4)	43(2)
C22	6451(15)	6303(10)	4400(7)	58(4)
C23	6628(18)	6702(12)	3865(6)	66(4)
C24	7279(18)	6156(14)	3471(7)	78(5)
C25	7810(15)	5250(14)	3616(6)	67(4)
C26	7643(13)	4852(9)	4140(6)	48(3)
C27	8204(19)	3932(10)	4337(6)	58(3)
C28	9321(19)	2515(13)	4393(7)	71(5)

C29	8677(15)	2704(11)	4960(7)	57(4)
C30	9516(15)	2745(11)	5468(7)	59(4)
C31	10418(16)	3547(13)	5548(8)	76(5)
C32	10570(20)	4436(14)	5151(10)	108(8)
C33	11200(20)	3524(19)	6020(11)	103(8)
C34	11110(20)	2800(20)	6423(11)	109(8)
C35	11930(30)	2830(20)	6965(12)	161(13)
C36	10270(19)	2010(17)	6336(8)	82(5)
C37	9546(17)	1982(13)	5878(7)	62(4)
C38	8570(20)	1124(13)	5825(7)	84(6)
N1	7957(10)	3647(8)	4845(4)	46(3)
O1	6923(10)	3686(7)	5960(4)	50(2)
O2	3756(10)	4890(9)	5428(4)	74(4)
O3	8957(13)	3354(9)	4038(5)	80(4)

Table S2.13 Anisotropic Displacement Parameters ($\mathring{A}^2 \times 10^3$) for (*R,R*)-**2.3a**.

Atom	U_{11}	U_{22}	U_{33}	U_{23}	U_{13}	U_{12}
Au1	35.28(19)	37.42(19)	43.8(2)	0.6(2)	3.1(2)	-0.7(2)
C1	45(7)	51(8)	44(7)	10(6)	-5(6)	-3(6)
C2	62(10)	71(11)	66(10)	28(8)	-5(8)	6(8)
C3	89(13)	80(12)	43(8)	29(8)	0(8)	-17(10)
C4	77(10)	64(9)	41(7)	7(7)	3(7)	-17(10)
C5	116(16)	95(15)	41(8)	11(9)	17(9)	-21(13)
C6	130(19)	82(13)	60(10)	-5(8)	45(12)	-1(14)
C7	118(15)	65(10)	62(9)	-12(8)	45(11)	-4(12)
C8	88(12)	60(9)	43(8)	-5(7)	22(8)	-13(9)
C9	58(8)	52(9)	38(6)	-5(6)	4(6)	-19(7)
C10	45(7)	42(7)	37(6)	-2(5)	0(5)	-6(5)
C11	43(6)	26(6)	42(6)	2(5)	15(5)	-1(5)
C12	64(9)	32(6)	48(8)	1(6)	15(7)	-11(6)
C13	74(12)	74(11)	70(11)	-21(9)	12(9)	-37(9)
C14	110(17)	112(17)	93(14)	-30(13)	23(14)	-74(16)
C15	130(20)	79(14)	108(17)	-34(12)	48(16)	-60(16)
C16	124(19)	41(8)	88(13)	-4(8)	46(14)	-1(11)
C17	92(13)	42(8)	54(9)	-4(6)	25(9)	3(8)
C18	92(14)	66(11)	65(11)	20(8)	28(10)	31(10)
C19	51(9)	102(13)	59(9)	14(11)	-1(8)	34(9)
C20	45(7)	55(8)	37(6)	-1(5)	15(5)	10(6)
C21	37(5)	47(6)	44(6)	-5(5)	8(5)	-6(7)
C22	64(10)	34(7)	76(10)	19(7)	-10(7)	0(6)
C23	70(12)	63(9)	64(9)	19(7)	15(8)	15(9)
C24	97(15)	75(11)	62(10)	26(9)	19(9)	15(10)
C25	69(11)	78(11)	54(8)	14(8)	19(7)	9(9)
C26	41(7)	42(8)	61(8)	4(6)	16(6)	-2(5)
C27	70(9)	47(7)	57(8)	1(6)	18(9)	-7(9)
C28	72(13)	57(10)	86(13)	-4(9)	16(10)	23(10)

C29	47(8)	43(8)	83(10)	3(7)	4(7)	8(6)
C30	41(8)	50(8)	88(12)	-6(7)	11(8)	9(7)
C31	41(8)	72(11)	115(15)	18(10)	-4(9)	-15(8)
C32	76(13)	71(12)	180(20)	59(14)	-12(14)	-32(10)
C33	66(13)	111(18)	130(20)	10(15)	-26(13)	-39(12)
C34	79(15)	130(20)	113(19)	2(17)	-17(13)	-28(15)
C35	130(30)	200(30)	160(30)	0(20)	-70(20)	-30(30)
C36	75(13)	100(15)	72(12)	4(11)	13(10)	-4(11)
C37	58(9)	64(10)	62(10)	-10(8)	12(8)	-4(8)
C38	140(20)	59(9)	57(9)	0(8)	9(10)	-7(11)
N1	37(6)	41(5)	60(7)	1(4)	6(5)	1(4)
O1	46(5)	53(5)	51(5)	5(4)	1(5)	3(5)
O2	66(7)	95(8)	61(7)	7(5)	-24(5)	-52(6)
O3	103(10)	58(7)	79(8)	2(6)	47(7)	25(6)

Table S2.14 Bond Lengths for (*R*,*R*)-**2.3a**.

Atom	Atom	Length/Å	Atom	Atom	Length/Å
Au1	C11	2.125(11)	C18	C19	1.35(3)
Au1	C21	2.045(11)	C19	C20	1.47(2)
Au1	N1	2.047(10)	C20	O2	1.220(16)
Au1	O1	2.009(8)	C21	C22	1.325(18)
C1	C2	1.410(19)	C21	C26	1.464(17)
C1	C10	1.383(18)	C22	C23	1.39(2)
C1	O1	1.324(16)	C23	C24	1.37(2)
C2	C3	1.36(2)	C24	C25	1.36(2)
C3	C4	1.38(2)	C25	C26	1.368(19)
C4	C5	1.41(2)	C26	C27	1.43(2)
C4	C9	1.431(19)	C27	N1	1.296(16)
C5	C6	1.36(3)	C27	O3	1.306(18)
C6	C7	1.39(2)	C28	C29	1.53(2)
C7	C8	1.36(2)	C28	O3	1.45(2)
C8	C9	1.40(2)	C29	C30	1.49(2)
C9	C10	1.419(18)	C29	N1	1.480(17)
C10	C11	1.540(15)	C30	C31	1.43(2)
C11	C12	1.505(17)	C30	C37	1.40(2)
C11	C20	1.505(19)	C31	C32	1.52(2)
C12	C13	1.34(2)	C31	C33	1.39(3)
C12	C17	1.38(2)	C33	C34	1.36(3)
C13	C14	1.37(2)	C34	C35	1.55(3)
C14	C15	1.36(4)	C34	C36	1.38(3)
C15	C16	1.39(3)	C36	C37	1.33(3)
C16	C17	1.41(3)	C37	C38	1.53(2)
C17	C18	1.41(3)			

Table S2.15 Bond Angles for (*R*,*R*)-**2.3a**.

Atom	Atom	Atom	Angle/°	Atom	Atom	Atom	Angle/°
C21	Au1	C11	103.2(5)	C18	C19	C20	120.4(15)
C21	Au1	N1	81.2(5)	C19	C20	C11	116.3(13)
N1	Au1	C11	175.5(4)	O2	C20	C11	119.1(12)
O1	Au1	C11	85.5(4)	O2	C20	C19	124.6(15)
O1	Au1	C21	171.3(4)	C22	C21	Au1	133.5(10)
O1	Au1	N1	90.1(4)	C22	C21	C26	116.0(12)
C10	C1	C2	121.2(14)	C26	C21	Au1	110.4(9)
O1	C1	C2	117.9(13)	C21	C22	C23	123.6(15)
O1	C1	C10	120.8(11)	C24	C23	C22	119.8(15)
C3	C2	C1	119.3(15)	C25	C24	C23	119.4(15)
C2	C3	C4	121.7(14)	C24	C25	C26	121.2(15)
C3	C4	C5	121.5(15)	C25	C26	C21	119.9(13)
C3	C4	C9	120.0(14)	C25	C26	C27	125.1(13)
C5	C4	C9	118.6(17)	C27	C26	C21	114.9(12)
C6	C5	C4	121.6(16)	N1	C27	C26	118.2(14)
C5	C6	C7	120.1(17)	N1	C27	O3	117.5(14)
C8	C7	C6	119.8(19)	O3	C27	C26	124.3(13)
C7	C8	C9	122.4(15)	O3	C28	C29	106.2(12)
C8	C9	C4	117.6(13)	C30	C29	C28	117.9(13)
C8	C9	C10	124.0(12)	N1	C29	C28	101.2(12)
C10	C9	C4	118.2(14)	N1	C29	C30	114.6(13)
C1	C10	C9	119.6(12)	C31	C30	C29	121.3(15)
C1	C10	C11	118.6(11)	C37	C30	C29	123.4(15)
C9	C10	C11	121.8(11)	C37	C30	C31	115.1(16)
C10	C11	Au1	102.3(7)	C30	C31	C32	123.8(17)
C12	C11	Au1	106.9(8)	C33	C31	C30	118.5(17)
C12	C11	C10	111.2(10)	C33	C31	C32	117.7(17)
C20	C11	Au1	106.4(8)	C34	C33	C31	123.3(19)
C20	C11	C10	109.9(10)	C33	C34	C35	122(2)
C20	C11	C12	118.7(11)	C33	C34	C36	118(2)

C13	C12	C11	122.1(14)	C36	C34	C35	119(2)
C13	C12	C17	118.6(15)	C37	C36	C34	120(2)
C17	C12	C11	119.3(14)	C30	C37	C38	117.4(16)
C12	C13	C14	124(2)	C36	C37	C30	124.4(17)
C15	C14	C13	118(3)	C36	C37	C38	117.8(17)
C14	C15	C16	120.4(19)	C27	N1	Au1	115.1(10)
C15	C16	C17	119.4(18)	C27	N1	C29	108.5(12)
C12	C17	C16	119.1(19)	C29	N1	Au1	136.2(9)
C12	C17	C18	120.4(16)	C1	O1	Au1	112.4(8)
C18	C17	C16	120.4(18)	C27	O3	C28	106.5(12)
C19	C18	C17	124.8(16)				

Table S2.16 Hydrogen Atom Coordinates $(\text{Å}\times10^4)$ and Isotropic Displacement Parameters $(\text{Å}^2\times10^3)$ for (R,R)-**2.3a**.

Atom	x	y	z	U(eq)
H2	6577.05	2760.94	6875.74	79
H3	5318.79	3252.92	7618.04	85
H5	3785.17	4409.47	8042.42	101
H6	2480.93	5802.04	7982.19	109
H7	2587.68	6859.2	7200.11	98
H8	3953.53	6480.94	6478.23	76
H13	7809.1	5833.36	6360.45	87
H14	9034.9	7237.99	6544.91	126
H15	8334.16	8799.27	6228.98	129
H16	6342.89	8941.22	5785.51	101
H18	4470.43	8130.61	5386.32	89
H19	3260.45	6781.64	5143.02	85
H22	5986.48	6688.79	4661.78	70
H23	6299.16	7345.03	3775.59	79
H24	7361.27	6402.21	3103.42	93

H25	8300.09	4891.74	3351.31	80
H28A	10256.81	2486.03	4435.19	86
H28B	9024.52	1873.43	4231.76	86
H29	8040.58	2157.62	5020.03	69
H32A	10136.43	5023.93	5306.81	162
H32B	10182.67	4268.08	4791.84	162
H32C	11470.08	4584.54	5099.37	162
H33	11818.9	4034.74	6062.92	124
H35A	11662.02	2286.08	7213.36	242
H35B	11821.06	3473.24	7150.45	242
H35C	12830.54	2734.83	6868.23	242
H36	10209.56	1487.52	6602.56	99
H38A	8867.27	541.4	6035.34	127
H38B	8474.75	940.12	5433.15	127
H38C	7747.64	1345.27	5971.45	127

2.4.13 Characterization Data
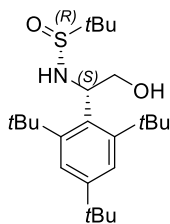
S2.2

¹H NMR (600 MHz, CDCl₃) δ 7.56 (s, 1H), 7.46 (s, 1H), 5.66 (dt, J = 7.2, 3.4 Hz, 1H), 4.49 (td, J = 7.6, 3.8 Hz, 1H), 3.92 – 3.84 (m, 1H), 3.60 (d, J = 3.3 Hz, 1H), 1.60 (s, 9H), 1.53 (s, 9H), 1.31 (s, 9H), 1.28 (s, 9H).

¹³C NMR (150 MHz, CDCl₃) δ 150.75, 149.92, 148.86, 133.59, 126.28, 123.01, 67.62, 58.80, 56.33, 38.69, 37.92, 35.26, 34.99, 33.69, 31.35, 22.92.

HRMS (ESI): [M + H]⁺ Calcd. for $[C_{24}H_{44}NO_2S]^+$ 410.3087, found 410.3094.
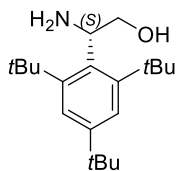
S2.3

¹H NMR (600 MHz, CDCl₃) δ 7.48 (s, 2H), 4.91 (dd, J = 10.7, 5.7 Hz, 1H), 4.08 (t, J = 10.6 Hz, 1H), 3.52 (dd, J = 10.6, 5.7 Hz, 1H), 1.52 (s, 18H), 1.31 (d, J = 1.3 Hz, 9H), 1.19 (d, J = 1.3 Hz, 1H).

¹³C NMR (150 MHz, CDCl₃) δ 149.60, 147.99, 137.12, 65.23, 52.70, 35.00, 31.45, 21.65.

HRMS (ESI): [M + Na]⁺ Calcd. for $[C_{20}H_{35}NNaO]^+$ 328.2611, found 328.2620.
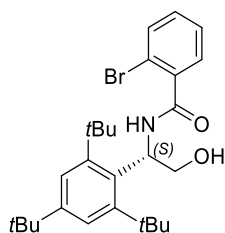
S2.4

¹H NMR (600 MHz, CDCl₃) δ 7.63 – 7.55 (m, 2H), 7.48 (s, 1H), 7.42 (dd, *J* = 7.6, 1.7 Hz, 1H), 7.34 (t, *J* = 7.5 Hz, 1H), 7.29 – 7.26 (m, 1H), 6.46 (s, 1H), 6.20 (td, *J* = 4.9, 2.2 Hz, 1H), 5.14 (d, *J* = 9.5 Hz, 1H), 4.71 (dd, *J* = 11.6, 7.6 Hz, 1H), 4.00 – 3.90 (m, 1H), 1.60 (s, 9H), 1.53 (s, 9H), 1.31 (s, 9H).

¹³C NMR (150 MHz, CDCl₃) δ 169.21, 149.55, 137.49, 133.73, 131.96, 131.59, 128.83, 127.68, 119.44, 68.86, 58.04, 35.26, 35.10, 33.40, 31.37.

HRMS (ESI): [M + Na]⁺ Calcd. for [C₂₇H₃₈BrNNaO₂]⁺ 510.1978, found 510.1985.
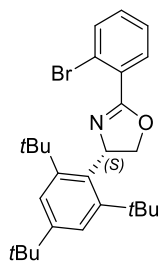
S2.5

¹H NMR (600 MHz, CDCl₃) δ 7.86 (d, *J* = 7.7 Hz, 1H), 7.67 (d, *J* = 8.1 Hz, 1H), 7.48 (s, 2H), 7.38 (td, *J* = 7.6, 1.3 Hz, 1H), 7.30 (td, *J* = 7.7, 1.7 Hz, 1H), 6.50 (t, *J* = 12.7 Hz, 1H), 4.64 (dd, *J* = 12.3, 8.3 Hz, 1H), 4.22 (dd, *J* = 13.2, 8.3 Hz, 1H), 1.52 (s, 18H), 1.33 (s, 9H).

¹³C NMR (150 MHz, CDCl₃) δ 161.96, 150.98, 148.35, 134.15, 133.86, 131.68, 131.65, 130.35, 127.29, 123.68, 121.94, 74.89, 67.64, 38.19, 35.02, 34.00, 31.48.

HRMS (ESI): [M + H]⁺ Calcd. for [C₂₇H₃₇BrNO]⁺ 470.2053, found 470.2059.

S2.6
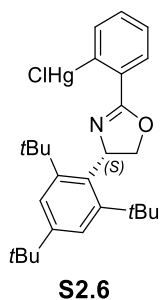
^{1}H NMR (600 MHz, CDCl$_3$) δ 8.01 (d, *J* = 7.7 Hz, 1H), 7.57 (td, *J* = 7.4, 1.3 Hz, 1H), 7.48 – 7.39 (m, 4H), 6.45 (t, *J* = 12.5 Hz, 1H), 4.65 (dd, *J* = 12.2, 8.3 Hz, 1H), 4.22 (dd, *J* = 12.9, 8.3 Hz, 1H), 1.53 – 1.36 (m, 18H), 1.32 (s, 9H).

^{13}C NMR (150 MHz, CDCl$_3$) δ 167.11, 150.97, 148.46, 137.35, 133.34, 132.64, 132.50, 128.85, 128.76, 66.80, 53.57, 35.03, 33.97, 33.20, 31.47, 30.65, 28.10, 13.67.

HRMS (ESI): [M + Na]$^+$ Calcd. for [C$_{27}$H$_{37}$ClHgNO]$^+$ 628.2264, found 628.2266.

(*S*)-**2.1c**
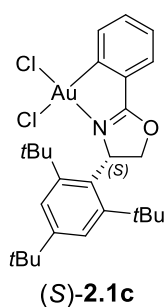
^{1}H NMR (600 MHz, CDCl$_3$) δ 8.06 (d, *J* = 7.9 Hz, 1H), 7.58 (d, *J* = 2.0 Hz, 1H), 7.53 – 7.47 (m, 2H), 7.44 – 7.39 (m, 2H), 6.55 (t, *J* = 12.0 Hz, 1H), 5.45 – 5.38 (m, 1H), 5.17 – 5.10 (m, 1H), 1.55 (s, 9H), 1.47 (s, 9H), 1.31 (s, 9H).

^{13}C NMR (150 MHz, CDCl$_3$) δ 180.96, 151.25, 150.61, 150.26, 148.90, 135.29, 131.04, 128.65, 128.56, 128.09, 127.90, 127.14, 123.29, 65.12, 39.31, 37.60, 35.24, 35.01, 34.56, 31.31.

HRMS (ESI): [M - Cl]$^+$ Calcd. for [C$_{27}$H$_{36}$AuClNO]$^+$ 622.2145, found 622.2153.

(*R,R*)-**2.3a**   (*S,S*)-**2.3a**
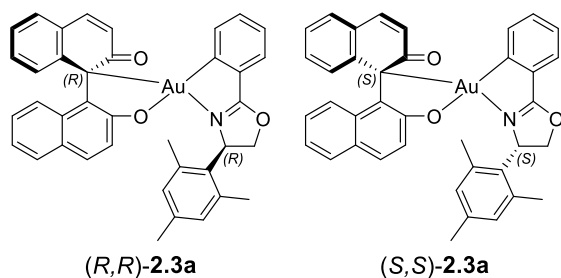
¹H NMR (600 MHz, CDCl₃) δ 7.85 (d, *J* = 10.0 Hz, 1H), 7.60 (d, *J* = 7.6 Hz, 1H), 7.55 (d, *J* = 8.9 Hz, 1H), 7.43 – 7.40 (m, 1H), 7.31 (d, *J* = 7.9 Hz, 1H), 7.25 – 7.20 (m, 2H), 7.18 (t, *J* = 7.5 Hz, 1H), 7.16 – 7.14 (m, 1H), 7.06 (t, *J* = 7.6 Hz, 1H), 7.04 – 7.01 (m, 1H), 6.98 – 6.91 (m, 2H), 6.90 (d, *J* = 8.9 Hz, 1H), 6.85 (s, 1H), 6.61 (d, *J* = 9.0 Hz, 1H), 6.52 (d, *J* = 10.0 Hz, 1H), 6.10 (dd, *J* = 11.9, 8.0 Hz, 1H), 5.18 (dd, *J* = 11.8, 8.6 Hz, 1H), 4.81 (t, *J* = 8.3 Hz, 1H), 2.78 (s, 3H), 2.31 (s, 3H), 2.09 (s, 3H).

¹³C NMR (100 MHz, CDCl₃) δ 200.84, 179.13, 170.85, 146.75, 144.84, 140.42, 138.42, 133.52, 132.75, 130.72, 130.66, 130.29, 130.11, 129.56, 129.52, 128.89, 128.83, 128.58, 128.51, 128.10, 127.61, 126.76, 126.49, 125.92, 124.94, 121.65, 120.60, 120.54, 77.53, 70.10, 61.77, 20.98.

HRMS (ESI): [M + H]⁺ Calcd. for [C₃₈H₃₁AuNO₃]⁺ 746.1964, found 746.1967.

(*R,S*)-**2.3a**   (*S,R*)-**2.3a**
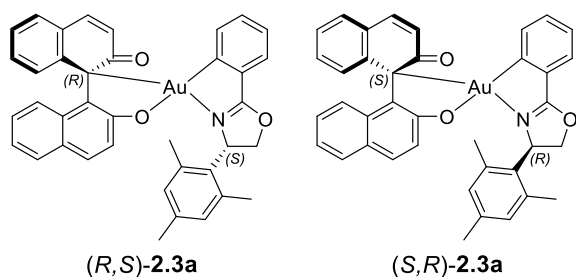
¹H NMR (400 MHz, CDCl₃) δ 7.89 (d, J = 9.8 Hz, 1H), 7.62 – 7.56 (m, 1H), 7.53 (d, J = 8.4 Hz, 1H), 7.48 – 7.42 (m, 2H), 7.40 – 7.35 (m, 2H), 7.25 – 7.17 (m, 2H), 7.12 (td, J = 7.5, 1.4 Hz, 1H), 7.04 (td, J = 7.6, 1.5 Hz, 1H), 6.99 – 6.91 (m, 3H), 6.85 – 6.78 (m,

2H), 6.68 – 6.57 (m, 2H), 6.10 (dd, J = 11.6, 7.8 Hz, 1H), 5.17 (dd, J = 11.4, 8.9 Hz, 1H), 4.83 (dd, J = 8.9, 8.0 Hz, 1H), 2.75 (s, 3H), 2.28 (s, 3H), 2.17 (s, 3H).

^{13}C NMR (150 MHz, CDCl$_3$) δ 200.84, 179.18, 170.94, 147.38, 145.11, 141.57, 138.64, 134.10, 132.76, 132.19, 130.53, 130.47, 130.38, 130.35, 129.73, 129.22, 129.15, 128.97, 128.86, 128.61, 128.24, 127.74, 126.77, 126.48, 126.04, 125.10, 121.67, 120.72, 120.62, 77.59, 70.12, 61.96, 21.01.

HRMS (ESI): [M + H]$^+$ Calcd. for [C$_{38}$H$_{31}$AuNO$_3$]$^+$ 746.1964, found 746.1966.

(*R,S*)-**2.3b**
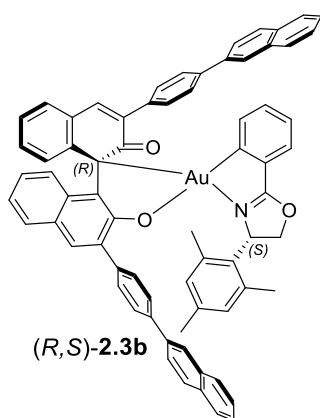
^{1}H NMR (600 MHz, CDCl$_3$) δ 8.22 – 8.19 (m, 1H), 8.09 (s, 1H), 8.06 – 7.99 (m, 3H), 7.95 – 7.89 (m, 4H), 7.86 (dd, *J* = 8.8, 1.1 Hz, 1H), 7.78 – 7.72 (m, 4H), 7.72 – 7.68 (m, 4H), 7.68 – 7.64 (m, 1H), 7.61 (s, 1H), 7.59 – 7.52 (m, 4H), 7.52 – 7.46 (m, 4H), 7.40 (dd, *J* = 7.4, 1.7 Hz, 1H), 7.35 (td, *J* = 7.7, 1.7 Hz, 1H), 7.21 (dtd, *J* = 18.7, 7.4, 1.1 Hz, 2H), 7.15 – 7.09 (m, 2H), 7.03 – 6.99 (m, 2H), 6.80 (s, 1H), 6.65 (s, 1H), 5.93 (dd, *J* = 11.0, 8.7 Hz, 1H), 5.17 (dd, *J* = 11.0, 8.6 Hz, 1H), 4.55 (t, *J* = 8.6 Hz, 1H), 2.41 (s, 3H), 2.22 (s, 3H), 2.13 (s, 3H).

^{13}C NMR (150 MHz, CDCl$_3$) δ 199.26, 179.42, 168.09, 146.96, 143.17, 141.64, 140.95, 139.33, 138.98, 138.81, 138.54, 138.32, 137.54, 135.80, 134.10, 134.02, 133.79, 133.58, 132.78, 132.73, 132.46, 131.33, 131.08, 130.68, 130.55, 130.29, 130.07, 129.63, 129.52,

129.49, 129.27, 129.08, 128.69, 128.58, 128.54, 128.38, 127.87, 127.78, 127.28, 127.10, 126.92, 126.87, 126.85, 126.48, 126.43, 126.16, 126.10, 125.98, 125.89, 125.65, 125.62, 125.43, 121.20, 120.51, 78.25, 70.08, 63.55, 20.94.

HRMS (ESI): $[M + H]^+$ Calcd. for $[C_{70}H_{51}AuNO_3]^+$ 1150.3529, found 1150.3527.

(S,S)-**2.3b**

^{1}H NMR (600 MHz, CDCl$_3$) δ 8.27 – 8.24 (m, 1H), 8.05 – 7.99 (m, 4H), 7.98 – 7.93 (m, 2H), 7.88 (dd, J = 8.9, 5.8 Hz, 2H), 7.86 – 7.84 (m, 1H), 7.72 (dd, J = 8.5, 1.8 Hz, 1H), 7.70 – 7.67 (m, 2H), 7.67 – 7.64 (m, 4H), 7.64 – 7.61 (m, 2H), 7.57 (ddd, J = 8.2, 4.5, 1.1 Hz, 2H), 7.55 – 7.52 (m, 3H), 7.51 – 7.45 (m, 3H), 7.40 (dd, J = 7.4, 1.7 Hz, 1H), 7.34 – 7.26 (m, 3H), 7.22 (dtd, J = 17.7, 7.4, 1.2 Hz, 2H), 7.03 – 6.98 (m, 2H), 6.97 – 6.92 (m, 1H), 6.79 (s, 1H), 6.49 (s, 1H), 5.82 (dd, J = 11.4, 8.3 Hz, 1H), 5.09 (dd, J = 11.4, 8.8 Hz, 1H), 4.52 (d, J = 8.5 Hz, 1H), 2.19 (s, 3H), 2.16 (d, J = 16.5 Hz, 3H), 1.79 (s, 3H).

^{13}C NMR (150 MHz, CDCl$_3$) δ 198.92, 179.54, 168.46, 146.53, 142.79, 140.71, 140.67, 139.72, 138.80, 138.52, 138.30, 138.13, 137.35, 135.59, 134.06, 133.92, 133.77, 133.53, 132.76, 132.74, 132.48, 131.45, 130.99, 130.63, 130.32, 129.96, 129.87, 129.57, 129.40, 129.03, 128.71, 128.53, 128.49, 128.37, 128.34, 127.87, 127.76, 127.72, 127.07, 127.04, 126.99, 126.87, 126.68, 126.47, 126.40, 126.16, 126.05, 125.96, 125.80, 125.63, 125.54, 125.30, 121.14, 120.49, 78.10, 70.48, 62.74, 31.73, 22.80, 20.92, 14.28.

HRMS (ESI): $[M + H]^+$ Calcd. for $[C_{70}H_{51}AuNO_3]^+$ 1150.3529, found 1150.3528.

(R,S)-**2.3c**

¹H NMR (600 MHz, CDCl₃) δ 8.13 (s, 1H), 8.09 (s, 1H), 7.98 – 7.94 (m, 1H), 7.94 – 7.90 (m, 1H), 7.89 (s, 1H), 7.85 – 7.79 (m, 3H), 7.75 (dd, *J* = 8.3, 2.0 Hz, 2H), 7.68 – 7.65 (m, 1H), 7.64 (dd, *J* = 8.5, 1.7 Hz, 1H), 7.61 (dd, *J* = 7.8, 1.2 Hz, 1H), 7.60 – 7.52 (m, 5H), 7.46 (dt, *J* = 6.2, 3.4 Hz, 2H), 7.38 – 7.33 (m, 2H), 7.21 (tdd, *J* = 7.6, 4.8, 1.1 Hz, 2H), 7.18 – 7.11 (m, 2H), 7.04 – 6.99 (m, 2H), 6.66 (s, 1H), 5.89 (s, 1H), 5.80 (dd, *J* = 11.1, 8.9 Hz, 1H), 5.06 (dd, *J* = 11.2, 8.7 Hz, 1H), 4.47 (t, *J* = 8.8 Hz, 1H), 2.26 (s, 3H), 2.05 (s, 3H), 1.71 (s, 3H).

¹³C NMR (150 MHz, CDCl₃) δ 199.41, 179.28, 168.35, 147.01, 143.51, 141.59, 139.13, 138.36, 137.22, 134.37, 134.19, 133.99, 133.88, 133.39, 133.19, 132.55, 131.42, 130.63, 130.50, 130.47, 130.24, 129.47, 129.41, 129.26, 129.10, 128.66, 128.52, 128.47, 128.42, 128.18, 127.76, 127.65, 127.54, 127.52, 127.39, 127.09, 126.98, 126.89, 126.87, 126.83, 126.23, 126.14, 126.09, 125.44, 121.12, 120.48, 77.91, 70.13, 63.06, 20.98, 20.79.

HRMS (ESI): [M + H]⁺ Calcd. for [C₅₈H₄₃AuNO₃]⁺ 998.2903, found 998.2902.

(S,S)-**2.3c**
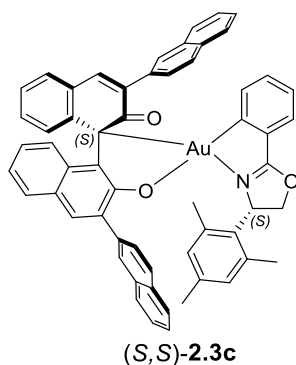
¹H NMR (400 MHz, CDCl₃) δ 8.06 (s, 1H), 7.98 – 7.93 (m, 3H), 7.89 – 7.85 (m, 1H), 7.81 – 7.76 (m, 2H), 7.74 (d, J = 8.5 Hz, 1H), 7.70 – 7.61 (m, 4H), 7.60 – 7.51 (m, 4H), 7.47 (dt, J = 8.4, 1.5 Hz, 2H), 7.45 – 7.40 (m, 2H), 7.38 (dd, J = 7.3, 1.7 Hz, 1H), 7.29 (tt, J = 7.4, 1.6 Hz, 2H), 7.24 – 7.18 (m, 2H), 7.04 – 6.98 (m, 2H), 6.98 – 6.94 (m, 1H), 6.74 (s, 1H), 6.07 (s, 1H), 5.71 (dd, J = 11.4, 8.3 Hz, 1H), 5.01 (dd, J = 11.4, 8.8 Hz, 1H), 4.47 (t, J = 8.5 Hz, 1H), 2.22 (s, 3H), 2.09 (s, 3H), 1.35 (s, 3H).

¹³C NMR (150 MHz, CDCl₃) δ 198.98, 179.44, 168.60, 146.58, 143.21, 140.68, 138.86, 138.65, 137.32, 134.68, 134.04, 133.88, 133.47, 133.32, 133.09, 132.58, 132.52, 131.49, 131.02, 130.67, 130.29, 129.95, 129.86, 129.69, 129.33, 129.01, 128.81, 128.66, 128.55, 128.44, 128.38, 128.13, 127.84, 127.64, 127.62, 127.59, 127.54, 127.41, 127.36, 127.19, 127.06, 127.01, 126.48, 126.15, 125.99, 125.49, 125.46, 121.11, 120.55, 77.91, 70.67, 62.49, 29.84, 20.96, 20.08.

HRMS (ESI): [M + H]⁺ Calcd. for [C₅₈H₄₃AuNO₃]⁺ 998.2903, found 998.2902.
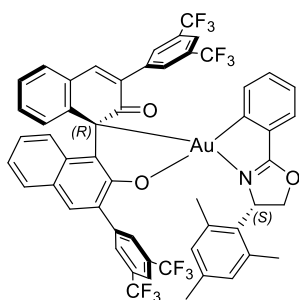
(*R,S*)-**2.3d**

¹H NMR (400 MHz, CDCl₃) δ 8.07 (s, 1H), 8.03 – 7.98 (m, 2H), 7.94 – 7.89 (m, 3H),

7.80 (s, 1H), 7.67 – 7.60 (m, 2H), 7.57 (dd, *J* = 7.7, 1.5 Hz, 1H), 7.45 – 7.40 (m, 2H),

7.34 (dd, *J* = 7.6, 1.5 Hz, 1H), 7.33 – 7.26 (m, 3H), 7.26 – 7.22 (m, 1H), 7.04 – 6.97 (m,

2H), 6.87 – 6.79 (m, 1H), 6.66 (s, 1H), 6.25 (s, 1H), 5.82 (dd, *J* = 11.1, 8.4 Hz, 1H), 5.14

(dd, *J* = 11.1, 8.9 Hz, 1H), 4.60 (t, *J* = 8.6 Hz, 1H), 2.29 –2.00 (s, 6H), 1.78 (s, 3H).

¹³C NMR (150 MHz, CDCl₃) δ 198.04, 179.25, 167.66, 146.64, 144.09, 142.94, 140.10,

138.41, 138.05, 135.92, 135.83, 133.79, 132.91, 131.84, 131.55, 131.41, 131.33, 131.23,

131.01, 130.68, 130.23, 129.89, 129.67, 129.58, 129.51, 129.27, 129.12, 129.04, 128.83,

128.64, 128.21, 127.39, 127.28, 127.02, 126.58, 124.87, 124.36, 123.06, 122.55, 121.64,

120.17, 77.96, 70.14, 62.28, 20.55.

HRMS (ESI): [M + H]⁺ Calcd. for [C₅₄H₃₅AuF₁₂NO₃]⁺ 1170.2085, found 1170.2084.
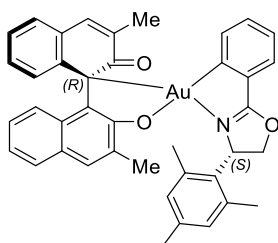
(*R,S*)-**2.3e**

¹H NMR (400 MHz, CDCl₃) δ 7.72 (d, *J* = 1.5 Hz, 1H), 7.50 (td, *J* = 7.5, 1.5 Hz, 2H),

7.39 (dd, *J* = 7.3, 1.8 Hz, 1H), 7.36 (dd, *J* = 7.6, 1.4 Hz, 2H), 7.32 (t, *J* = 1.0 Hz, 1H),

7.24 (dd, *J* = 7.6, 1.9 Hz, 1H), 7.19 (td, *J* = 7.4, 1.2 Hz, 1H), 7.09 (td, *J* = 7.4, 1.3 Hz,

1H), 6.98 (td, J = 7.5, 1.4 Hz, 1H), 6.95 – 6.84 (m, 4H), 6.73 – 6.67 (m, 1H), 6.09 (dd, J = 11.2, 9.5 Hz, 1H), 5.20 (dd, J = 11.2, 8.8 Hz, 1H), 4.70 (t, J = 9.2 Hz, 1H), 2.58 (s, 3H), 2.33 (s, 3H), 2.29 (s, 3H), 2.10 (d, J = 1.3 Hz, 3H), 1.95 (d, J = 1.0 Hz, 3H).

13C NMR (150 MHz, CDCl₃) δ 200.80, 179.37, 169.79, 146.83, 142.07, 141.65, 138.26, 136.84, 136.73, 134.20, 132.31, 131.70, 130.78, 130.67, 130.52, 130.48, 129.66, 129.42, 129.16, 129.14, 127.92, 127.68, 127.36, 126.61, 126.41, 124.84, 124.68, 120.46, 120.23, 77.42, 69.44, 62.81, 29.84, 20.96, 16.65, 16.36.

HRMS (ESI): [M + H]⁺ Calcd. for [C₄₀H₃₅AuNO₃]⁺ 774.2277, found 774.2276.

(S,S)-**2.3e**
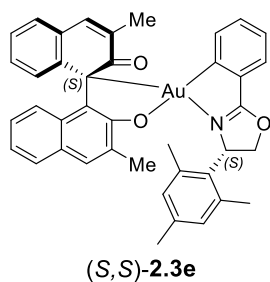
1H NMR (400 MHz, CDCl₃) δ 7.70 (d, J = 1.6 Hz, 1H), 7.51 (dd, J = 8.0, 1.5 Hz, 1H), 7.43 – 7.38 (m, 2H), 7.34 (t, J = 1.0 Hz, 1H), 7.23 (ddd, J = 14.5, 6.7, 1.9 Hz, 4H), 7.14 (td, J = 7.5, 1.3 Hz, 1H), 6.98 (td, J = 7.6, 1.4 Hz, 2H), 6.94 – 6.82 (m, 3H), 6.62 (dd, J = 8.5, 1.1 Hz, 1H), 6.08 (dd, J = 11.3, 9.5 Hz, 1H), 5.20 (dd, J = 11.3, 8.8 Hz, 1H), 4.72 – 4.63 (m, 1H), 2.58 (s, 3H), 2.32 (s, 3H), 2.20 (s, 3H), 2.05 (dd, J = 6.4, 1.2 Hz, 6H).

13C NMR (150 MHz, CDCl₃) δ 200.72, 179.39, 169.94, 146.52, 141.66, 141.40, 138.24, 136.30, 133.84, 131.84, 130.73, 130.35, 129.79, 129.76, 129.63, 129.44, 129.23, 129.07, 127.77, 127.69, 127.68, 127.34, 126.72, 126.53, 124.87, 124.44, 120.46, 120.30, 77.43, 69.78, 62.61, 29.84, 21.04, 16.54, 16.51.

HRMS (ESI): [M + H]⁺ Calcd. for [C₄₀H₃₅AuNO₃]⁺ 774.2277, found 774.2276.

(*R*,*S*)-**2.3f**
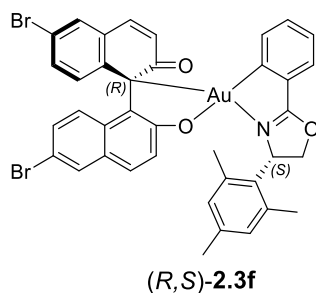
¹H NMR (600 MHz, CDCl₃) δ 7.81 (d, *J* = 9.9 Hz, 1H), 7.73 (d, *J* = 2.3 Hz, 1H), 7.59 (d, *J* = 2.1 Hz, 1H), 7.47 – 7.37 (m, 3H), 7.29 – 7.22 (m, 2H), 7.22 – 7.12 (m, 2H), 7.03 (dd, *J* = 9.0, 2.1 Hz, 1H), 6.97 (s, 1H), 6.84 (s, 1H), 6.80 (d, *J* = 8.9 Hz, 1H), 6.66 (d, *J* = 9.9 Hz, 1H), 6.44 (d, *J* = 9.0 Hz, 1H), 6.08 (dd, *J* = 11.5, 8.0 Hz, 1H), 5.19 (dd, *J* = 11.5, 9.0 Hz, 1H), 4.83 (t, *J* = 8.5 Hz, 1H), 2.73 (s, 3H), 2.28 (s, 3H), 2.18 (s, 3H).

¹³C NMR (150 MHz, CDCl₃) δ 200.01, 179.25, 171.43, 146.04, 143.58, 140.96, 138.75, 134.39, 133.25, 132.21, 131.91, 131.24, 131.16, 130.25, 130.22, 130.19, 130.08, 129.73, 129.23, 129.07, 128.04, 127.09, 124.76, 122.89, 122.10, 120.06, 114.20, 77.64, 67.97, 61.50, 20.54.

HRMS (ESI): [M + H]⁺ Calcd. for [C₃₈H₂₉AuBr₂NO₃]⁺ 902.0174, found 902.0171.

(*S*,*S*)-**2.3f**
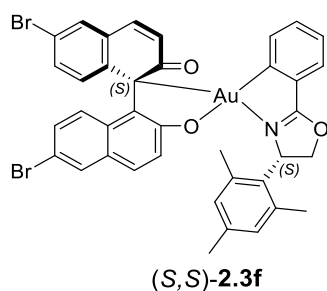
¹H NMR (600 MHz, CDCl₃) δ 7.80 – 7.73 (m, 2H), 7.65 (d, *J* = 2.0 Hz, 1H), 7.46 (d, *J* = 8.9 Hz, 1H), 7.43 (dd, *J* = 7.0, 2.1 Hz, 1H), 7.28 – 7.23 (m, 2H), 7.18 – 7.08 (m, 3H), 7.05 – 7.00 (m, 2H), 6.89 (d, *J* = 8.9 Hz, 1H), 6.85 (d, *J* = 10.6 Hz, 1H), 6.55 (d, *J* = 9.9

Hz, 1H), 6.42 (d, *J* = 9.0 Hz, 1H), 6.08 (dd, *J* = 11.6, 8.0 Hz, 1H), 5.19 (dd, *J* = 11.6, 8.9

Hz, 1H), 4.81 (t, *J* = 8.5 Hz, 1H), 2.75 (s, 3H), 2.31 (s, 3H), 2.09 (s, 3H).

¹³C NMR (150 MHz, CDCl₃) δ 200.13, 179.34, 171.45, 145.52, 143.43, 139.81, 138.67,

133.88, 133.34, 132.17, 131.79, 131.27, 131.09, 130.64, 130.49, 130.24, 130.21, 130.00,

129.70, 129.62, 129.49, 129.46, 129.25, 128.04, 127.20, 124.74, 122.98, 122.15, 120.25,

114.24, 77.72, 69.14, 61.86, 21.10.

HRMS (ESI): [M + H]⁺ Calcd. for [C₃₈H₂₉AuBr₂NO₃]⁺ 902.0174, found 902.0172.

(*R*,*R*)-**2.3g**
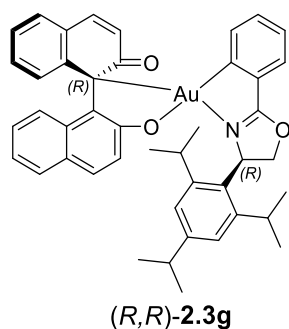
¹H NMR (600 MHz, CDCl₃) δ 7.84 (d, *J* = 10.0 Hz, 1H), 7.60 – 7.55 (m, 1H), 7.50 (d, *J*

= 8.6 Hz, 1H), 7.44 (dd, *J* = 7.7, 1.5 Hz, 1H), 7.41 – 7.38 (m, 1H), 7.24 (dd, *J* = 7.9, 1.2

Hz, 1H), 7.23 – 7.20 (m, 2H), 7.20 – 7.18 (m, 1H), 7.18 – 7.16 (m, 1H), 7.11 (td, *J* = 7.4,

1.2 Hz, 1H), 7.06 (d, *J* = 2.0 Hz, 1H), 6.99 – 6.95 (m, 1H), 6.95 – 6.89 (m, 2H), 6.76 (d,

J = 9.0 Hz, 1H), 6.69 – 6.64 (m, 1H), 6.54 (d, *J* = 9.8 Hz, 1H), 6.22 – 6.15 (m, 1H), 5.18

(dd, *J* = 11.7, 8.7 Hz, 1H), 4.68 (dd, *J* = 9.9, 8.6 Hz, 1H), 3.71 (p, *J* = 6.8 Hz, 1H), 2.93

(p, *J* = 6.9 Hz, 1H), 2.70 (p, *J* = 6.7 Hz, 1H), 2.13 (s, 1H), 2.03 (s, 2H), 1.63 (d, *J* = 6.7

Hz, 3H), 1.30 (t, *J* = 7.0 Hz, 6H), 1.18 (d, *J* = 6.9 Hz, 3H), 1.03 (d, *J* = 6.7 Hz, 3H).

¹³C NMR (100 MHz, CDCl₃) δ 201.00, 179.11, 171.11, 149.35, 148.70, 148.29, 147.14,

145.02, 141.10, 133.70, 132.81, 130.65, 130.22, 130.11, 129.87, 129.63, 129.02, 128.85,

128.72, 128.19, 127.94, 127.64, 126.73, 126.60, 125.99, 125.04, 123.31, 121.88, 121.25,

120.59, 79.16, 70.07, 61.32, 34.30, 29.93, 29.84, 28.69, 26.24, 25.85, 24.18, 23.97, 23.89, 23.78.

HRMS (ESI): [M + H]$^+$ Calcd. for [C$_{44}$H$_{43}$AuNO$_3$]$^+$ 830.2903, found 830.2904.

(*R*,*S*)-**2.3h**
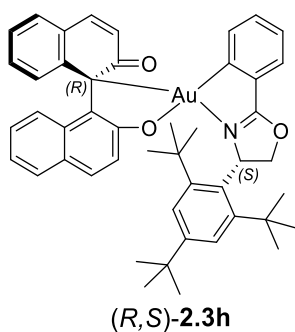
^{1}H NMR (600 MHz, CDCl$_3$) δ 7.87 (d, *J* = 9.9 Hz, 1H), 7.69 (s, 1H), 7.63 (s, 1H), 7.56 – 7.51 (m, 1H), 7.47 – 7.37 (m, 4H), 7.28 (s, 1H), 7.25 – 7.21 (m, 1H), 7.19 (t, *J* = 7.4 Hz, 1H), 7.13 (t, *J* = 7.5 Hz, 1H), 7.04 (t, *J* = 7.6 Hz, 1H), 6.90 (m, 2H), 6.70 (t, *J* = 12.5 Hz, 1H), 6.67 – 6.62 (m, 1H), 6.60 (d, *J* = 9.8 Hz, 1H), 6.28 (d, *J* = 8.9 Hz, 1H), 5.22 (dd, *J* = 12.2, 8.8 Hz, 1H), 4.99 (dd, *J* = 12.6, 8.7 Hz, 1H), 1.68 (s, 9H), 1.52 (s, 9H), 1.41 (s, 9H).

^{13}C NMR (150 MHz, CDCl$_3$) δ 200.70, 178.57, 171.12, 151.64, 151.29, 149.45, 147.47, 144.89, 141.93, 133.89, 132.67, 130.55, 130.48, 130.35, 129.98, 129.96, 129.18, 128.82, 128.79, 128.71, 128.22, 127.88, 127.72, 126.67, 126.48, 125.90, 124.66, 122.29, 121.68, 120.40, 120.37, 78.56, 70.41, 63.74, 39.54, 37.75, 35.32, 35.16, 34.34, 31.50.

HRMS (ESI): [M + H]$^+$ Calcd. for [C$_{47}$H$_{49}$AuNO$_3$]$^+$ 872.3372, found 872.3370.

(*R,R*)-**2.3j**
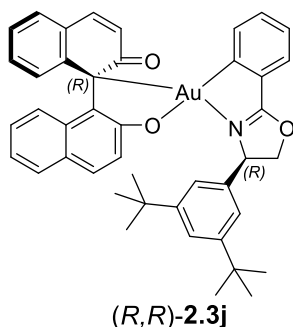
¹H NMR (600 MHz, CDCl₃) δ 7.88 (d, *J* = 10.0 Hz, 1H), 7.63 (dd, *J* = 7.3, 2.2 Hz, 1H), 7.59 (d, *J* = 9.0 Hz, 1H), 7.49 (dd, *J* = 7.6, 1.4 Hz, 1H), 7.45 (s, 3H), 7.41 (dt, *J* = 7.0, 0.9 Hz, 1H), 7.27 (d, *J* = 1.2 Hz, 1H), 7.25 – 7.22 (m, 2H), 7.22 – 7.18 (m, 1H), 7.16 (td, *J* = 7.4, 1.2 Hz, 1H), 7.04 – 6.99 (m, 2H), 6.99 – 6.94 (m, 2H), 6.69 (d, *J* = 8.5 Hz, 1H), 6.58 (d, *J* = 9.8 Hz, 1H), 5.73 (dd, *J* = 9.8, 5.8 Hz, 1H), 5.18 (t, *J* = 9.4 Hz, 1H), 5.09 (dd, *J* = 9.0, 5.8 Hz, 1H), 1.36 (s, 18H).

¹³C NMR (150 MHz, CDCl₃) δ 200.84, 178.83, 170.68, 151.61, 147.13, 145.02, 140.98, 137.33, 133.80, 132.89, 130.53, 130.39, 130.32, 129.74, 129.51, 129.06, 128.96, 128.83, 128.81, 128.25, 127.93, 126.82, 126.62, 126.08, 125.27, 122.75, 121.87, 121.64, 120.81, 120.68, 78.82, 70.07, 66.08, 35.18, 31.64.

HRMS (ESI): [M + H]⁺ Calcd. for [C₄₃H₄₁AuNO₃]⁺ 816.2746, found 816.2749.

2.4f
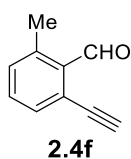
¹H NMR (400 MHz, CDCl₃) δ 10.75 (s, 1H), 7.51 – 7.46 (m, 1H), 7.40 (t, *J* = 7.6 Hz, 1H), 7.24 (d, *J* = 7.7 Hz, 1H), 3.45 (s, 1H), 2.61 (s, 3H).

¹³C NMR (100 MHz, CDCl₃) δ 193.96, 140.86, 134.72, 132.75, 132.65, 132.12, 127.35, 84.62, 80.13, 21.47.

HRMS (ESI): [M + H]⁺ Calcd. for [C₁₀H₉O₃]⁺ 145.0648, found 145.0648.

2.5a
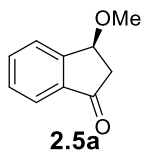
¹H NMR (600 MHz, CDCl₃) δ 7.76 (d, J = 7.8 Hz, 1H), 7.71 – 7.65 (m, 2H), 7.51 – 7.47 (m, 1H), 5.03 (dd, J = 6.5, 2.8 Hz, 1H), 3.50 (s, 3H), 3.00 (dd, J = 18.5, 6.5 Hz, 1H), 2.66 (dd, J = 18.5, 2.8 Hz, 1H).

HPLC (Chiralpak IC column, 98:2 hexane/isopropanol, 1 mL/min), t_R = 32.0 min (minor), 34.9 min (major); ee = 99%.

2.5b
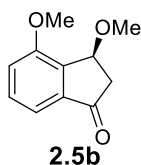
¹H NMR (400 MHz, CDCl₃) δ 7.45 (t, J = 7.8 Hz, 1H), 7.34 (d, J = 7.7 Hz, 1H), 7.11 (d, J = 8.0 Hz, 1H), 5.15 (dd, J = 6.4, 1.6 Hz, 1H), 3.93 (s, 3H), 3.45 (s, 3H), 2.90 (dd, J = 18.8, 6.3 Hz, 1H), 2.68 (dd, J = 18.8, 1.6 Hz, 1H).

¹³C NMR (100 MHz, CDCl₃) δ 203.98, 157.85, 140.71, 138.88, 131.62, 116.27, 115.10, 74.71, 57.25, 55.92, 43.32.

HRMS (ESI): [M + H]⁺ Calcd. for [$C_{11}H_{13}O_3$]⁺ 193.0859, found 193.0862.

HPLC (Chiralpak IC column, 50:50 hexane/isopropanol, 1 mL/min), t_R = 10.6 min (minor), 12.7 min (major); ee = 72%.

2.5c
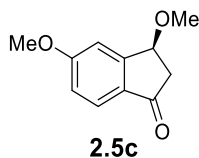
¹H NMR (600 MHz, CDCl₃) δ 7.68 (d, *J* = 8.4 Hz, 1H), 7.10 (d, *J* = 2.3 Hz, 1H), 7.00 (dd, *J* = 8.5, 2.3 Hz, 1H), 4.99 – 4.95 (m, 1H), 3.91 (s, 3H), 3.49 (s, 3H), 2.97 (dd, *J* = 18.4, 6.4 Hz, 1H), 2.64 (dd, *J* = 18.4, 3.0 Hz, 1H).

HPLC (Chiralpak IC column, 50:50 hexane/isopropanol, 1 mL/min), t$_R$ = 8.4 min (major), 9.5 min (minor); ee = 97%.

2.5d
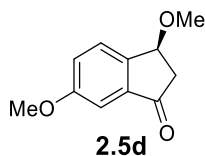
¹H NMR (600 MHz, CDCl₃) δ 7.55 (d, *J* = 8.4 Hz, 1H), 7.22 (dd, *J* = 8.4, 2.5 Hz, 1H), 7.15 (d, *J* = 2.5 Hz, 1H), 4.95 (dd, *J* = 6.2, 2.5 Hz, 1H), 3.82 (s, 3H), 3.45 (s, 3H), 2.98 (dd, *J* = 18.7, 6.2 Hz, 1H), 2.64 (dd, *J* = 18.6, 2.4 Hz, 1H).

¹³C NMR (100 MHz, CDCl₃) δ 202.98, 161.02, 146.07, 138.30, 127.38, 124.09, 104.47, 76.29, 56.96, 55.65, 43.99.

HRMS (ESI): [M + H]⁺ Calcd. for [C₁₁H₁₃O₃]⁺ 193.0859, found 193.0862.

HPLC (Chiralpak IC column, 50:50 hexane/isopropanol, 1 mL/min), t$_R$ = 7.6 min (minor), 8.3 min (major); ee = 82%.

2.5e
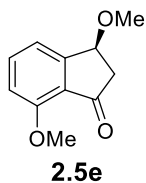
¹H NMR (400 MHz, CDCl₃) δ 7.60 (t, *J* = 7.9 Hz, 1H), 7.22 (d, *J* = 7.6 Hz, 1H), 6.89 (d, *J* = 8.3 Hz, 1H), 4.94 (dd, *J* = 6.5, 3.0 Hz, 1H), 3.94 (s, 4H), 3.46 (s, 3H), 2.95 (dd, *J* = 18.3, 6.5 Hz, 1H), 2.64 (dd, *J* = 18.3, 3.0 Hz, 1H).

¹³C NMR (100 MHz, CDCl₃) δ 200.76, 157.63, 155.76, 136.95, 124.87, 118.19, 111.12, 76.21, 57.07, 56.01, 43.92.

HRMS (ESI): [M + H]⁺ Calcd. for [$C_{11}H_{13}O_3$]⁺ 193.0859, found 193.0861.

HPLC (Chiralpak IC column, 50:50 hexane/isopropanol, 1 mL/min), t_R = 16.6 min (minor), 32.0 min (major); ee = 40%.

2.5f
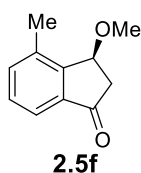
¹H NMR (600 MHz, CDCl₃) δ 7.59 (d, *J* = 7.6 Hz, 1H), 7.45 (dt, *J* = 7.3, 1.0 Hz, 1H), 7.39 (t, *J* = 7.5 Hz, 1H), 5.09 (dd, *J* = 6.4, 2.0 Hz, 1H), 3.43 (s, 3H), 2.95 (dd, *J* = 18.8, 6.4 Hz, 1H), 2.69 (dd, *J* = 18.8, 2.0 Hz, 1H), 2.48 (s, 3H).

¹³C NMR (150 MHz, CDCl₃) δ 204.00, 151.15, 137.77, 137.18, 136.45, 129.99, 120.82, 76.29, 56.74, 42.78, 29.84, 17.80.

HRMS (ESI): [M + H]⁺ Calcd. for [$C_{11}H_{13}O_2$]⁺ 177.0910, found 177.0911.

HPLC (Chiralpak IC column, 80:20 hexane/isopropanol, 1 mL/min), t_R = 11.1 min (minor), 13.0 min (major); ee = 46%.

2.5g
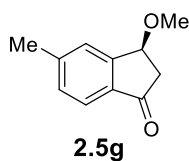
**¹H NMR (400 MHz, CDCl₃)** δ 7.65 (d, J = 7.9 Hz, 1H), 7.49 (s, 1H), 7.29 (d, J = 8.1 Hz, 1H), 4.98 (dd, J = 6.5, 2.9 Hz, 1H), 3.49 (s, 3H), 2.98 (dd, J = 18.5, 6.4 Hz, 1H), 2.64 (dd, J = 18.6, 2.8 Hz, 2H), 2.47 (s, 3H).

HPLC (Chiralpak IC column, 80:20 hexane/isopropanol, 1 mL/min), t_R = 11.1 min (major), 12.8 min (minor); ee = 99%.

2.5h
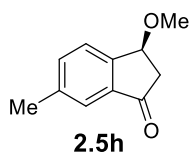
¹H NMR (400 MHz, CDCl₃) δ 7.58 – 7.49 (m, 2H), 7.46 (dd, *J* = 7.8, 1.8 Hz, 1H), 4.97 (dd, *J* = 6.4, 2.8 Hz, 1H), 3.45 (s, 3H), 2.95 (dd, *J* = 18.6, 6.4 Hz, 1H), 2.62 (dd, *J* = 18.8, 2.6 Hz, 1H), 2.40 (s, 3H).

HPLC (Chiralpak IC column, 90:10 hexane/isopropanol, 1 mL/min), t_R = 15.6 min (minor), 18.8 min (major); ee = 92%.

2.5i
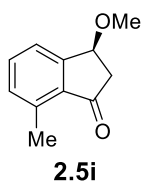
¹H NMR (400 MHz, CDCl₃) δ 7.54 – 7.48 (m, 2H), 7.24 – 7.20 (m, 1H), 4.96 (dd, *J* = 6.5, 2.9 Hz, 1H), 3.48 (s, 3H), 2.95 (dd, *J* = 18.4, 6.5 Hz, 1H), 2.68 – 2.60 (m, 4H).

¹³C NMR (100 MHz, CDCl₃) δ 204.04, 153.98, 138.60, 134.41, 134.32, 131.45, 123.90, 76.35, 57.11, 44.00, 18.51.

HRMS (ESI): $[M + H]^+$ Calcd. for $[C_{11}H_{13}O_2]^+$ 177.0910, found 177.0913.

HPLC (Chiralpak IC column, 98:2 hexane/isopropanol, 1 mL/min), $t_R = 21.9$ min (minor), 24.2 min (major); ee = 11%.

2.5j
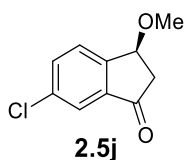
¹H NMR (60 MHz, CDCl₃) δ 7.72 (t, $J = 1.3$ Hz, 1H), 7.65 – 7.62 (m, 2H), 4.99 (dd, $J = 6.4, 2.8$ Hz, 1H), 3.49 (s, 3H), 3.03 (dd, $J = 18.6, 6.4$ Hz, 1H), 2.69 (dd, $J = 18.6, 2.8$ Hz, 1H).

¹³C NMR (100 MHz, CDCl₃) δ 201.66, 150.19, 140.35, 136.26, 135.18, 127.91, 123.33, 75.86, 57.43, 43.40.

HRMS (ESI): $[M + H]^+$ Calcd. for $[C_{10}H_{10}O_2]^+$ 197.0364, found 197.0366.

HPLC (Chiralpak IC column, 90:10 hexane/isopropanol, 1 mL/min), $t_R = 10.8$ min (minor), 11.6 min (major); ee = 92%.

2.5l
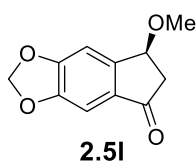
¹H NMR (400 MHz, CDCl₃) δ 7.09 (s, 1H), 7.03 (s, 1H), 6.11 – 6.08 (m, 2H), 4.90 (dd, $J = 6.2, 2.7$ Hz, 1H), 3.46 (s, 3H), 2.96 (dd, $J = 18.5, 6.2$ Hz, 1H), 2.63 (dd, $J = 18.4, 2.5$ Hz, 1H).

HPLC (Chiralpak IC column, 80:20 hexane/isopropanol, 1 mL/min), $t_R = 22.5$ min (minor), 25.4 min (major); ee = 57%.

2.5m
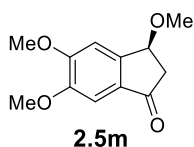
¹H NMR (400 MHz, CDCl₃) δ 7.17 (s, 1H), 7.09 (s, 1H), 4.96 (dd, J = 6.2, 2.6 Hz, 1H), 4.00 (s, 3H), 3.92 (s, 3H), 3.48 (s, 3H), 2.96 (dd, J = 18.3, 6.2 Hz, 1H), 2.63 (dd, J = 18.3, 2.6 Hz, 1H).

HPLC (Chiralpak IC column, 70:30 hexane/isopropanol, 1 mL/min), t_R = 19.2 min (major), 20.9 min (minor); ee = 55%.

2.5n
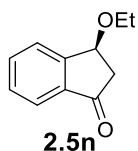
¹H NMR (400 MHz, CDCl₃) δ 7.76 (d, J = 7.7 Hz, 1H), 7.72 – 7.64 (m, 2H), 7.48 (t, J = 7.3 Hz, 1H), 5.11 (dd, J = 6.5, 2.9 Hz, 1H), 3.70 (qd, J = 7.0, 3.1 Hz, 2H), 3.02 (dd, J = 18.6, 6.4 Hz, 1H), 2.67 (dd, J = 18.6, 2.9 Hz, 1H), 1.29 (t, J = 7.0 Hz, 3H).

HPLC (Chiralpak IC column, 95:5 hexane/isopropanol, 1 mL/min), t_R = 15.6 min (minor), 17.8 min (major); ee = 67%.

2.5o
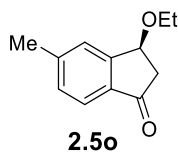
¹H NMR (400 MHz, CDCl₃) δ 7.65 (d, J = 7.8 Hz, 1H), 7.49 (s, 1H), 7.28 (d, J = 7.9 Hz, 1H), 5.06 (dd, J = 6.4, 2.8 Hz, 1H), 3.69 (qd, J = 7.0, 1.9 Hz, 2H), 2.99 (dd, J = 18.4, 6.4 Hz, 1H), 2.65 (dd, J = 18.4, 2.8 Hz, 1H), 2.47 (s, 3H), 1.30 (t, J = 7.0 Hz, 4H).

¹³C NMR (100 MHz, CDCl₃) δ 202.94, 154.17, 146.50, 134.65, 130.83, 126.85, 123.24, 75.27, 65.49, 44.48, 29.84, 22.28, 15.64.

HRMS (ESI): [M + H]⁺ Calcd. for $[C_{12}H_{15}O_2]^+$ 191.1067, found 191.1068.

HPLC (Chiralpak IC column, 80:20 hexane/isopropanol, 1 mL/min), t_R = 9.9 min (major), 10.6 min (minor); ee = 63%.

2.5p
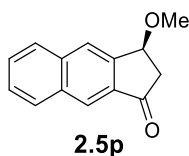
¹H NMR (400 MHz, CDCl₃) δ 8.33 (s, 1H), 8.14 (s, 1H), 8.02 (d, J = 8.2 Hz, 1H), 7.97 – 7.92 (m, 1H), 7.62 (ddd, J = 8.3, 6.8, 1.4 Hz, 1H), 7.56 (ddd, J = 8.2, 6.8, 1.3 Hz, 1H), 5.20 (dd, J = 6.8, 3.1 Hz, 1H), 3.55 (s, 3H), 3.17 – 3.07 (m, 1H), 2.84 – 2.76 (m, 1H).

¹³C NMR (100 MHz, CDCl₃) δ 203.48, 146.44, 137.08, 134.09, 133.48, 130.42, 128.78, 128.47, 127.00, 125.66, 124.24, 57.03, 44.42, 29.71.

2.5q
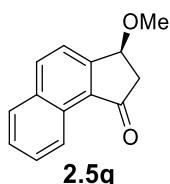
¹H NMR (400 MHz, CDCl₃) δ 9.13 (dd, *J* = 8.4, 1.0 Hz, 1H), 8.09 (d, *J* = 8.3 Hz, 1H), 7.93 – 7.87 (m, 1H), 7.74 – 7.64 (m, 2H), 7.58 (ddd, *J* = 8.3, 7.0, 1.3 Hz, 1H), 5.07 (dd, *J* = 6.3, 2.6 Hz, 1H), 3.52 (s, 3H), 3.14 – 3.02 (m, 1H), 2.82 – 2.71 (m, 1H).

HPLC (Chiralpak IC column, 80:20 hexanes/isopropanol, 1 mL/min), tr = 10.5 min (minor), 16.2 min (major); ee = 22% (r.t.).

2.4.14   NMR Spectra

^{1}H NMR of Compound S2.2
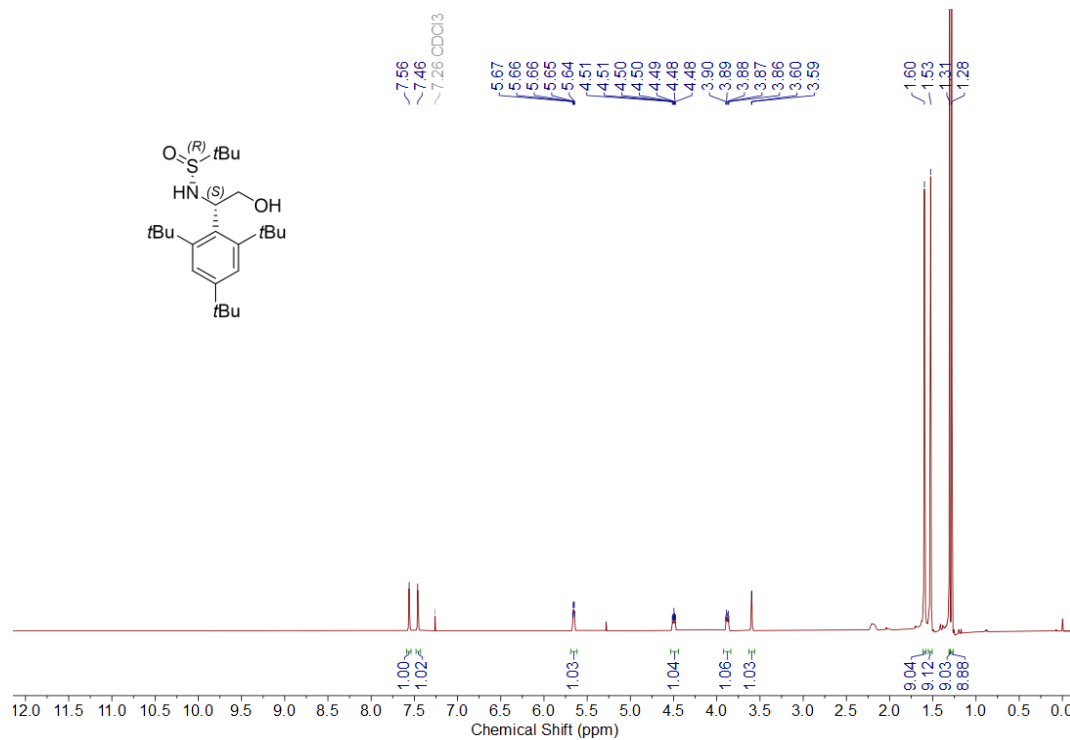
^{13}C NMR of Compound S2.2
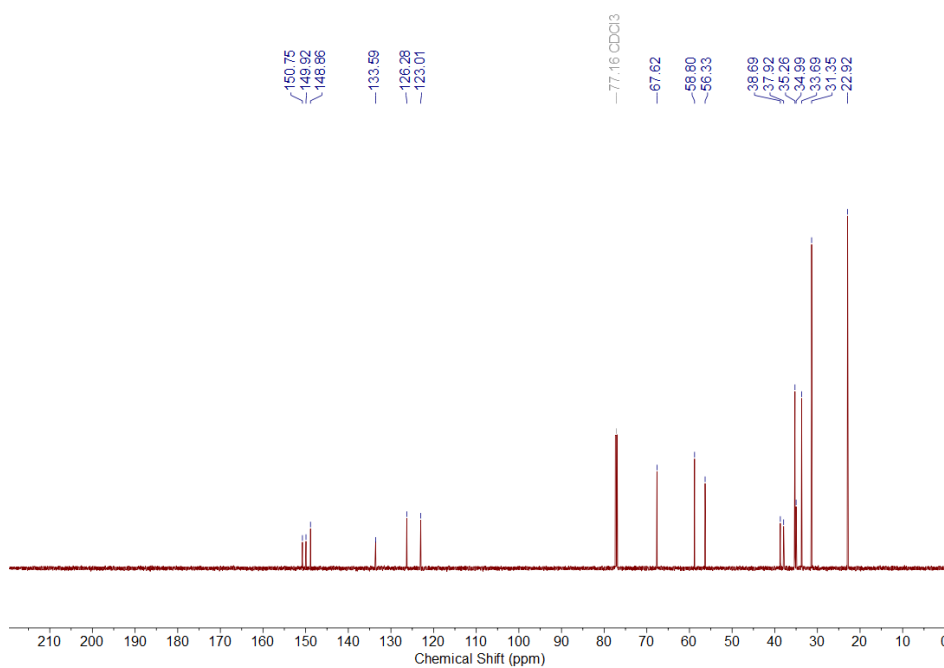
^{1}H NMR of Compound S2.3
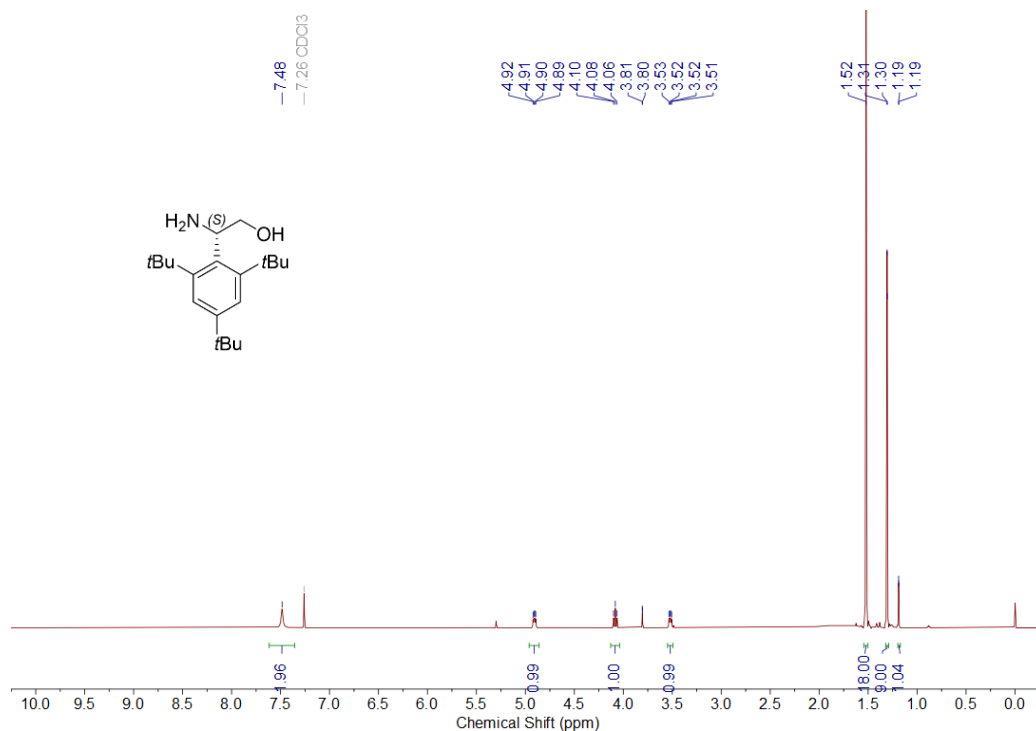
^{13}C NMR of Compound S2.3
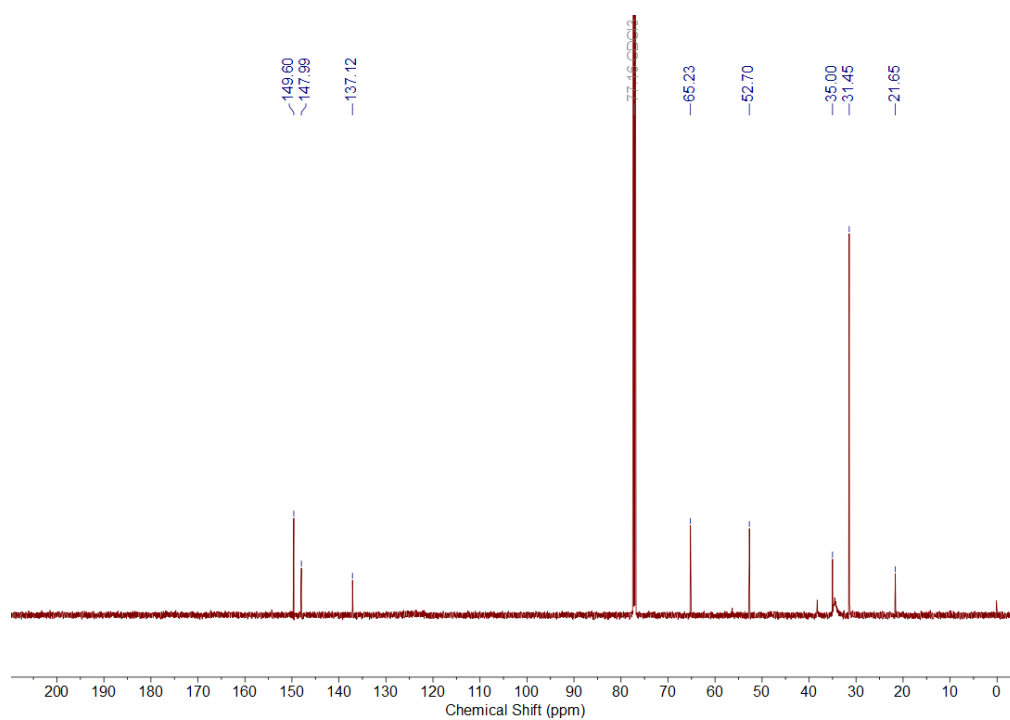
^{1}H NMR of Compound S2.4
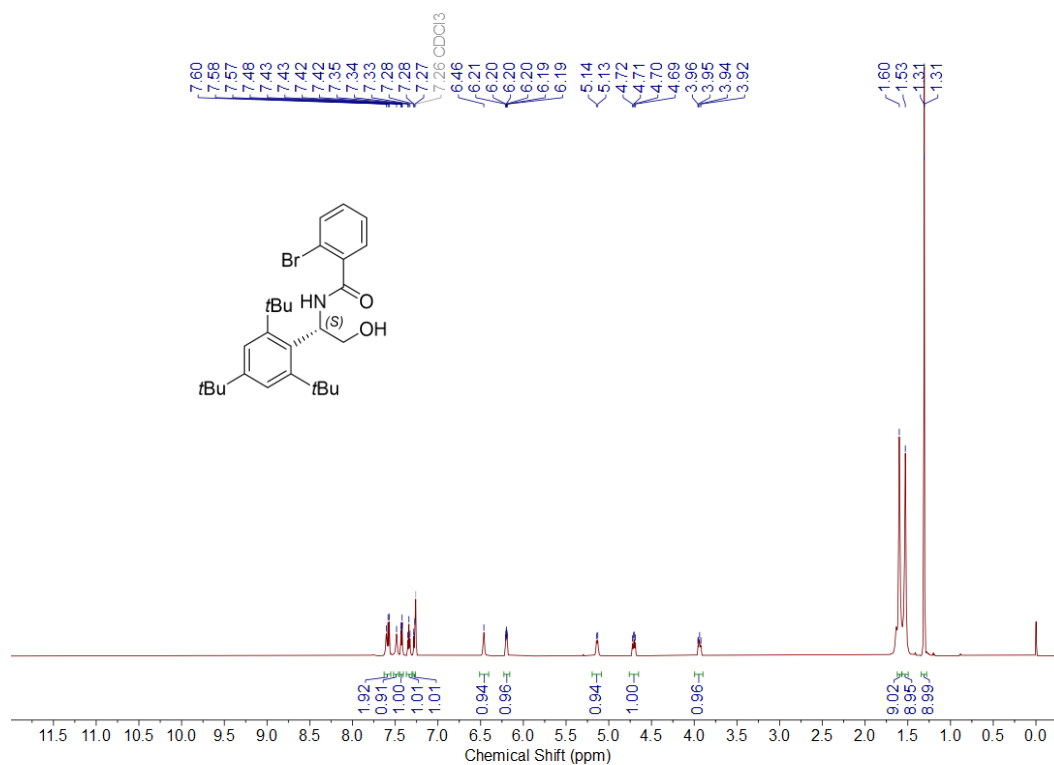
^{13}C NMR of Compound S2.4
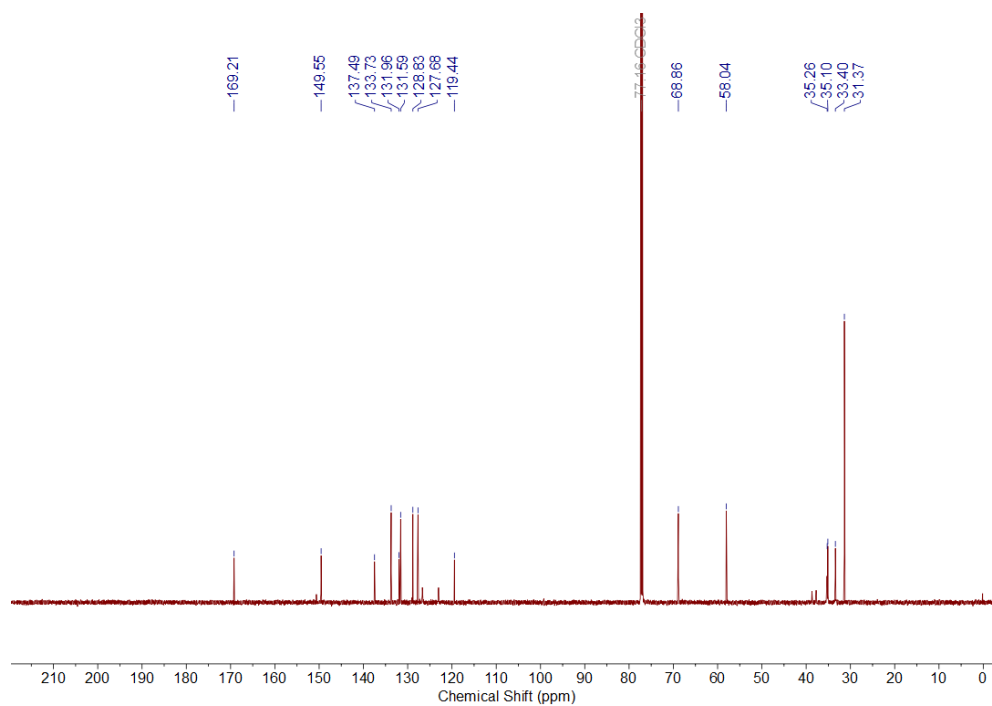
¹H NMR of Compound S2.5

¹³C NMR of Compound S2.5

141
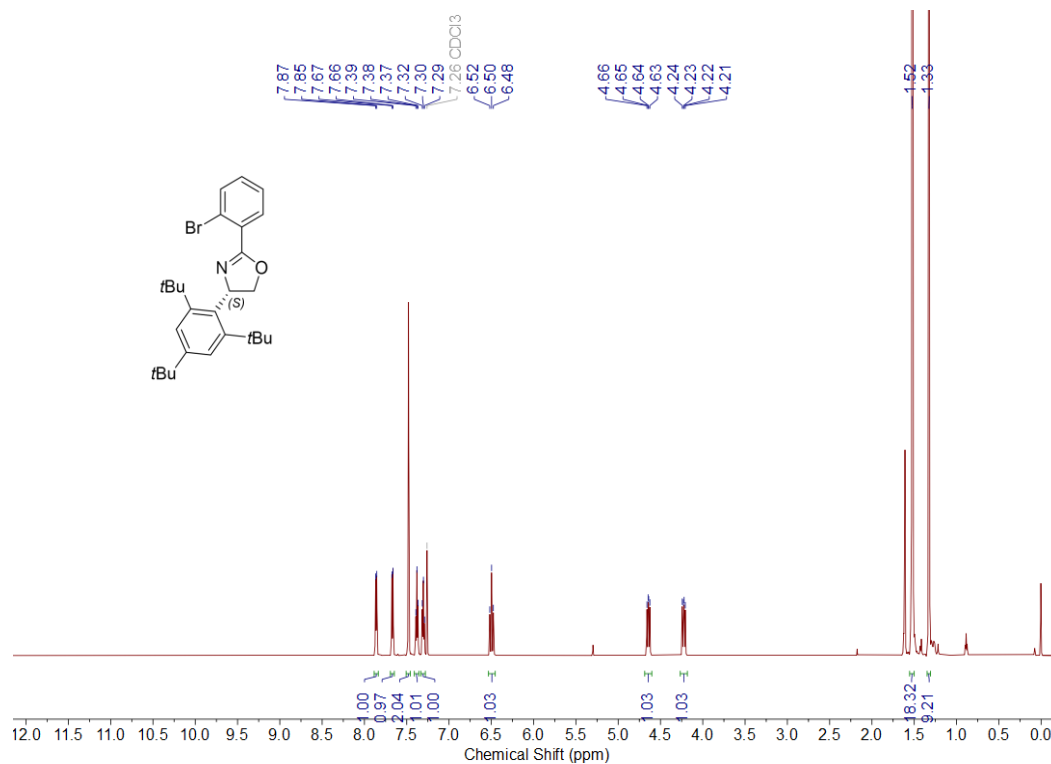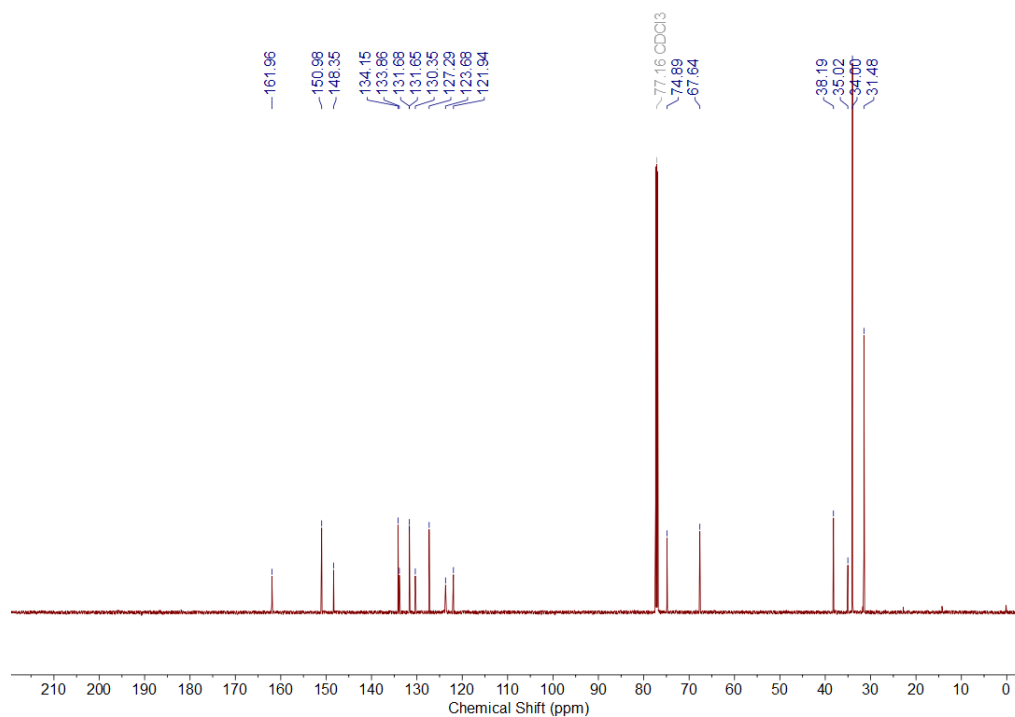
¹H NMR of Compound S2.6
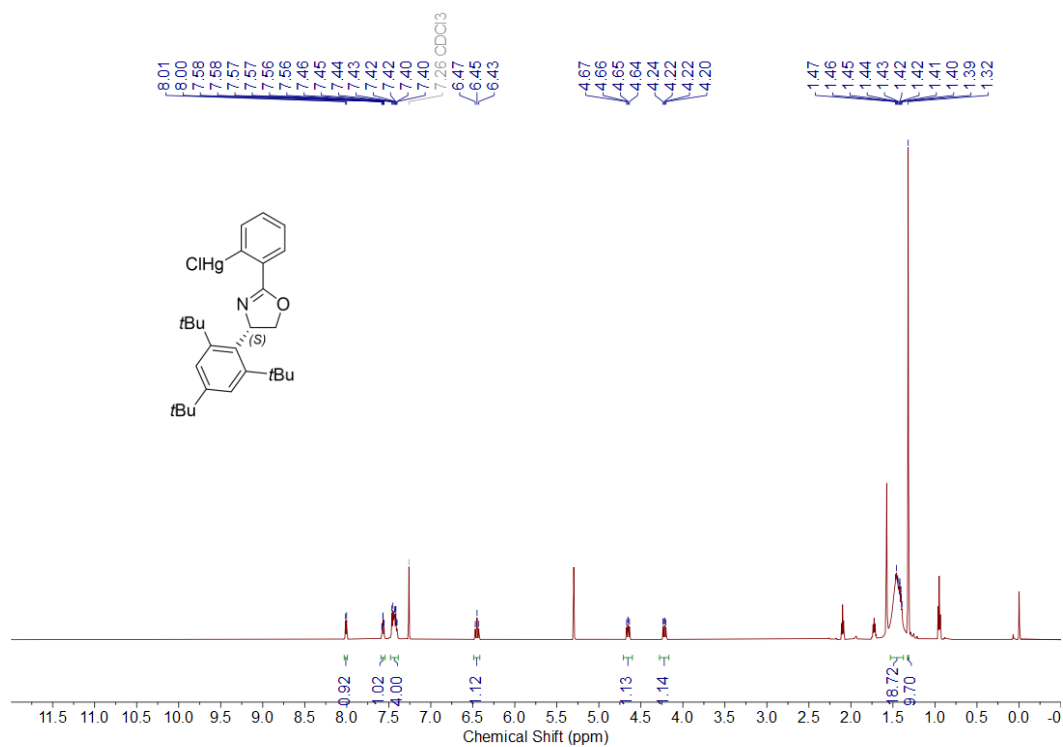
¹³C NMR of Compound S2.6
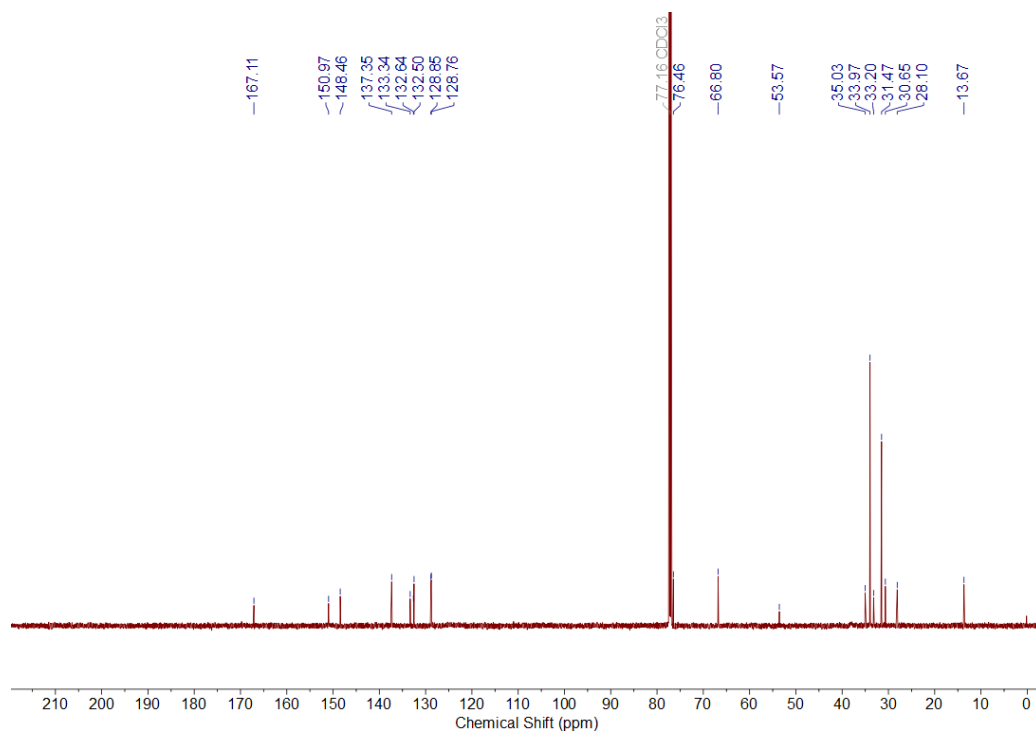
¹H NMR of (*S*)-2.1c
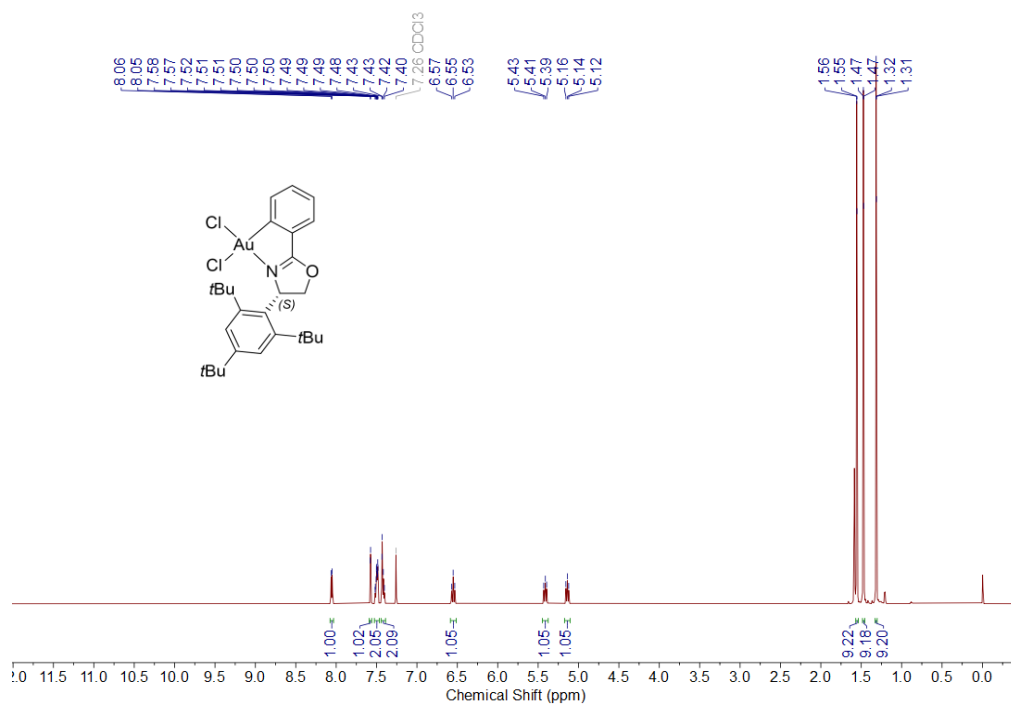
¹³C NMR of (*S*)-2.1c
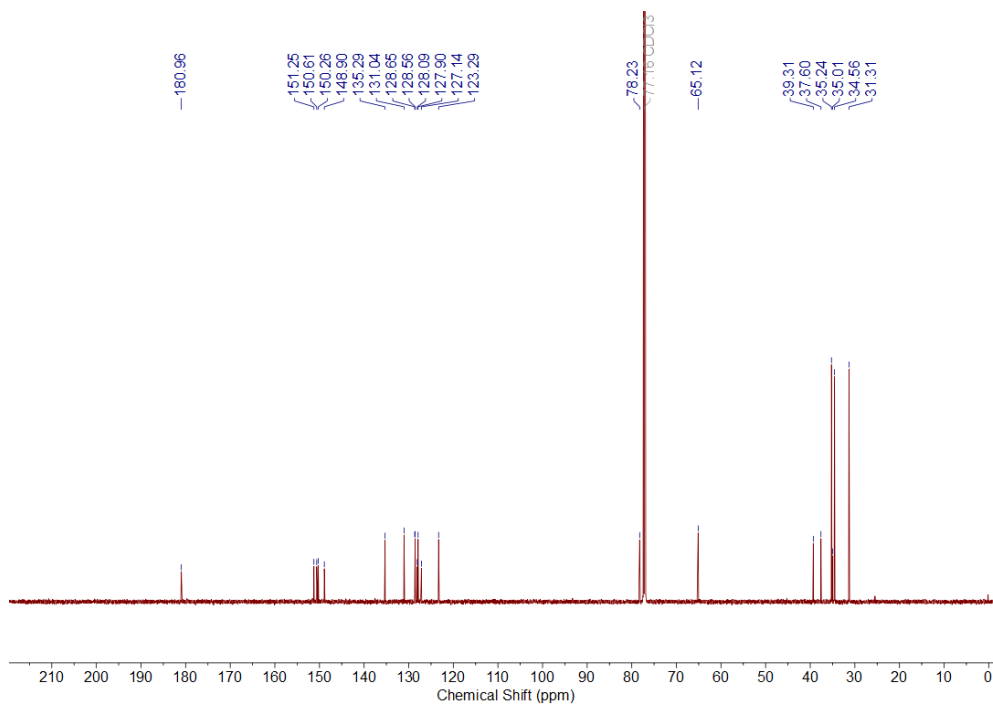
^{1}H NMR of (*R,R*)-2.3a and (*S,S*)-2.3a
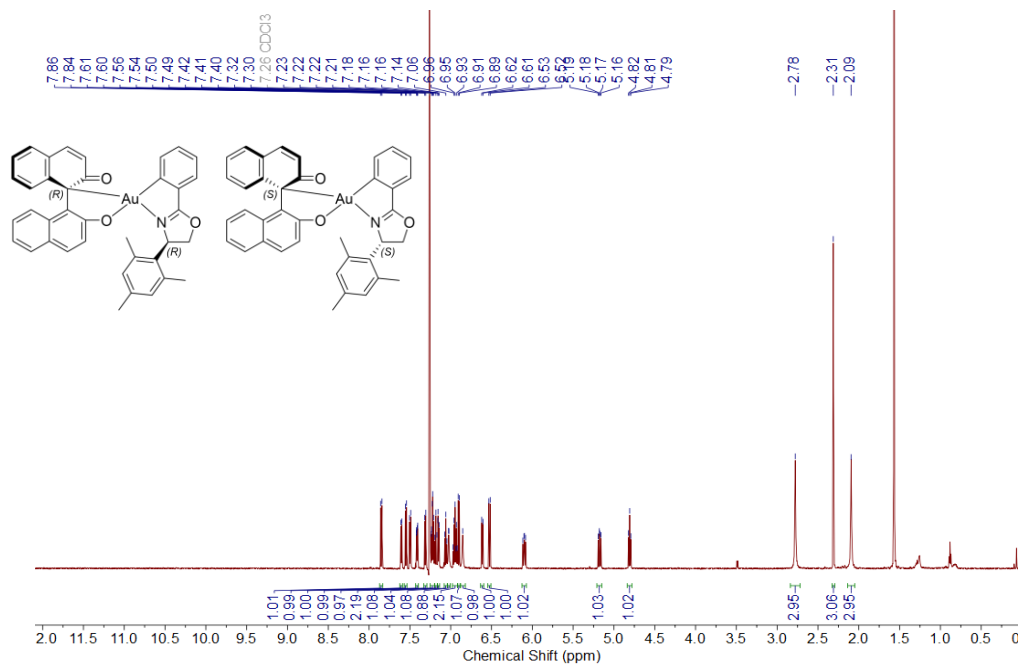
^{13}C NMR of (*R,R*)-2.3a and (*S,S*)-2.3a
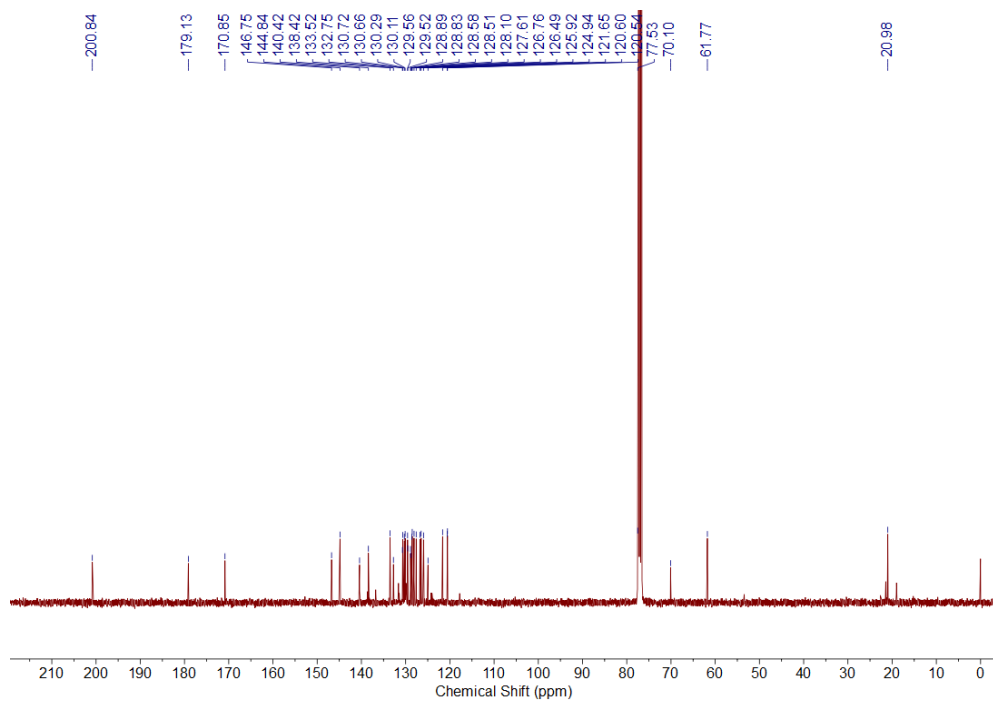
^{1}H NMR of (*R*,*S*)-2.3a and (*S*,*R*)-2.3a
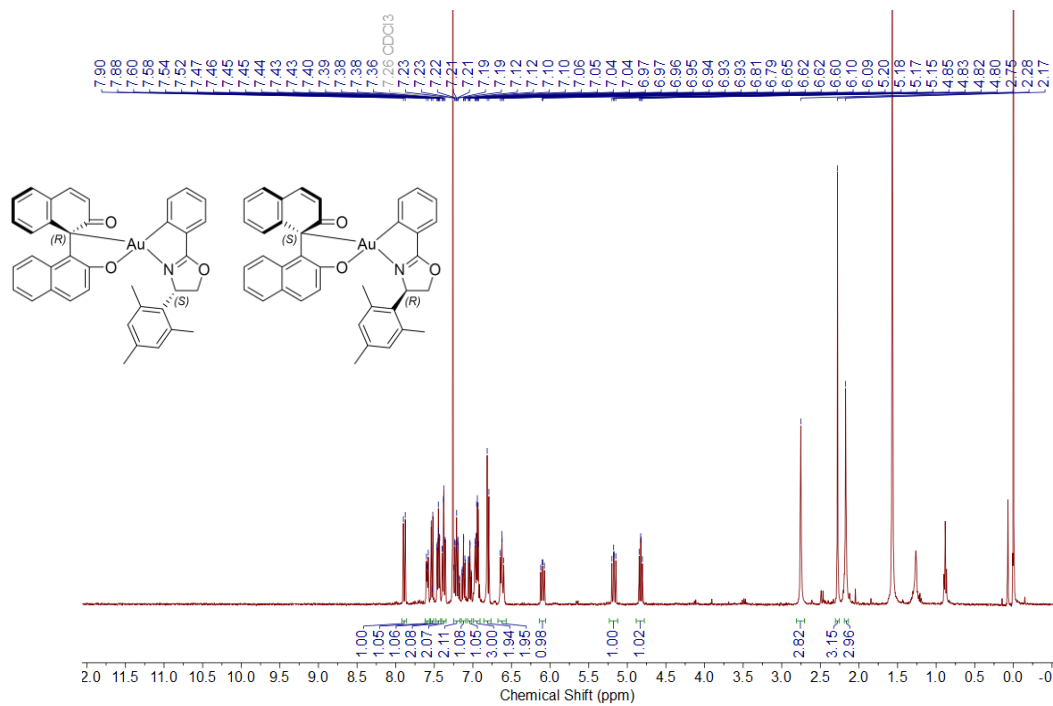
^{13}C NMR of (*R*,*S*)-2.3a and (*S*,*R*)-2.3a
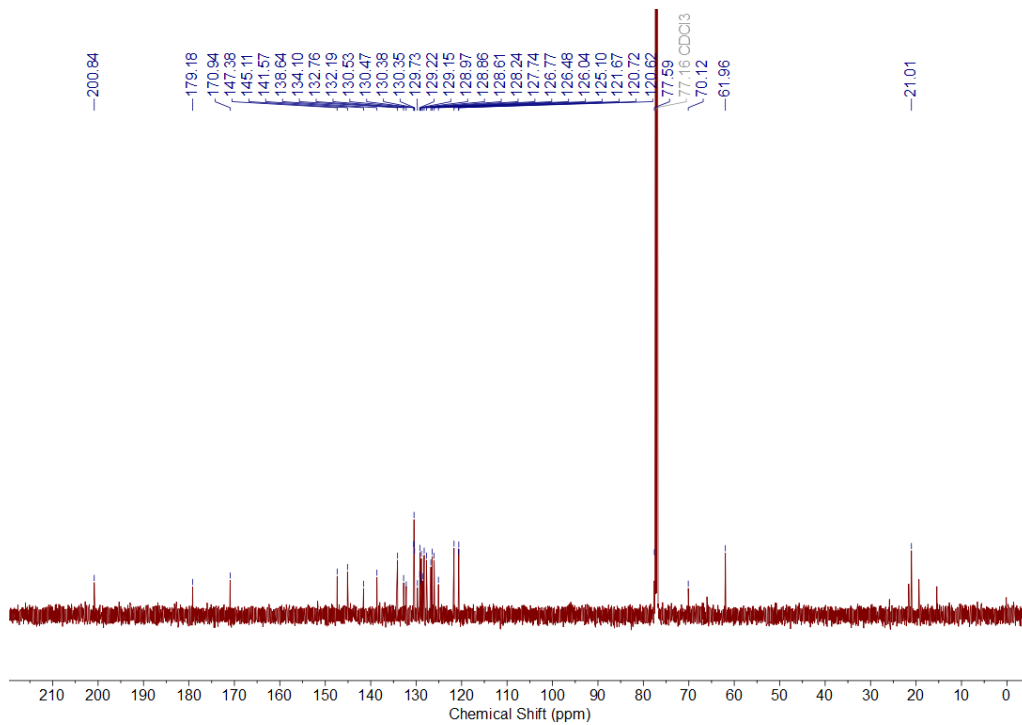
¹H NMR of (*R*,*S*)-2.3b
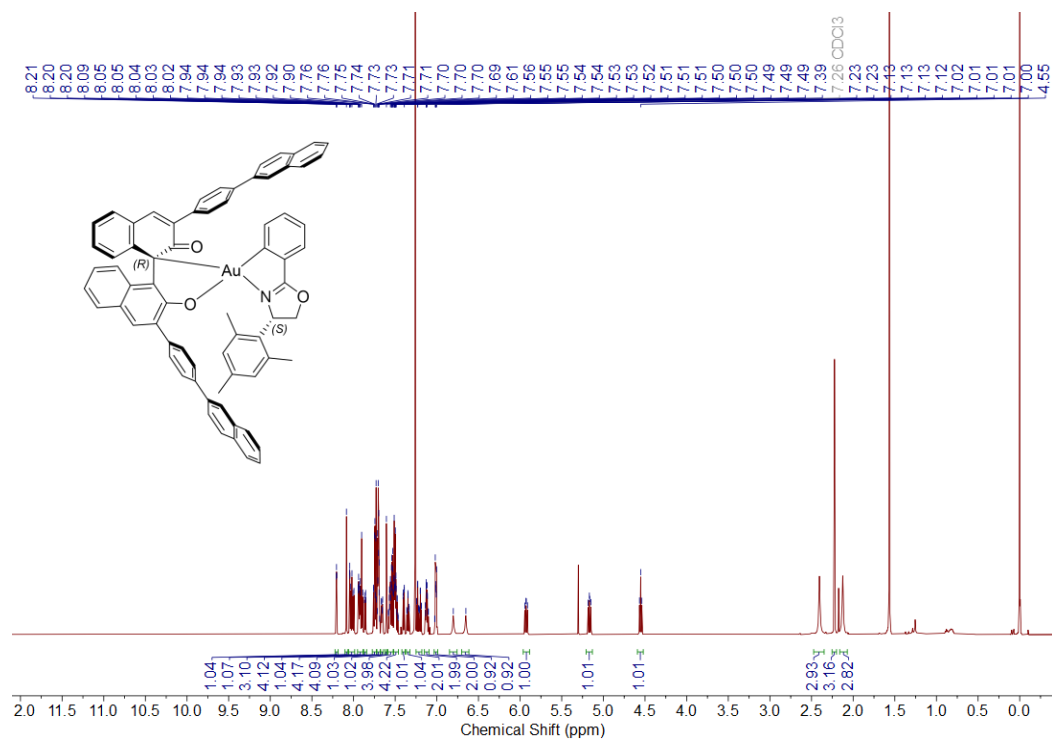
¹³C NMR of (*R*,*S*)-2.3b
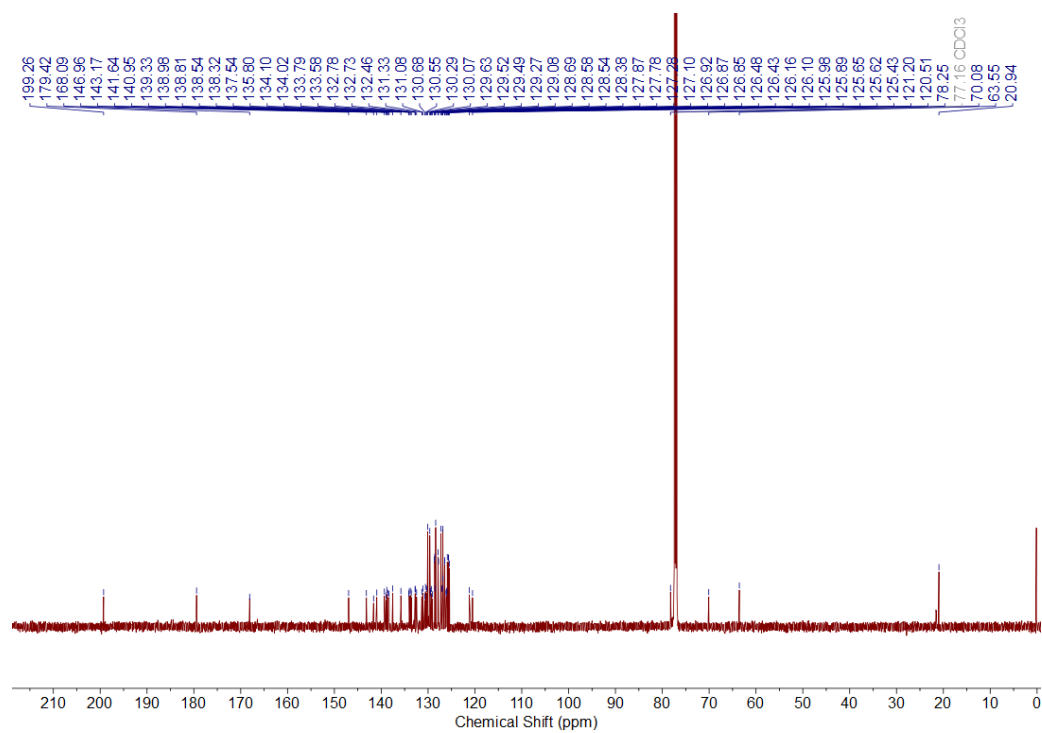
^{1}H NMR of (*S,S*)-2.3b
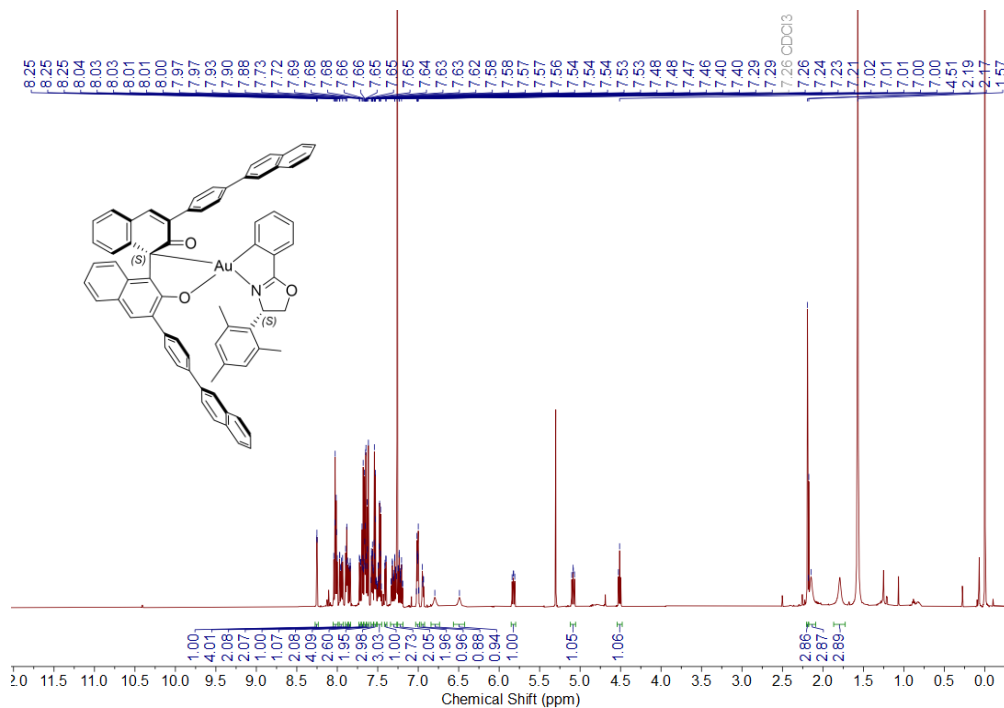
^{13}C NMR of (*S,S*)-2.3b
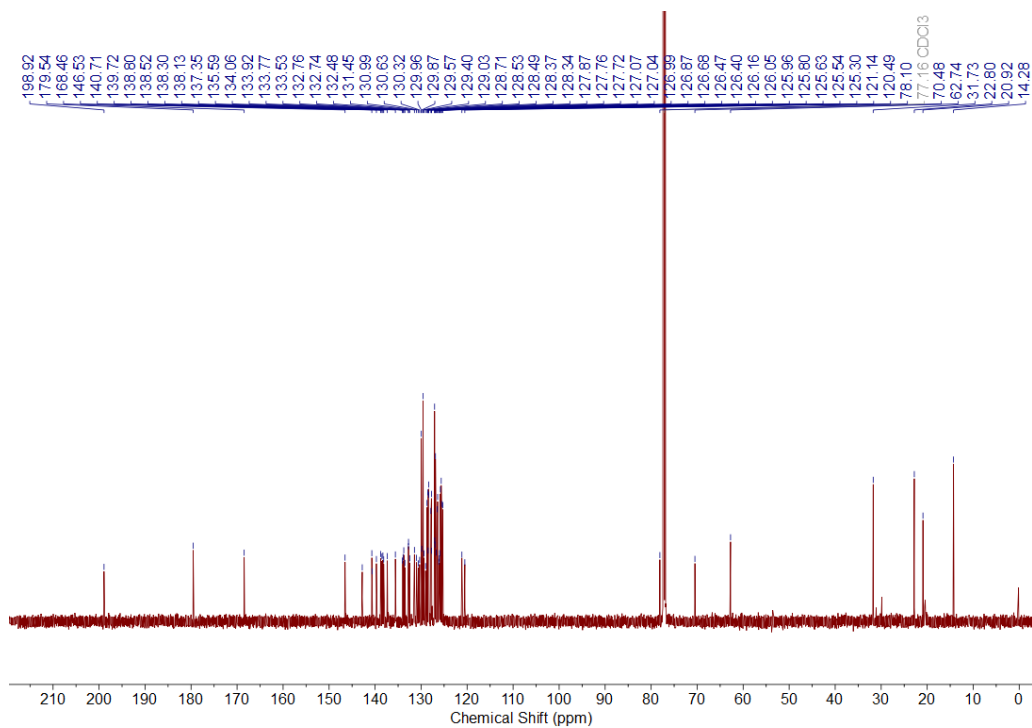
^{1}H NMR of (*R,S*)-2.3c
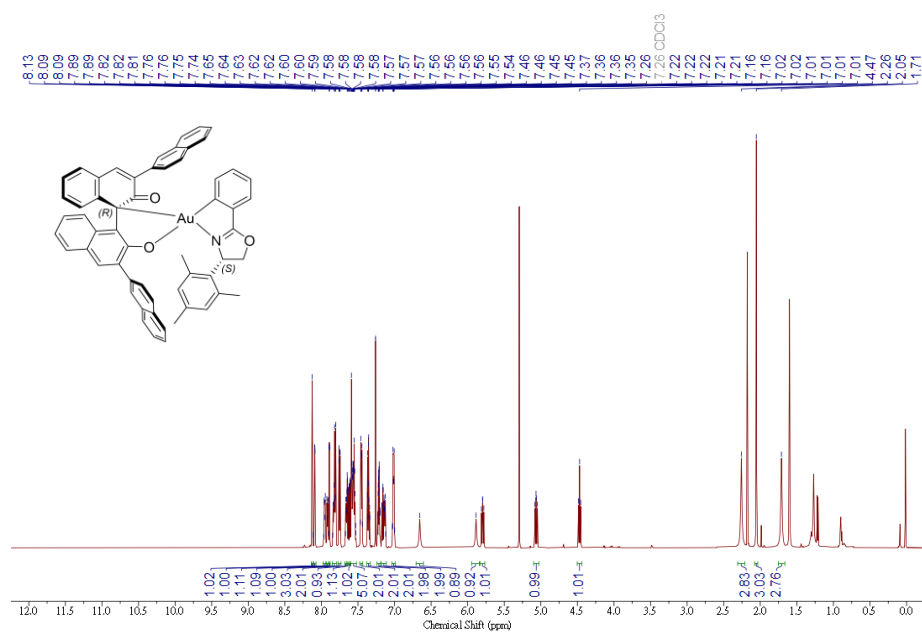
^{13}C NMR of (*R,S*)-2.3c
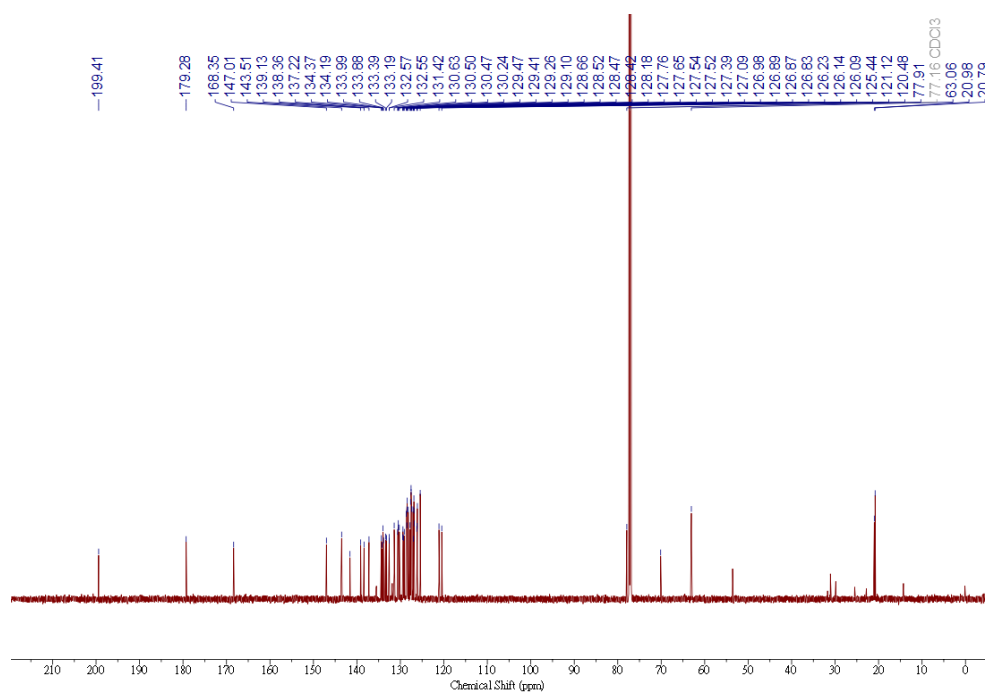
^{1}H NMR of (*S*,*S*)-2.3c
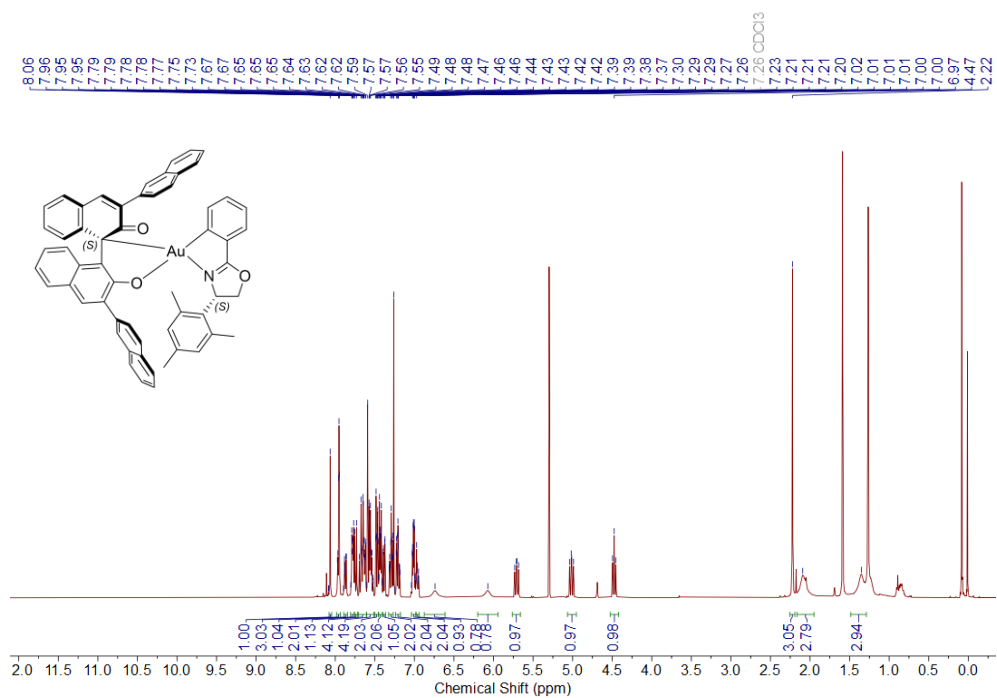
^{13}C NMR of (*S*,*S*)-2.3c
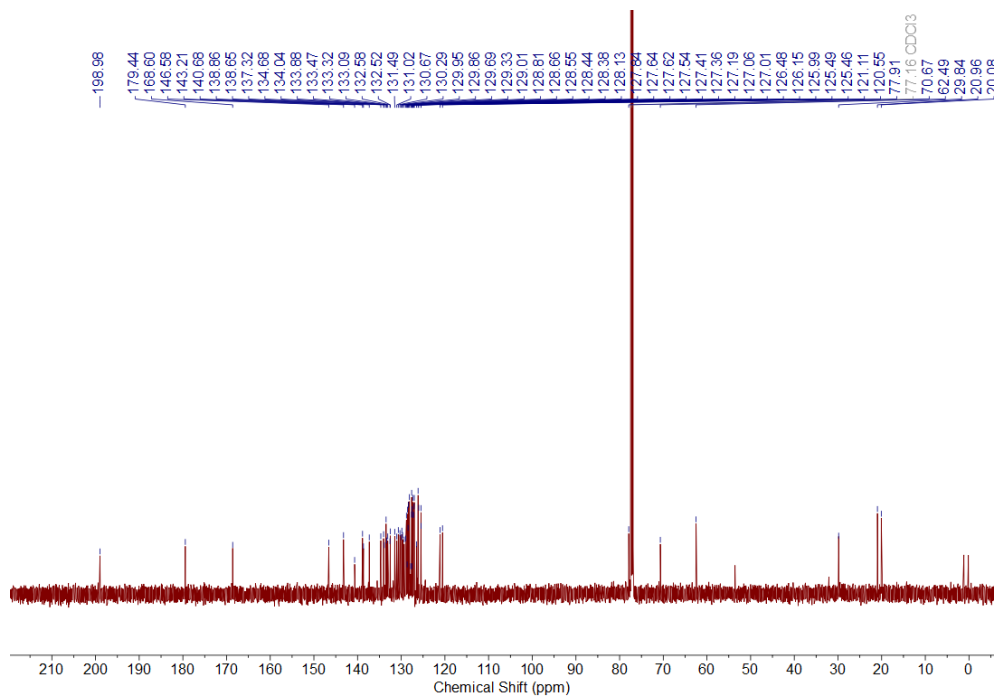
^{1}H NMR of (*R*,*S*)-2.3d
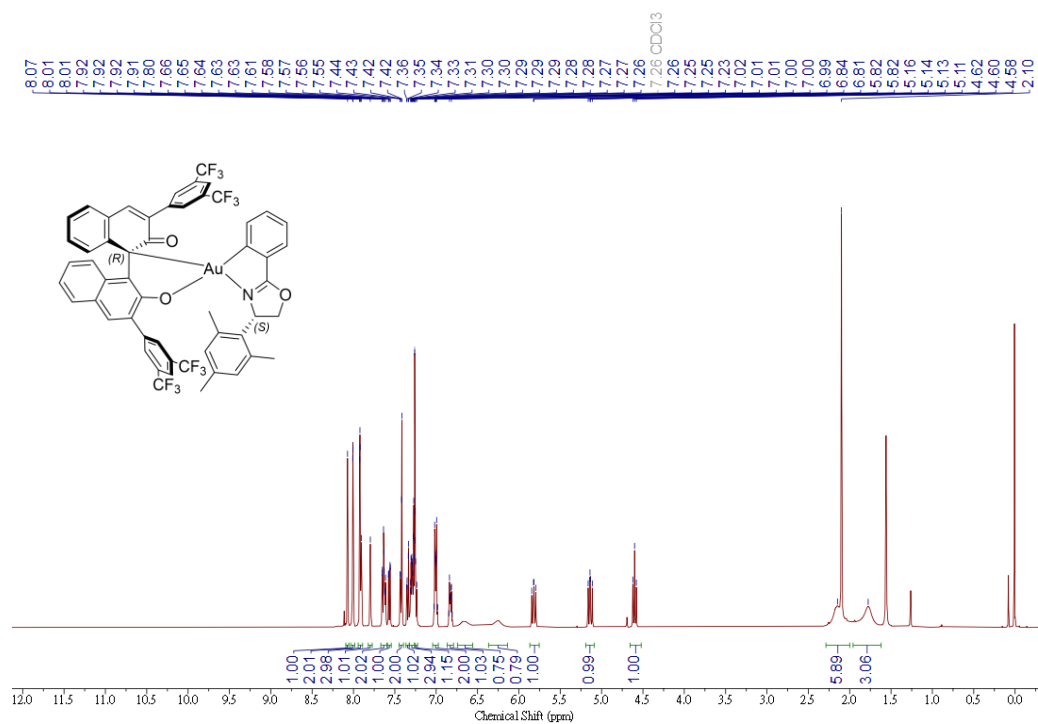
^{13}C NMR of (*R*,*S*)-2.3d
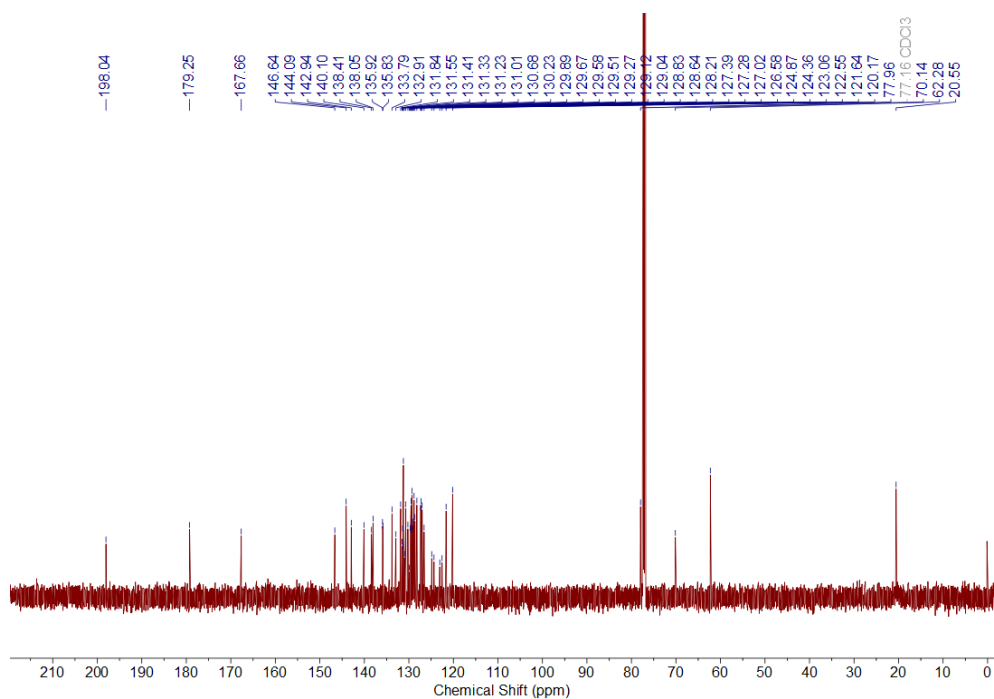
^{1}H NMR of (*R*,*S*)-2.3e
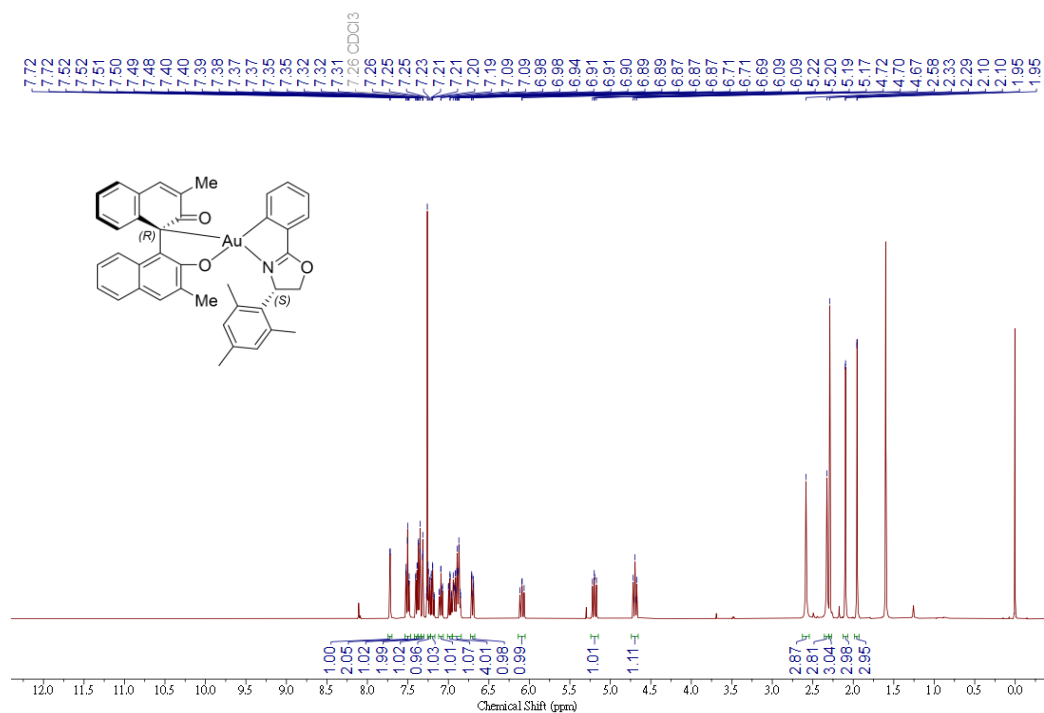
^{13}C NMR of (*R*,*S*)-2.3e
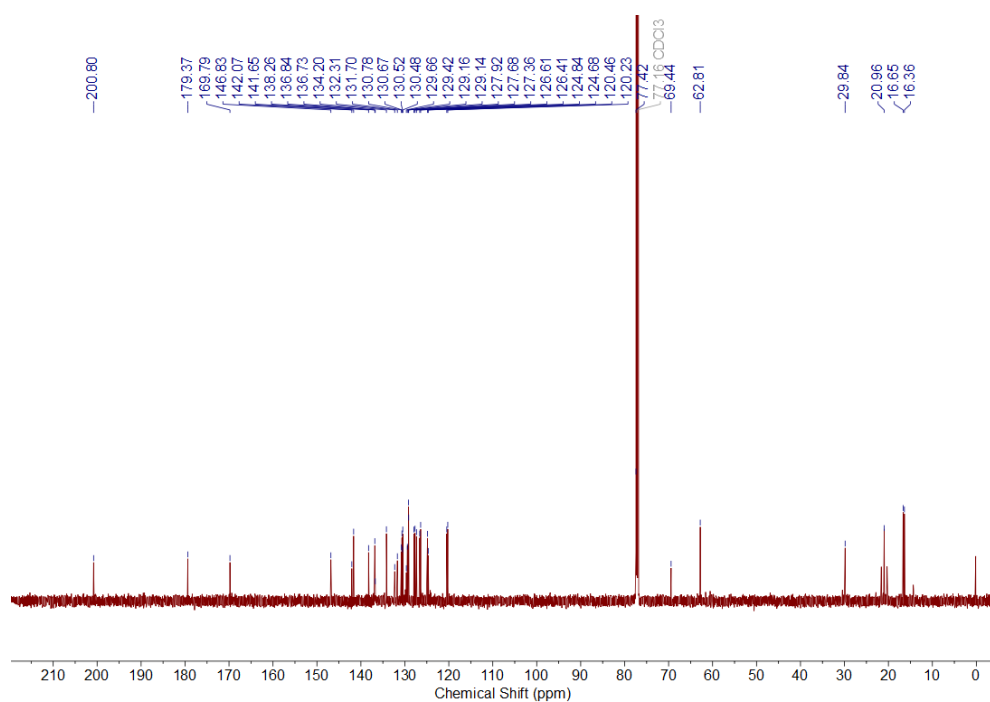
^{1}H NMR of (*S,S*)-2.3e

^{13}C NMR of (*S,S*)-2.3e
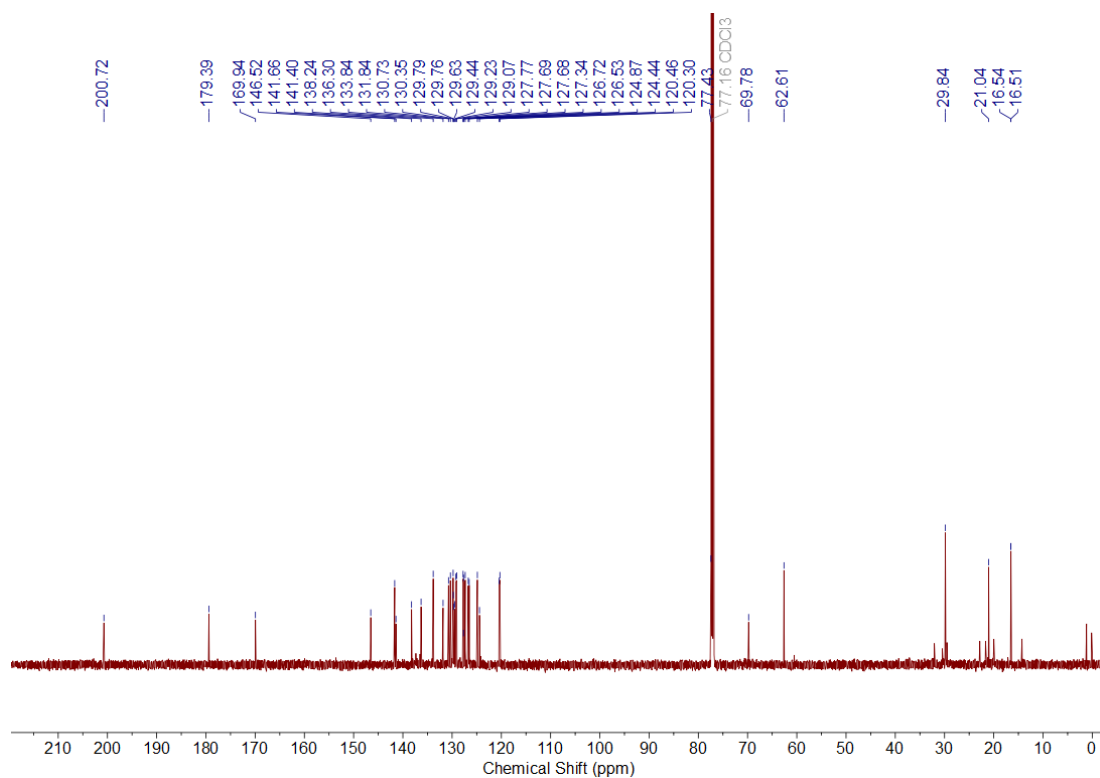
¹H NMR of (*R*,*S*)-2.3f
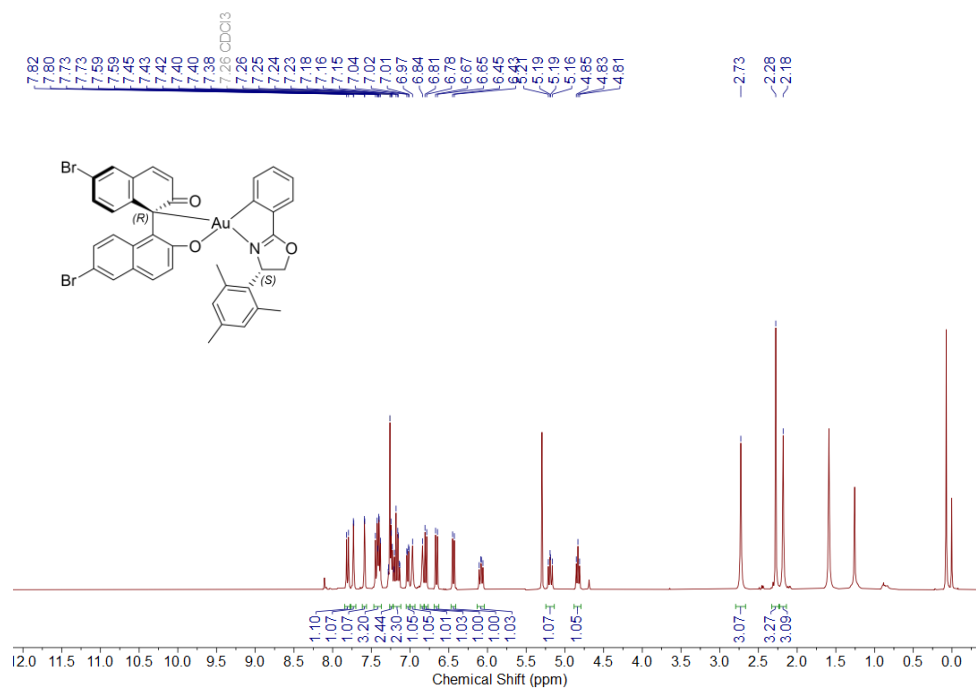
¹³C NMR of (*R*,*S*)-2.3f
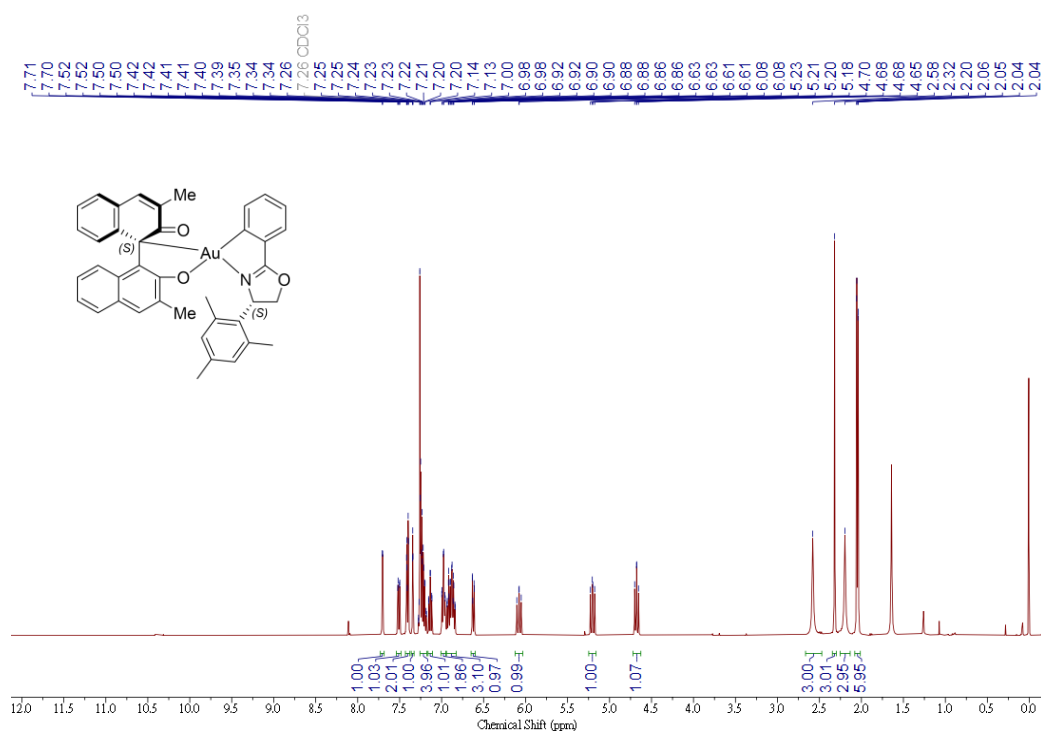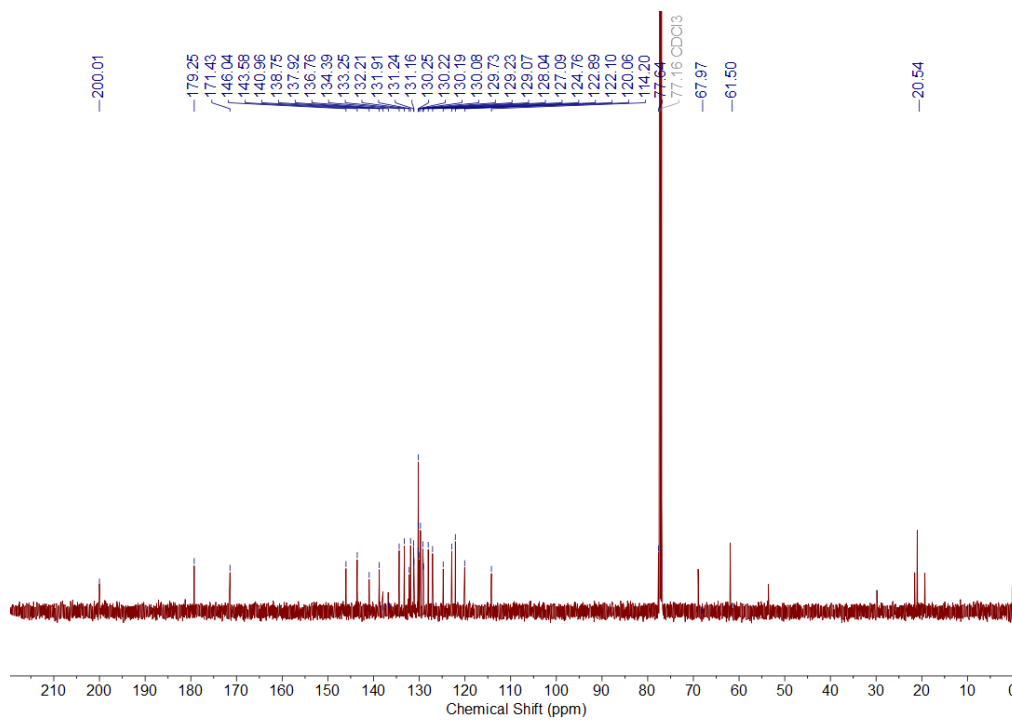
^{1}H NMR of (*S*,*S*)-2.3f
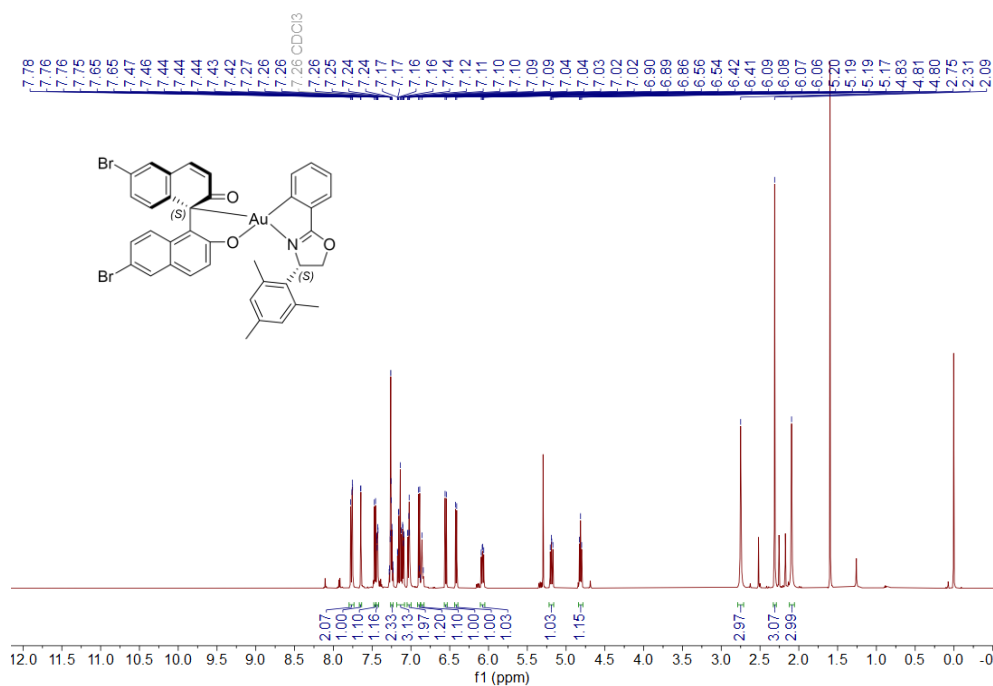
^{13}C NMR of (*S*,*S*)-2.3f
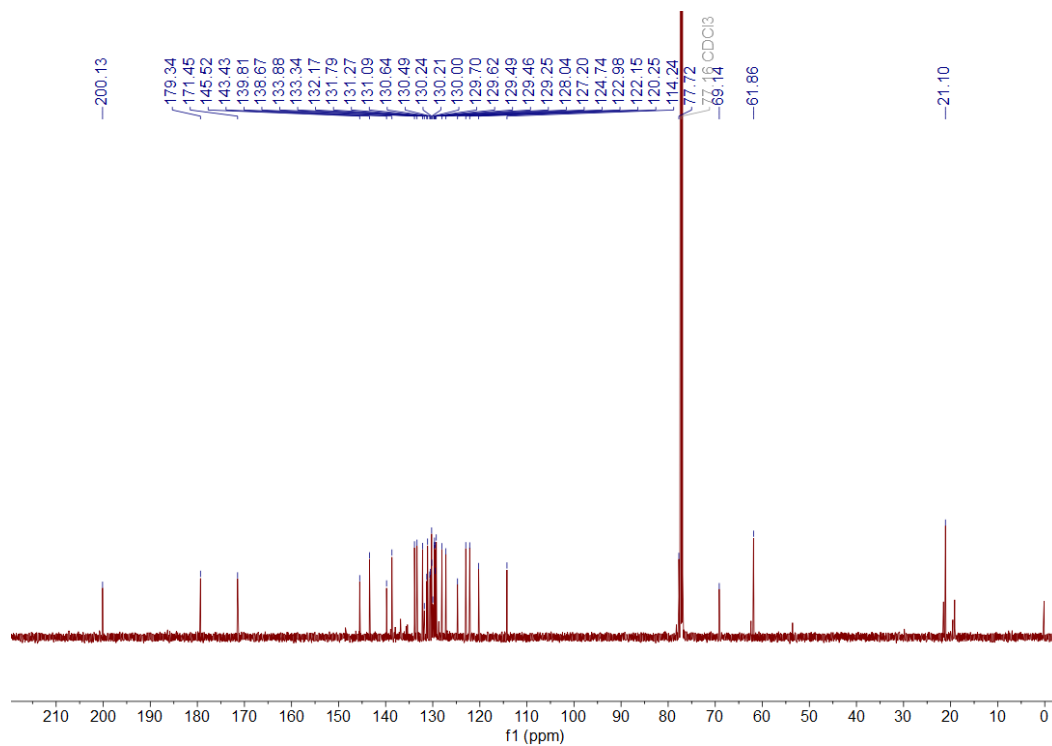
^{1}H NMR of (*R,R*)-2.3g
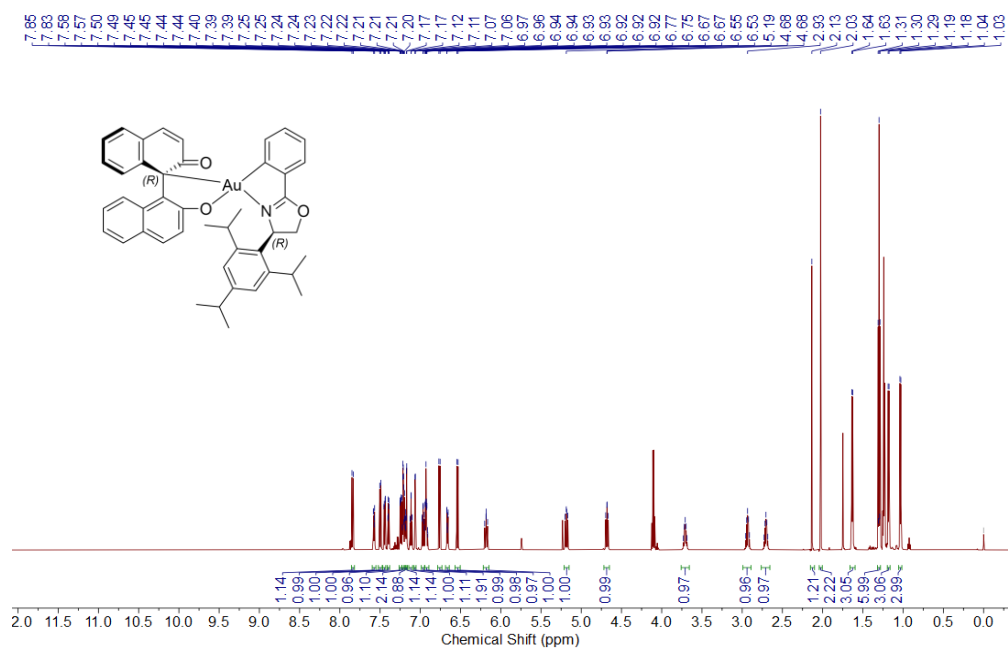
^{13}C NMR of (*R,R*)-2.3g
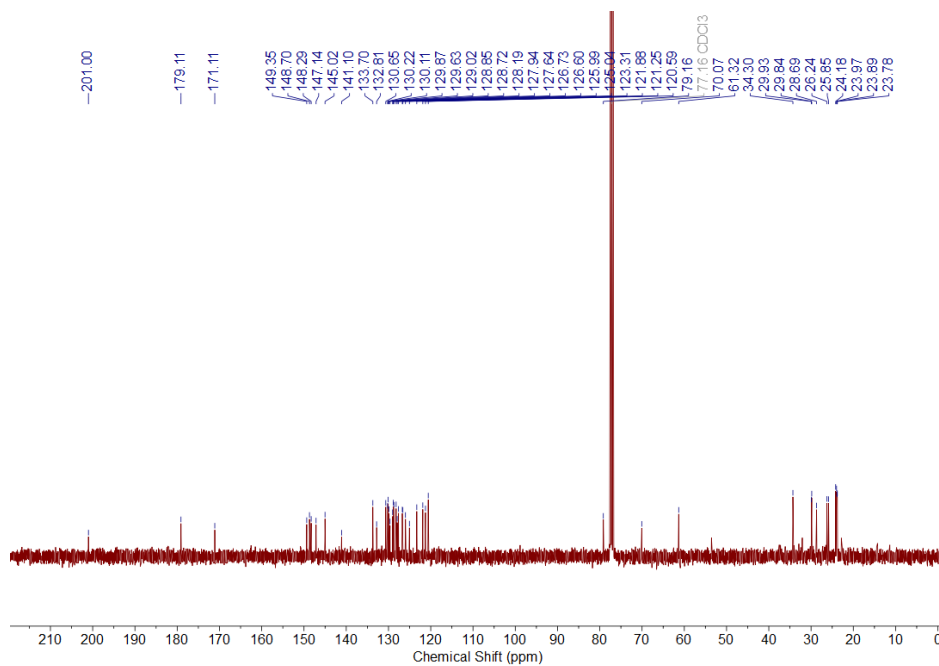
^{1}H NMR of (*R*,*S*)-2.3h
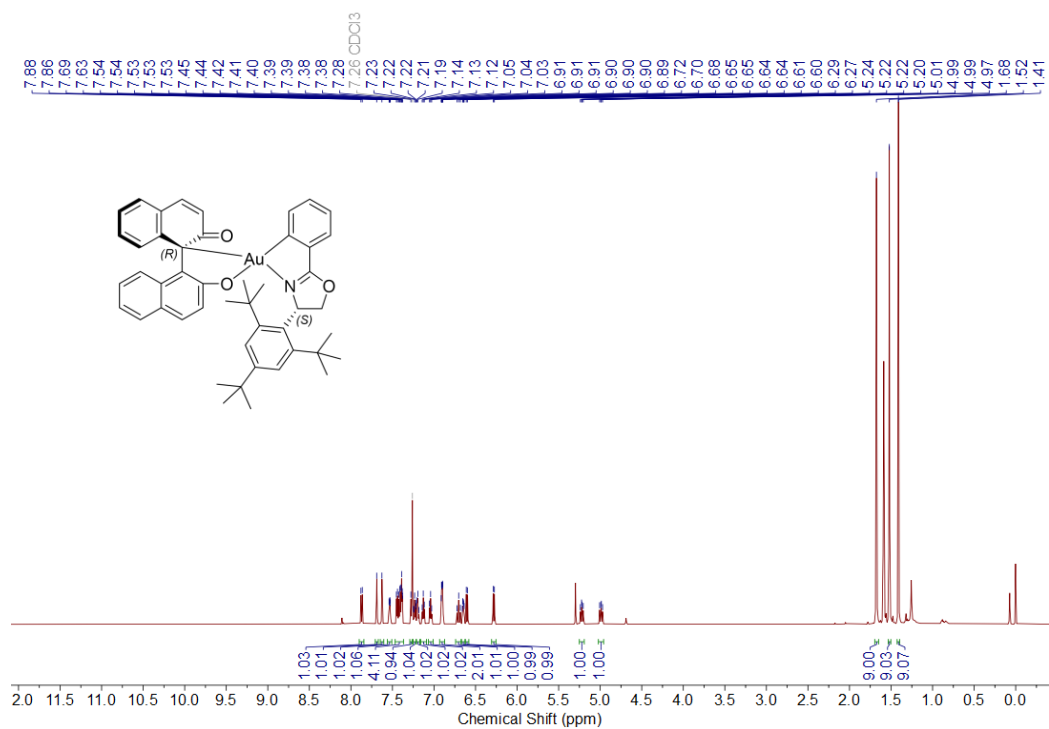
^{13}C NMR of (*R*,*S*)-2.3h
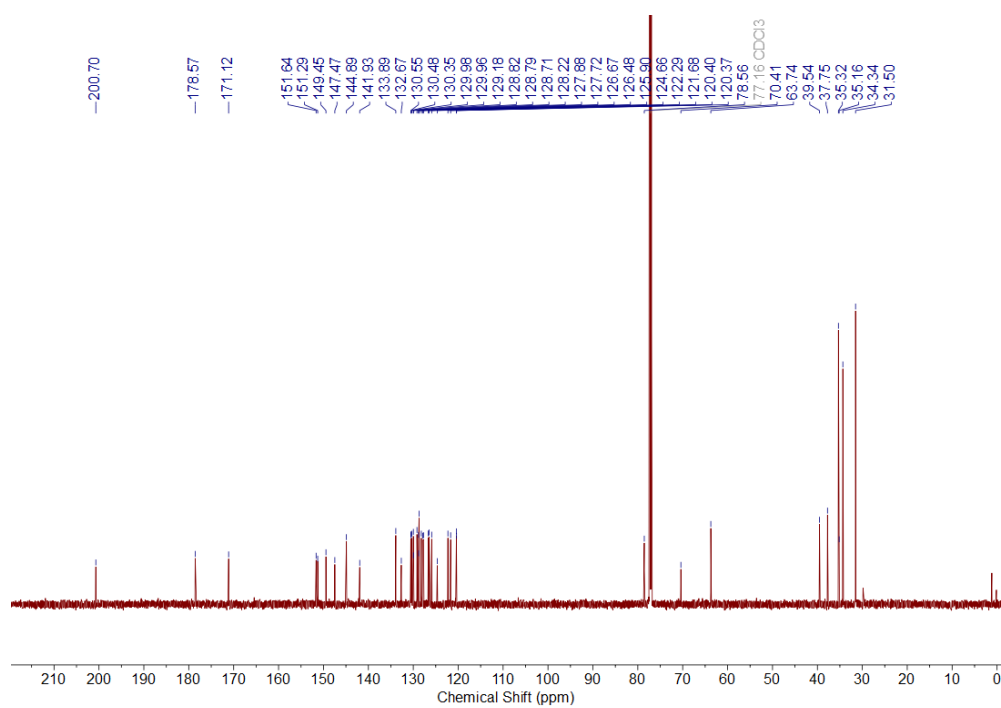
¹H NMR of (*R,R*)-2.3j
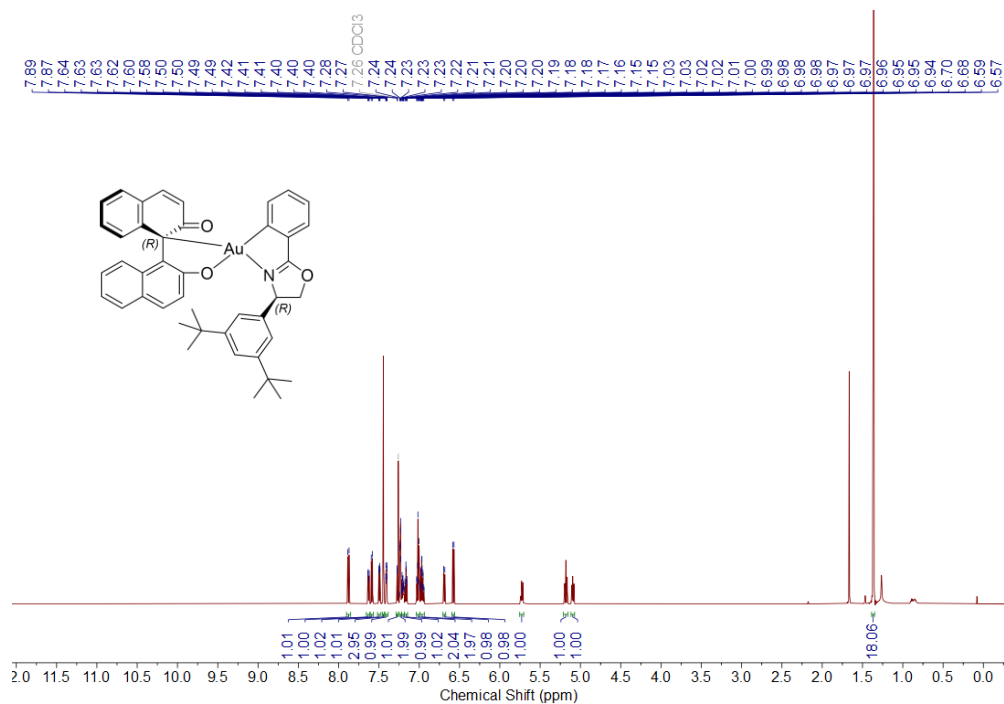
¹³C NMR of (*R,R*)-2.3j
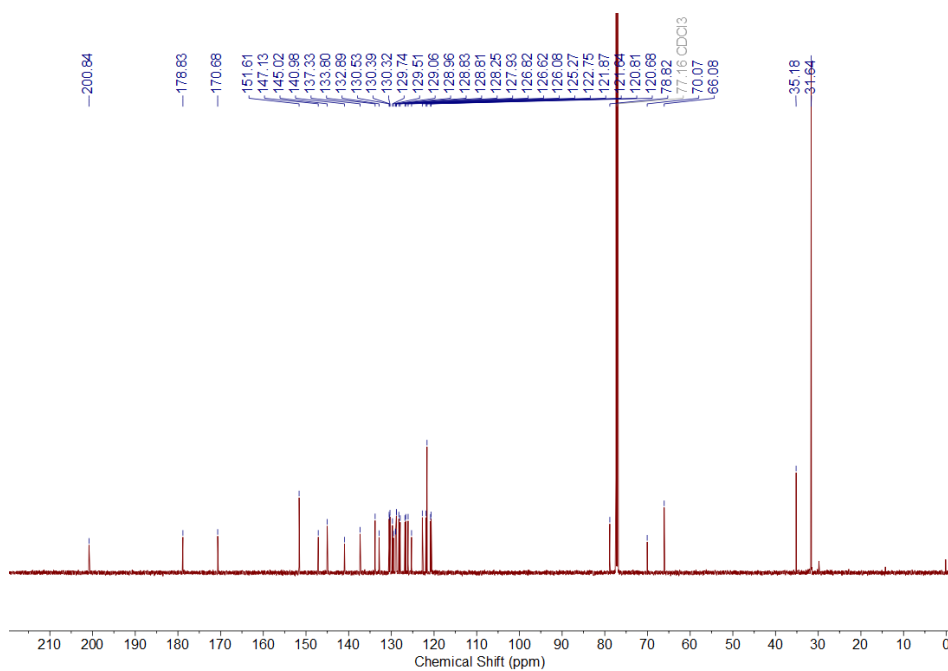
^{1}H NMR of 2.4f
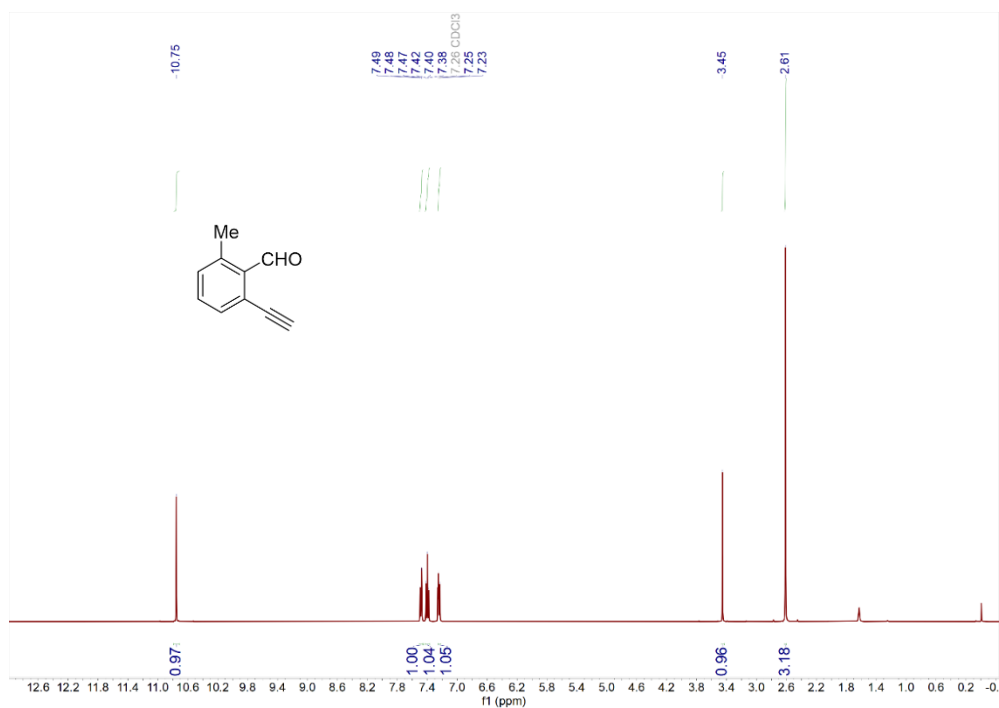
^{13}C NMR of 2.4f
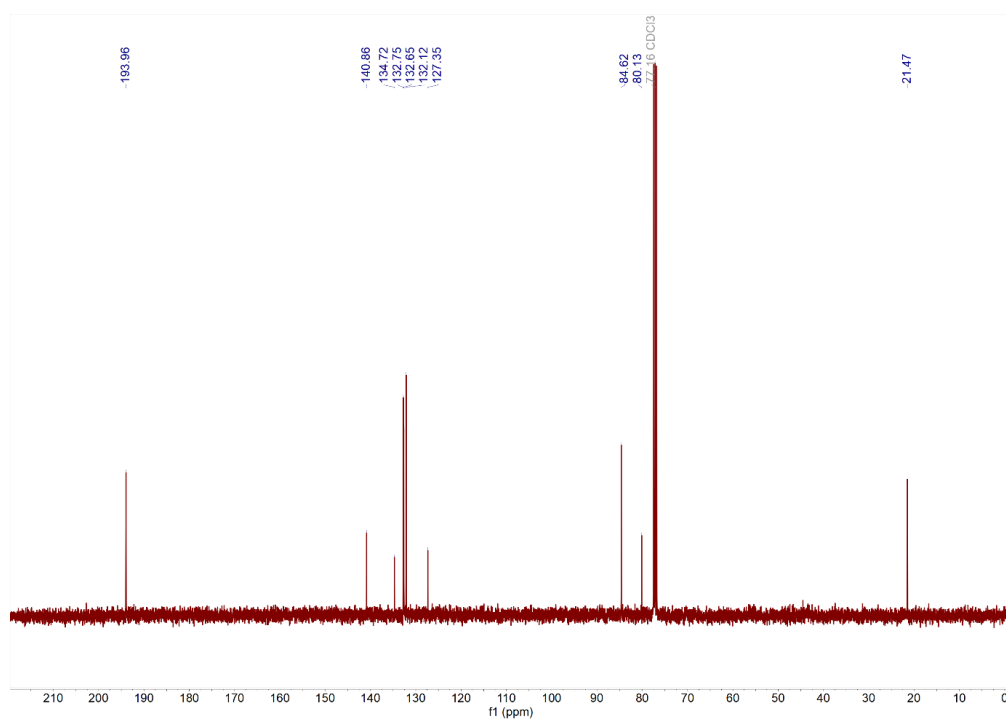
^{1}H NMR of 2.5a
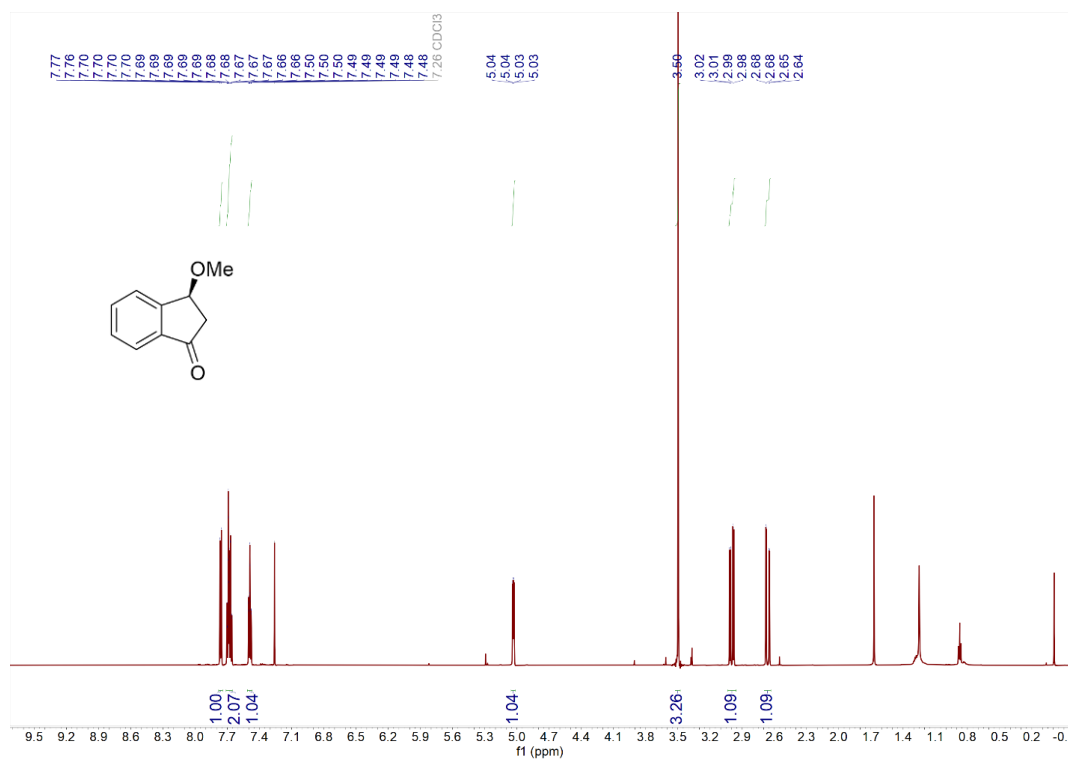
^{1}H NMR of 2.5b
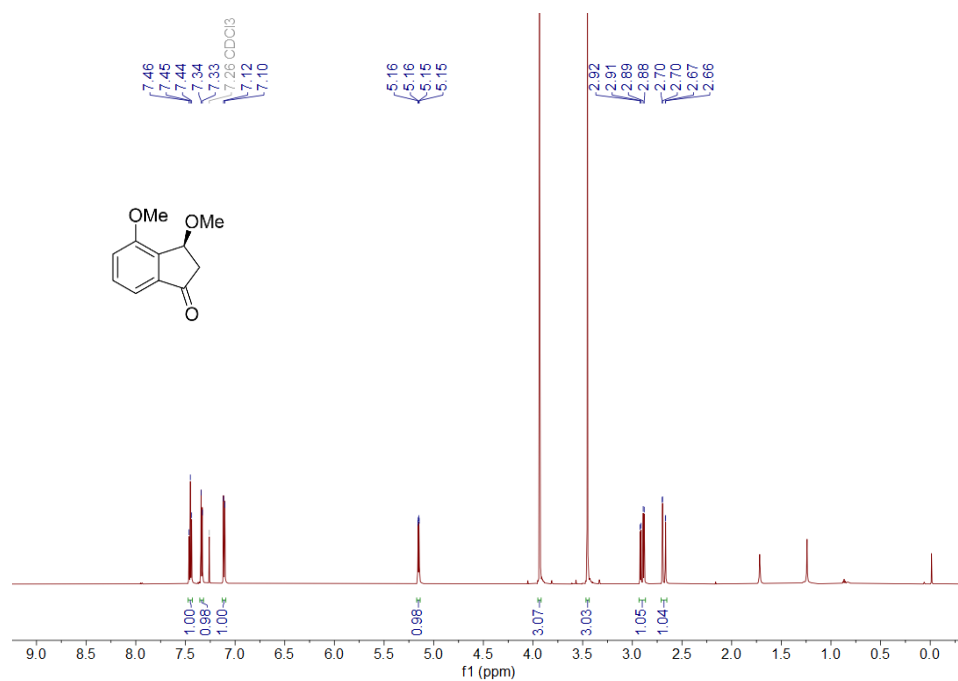
^{13}C NMR of 2.5b
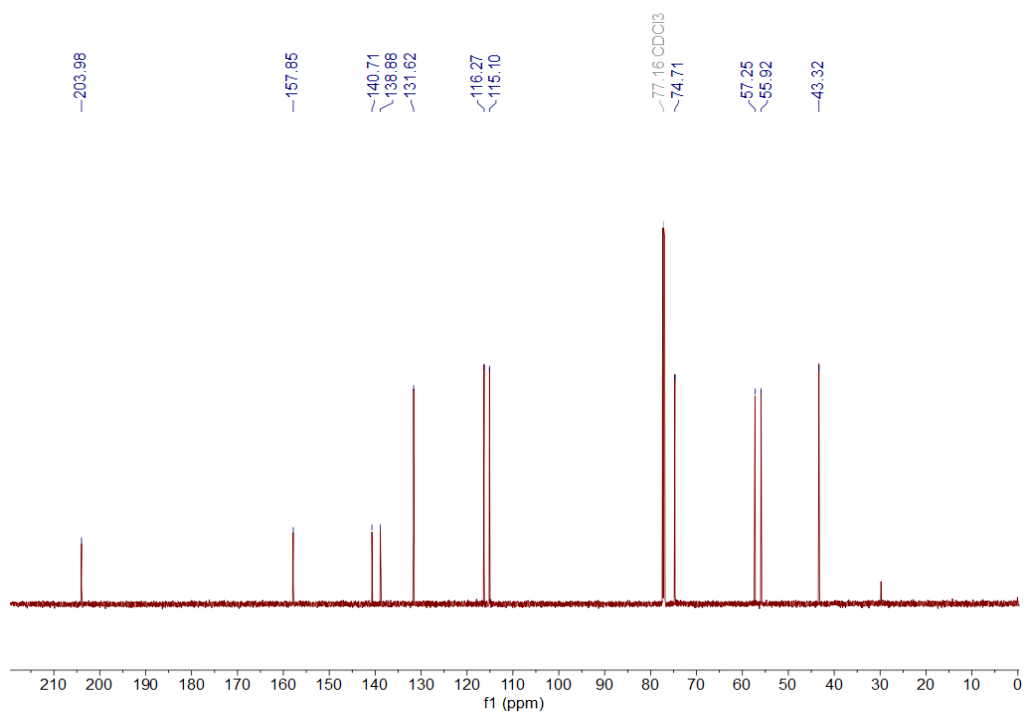
^{1}H NMR of 2.5c
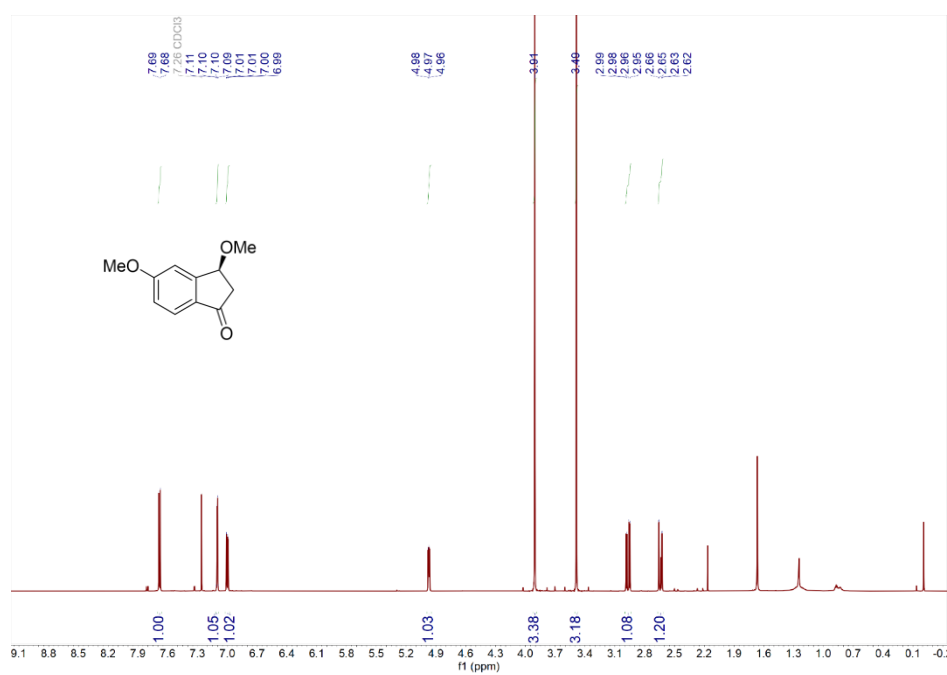
^{1}H NMR of 2.5d
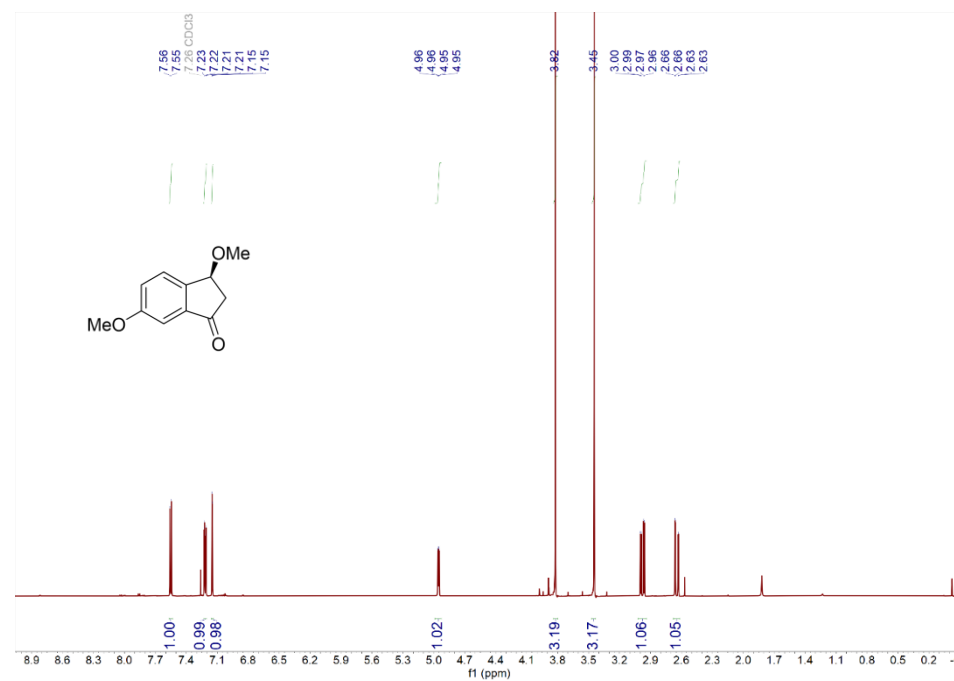
^{13}C NMR of 2.5d
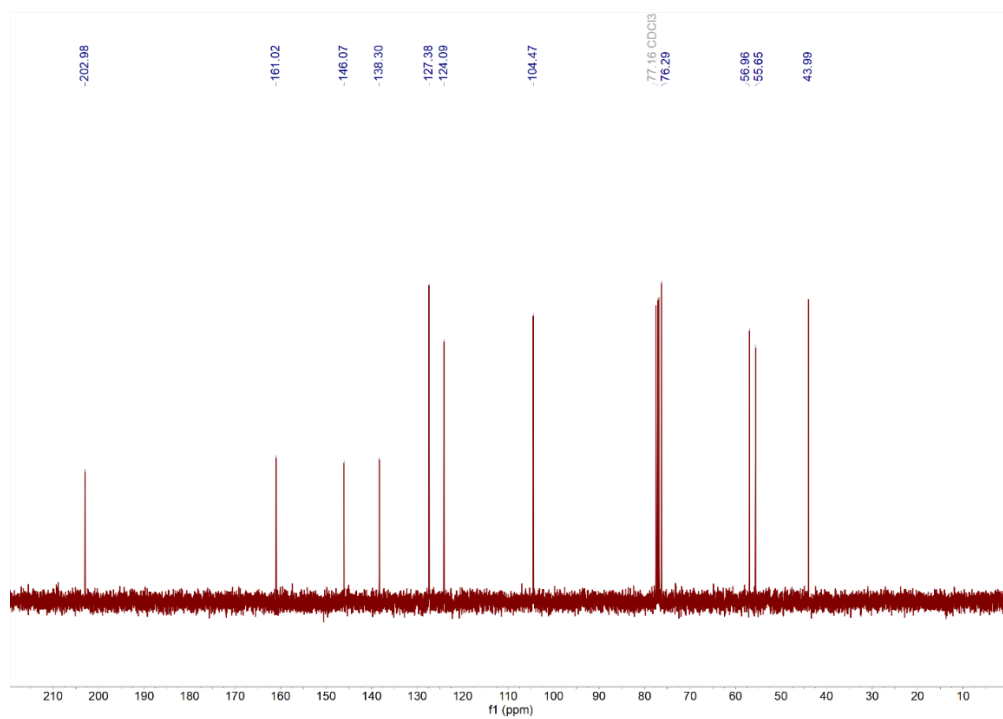
¹H NMR of 2.5e
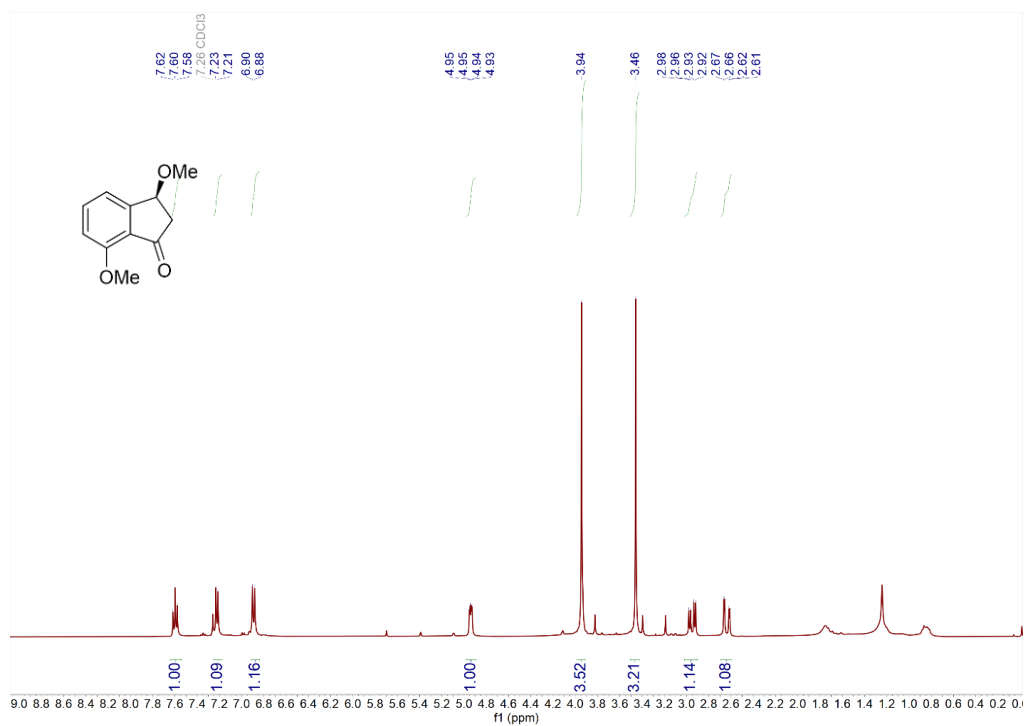
¹³C NMR of 2.5e
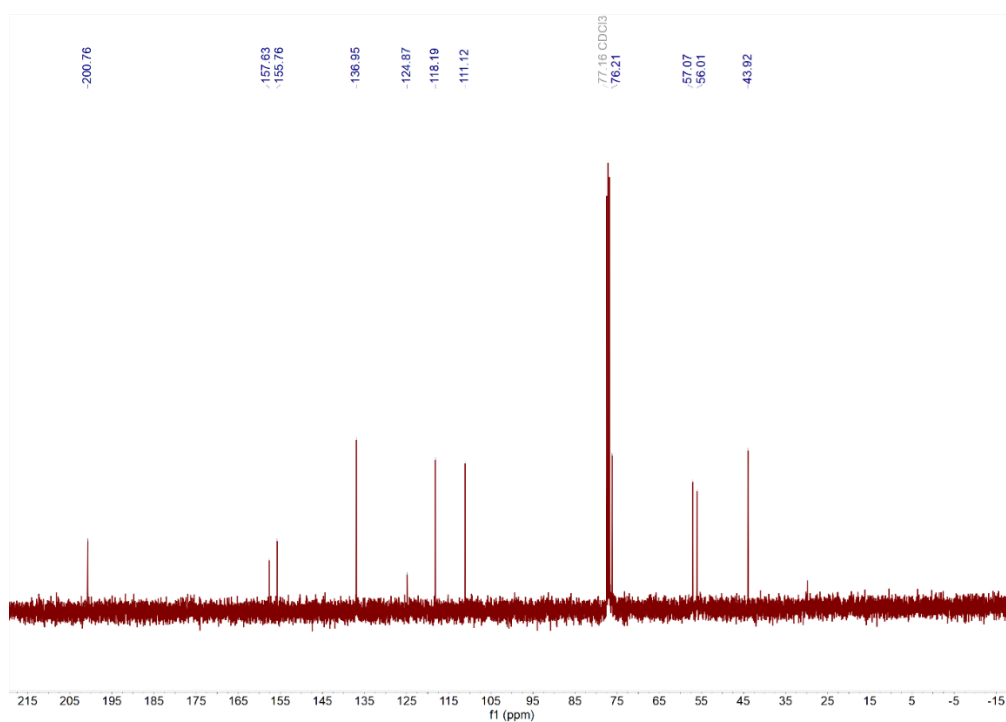
¹H NMR of 2.5f
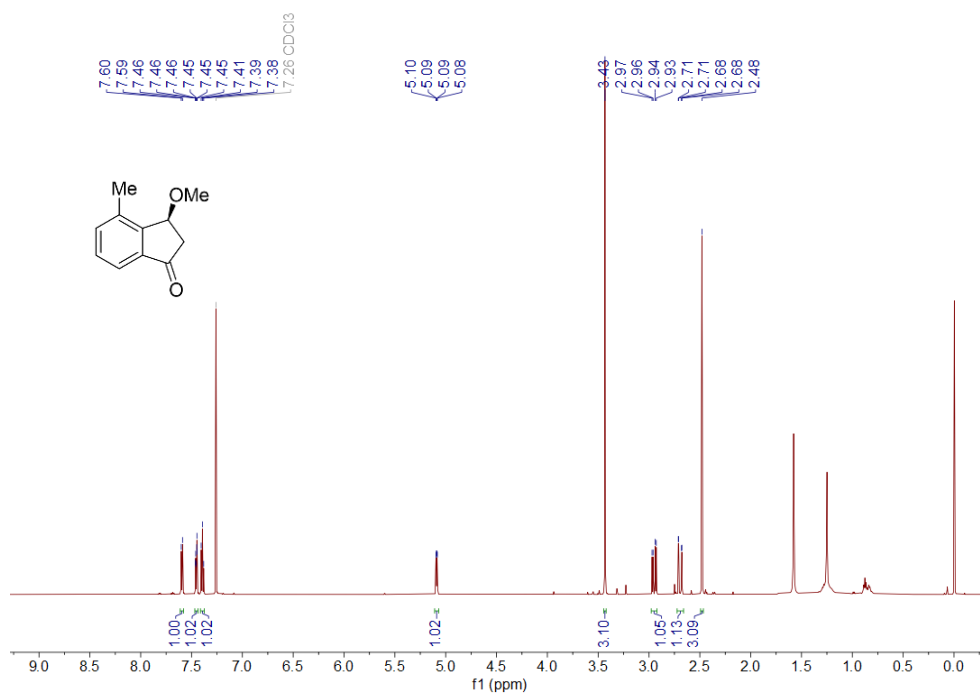
¹³C NMR of 2.5f
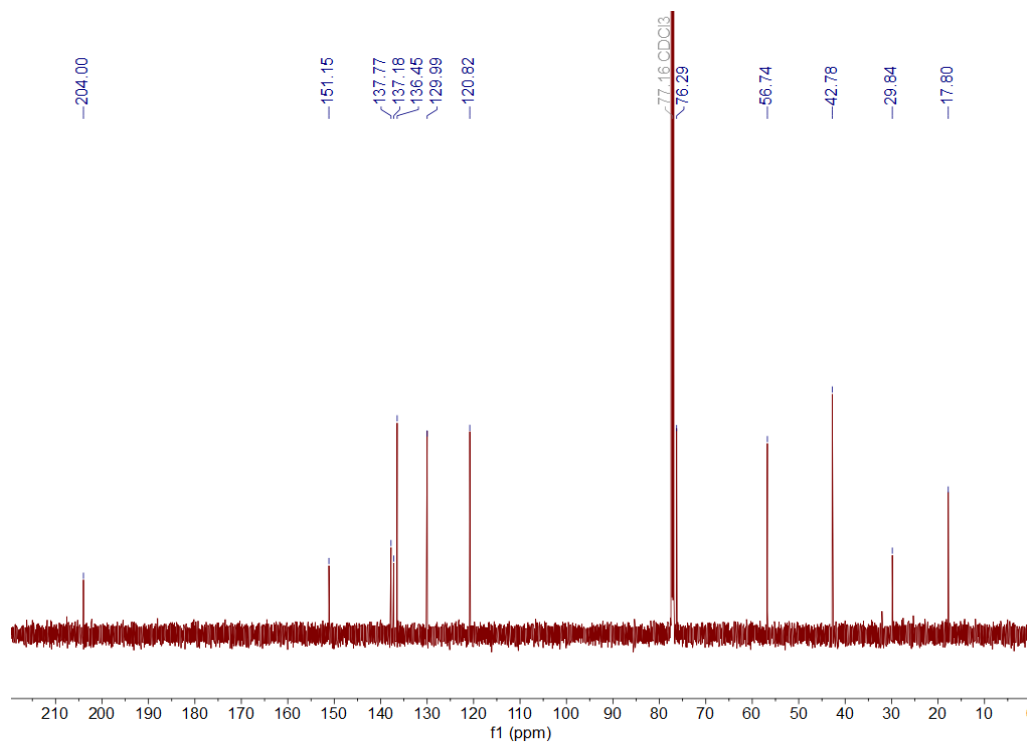
^{1}H NMR of 2.5g
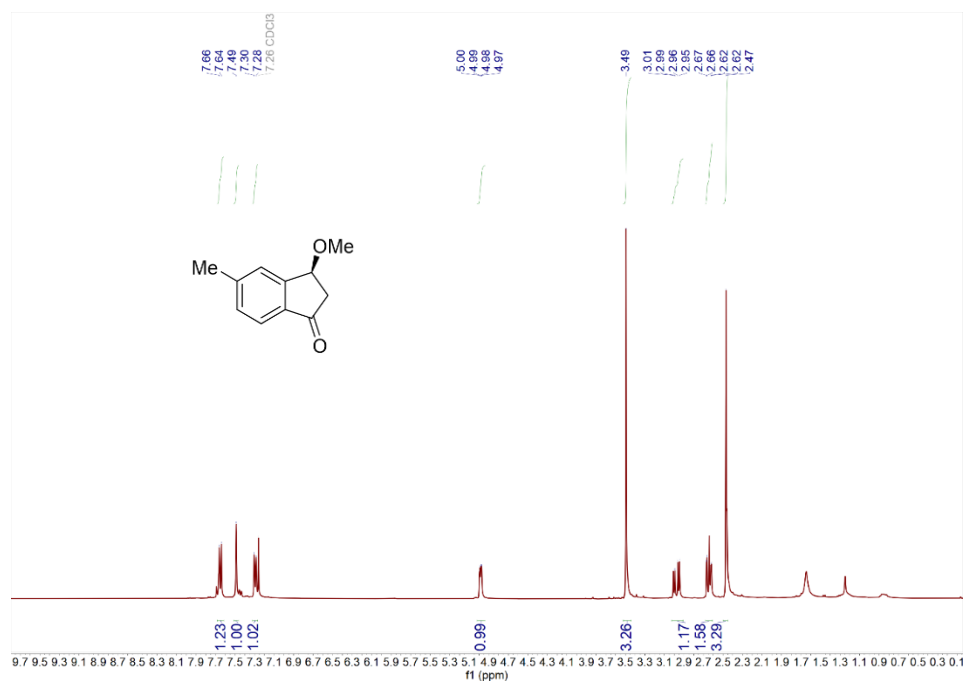
^{1}H NMR of 2.5h
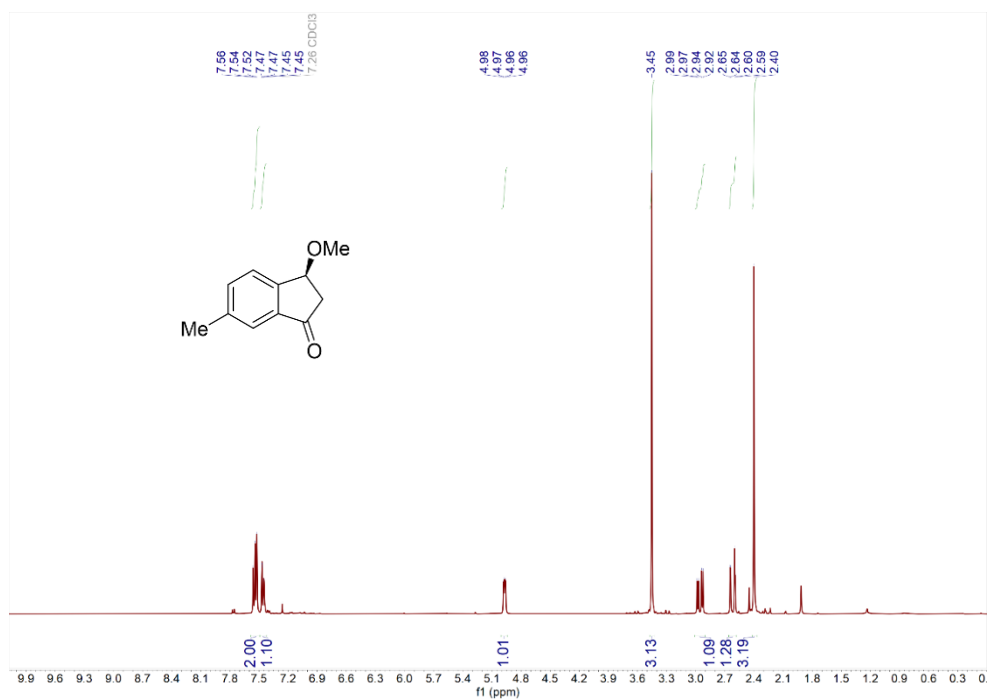
^{1}H NMR of 2.5i
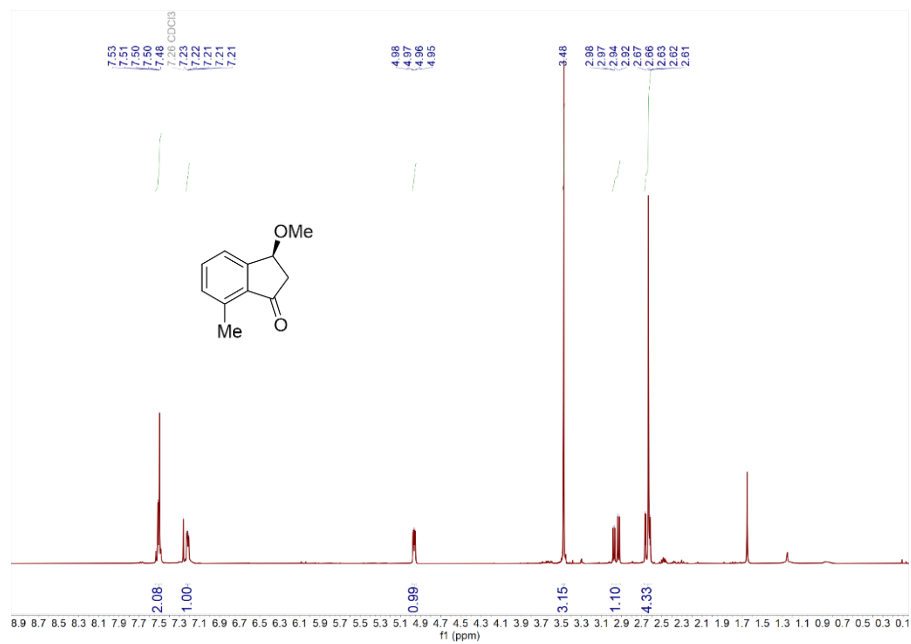
^{13}C NMR of 2.5i
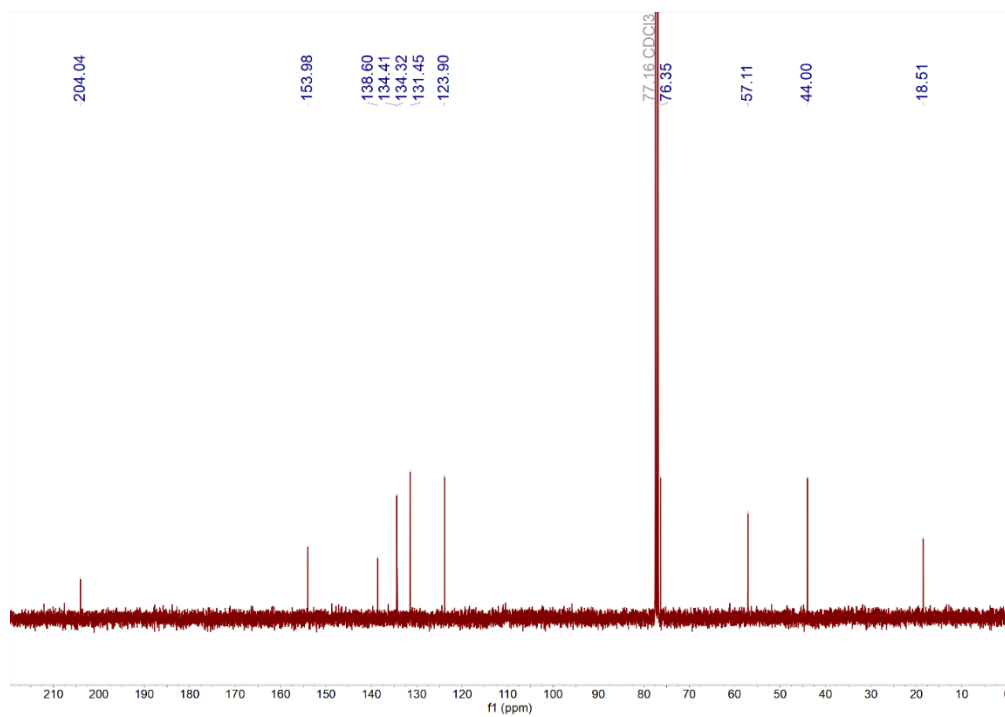
¹H NMR of 2.5j
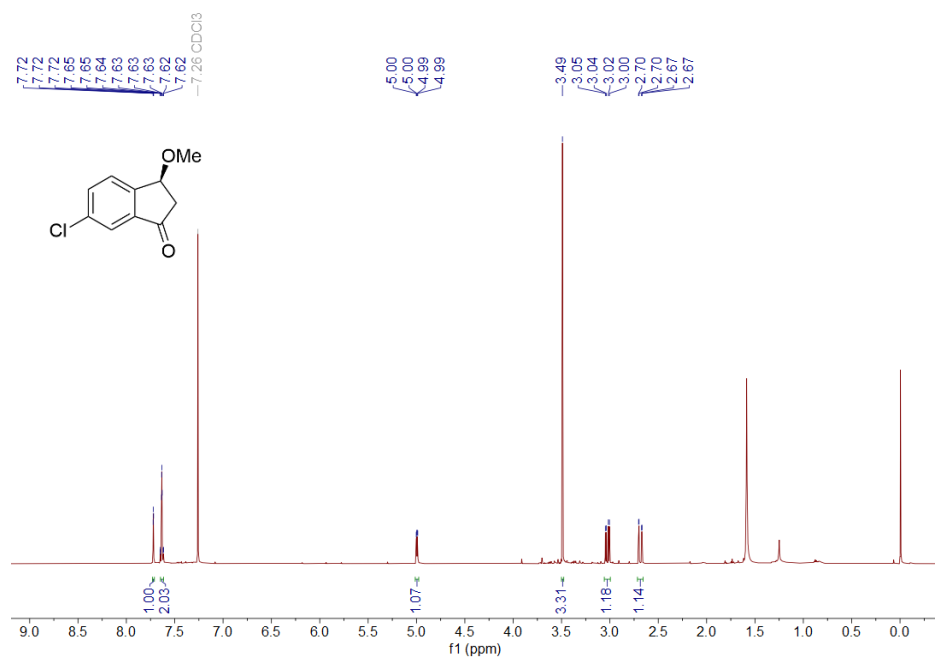
¹³C NMR of 2.5j
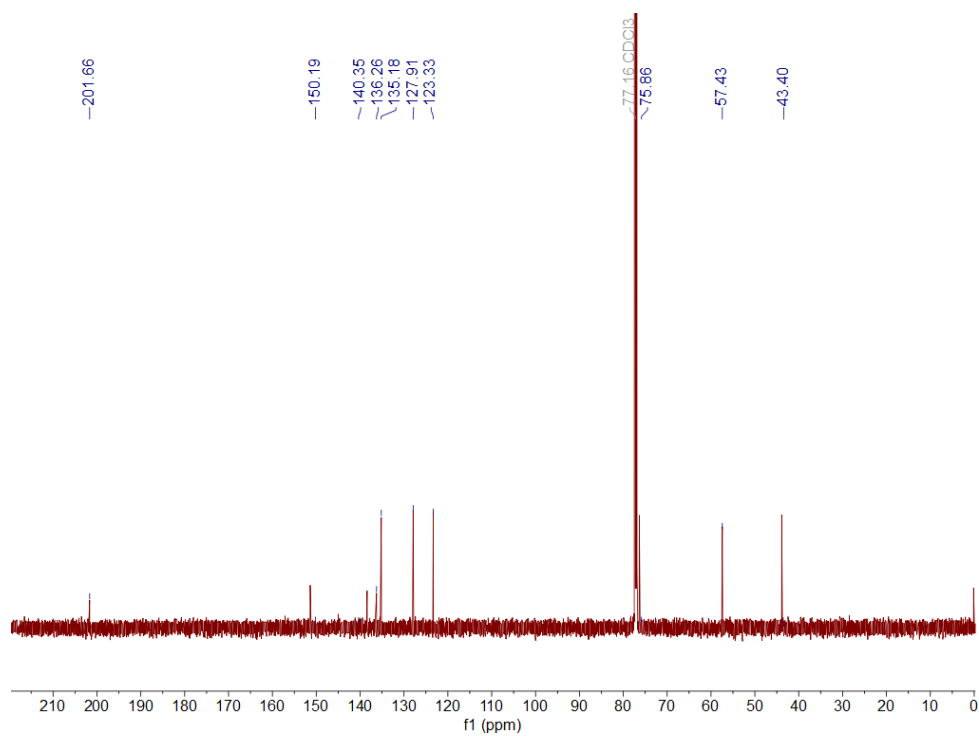
¹H NMR of 2.5l

¹H NMR of 2.5l
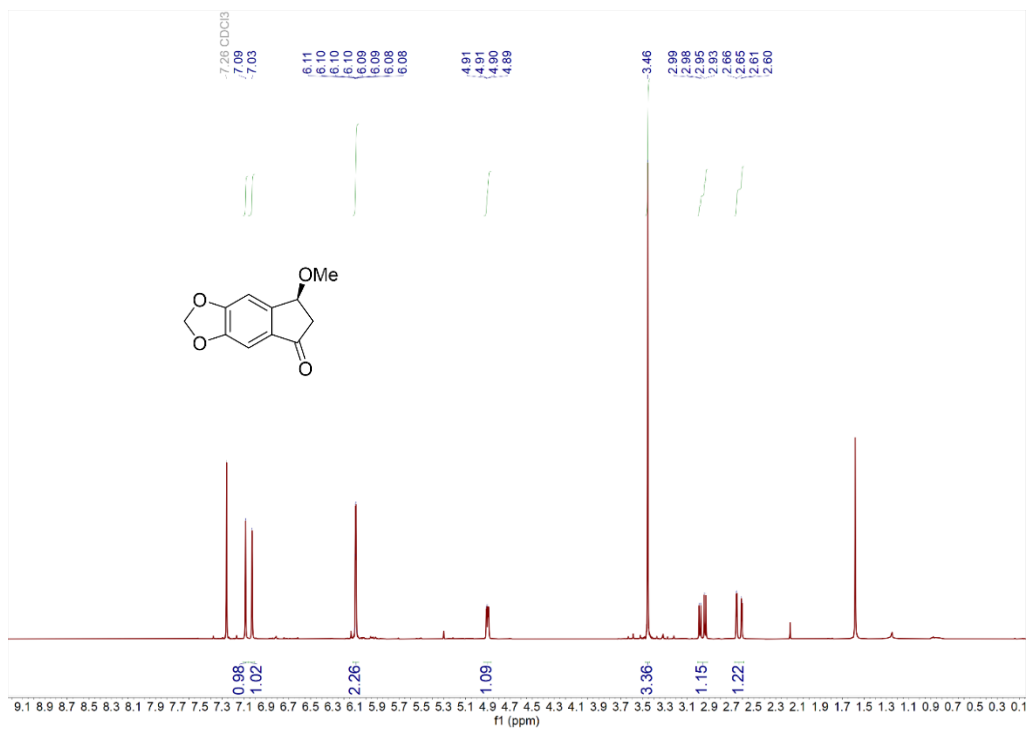
¹H NMR of 2.5m
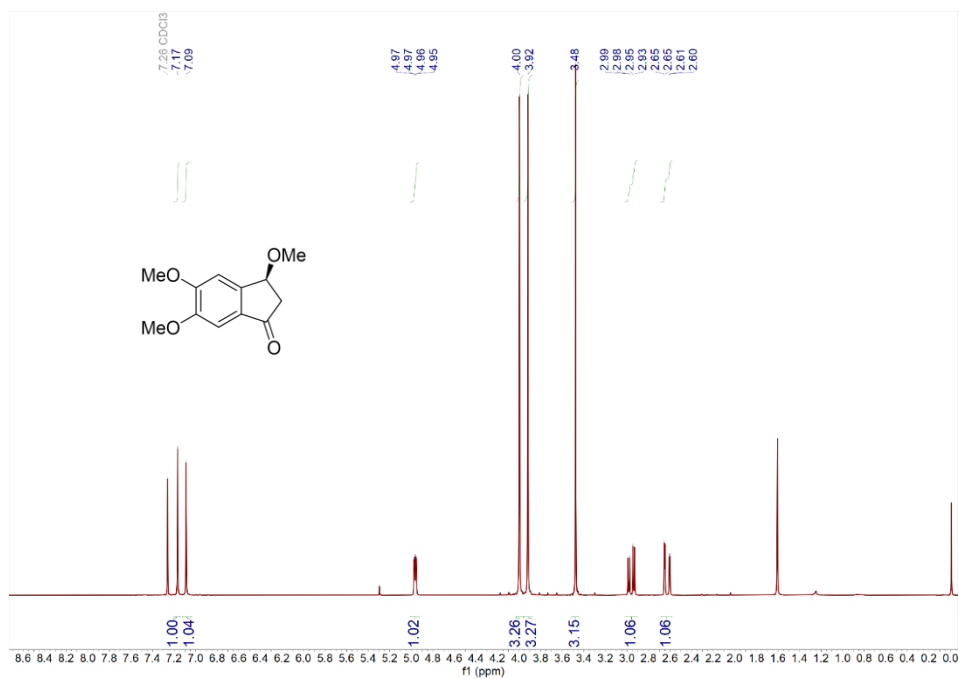
¹H NMR of 2.5m

^{1}H NMR of 2.5n
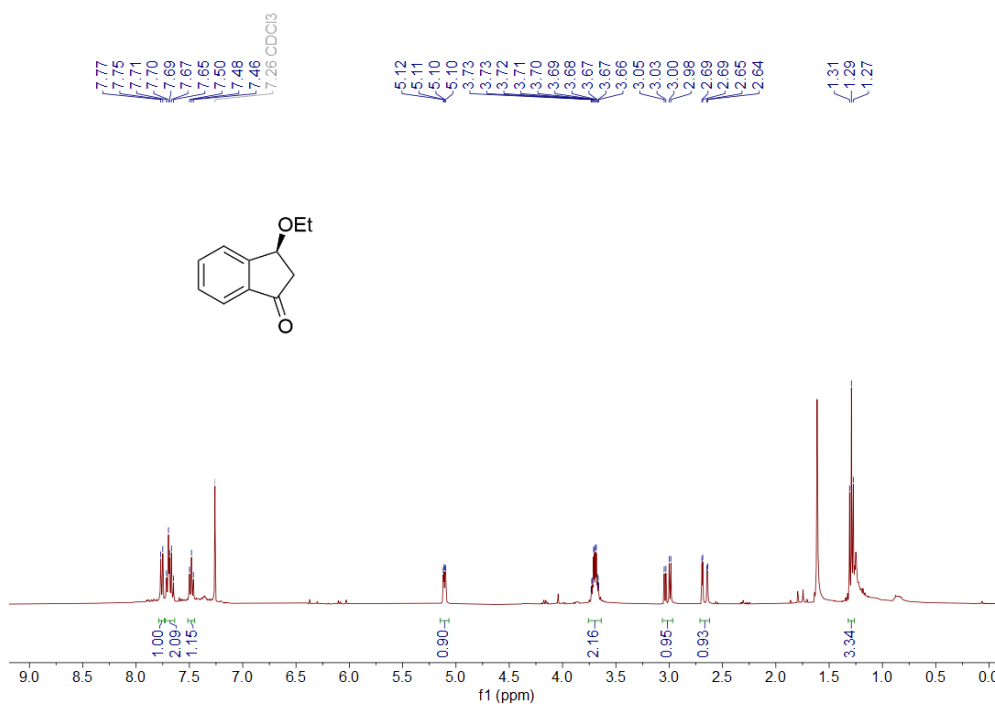
^{1}H NMR of 2.5o
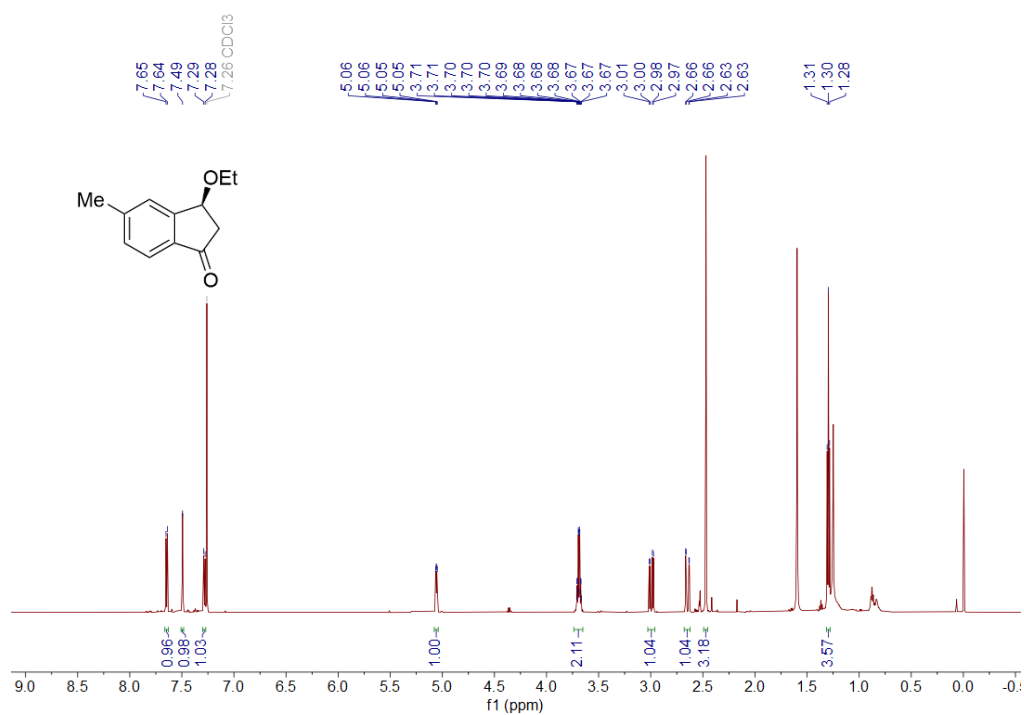
^{13}C NMR of 2.5o
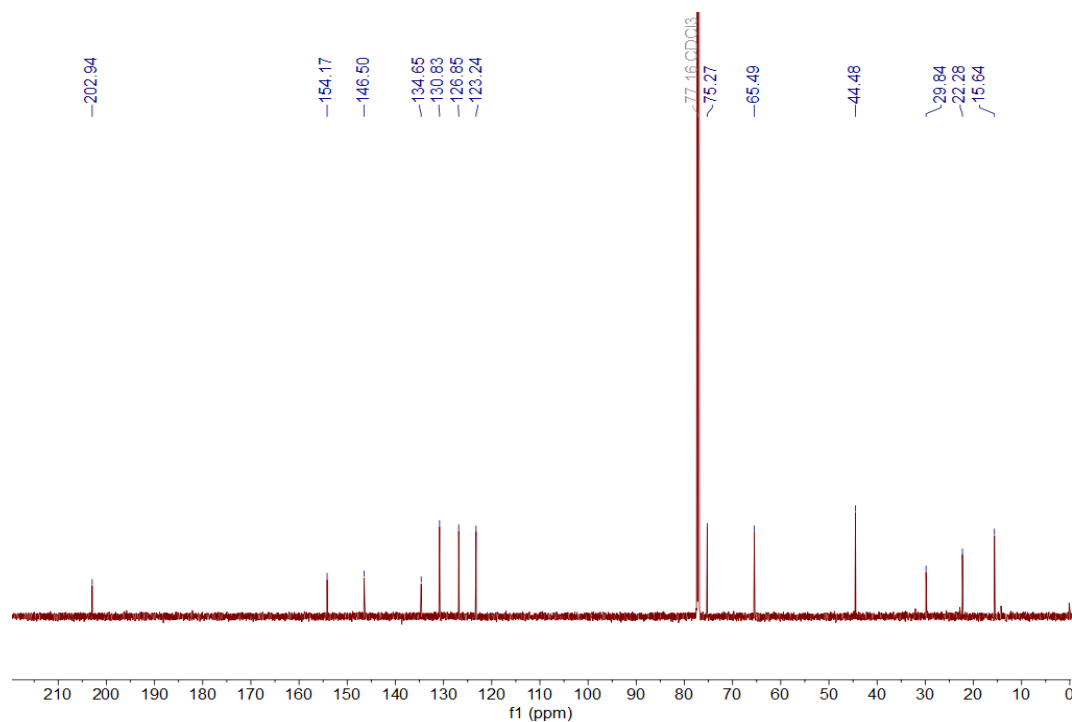
^{1}H NMR of 2.5p

^{13}C NMR of 2.5p

203.48

146.44
137.08
134.09
133.48
130.42
128.78
128.47
127.00
125.66
124.24

57.03

44.42

29.71

f1 (ppm)

^{1}H NMR of 2.5q

9.14
9.14
9.12
9.11
8.10
8.08
7.91
7.89
7.88
7.71
7.70
7.69
7.68
7.67
7.66
7.65
7.60
7.60
7.58
7.58
7.56
7.56
7.26 CDCl3

5.08
5.08
5.07
5.06

3.52
3.11
3.10
3.07
3.05
2.79
2.78
2.75
2.74

OMe

1.00

1.08
1.14
2.15
1.11

1.05

3.29

1.16

1.12

f1 (ppm)
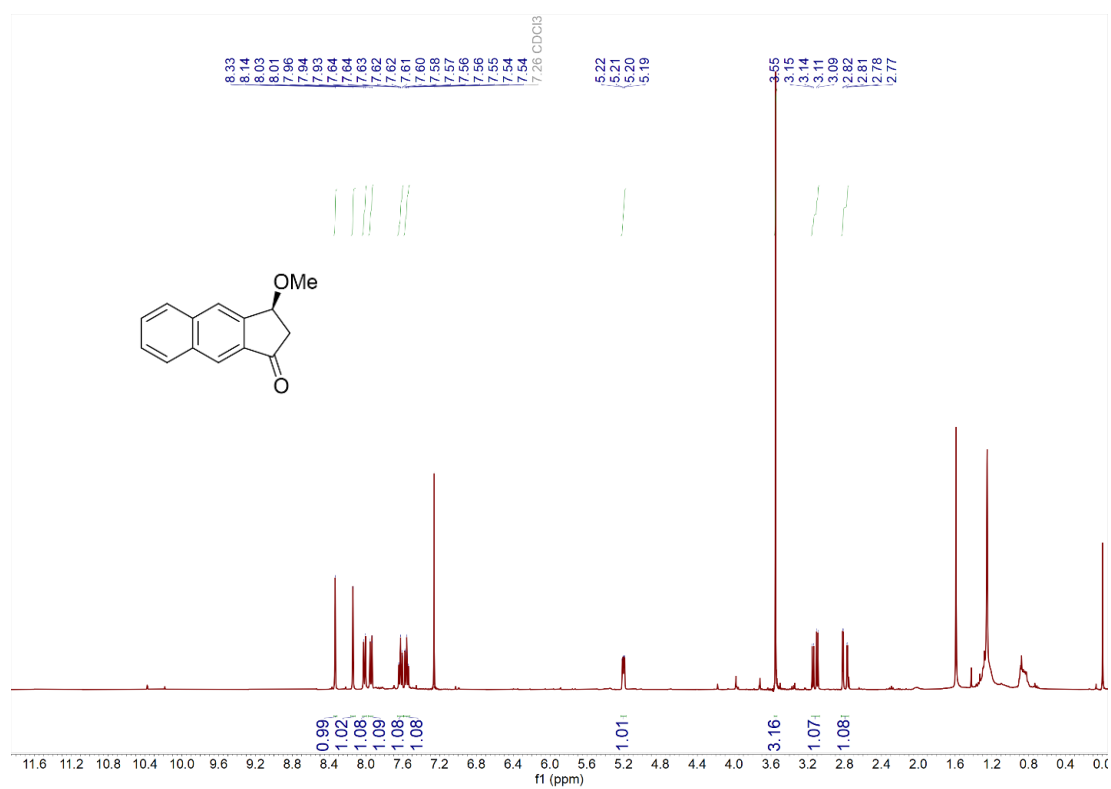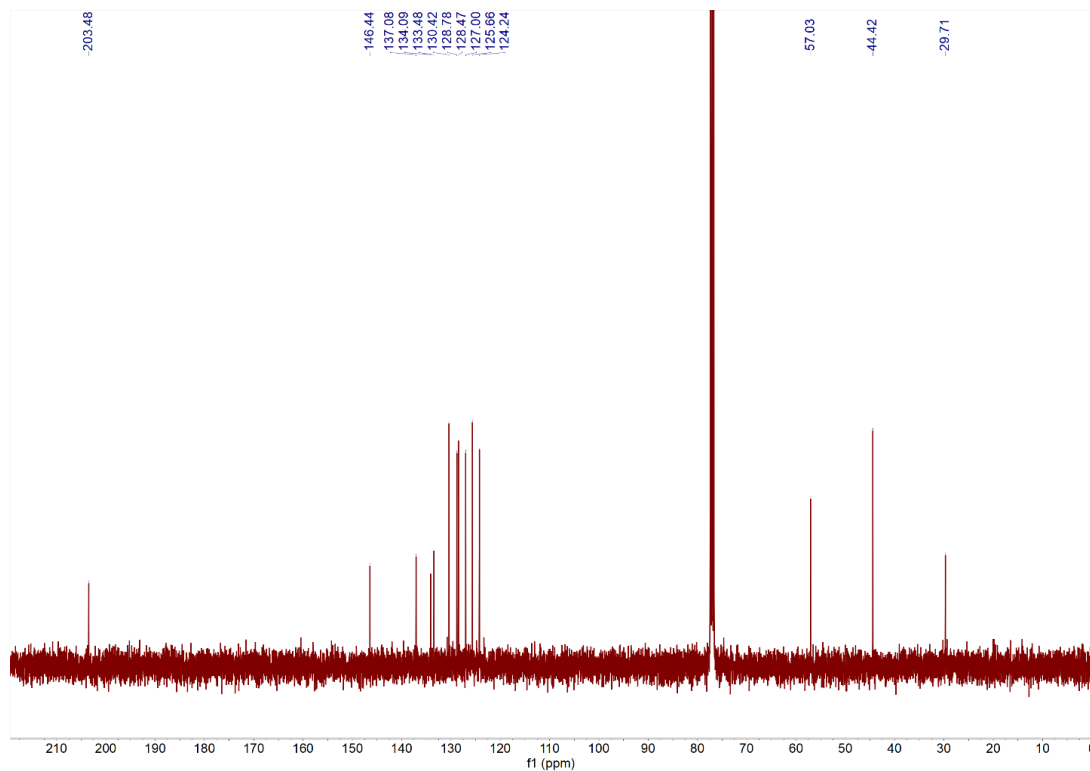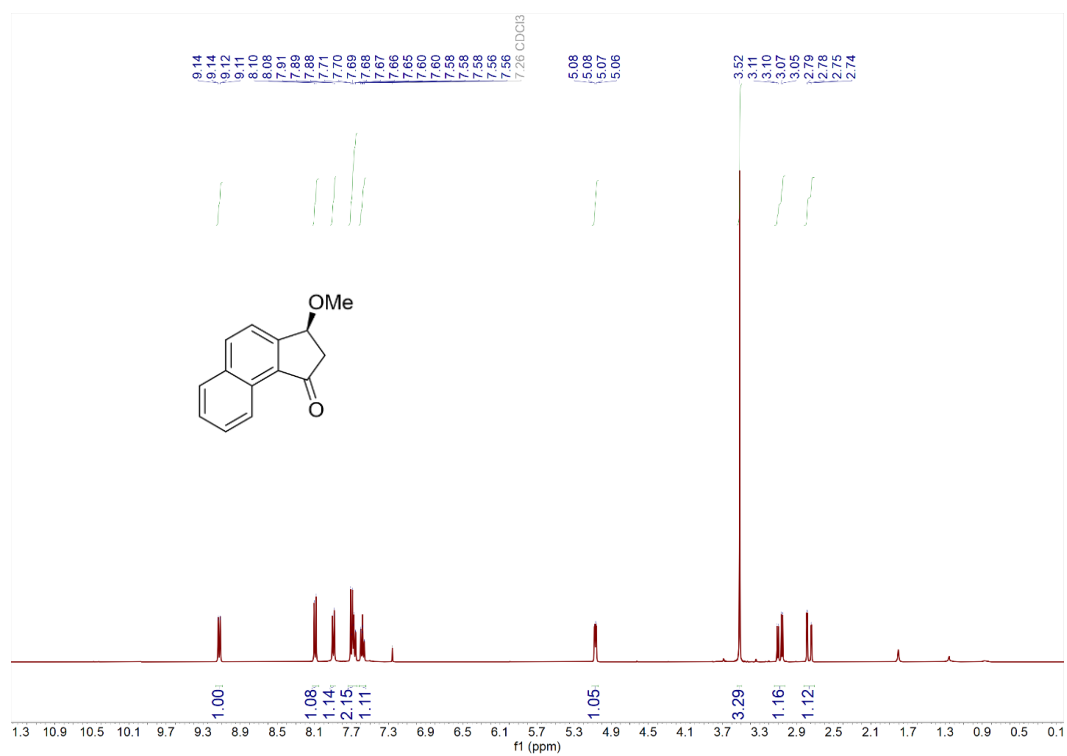
2.4.15 Circular Dichroism Spectra

CD spectra of (*R*)-2.1a & (*S*)-2.1a in CH$_3$CN (25 μM)
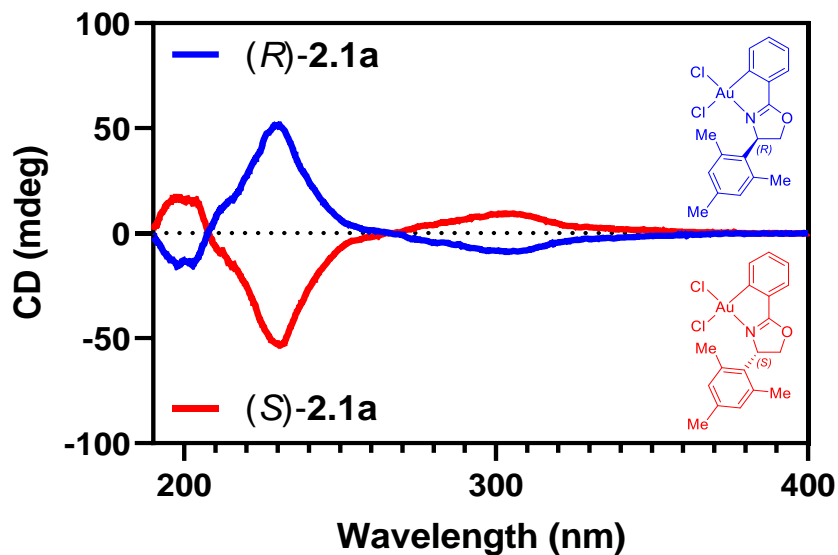
CD spectrum of (*R*)-2.1b in CH$_3$CN (25 μM)
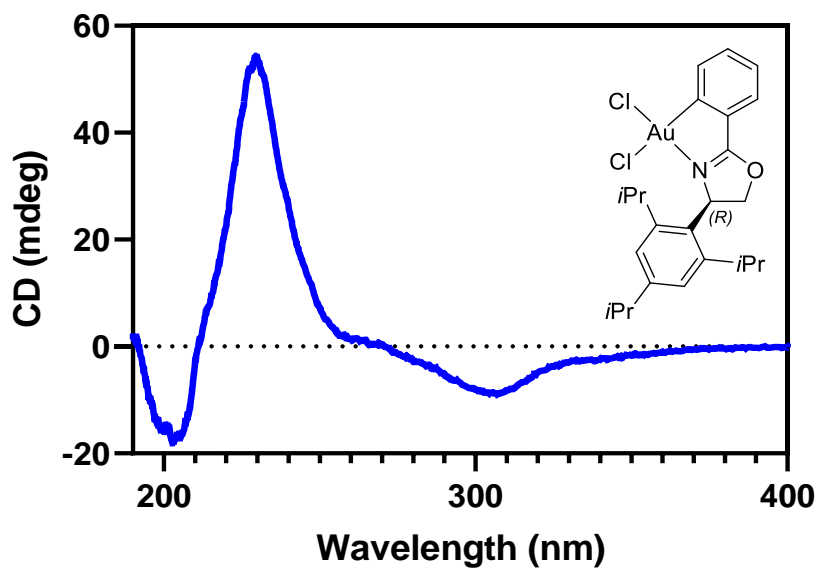
CD spectrum of (*S*)-2.1c in CH$_3$CN (25 µM)
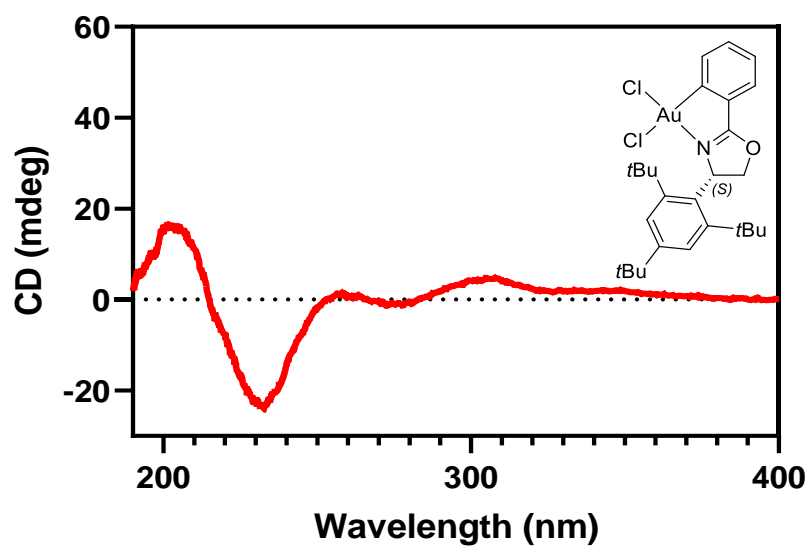
CD spectrum of (*R*)-2.1d in CH$_3$CN (25 µM)
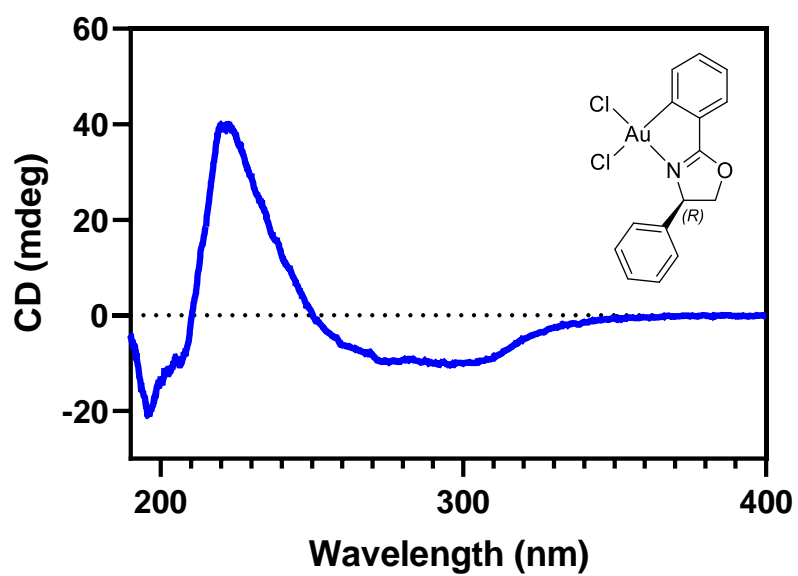
CD spectrum of (*R*)-2.1d in CH$_3$CN (25 µM)
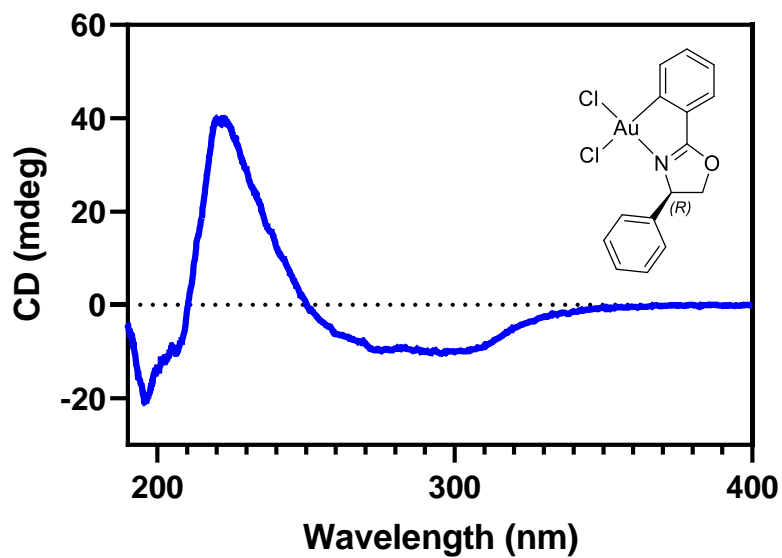
CD spectrum of (*R*)-2.1e in CH$_3$CN (25 µM)
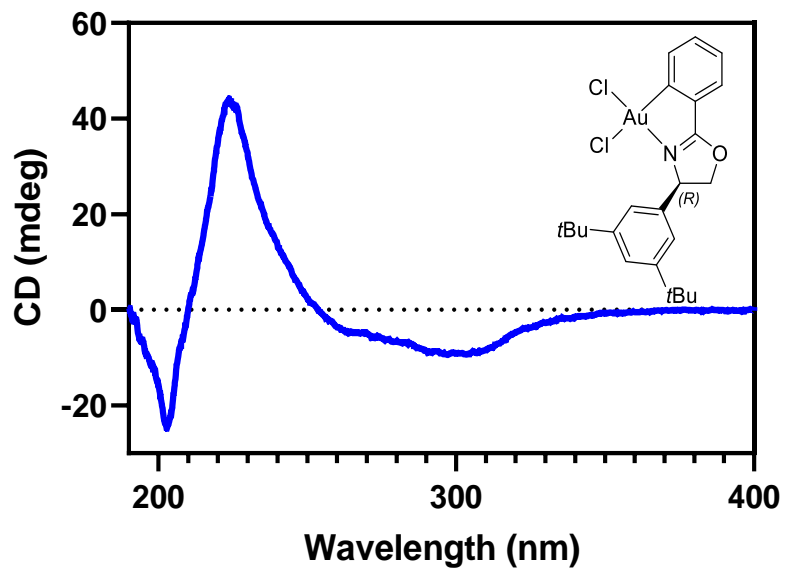
CD spectra of (*R*)-2.2b & (*S*)-2.2b in CH$_3$CN (10 µM)
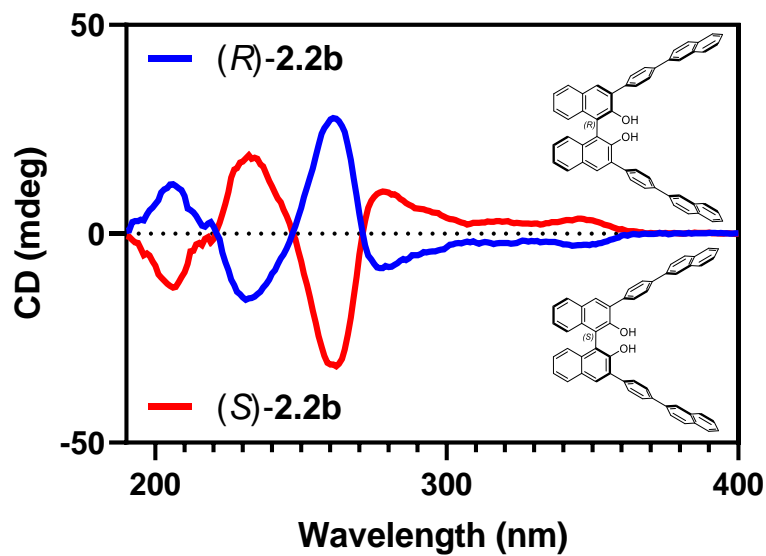
CD spectra of (*R*)-2.2c & (*S*)-2.2c in CH$_3$CN (10 µM)
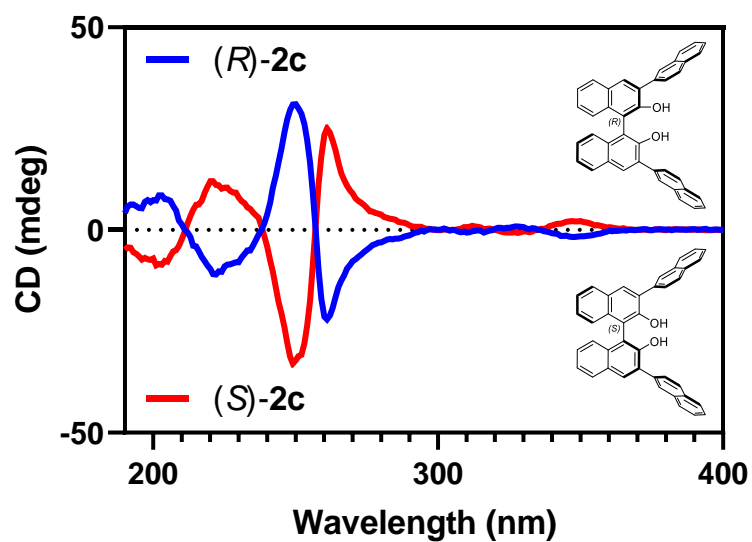
CD spectra of (*R*)-2.2d & (*S*)-2.2d in CH₃CN (10 µM)
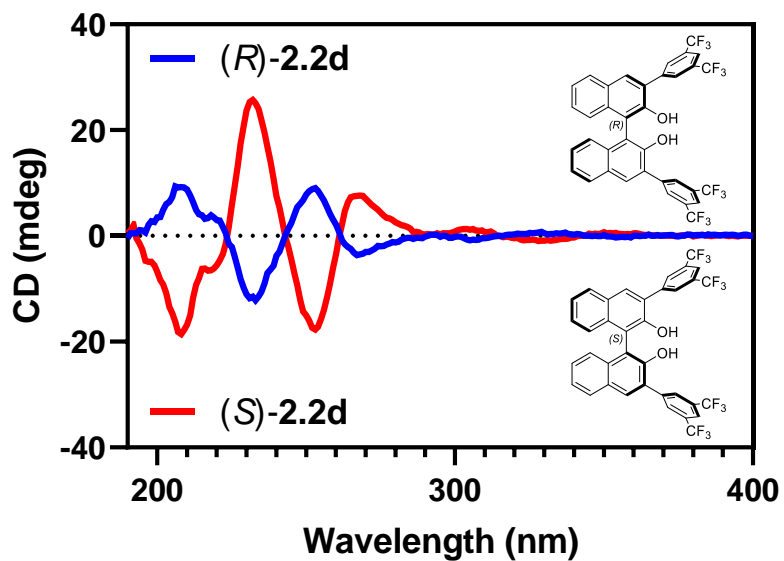
CD spectra of (*R*)-2.2e & (*S*)-2.2e in CH₃CN (10 µM)
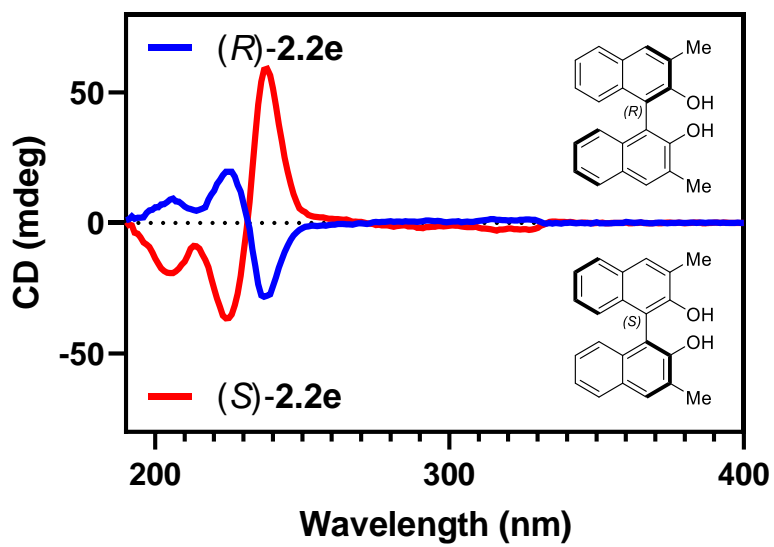
CD spectra of (*R*)-2.2f & (*S*)-2.2f in CH$_3$CN (10 µM)
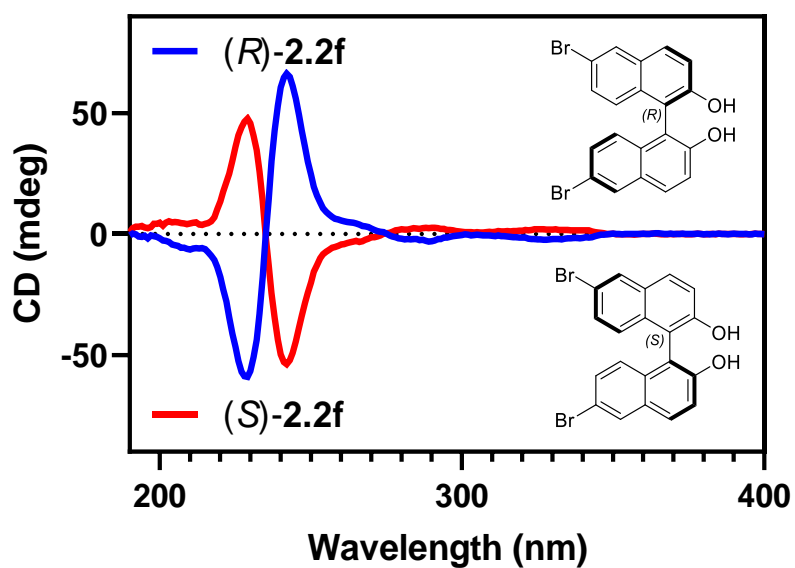
CD spectra of (*R,R*)-2.3a & (*S,S*)-2.3a in CH$_3$CN (25 µM)
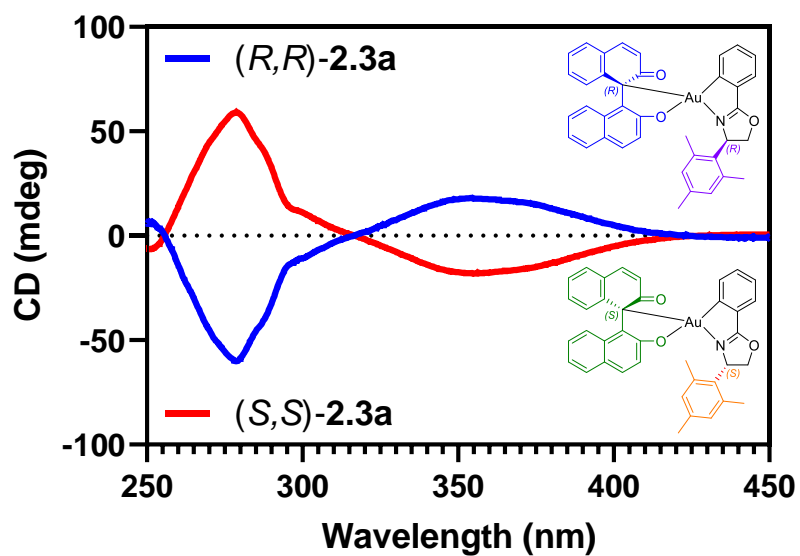
CD spectra of (*R,S*)-**2.3a** & (*S,R*)-**2.3a** in CH$_3$CN (25 µM)
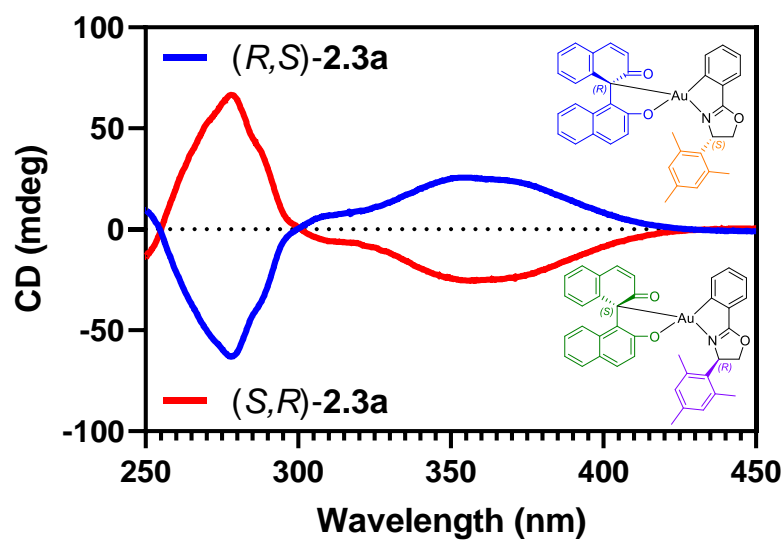
CD spectrum of (*R,S*)-**2.3b** in CH$_3$CN (25 µM)
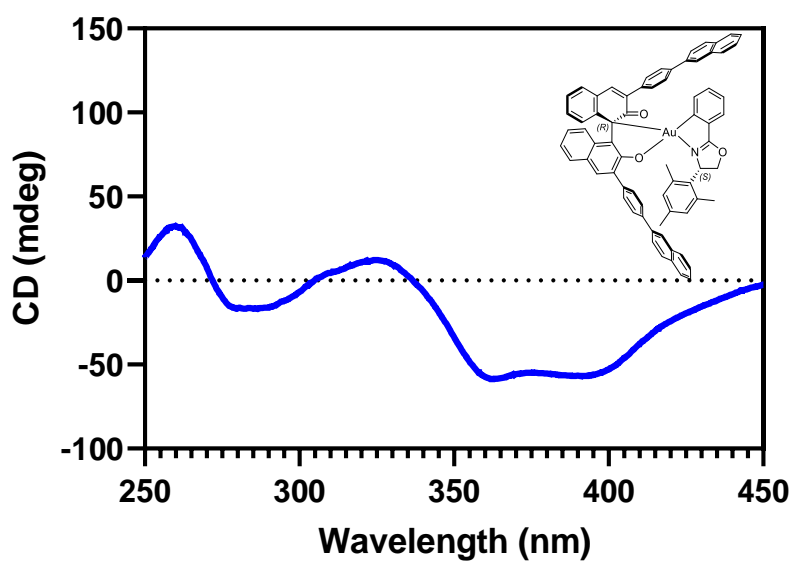
CD spectrum of (*S*,*S*)-2.3b in CH₃CN (25 µM)
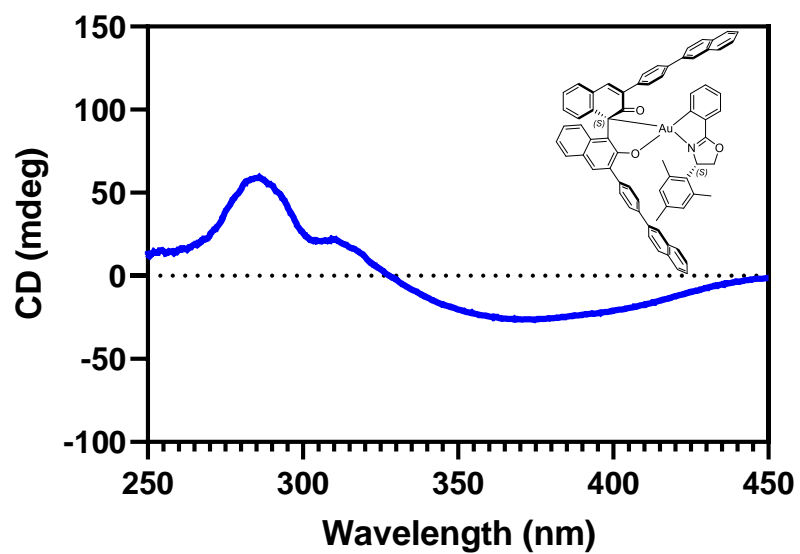
CD spectra of (*R*,*S*)-2.3c in CH₃CN (25 µM)
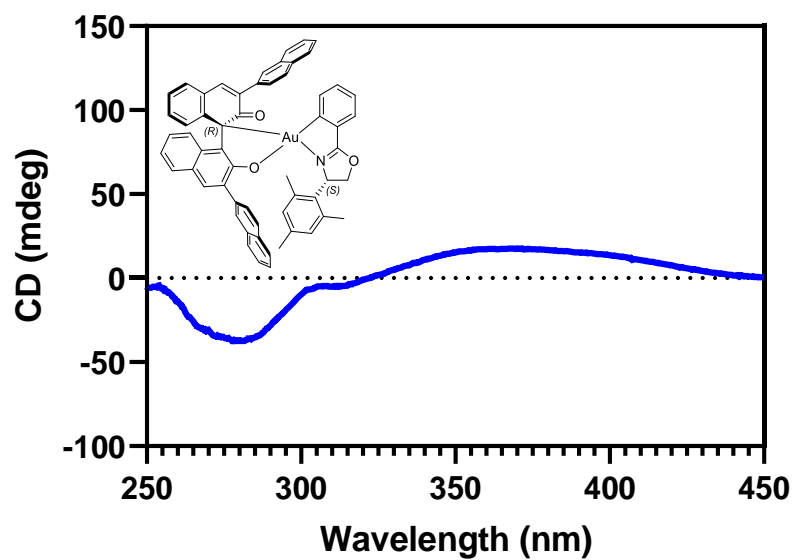
CD spectrum of (*S,S*)-2.3c in CH₃CN (25 µM)
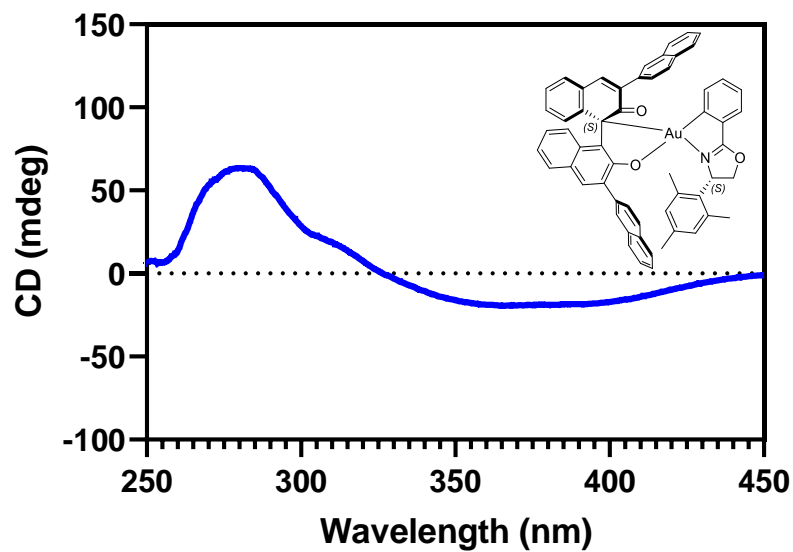
CD spectrum of (*R,S*)-2.3d in CH₃CN (25 µM)
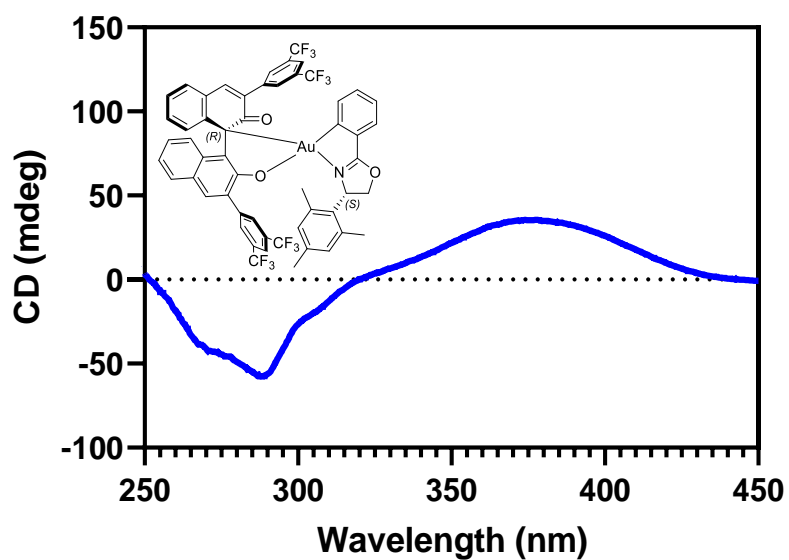
CD spectrum of (*R*,*S*)-2.3e in CH$_3$CN (25 µM)
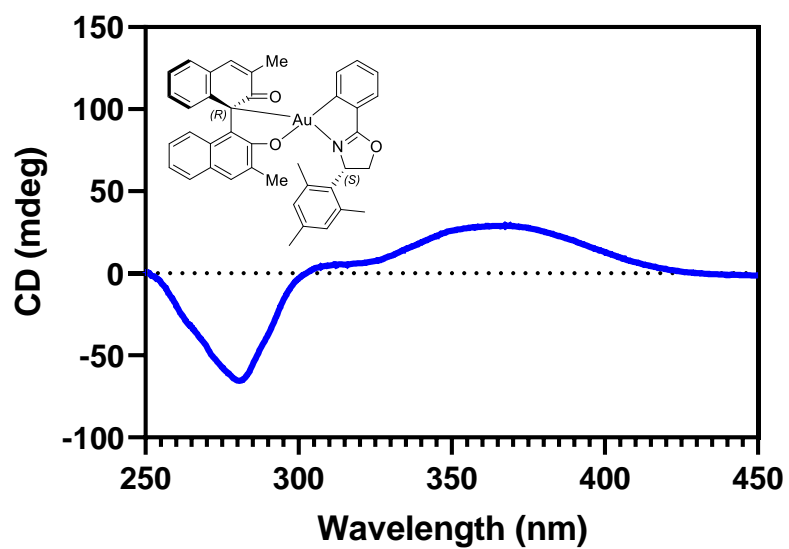
CD spectrum of (*S*,*S*)-2.3e in CH$_3$CN (25 µM)
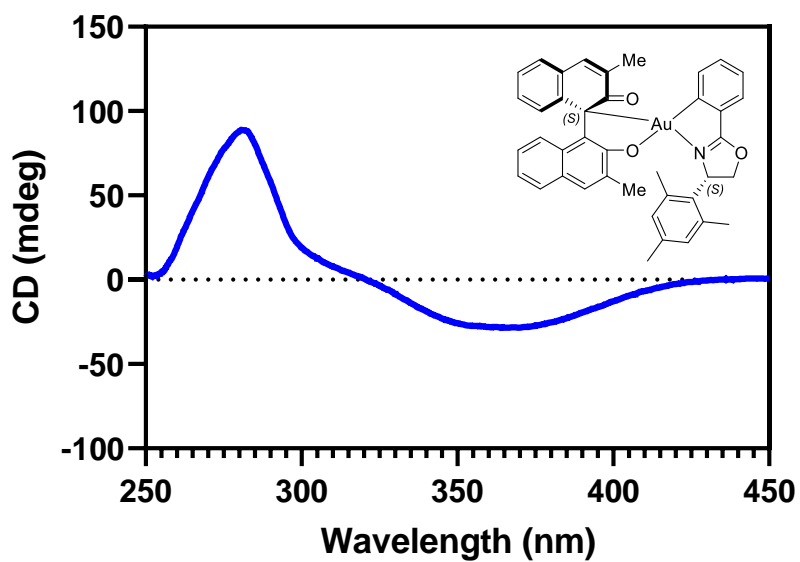
CD spectrum of (*R*,*S*)-2.3f in CH₃CN (25 µM)
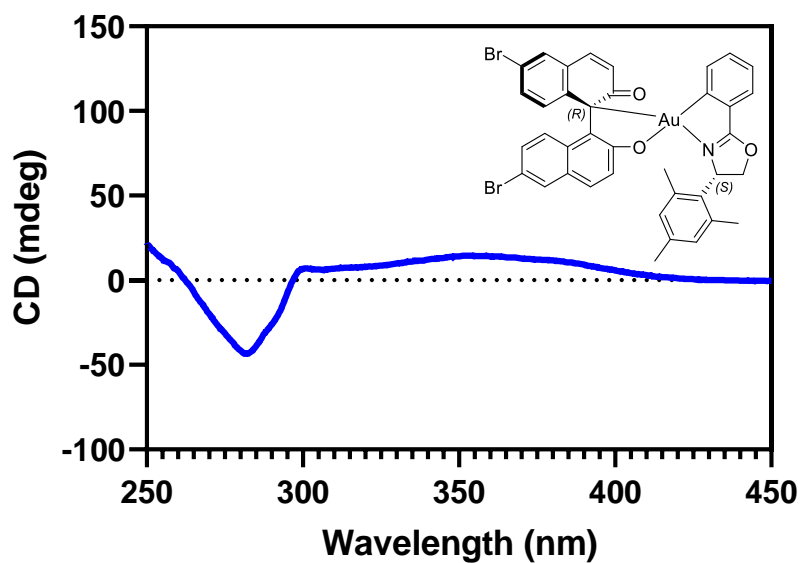
CD spectrum of (*S*,*S*)-2.3f in CH₃CN (25 µM)
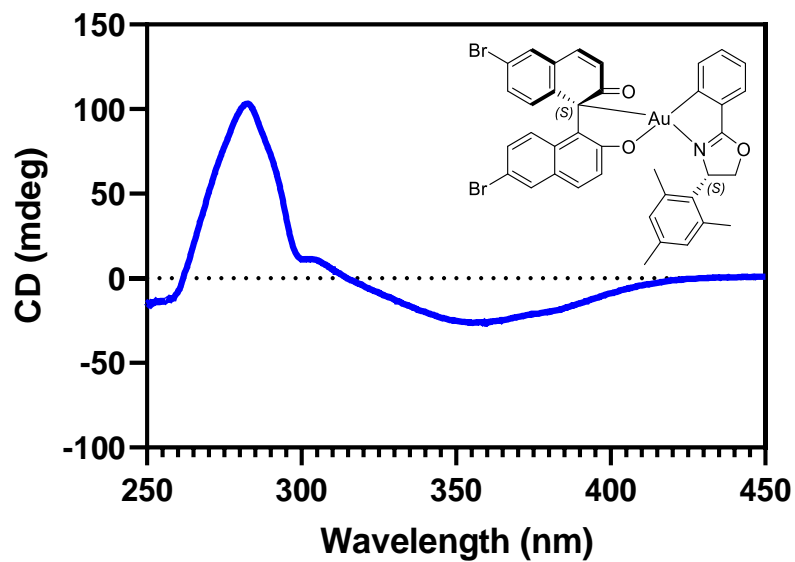
CD spectrum of (*R*,*R*)-2.3g in CH₃CN (25 μM)
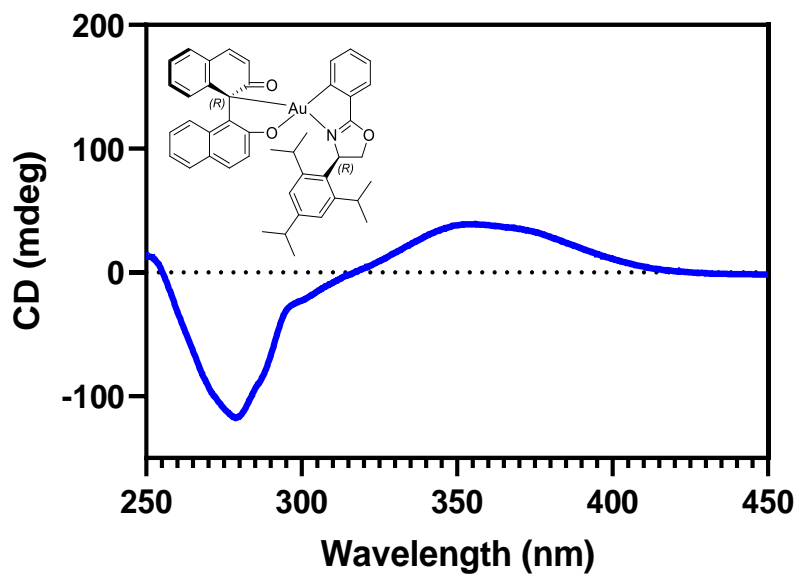
CD spectrum of (*R*,*S*)-2.3h in CH₃CN (25 μM)
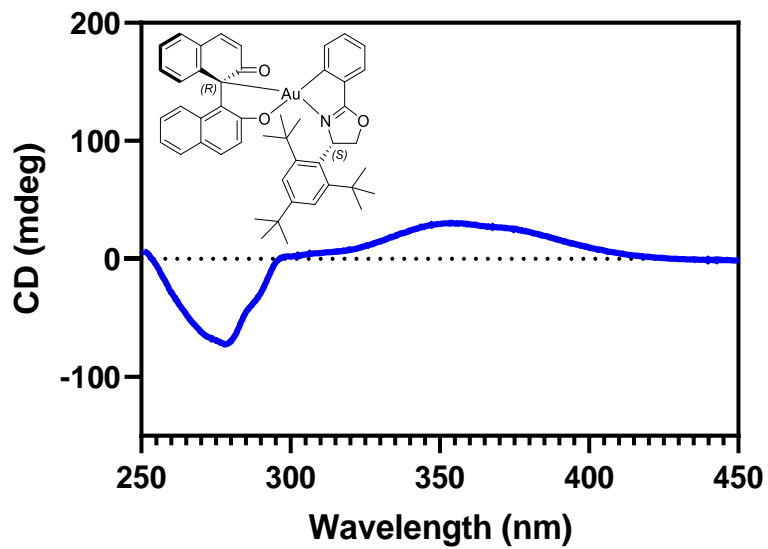
CD spectrum of (*R,R*)-2.3i in CH$_3$CN (25 µM)
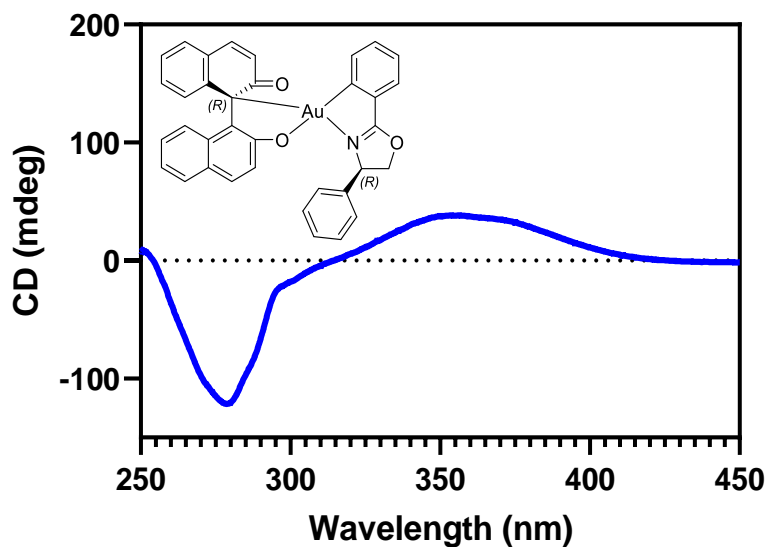
CD spectrum of (*R,R*)-2.3j in CH$_3$CN (25 µM)
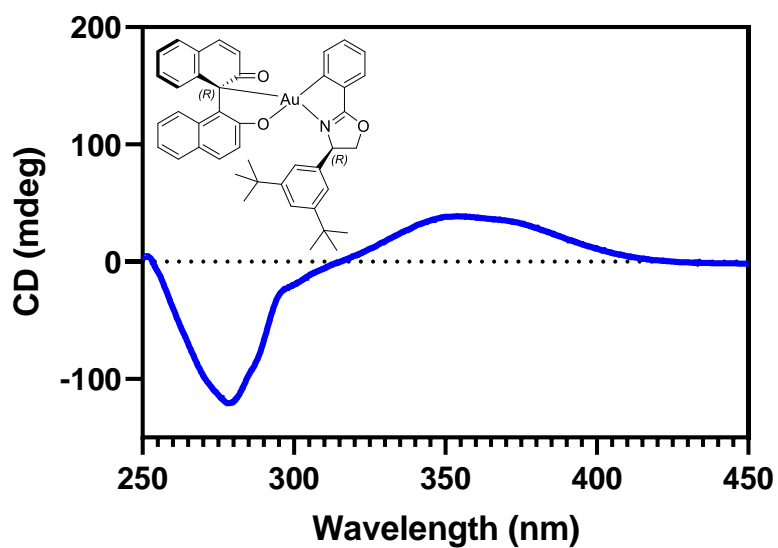
CD spectra of 2.5a in CH₃CN (50 µM)
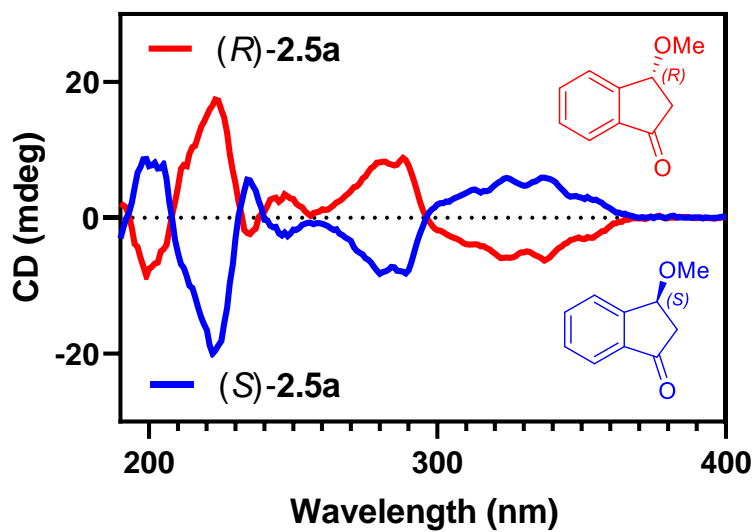
CD spectrum of 2.5b in CH₃CN (50 µM)
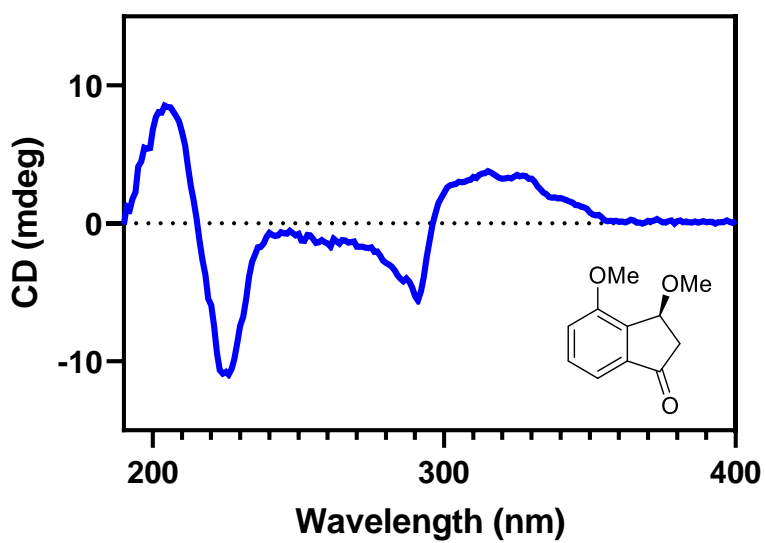
CD spectrum of 2.5c in CH$_3$CN (50 µM)
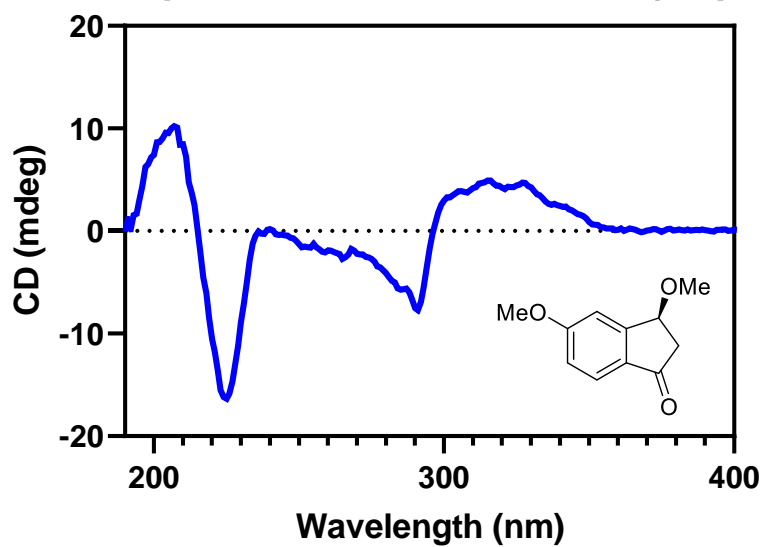
CD spectrum of 2.5d in CH$_3$CN (50 µM)
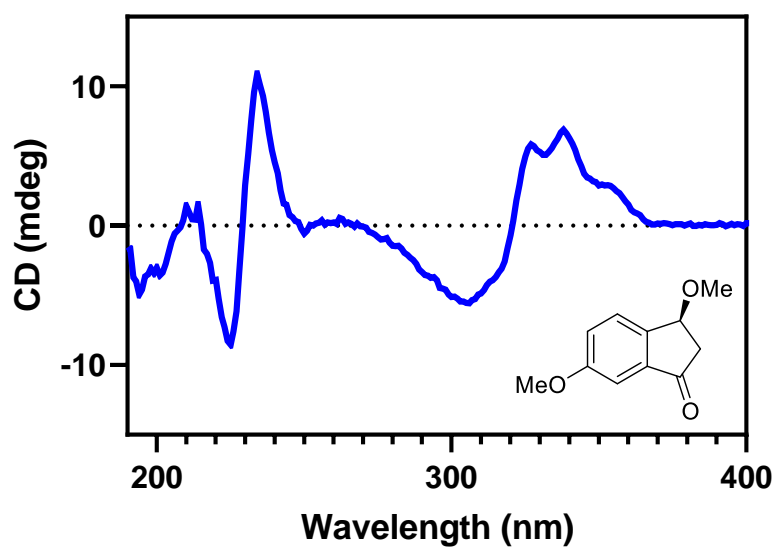
CD spectrum of 2.5e in CH₃CN (50 µM)
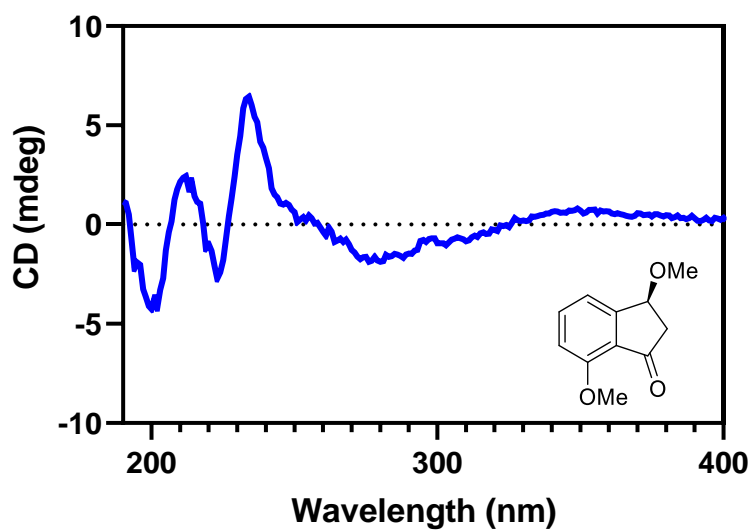
CD spectrum of 2.5f in CH₃CN (50 µM)
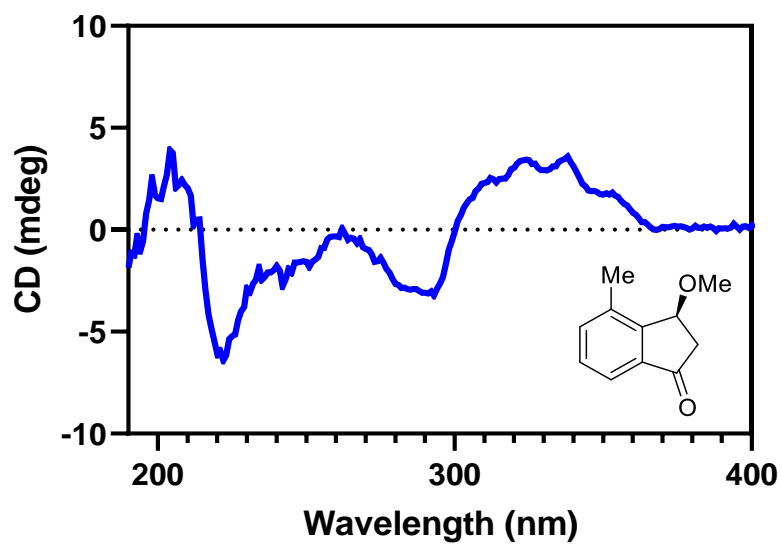
CD spectrum of 2.5g in CH$_3$CN (50 µM)
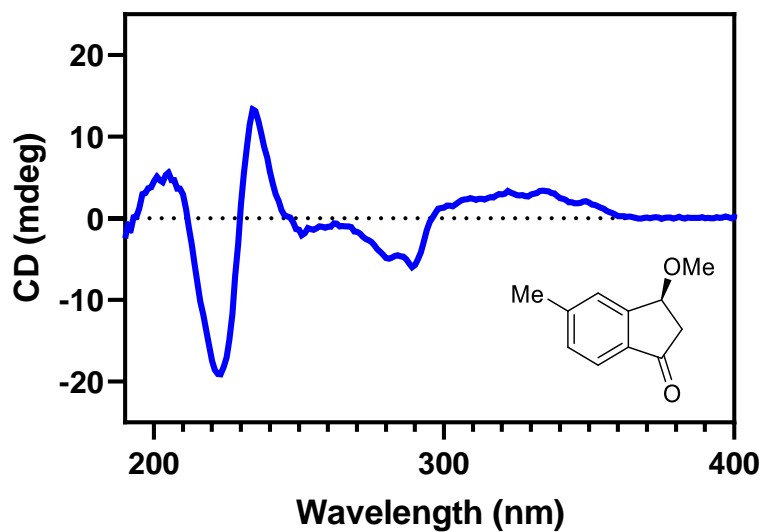
CD spectrum of 2.5h in CH$_3$CN (50 µM)
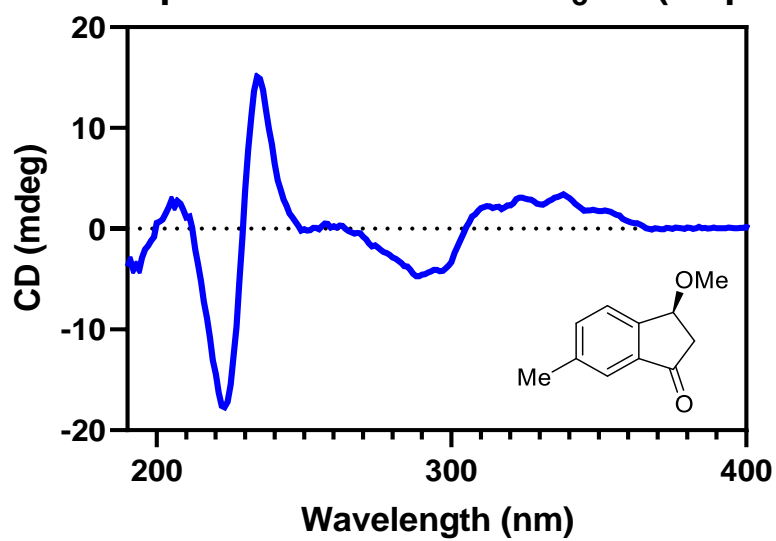
CD spectrum of 2.5i in CH₃CN (50 µM)
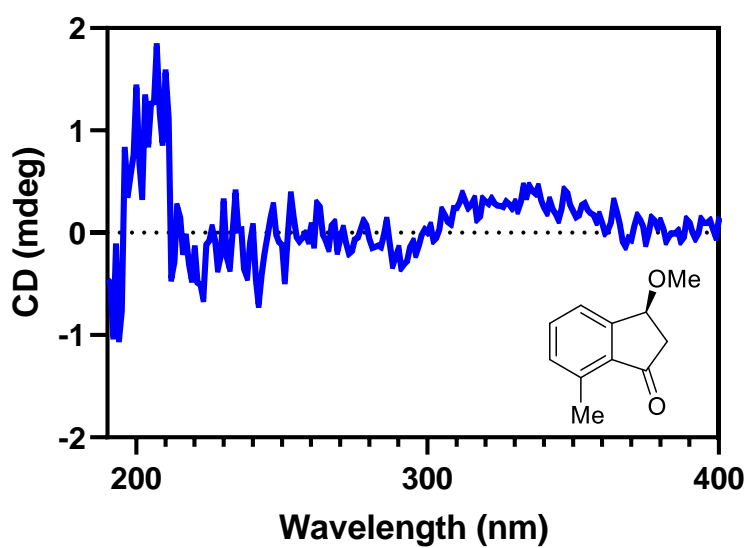
CD spectrum of 2.5j in CH₃CN (100 µM)
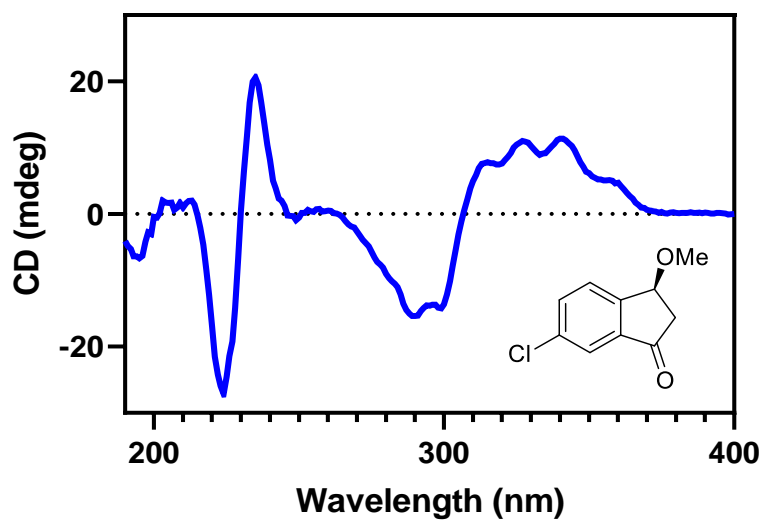
CD spectrum of 2.5l in CH₃CN (50 µM)
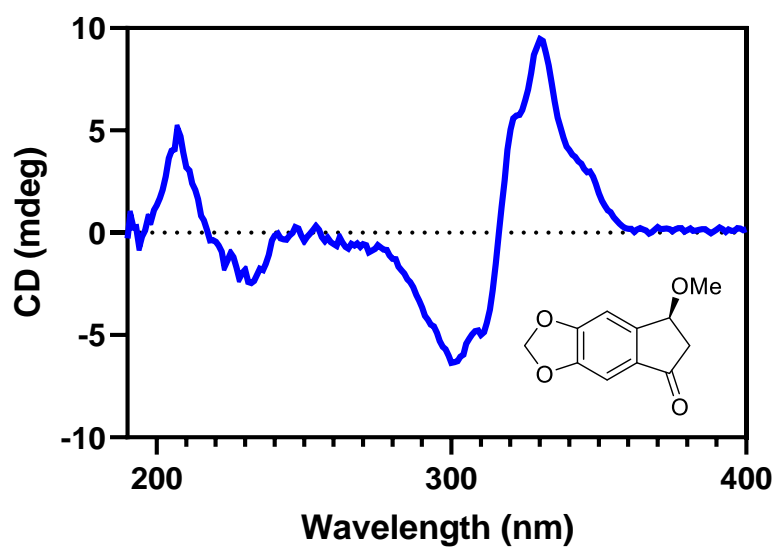
CD spectrum of 2.5m in CH₃CN (50 µM)

189
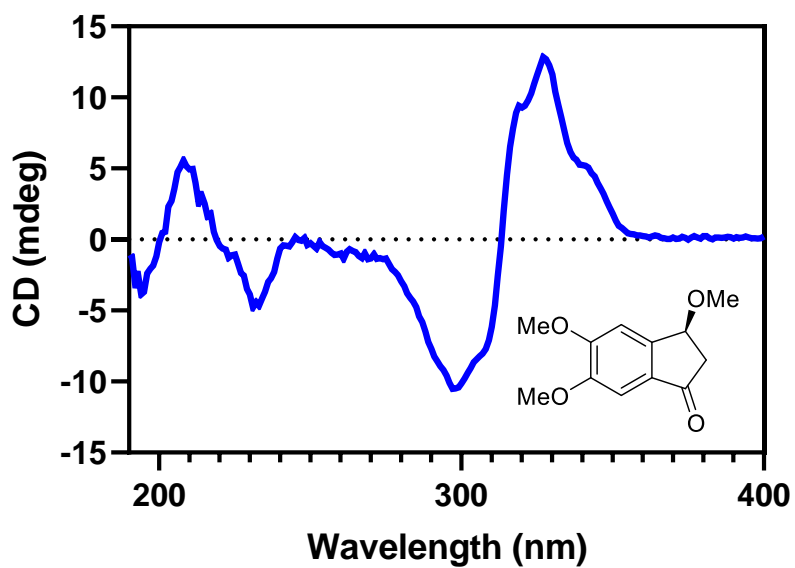
CD spectrum of 2.5p in CH₃CN (50 µM)
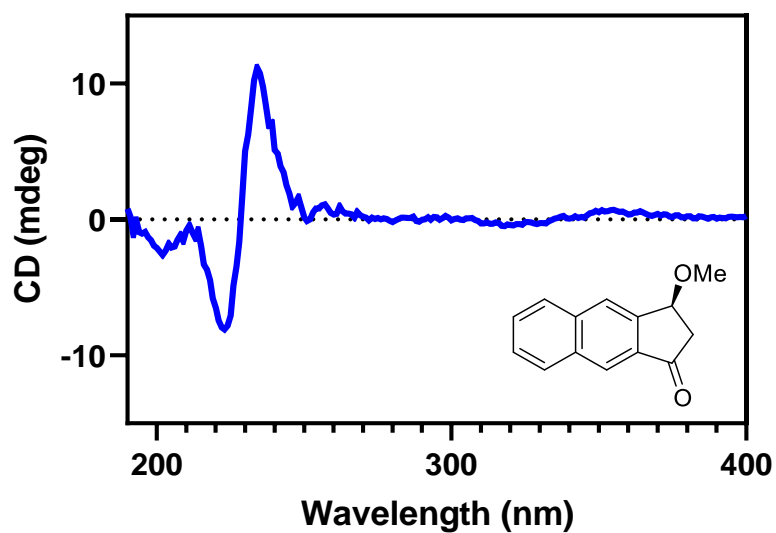
CD spectrum of 2.5q in CH₃CN (50 µM)
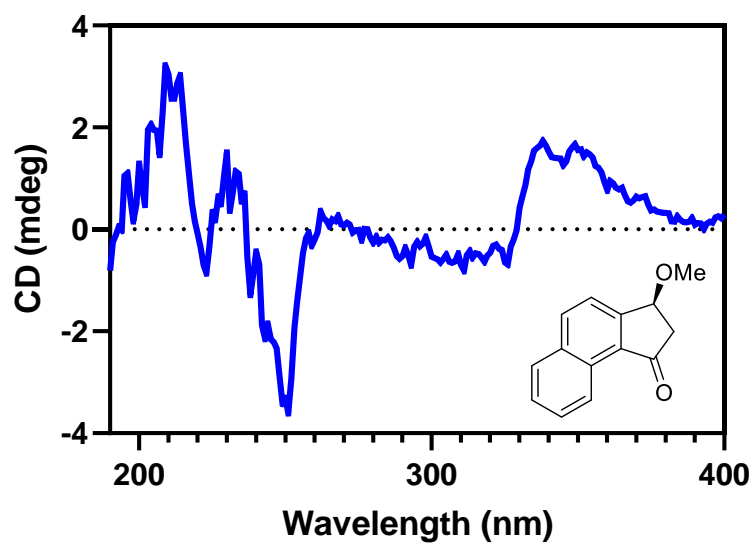
2.4.16 Chiral HPLC Spectra

2.5a
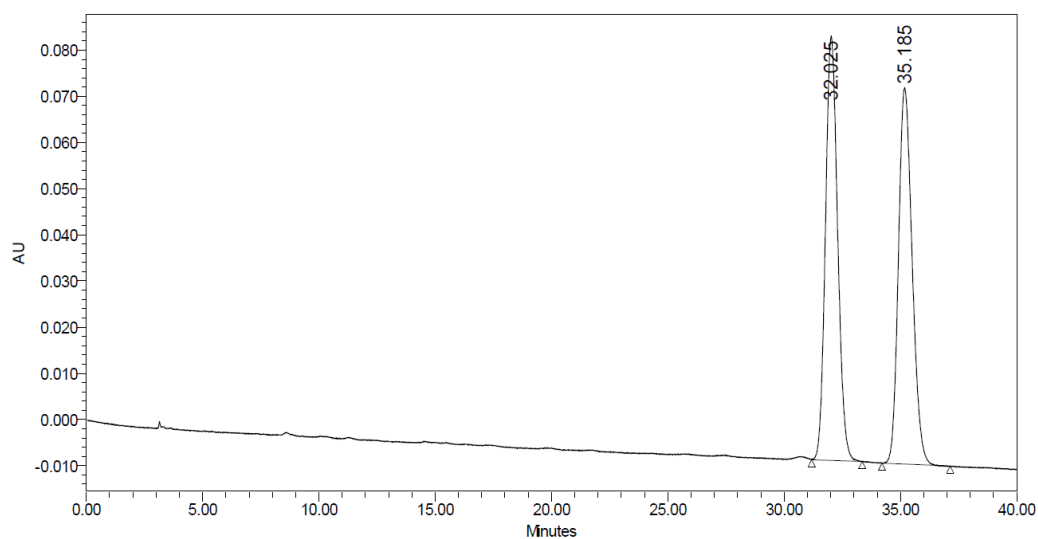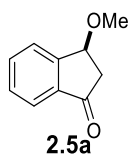
	RT	Area	% Area	Height
1	32.025	3335751	49.97	91905
2	35.185	3339876	50.03	81532
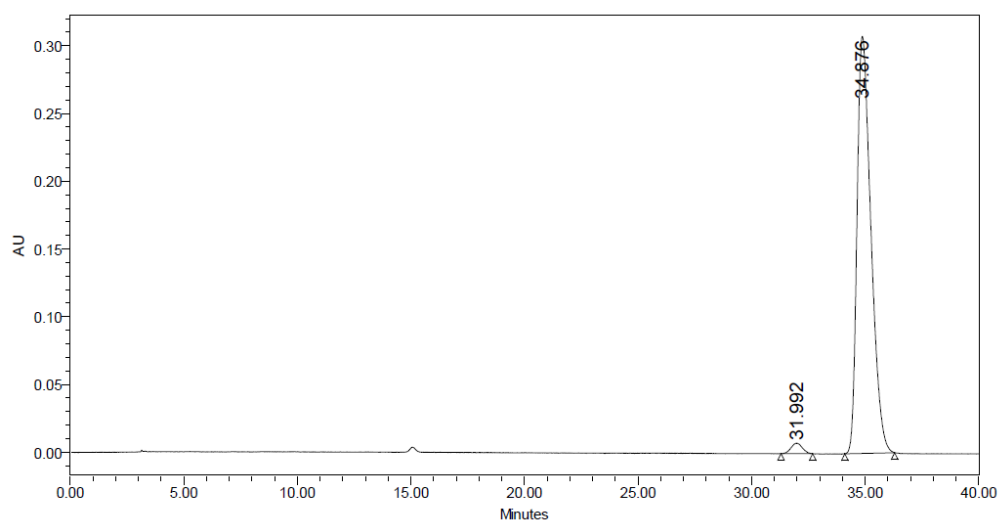
	RT	Area	% Area	Height
1	31.992	266726	2.00	7820
2	34.876	13090260	98.00	307810

2.5b
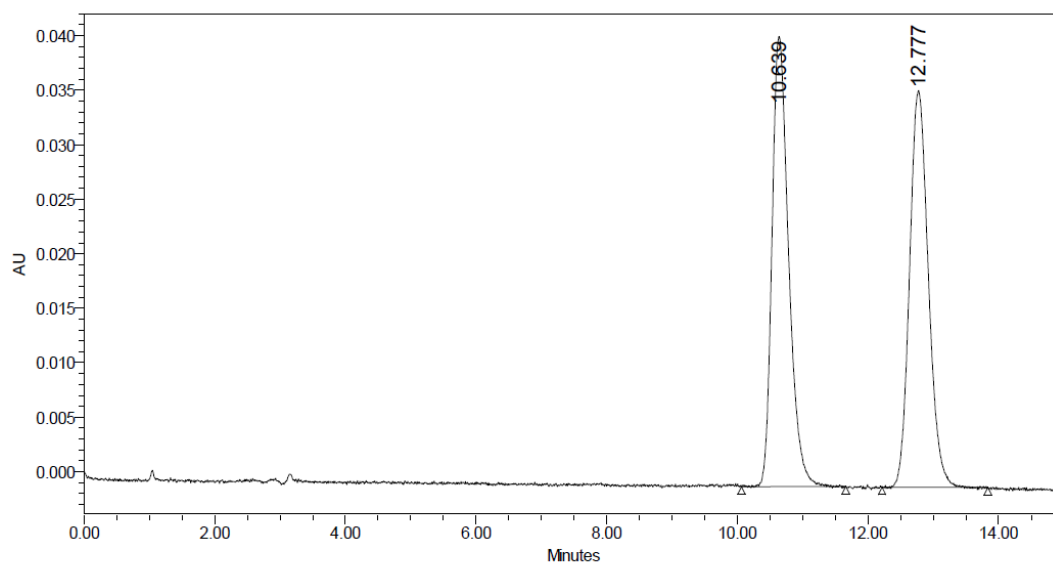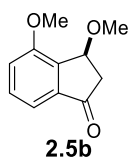
	RT	Area	% Area	Height
1	10.639	728809	50.10	41286
2	12.777	725877	49.90	36392
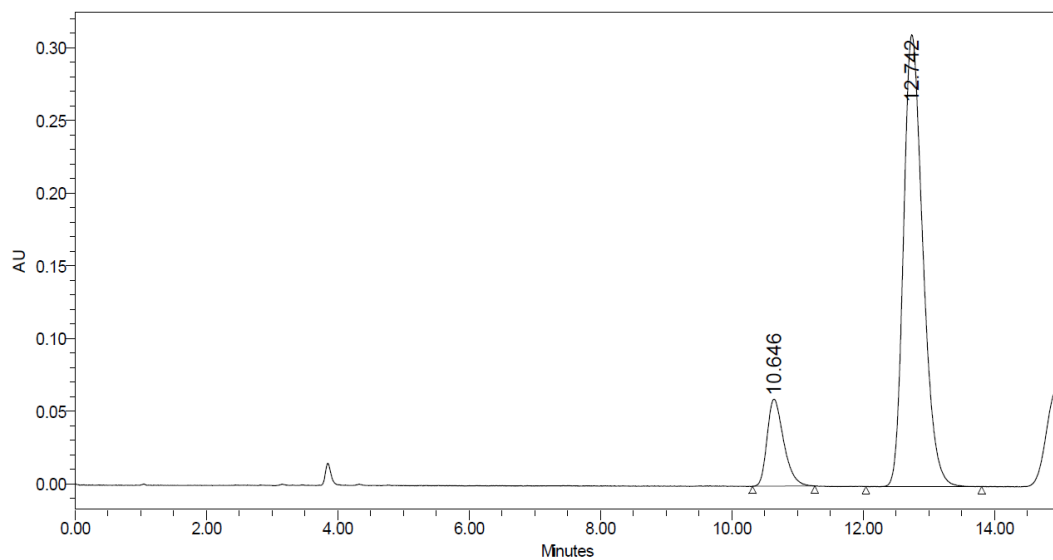
	RT	Area	% Area	Height
1	10.646	1045041	14.12	59786
2	12.742	6353486	85.88	310405

2.5c
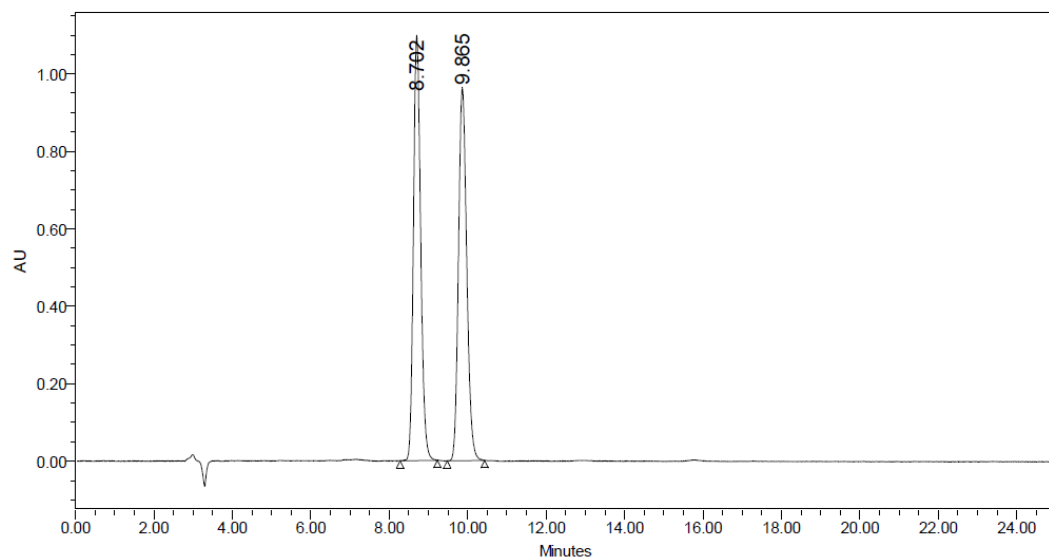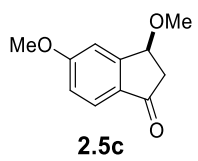
	RT	Area	% Area	Height
1	8.702	14067188	49.96	1097850
2	9.865	14090697	50.04	962786
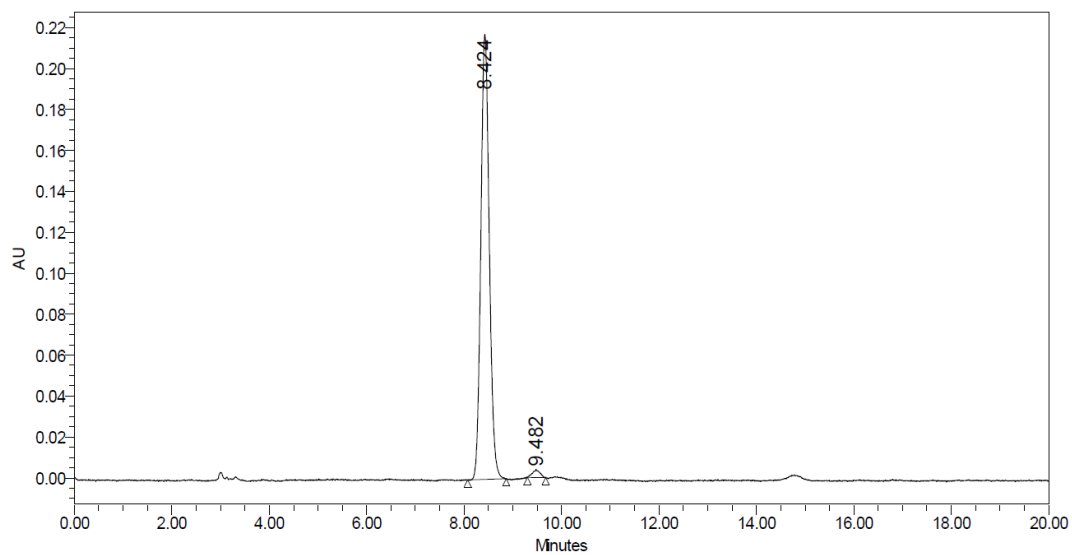
	RT	Area	% Area	Height
1	8.424	2606862	98.45	217243
2	9.482	41037	1.55	3822

193

2.5d
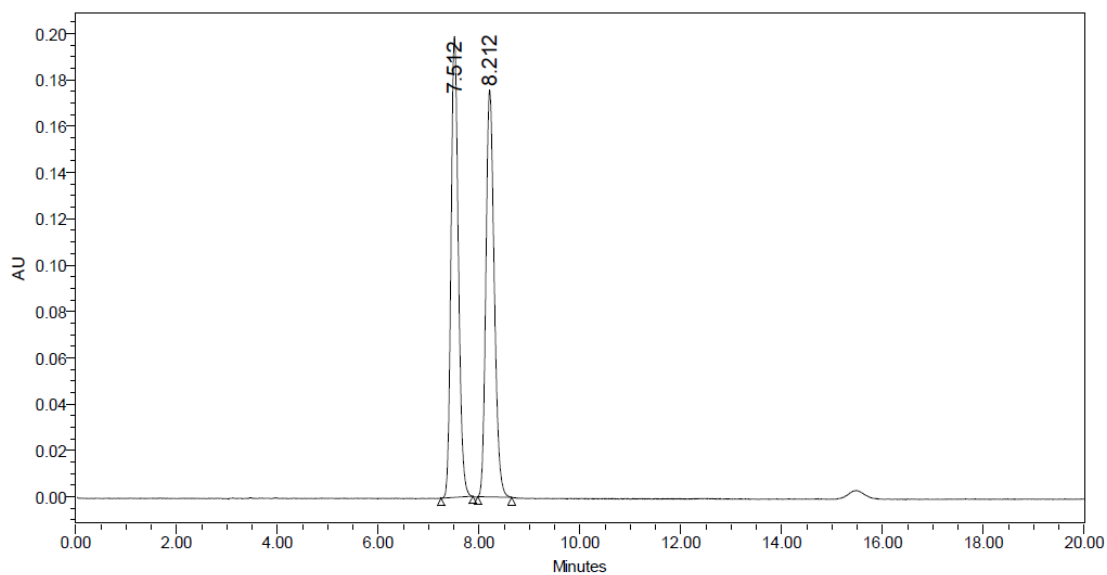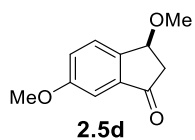
	RT	Area	% Area	Height
1	7.512	2017376	49.97	199046
2	8.212	2020108	50.03	175643
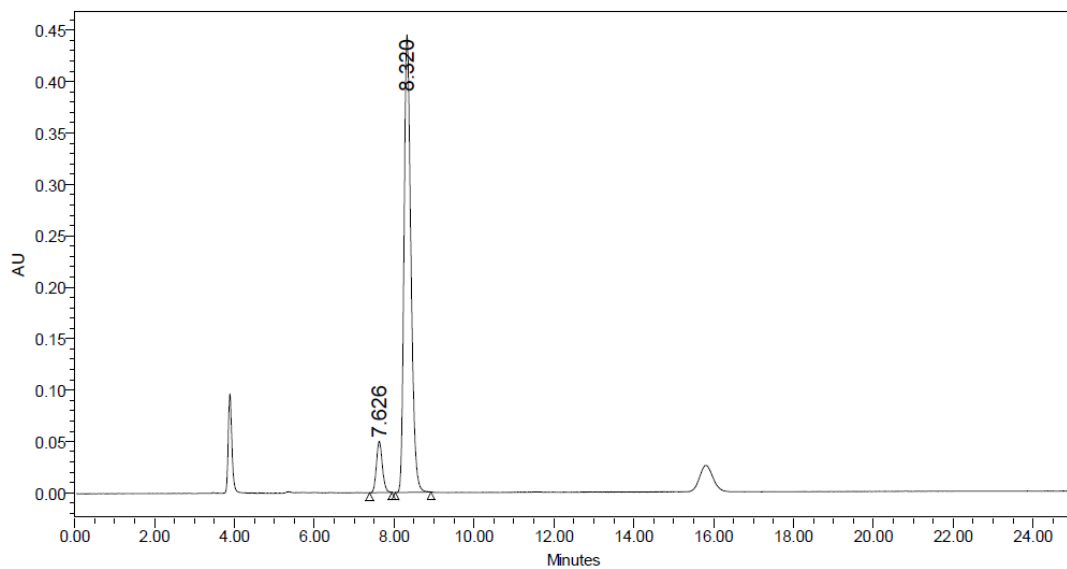
	RT	Area	% Area	Height
1	7.626	513803	8.80	49879
2	8.320	5322388	91.20	444969

2.5e
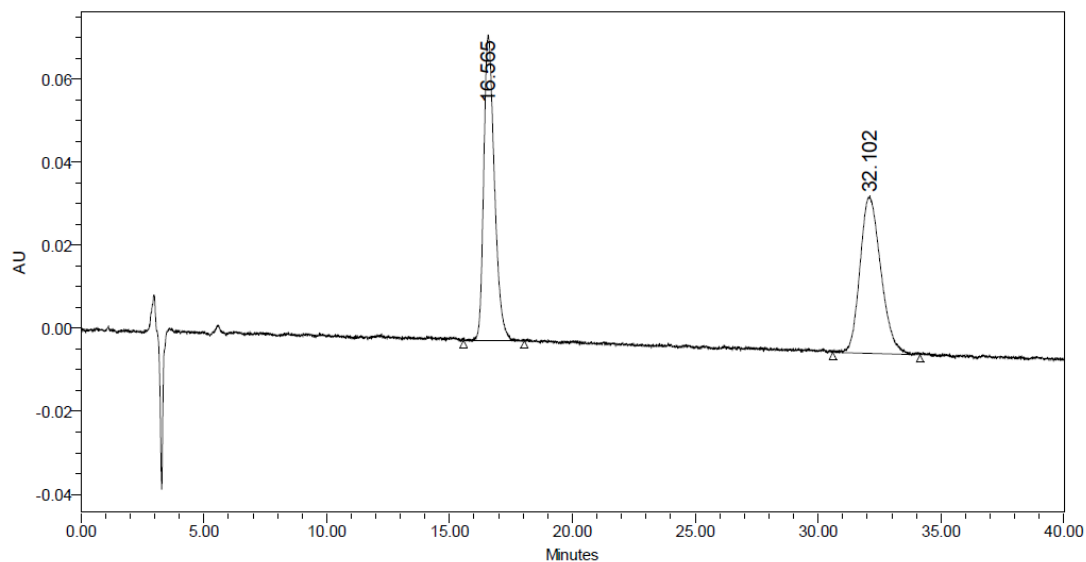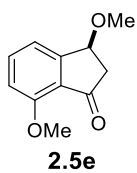
	RT	Area	% Area	Height
1	16.565	2215504	49.82	73561
2	32.102	2231404	50.18	37849
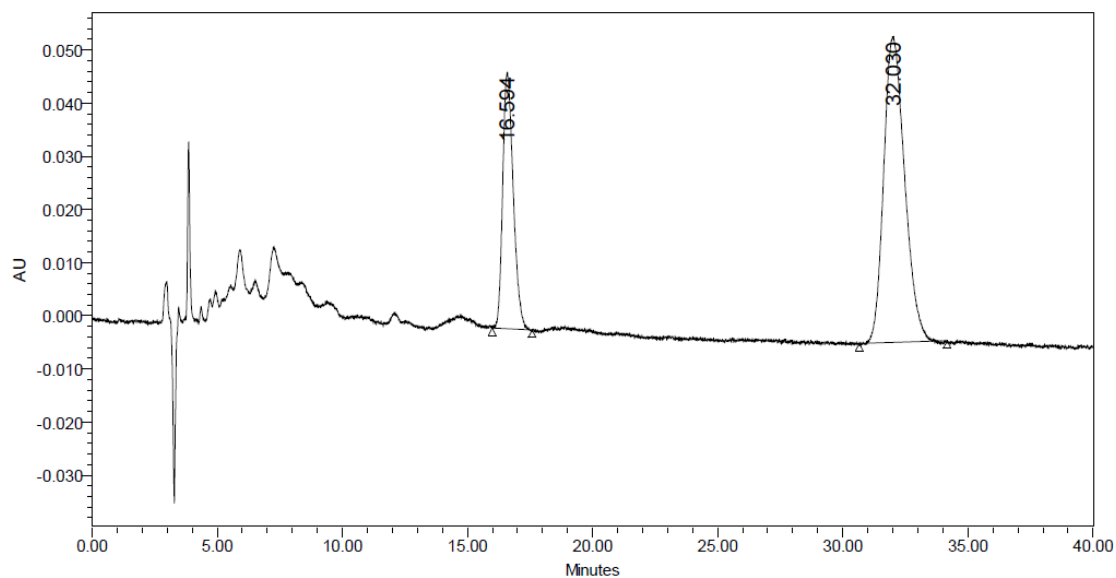
	RT	Area	% Area	Height
1	16.594	1413867	29.67	48268
2	32.030	3351940	70.33	57559

195

2.5f
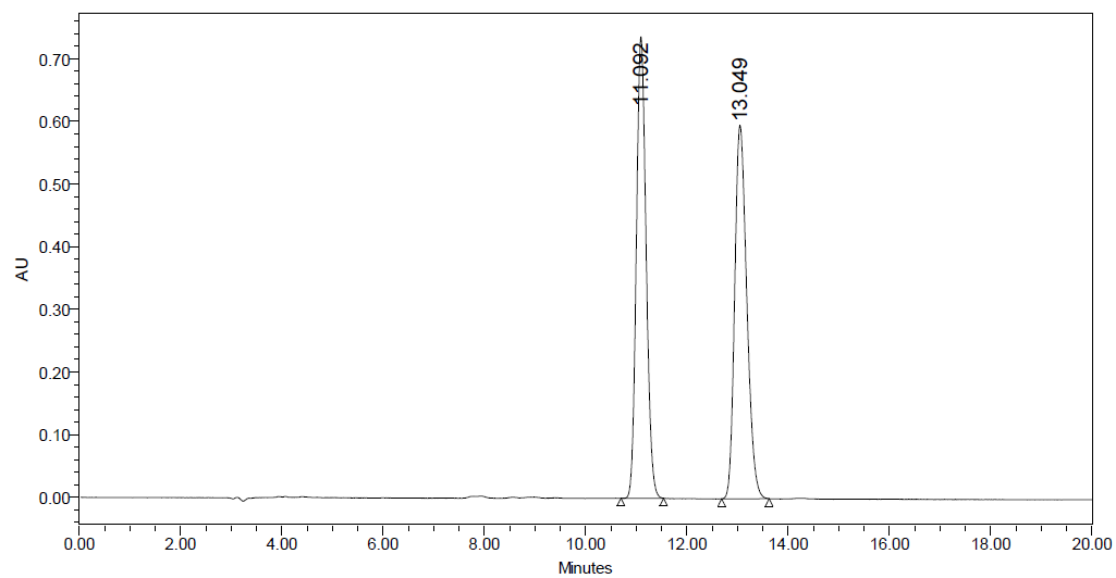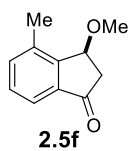
	RT	Area	% Area	Height
1	11.092	9868393	49.92	736806
2	13.049	9899020	50.08	595959
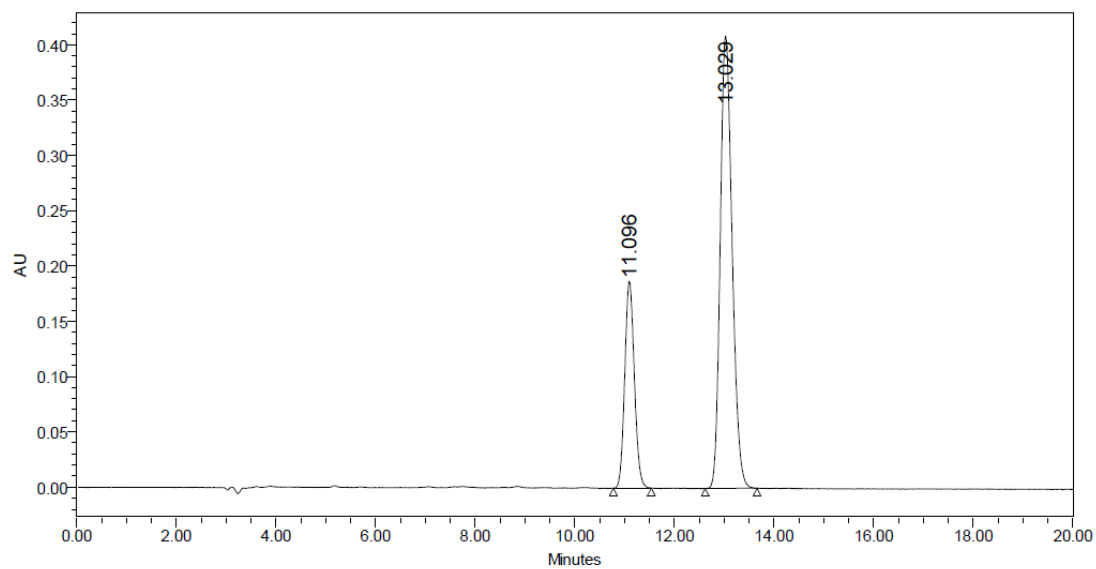
	RT	Area	% Area	Height
1	11.096	2497917	26.95	186921
2	13.029	6771027	73.05	409026

2.5g
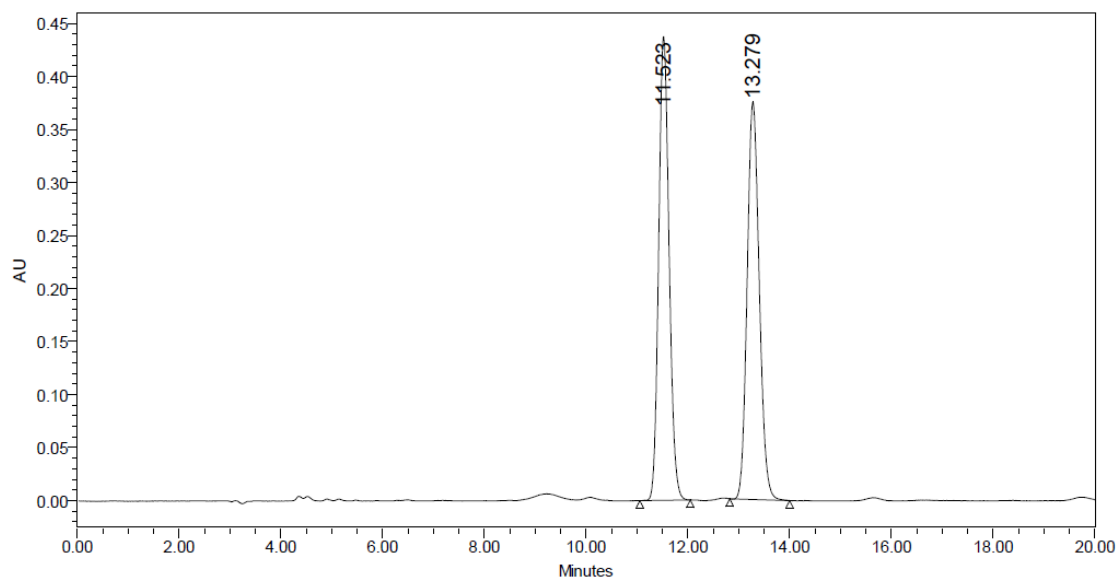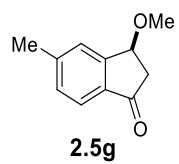
	RT	Area	% Area	Height
1	11.523	6209010	50.02	437394
2	13.279	6204488	49.98	375066
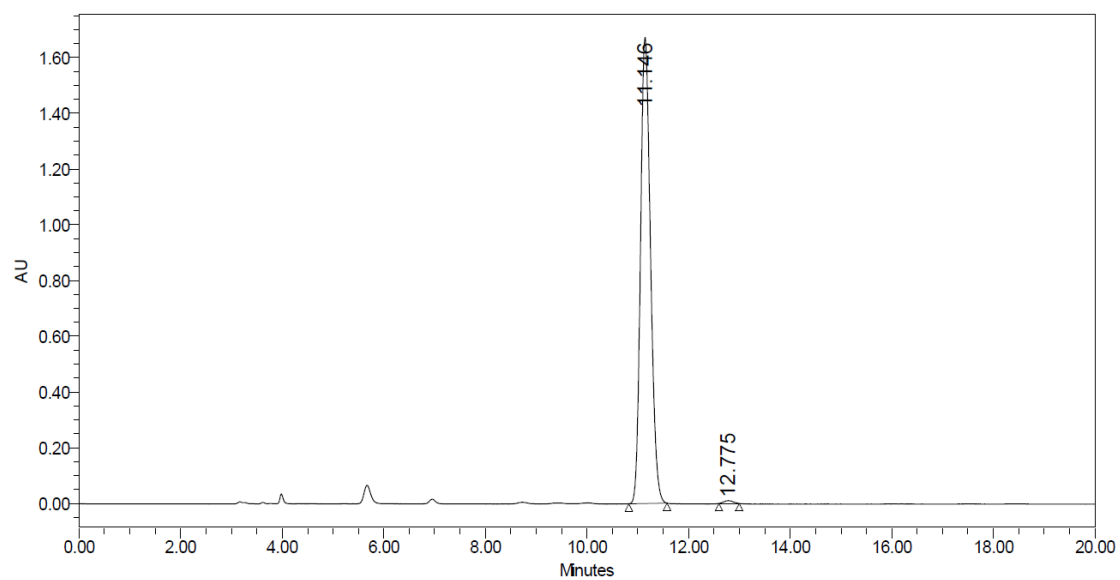
	RT	Area	% Area	Height
1	11.146	22756481	99.44	1670885
2	12.775	129130	0.56	10125

197

2.5h
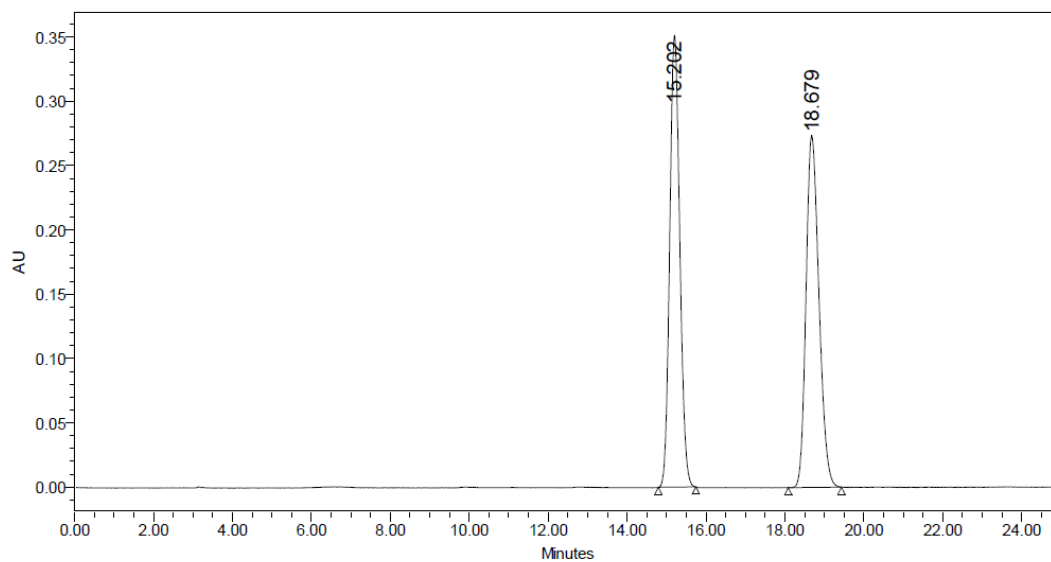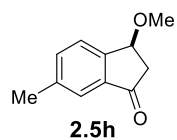
	RT	Area	% Area	Height
1	15.202	6216918	49.95	351253
2	18.679	6229821	50.05	273614
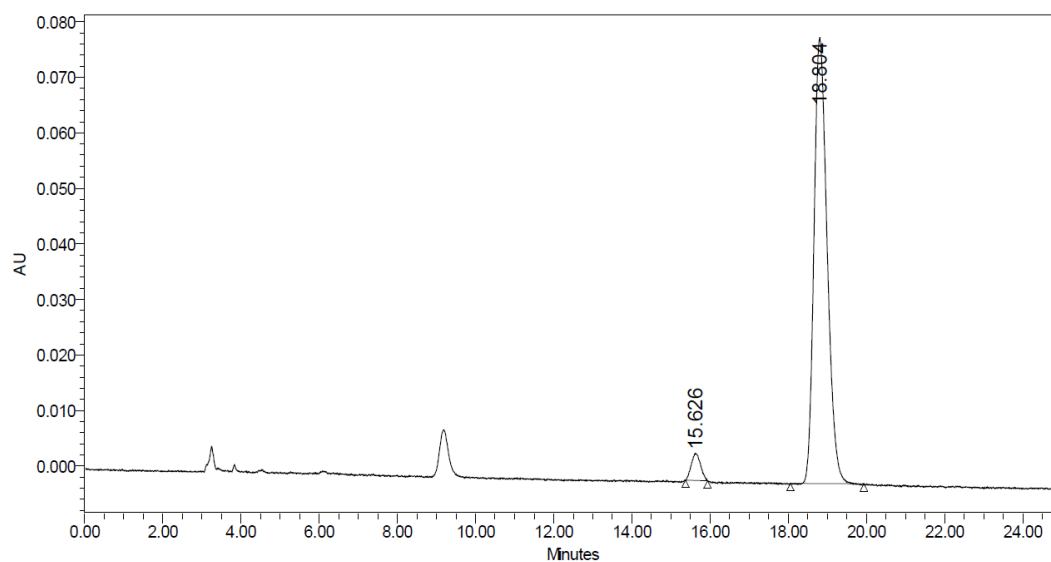
	RT	Area	% Area	Height
1	15.626	80493	4.12	4869
2	18.804	1870862	95.88	80325

2.5i
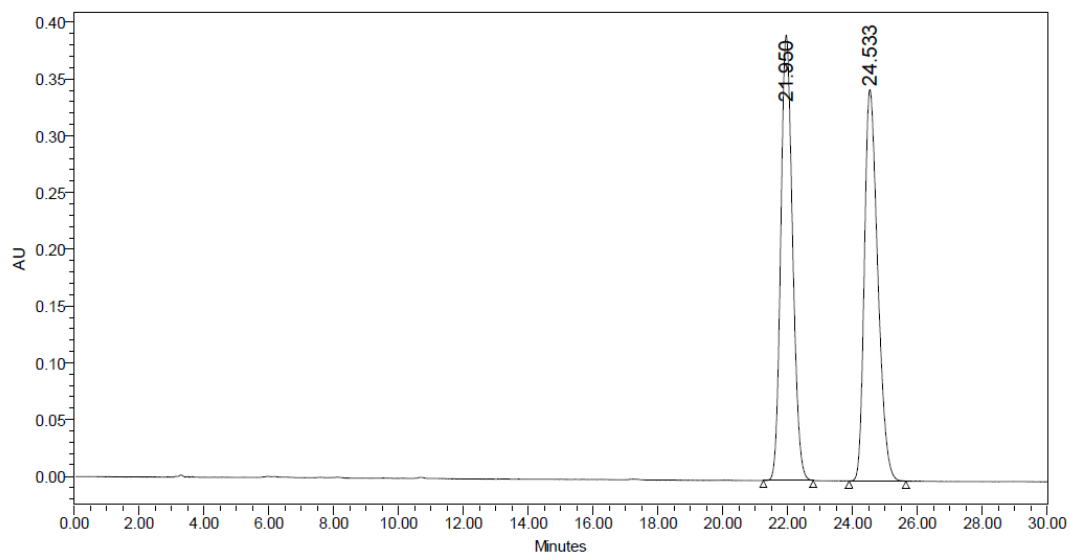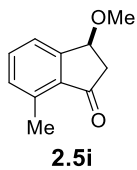
	RT	Area	% Area	Height
1	21.950	9882286	49.98	392346
2	24.533	9890811	50.02	344861
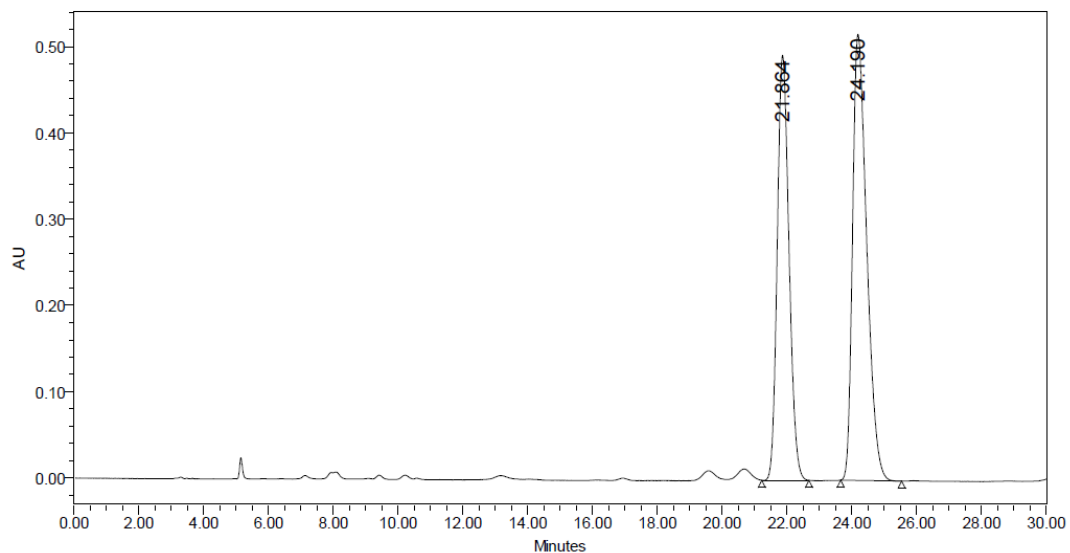
	RT	Area	% Area	Height
1	21.864	12420463	44.23	492907
2	24.190	15657952	55.77	517294

199

2.5j
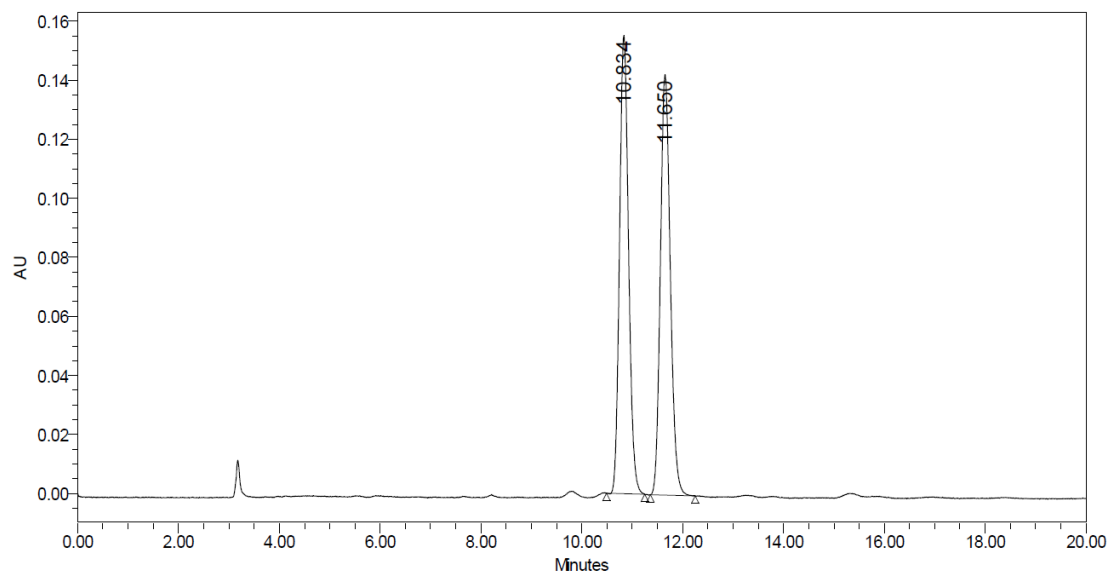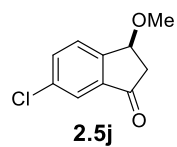
	RT	Area	% Area	Height
1	10.834	1926271	49.80	155179
2	11.650	1941972	50.20	142341
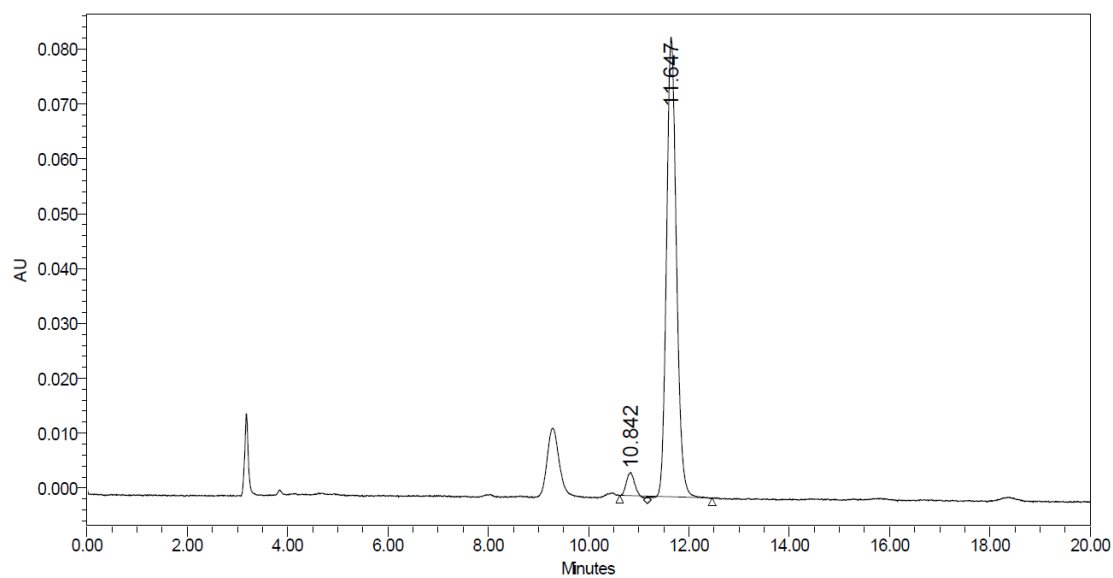
	RT	Area	% Area	Height
1	10.842	48848	4.08	4222
2	11.647	1148199	95.92	83746

200

2.5l
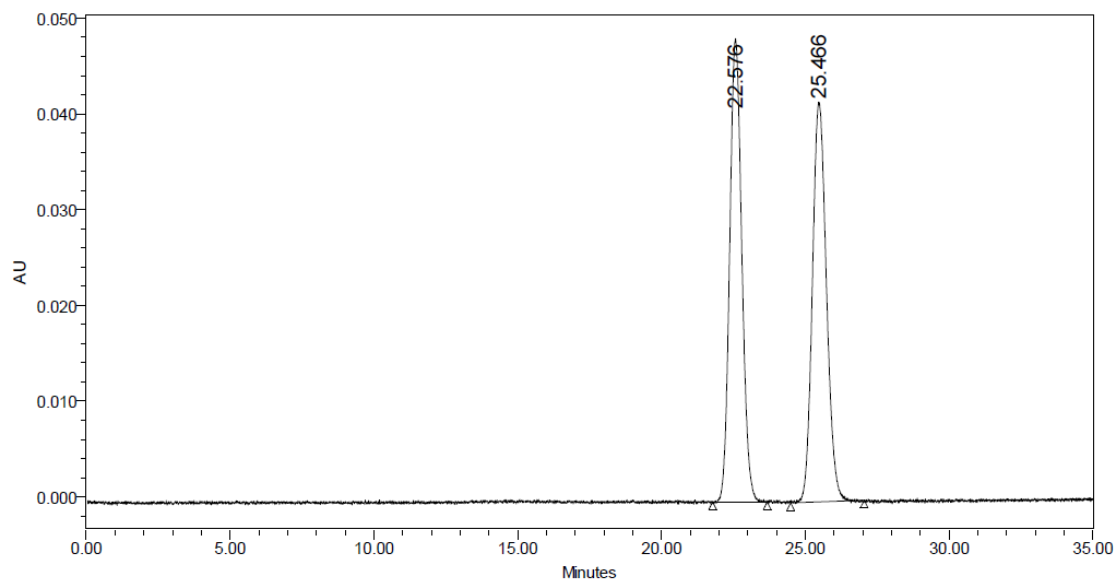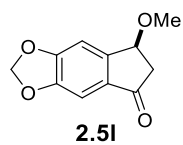
	RT	Area	% Area	Height
1	22.576	1414220	49.92	48379
2	25.466	1418849	50.08	41742
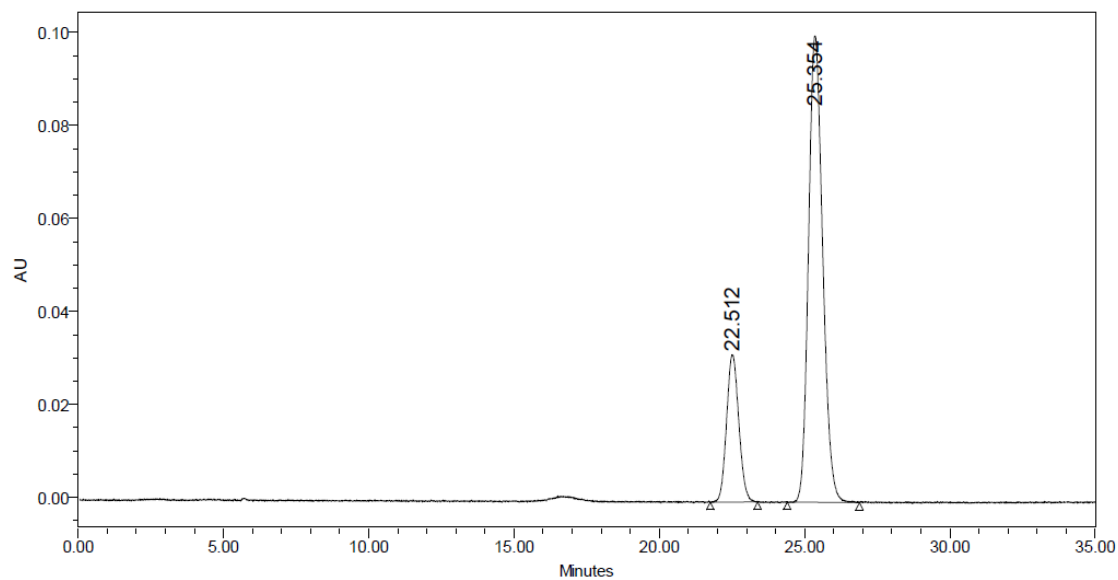
	RT	Area	% Area	Height
1	22.512	926649	21.42	31678
2	25.354	3398684	78.58	100307

2.5m
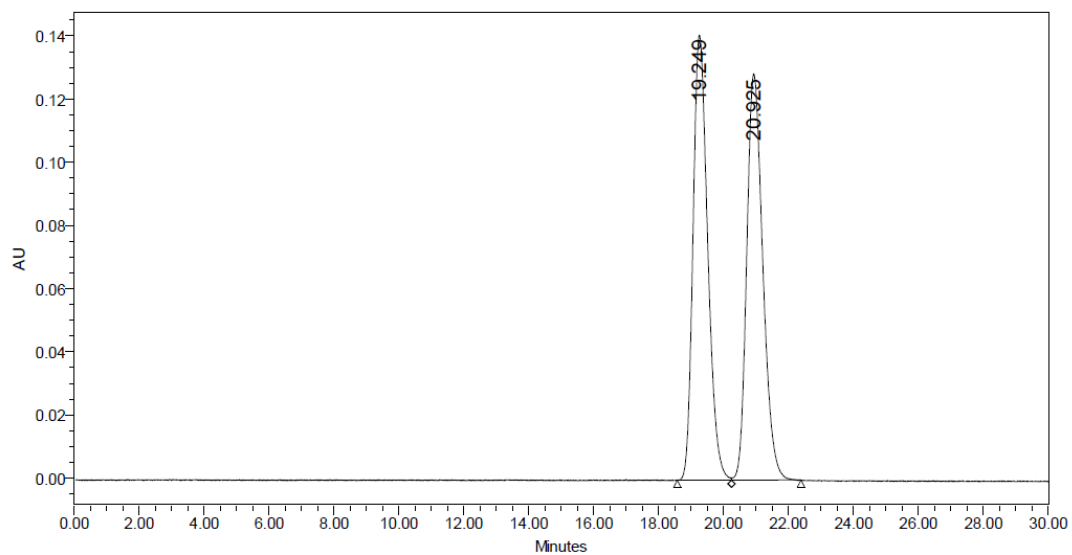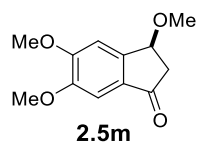
	RT	Area	% Area	Height
1	19.249	4413641	49.98	140948
2	20.925	4416559	50.02	128657
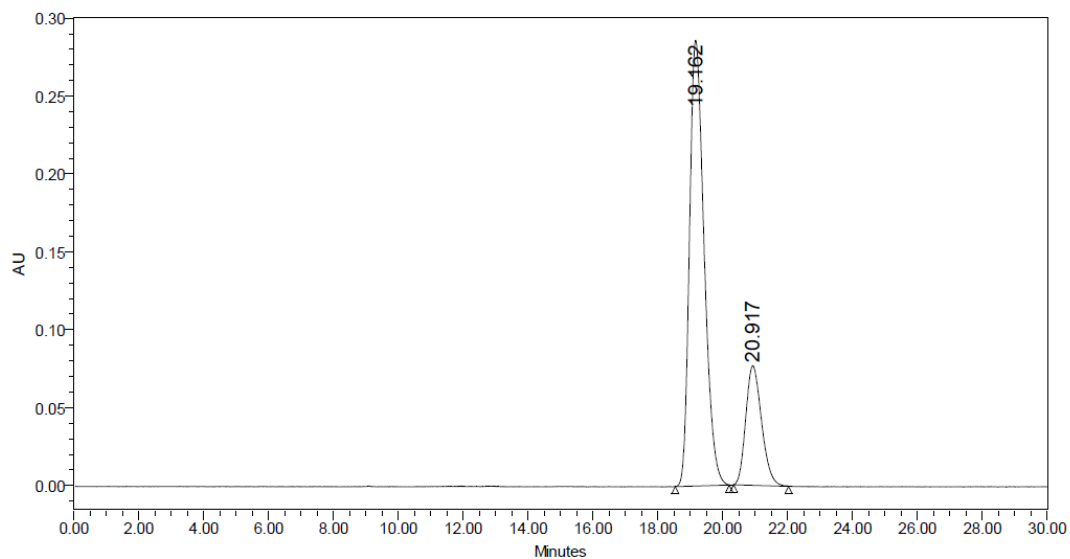
	RT	Area	% Area	Height
1	19.162	8949849	77.51	286188
2	20.917	2596948	22.49	76762

202

2.5n
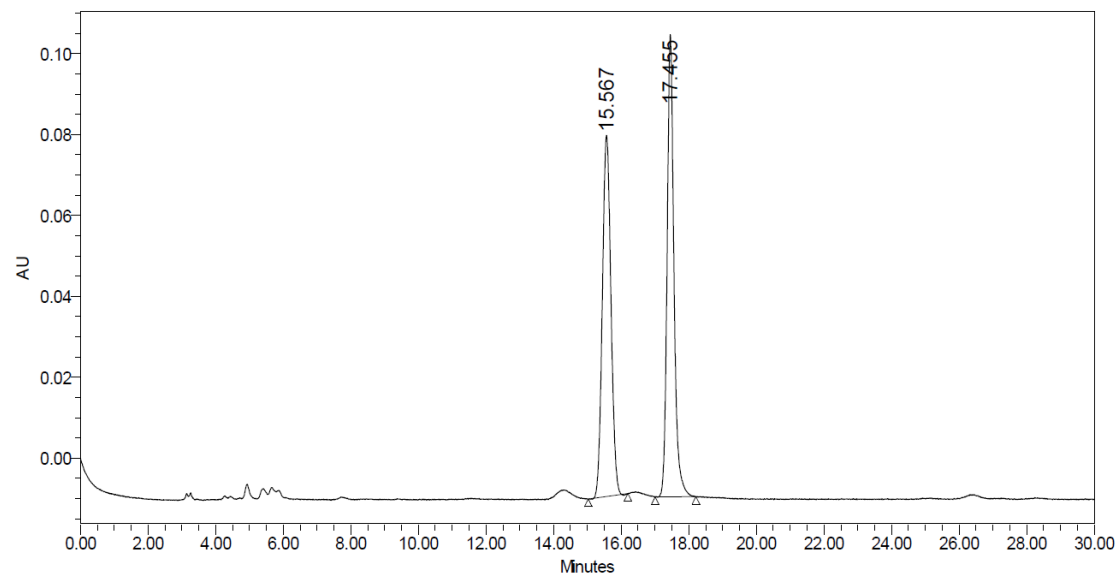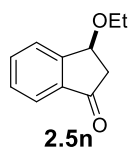
	RT	Area	% Area	Height
1	15.567	1575045	49.68	89313
2	17.455	1595096	50.32	114268
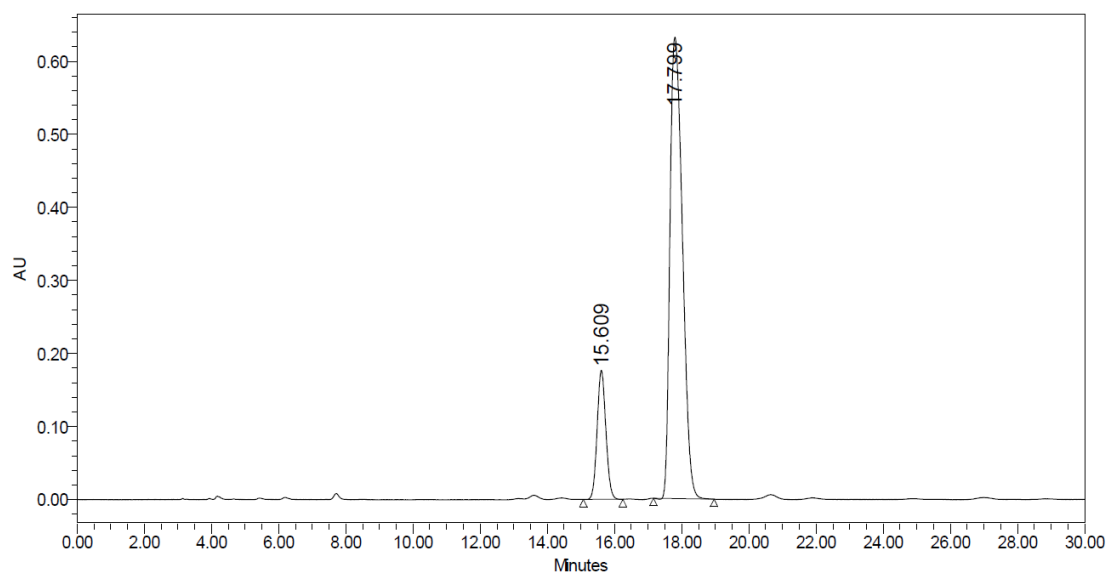
	RT	Area	% Area	Height
1	15.609	3183785	16.37	176664
2	17.799	16259591	83.63	631625

2.5o
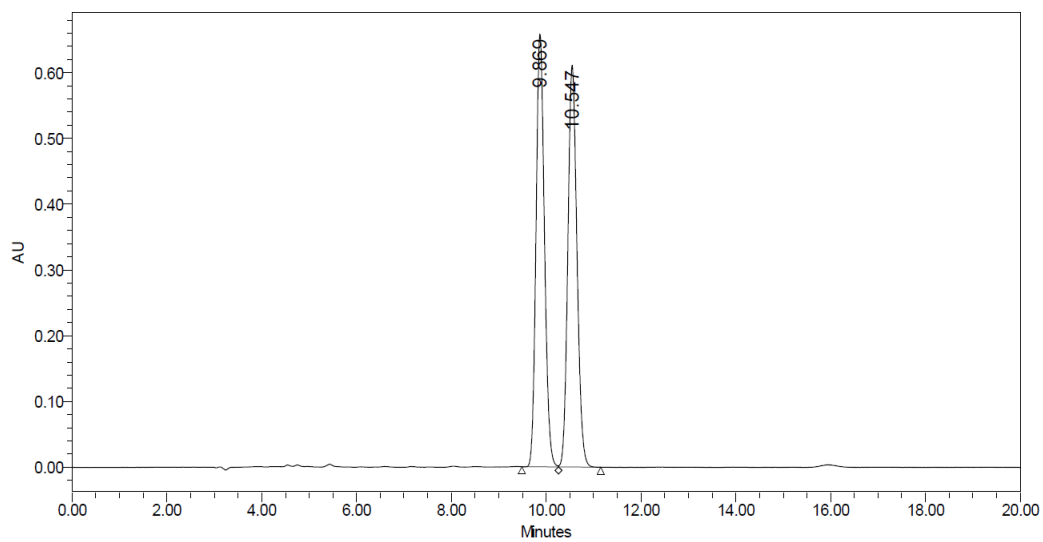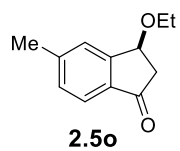
	RT	Area	% Area	Height
1	9.869	8106296	49.97	657677
2	10.547	8114833	50.03	610820
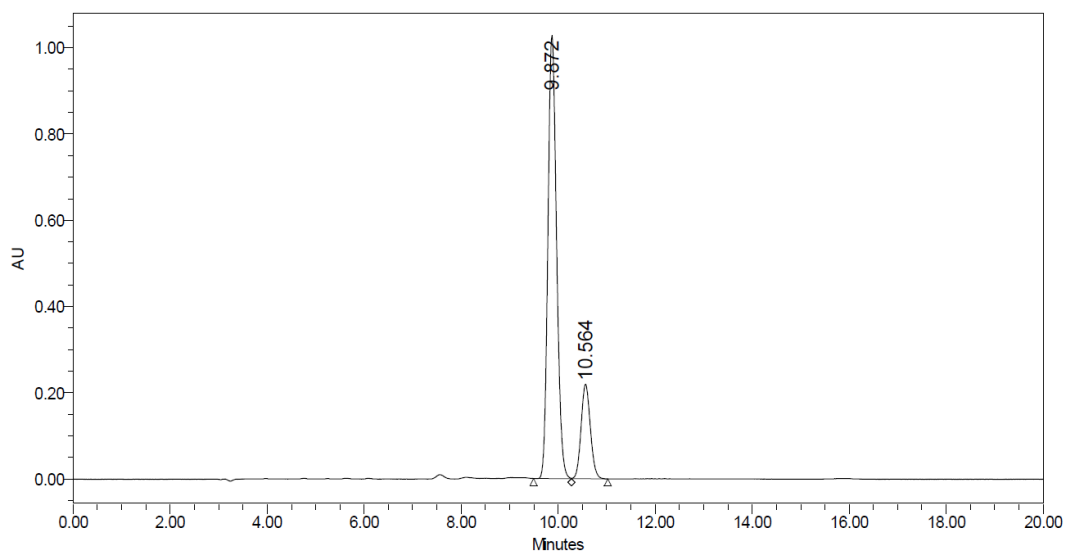
	RT	Area	% Area	Height
1	9.872	12719001	81.38	1027080
2	10.564	2909641	18.62	219077

2.5p
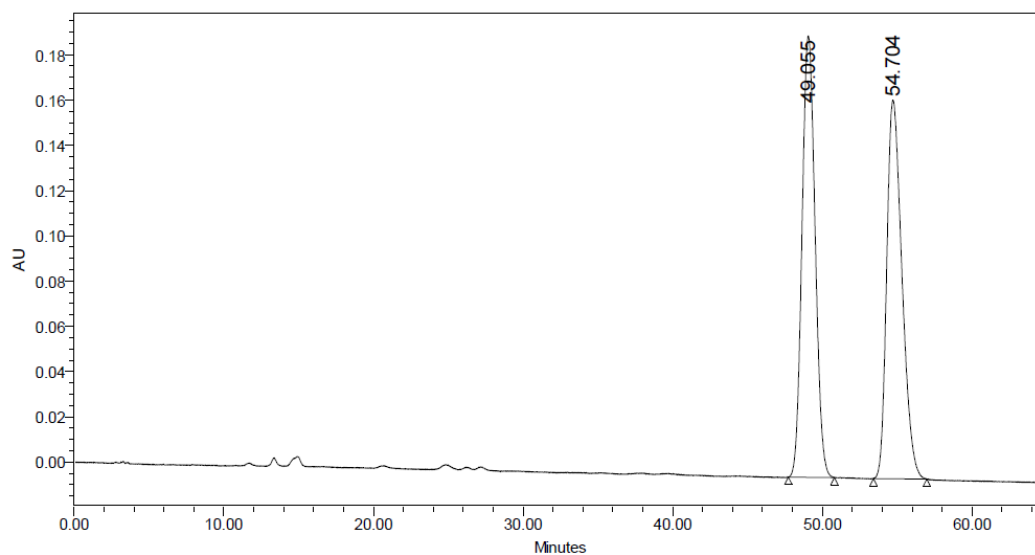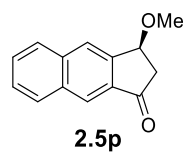
	RT	Area	% Area	Height
1	49.055	11844507	50.06	195124
2	54.704	11817601	49.94	167445
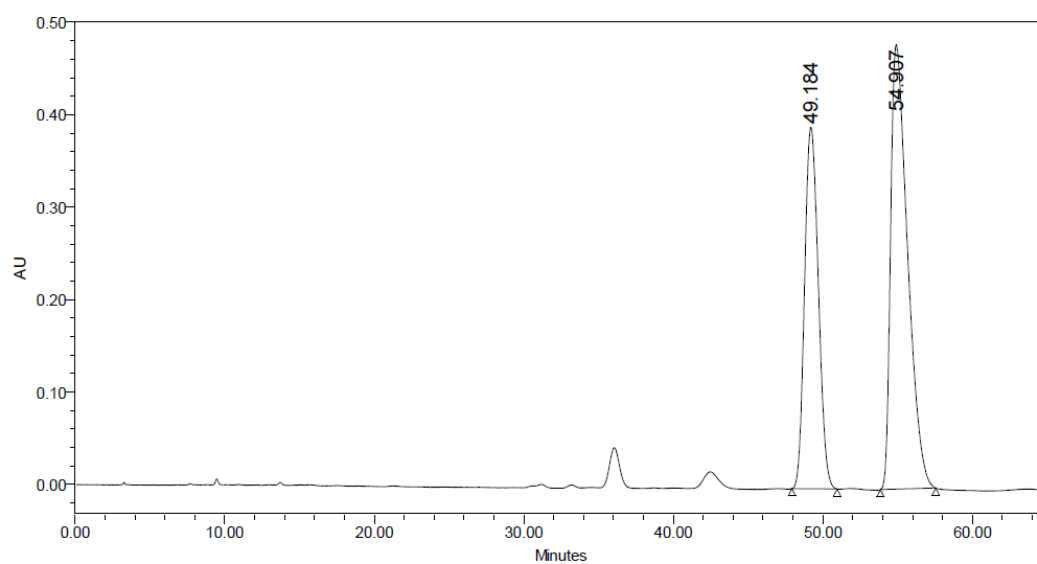
	RT	Area	% Area	Height
1	49.184	24992369	39.80	391142
2	54.907	37804338	60.20	480992

2.5q
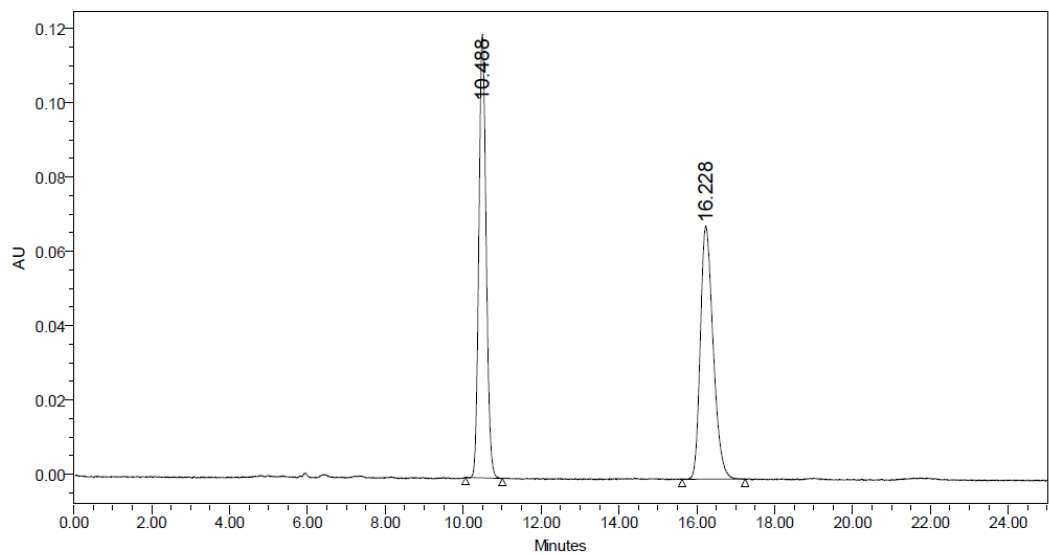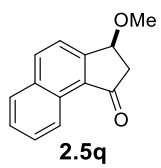
	RT	Area	% Area	Height
1	10.488	1553055	49.97	119407
2	16.228	1554911	50.03	68130
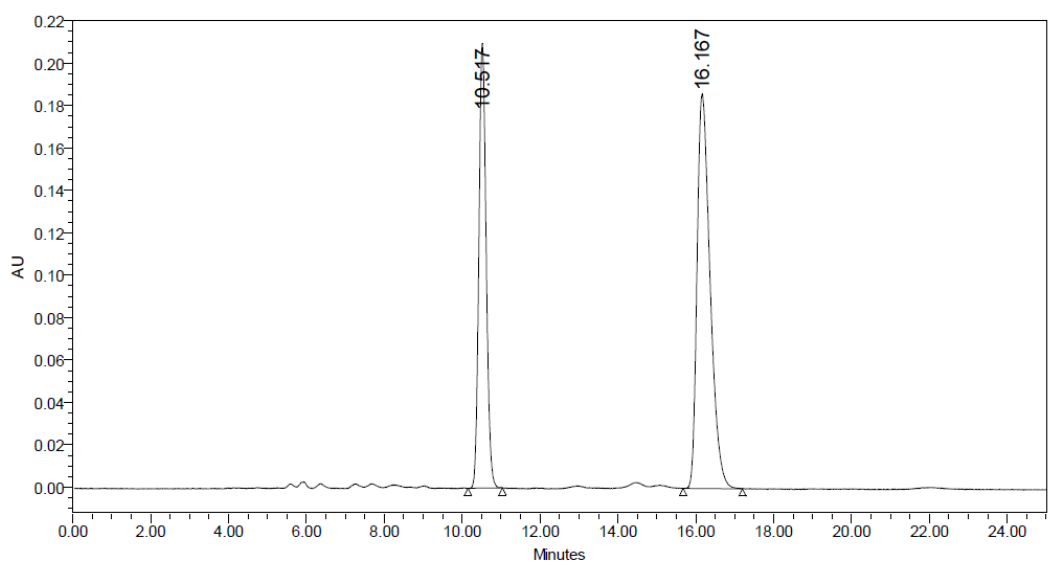
	RT	Area	% Area	Height
1	10.517	2731804	38.68	209786
2	16.167	4331282	61.32	186087

Chapter 3 Aqueous Supramolecular Assemblies of Luminescent Cyclometalated Gold(III) Amphiphiles with Biocompatibility

3.1 Introduction

Supramolecular assemblies are fundamental in forming the specific structure of biomolecules, which play a crucial role in biological functions.[81] Taking inspiration from natural systems, synthetic supramolecular assemblies are the alternative strategy mimicking the sophisticated structures and functions in nature, with the added advantage of exhibiting responsiveness to a range of abiotic stimuli,[82] such as pH and UV-light.[83] Amphiphiles are the common class of synthetic organic molecules since they bear hydrophilic and hydrophobic moieties leading to the intrinsic propensity to self-assemble in aqueous media.[84] Self-assembled organic amphiphiles in aqueous media have been substantially studied in the past few decades, including chromophore-based,[76a, 85] amino acid-based, and photoresponsive molecular amphiphiles.[82a, 86] As an alternative strategy to organic amphiphiles, metallosurfactants (or call metal-ligand amphiphiles) offer the structural diversity due to the variety of coordination modes and oxidation states of metal ions.[87] This inherent tunability of metallosurfactants afforded a powerful means of directing supramolecular interactions, thereby exerting precise control over the resulting supramolecular morphologies.[87a, d]

Gold(I) and gold(III) complexes are well-known for exhibiting exceptional aqueous stability as well as excellent luminescent properties, which are widely used in catalysis,[9r, 23g, 26a, 34-35] bioconjugation,[88] and optoelectronics.[63, 89] Beside, a few examples of gold complexes-based amphiphiles were reported since the first example demonstrated by Che

and co-workers in 2016 involving the use of C^N^C-cheleated cyclometalated gold(III) complexes attached to a long poly(ethylene glycol) chain. The amphiphilic nature of the complexes enabled the formation of nanoscale micelles for *in-vitro* phototoxicity.[55] In 2019, the same group reported the supramolecular assemblies of phosphorescent pincer-type gold(III) amphiphiles which were controlled kinetically in acetonitrile/water system.[56] In the same year, Yam reported a new class of tridentate C^N^C-chelated gold(III) amphiphiles showing intrinsic multiple responsiveness and self-assembled to nanostructures in both polar and non-polar media. Building upon these seminal works on cyclometalated gold(III) amphiphiles showing the high sensitivity to supramolecular transformations induced by slight changes in molecular structure,[55-56, 70, 90] our group reported the first example of reversibly supramolecular transformations of amphiphilic gold(III) complex controlled by counterion in aqueous system.[57] However, a comprehensive understanding of the luminescent properties and cytocompatibilities of these new class of gold(III) amphiphiles are not explored.

Building upon Yam's seminal work demonstrating the significant enhancement of ambient luminescence in cyclometalated gold(III) complexes through the incorporation of strongly σ-donating alkynyl ligands,[70, 91] this chapter demonstrated a novel series of luminescent and biocompatible gold(III) amphiphiles (GAs) with 2-phenylpyridine and alkynyl ligand in aqueous system. The amphiphilic nature of the gold(III) complexes arising from the hydrophilic charged quaternary ammonium ion connected with the hydrophobic cyclometalated gold(III) core by an alkyl-linker improved the aqueous solubility. Notably, the presence of strongly σ-donating alkynyl ligands coordinated to the gold(III) center exhibited the ambient luminescent properties. Besides, GAs self-assembled into nanostructure in aqueous media showing high aspect ratio. The reversible

supramolecular assembly transformation of GAs was observed by changing the packing parameters through counterion exchange process. Importantly, cytotoxicity studies demonstrate the biocompatibility of GAs at low concentrations, highlighting their potential for biological applications.
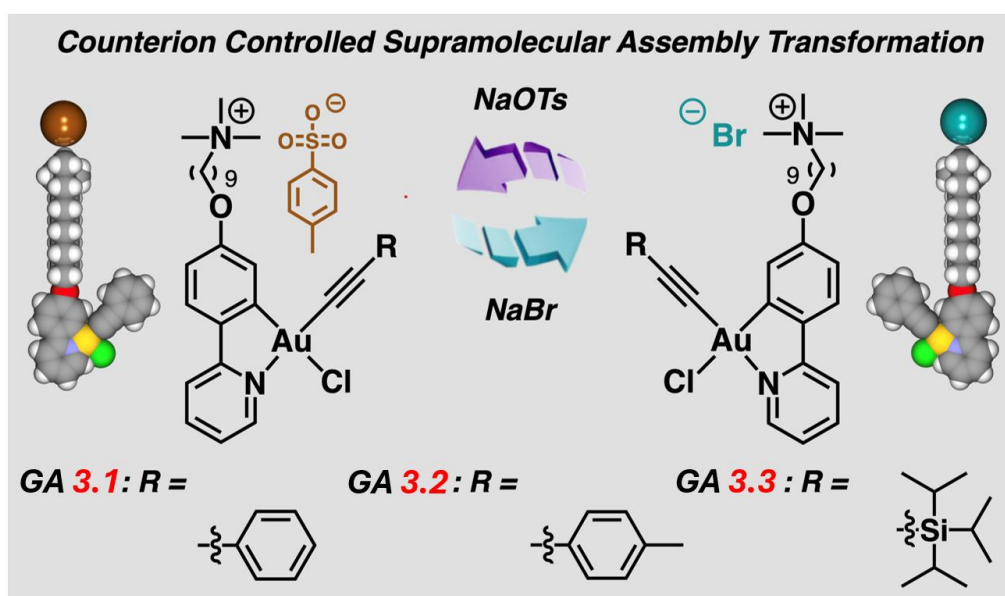
Scheme 3.1 Schematic illustration of the design of cyclometalated gold(III) amphiphiles.

3.2 Results and Discussion

3.2.1 Design and Synthesis of GAs

GAs were designed to exhibit the amphiphilicities and luminescent properties. The amphiphilic character of the GAs arose from the incorporation of both hydrophilic and hydrophobic moieties within the molecular structure. A hydrophilic quaternary ammonium ion was tethered to a hydrophobic cyclometalated gold(III) moiety through a nonyl aliphatic linker, imparting amphiphilicity.

The amphiphilic nature of GAs was introduced by connecting a hydrophilic quaternary ammonium ion motif through an aliphatic nonyl-linker to the hydrophobic cyclometalated gold(III) core, while the luminescent properties was functionalized by a σ-donating alkynyl ligand (Scheme 3.1). Notably, the alkynyl ligand could extend the conjugated system through the gold(III) center resulting in the decrease in aqueous solubilities as well as the difficulties in supramolecular assemblies. Hence, the current design involved the mono-alkynyl ligand instead of di-alkynal ligand. The detailed synthetic method of alkynyl gold(III) amphiphiles **GA 3.1**, **3.2**, and **3.3** was shown in the Experiment Section. GA precursor **S3.1** was first prepared in good yield according to the previously reported procedure.[69j, k, 92] By incorporating the alkynes reagents **S3.2** to the amphiphilic gold(III) dichloride precursor **S3.1**, a class of alkynyl gold(III) amphiphiles **GA 3.1**, **3.2**, and **3.3** was synthesized with 29 – 46% yield. These newly prepared GAs were characterized through ^{1}H NMR, ^{13}C NMR and HRMS (see details in Experimental Section).

3.2.2 Luminescent Properties and Counterion Controlled Supramolecular Assemblies Transformations of GA 3.1

To investigate the self-assembly and photophysical properties of **GA 3.1** in aqueous system, a 11.6 mM (1.0 weight%) solution of **GA 3.1** was subjected to a thermal annealing process, involving heating to 50 °C followed by slow cooling to 20 °C at a rate of 1.0 °C/min. Dynamic light scattering (DLS) analysis of the annealed solutions at various concentrations (0.01 - 1.0 mM) revealed a critical aggregation concentration (CAC) of 50 mM (Figure S3.1). UV-Vis absorption spectroscopy of a annealed solution of **GA 3.1** (400 μM) displayed an increase in the absorption maximum at 355 nm upon cooling, accompanied by a bathochromically shifted shoulder band at approximately 450

nm (Figure 3.1a, red-line). Luminescence measurements necessitated a higher concentration of **GA 3.1** (1.0 mM), with the emission spectrum exhibiting a broad band range of 470-600 nm upon excitation at 360 nm (Figure 3.1b). The vibronic structured emission band observed between 470 and 520 nm could be attributed to the intraligand excited state of the cyclometalated ligand.[69k, 70, 90b-d, 91] UV-Vis absorption spectrum of **GA 3.1** in a 1:1 DCM/MeOH mixture (Figure S3.2a) displayed an absorption maximum at 355 nm with the absorption band at 300 – 390 nm. In contrast to the emission spectrum of **GA 3.1** in organic media, the aqueous solution exhibited a significant enhancement in the emission intensity between 420 and 600 nm (Figures 3.1b and S3.2b). Control experiments using the GA precursor **S3.1** revealed negligible luminescence in aqueous solution, even at high concentrations (Figure S3.3), highlighting the crucial role of the strongly σ-donating alkynyl ligand in promoting luminescence in **GA 3.1**.

The supramolecular nanostructure of **GA 3.1** in aqueous solution was investigated using negative-stain transmission electron microscopy (TEM). The TEM image showed the supramolecular nanofibers with ~ 9 nm in diameter and ~ 100 nm to ~ 1 µm in length (Figure 3.1c). It was found that the supramolecular nanostructures of **GA 3.1** were close to the previously reported GA precursor **S3.1**. To study the influence of counterions on self-assembly, a counterion exchange experiment was performed. Addition of sodium bromide solution (2.0 equiv.) to a thermally annealed solution of **GA 3.1** (400 µM, final concentration) followed by the same thermal annealing protocol resulted in significant changes in the UV-Vis absorption spectrum. A decrease in the intensity of the absorption maximum at 355 nm was observed, concurrent with the appearance of a shoulder band between 400 and 500 nm (Figure 3.1d). Furthermore, the emission spectrum of the bromide-containing solution of **GA 3.1** (1.0 mM) displayed a substantial reduction in the

intensity of the emission band between 400 and 600 nm (Figure 3.1e). These spectral changes suggested that counterion exchange from tosylate to bromide influenced the photophysical properties of **GA 3.1**, potentially due to the external heavy atom effect of bromide ions and accompanying supramolecular transformations.[93] Indeed, TEM imaging of the bromide-containing **GA 3.1** solution (2.32 mM) revealed the formation of entangled nanotubular structures with an outer diameter of approximately 19 nm (Figure 3.1f), confirming the occurrence of a supramolecular transformation upon counterion exchange. To study the reversibility of the supramolecular transformation, the sodium tosylate (2.0 equiv.) was subsequently added to the solution of **GA 3.1** containing sodium bromide. The incomplete supramolecular transformation of **GA 3.1** was observed as the reformed nanotube structure was present in the TEM image (Figure S3.4), indicating that the supramolecular transformation is partially reversible. However, the presence of irregular aggregates suggests that the repeated addition of sodium salts may lead to an increase in ionic strength, influencing the self-assembly process.
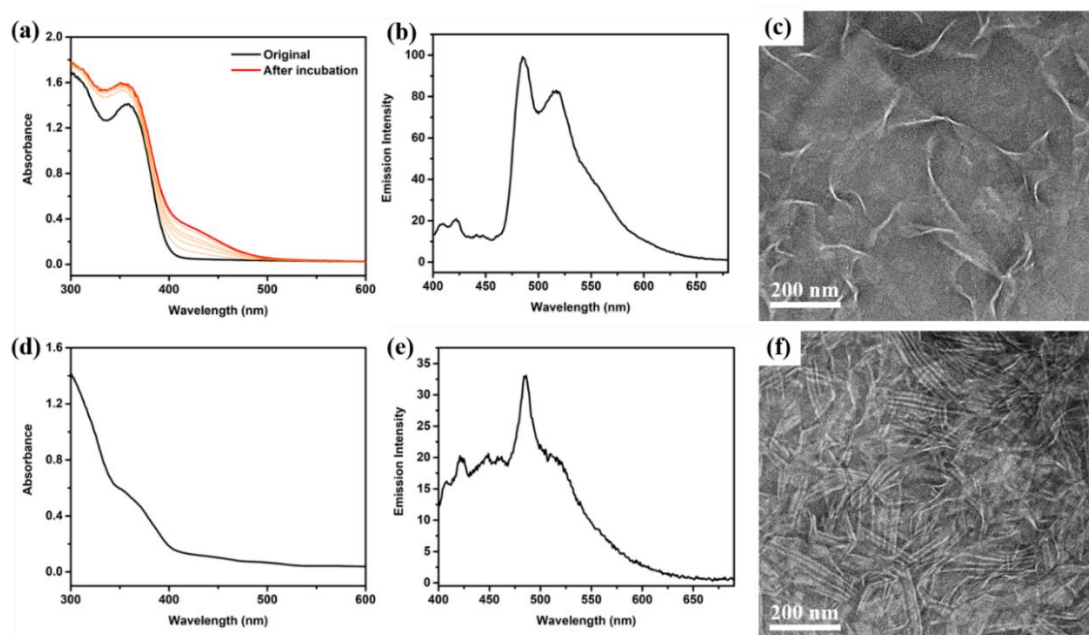
Figure 3.1 (a) UV-Vis absorption spectra of **GA 3.1** (400 μM) in DI water before (black-

line) and after incubation, (red-line); **(b)** Emission spectrum of **GA 3.1** (1 mM) in DI water; **(c)** TEM image of the thermal annealed solution of **GA 3.1** (2.32 mM); **(d)** UV-Vis absorption spectrum of **GA 3.1** (400 μM) in DI water after the addition of bromide counterion; **(e)** Emission spectrum of **GA 3.1** (1 mM) in DI water after the addition of bromide counterion; **(f)** TEM image of the thermal annealed solution of **GA 3.1** after the addition of bromide counterion (2.32 mM).

3.2.3 Luminescent Properties and Supramolecular Assemblies of Structurally Derived GAs

A structurally analogous gold(III) alkynyl complex, mono-alkynyl **GA 3.2**, was prepared by similar method with incorporating a 4-methylphenylacetylene ligand to the GA precursor. UV-Vis absorption spectroscopy of **GA 3.2** in a 1:1 DCM/MeOH mixture revealed an absorption maximum at 356 nm and a prominent absorption band between 320 and 390 nm (Figure S3.5a). The corresponding emission spectrum exhibited an emission band spanning 450-550 nm (Figure S3.5b). In contrast to the organic solution, the thermally annealed aqueous solution of **GA 3.2** displayed an enhanced absorption band between 320 and 500 nm (Figure 3.2a). Interestingly, the emission spectrum of the aqueous solution of **GA 3.2** (1.0 mM) showed a decrease in luminescence intensity compared to the organic solution, with two emission maxima observed at 470 and 530 nm (Figure 3.2b). Similar to the aqueous solution of **GA 3.1**, a vibronic structured emission band was also apparent, suggesting that the aggregated form of **GA 3.2** exhibits blue-green emission upon excitation at 320 nm. Dynamic light scattering (DLS) analysis determined the critical aggregation concentration (CAC) of **GA 3.2** in aqueous solution to be 50 mM (Figure S3.6). Transmission electron microscopy (TEM) imaging of the

annealed solution of **GA 3.2** (2.28 mM) revealed the formation of nanofibers with a diameter of approximately 6 nm (Figure 3.2c), consistent with the morphology observed for the GA precursor **S3.1**. Counterion exchange with bromide, achieved by treating the thermally annealed solution of **GA 3.2** (2.28 μM, final concentration) with sodium bromide solution (2.0 equiv.) followed by thermal annealing, resulted in the formation of a mixture of bundled nanofibers and vesicles, as observed by TEM (Figure S3.7), indicating that counterion exchange can influence the supramolecular organization of **GA 3.2**.
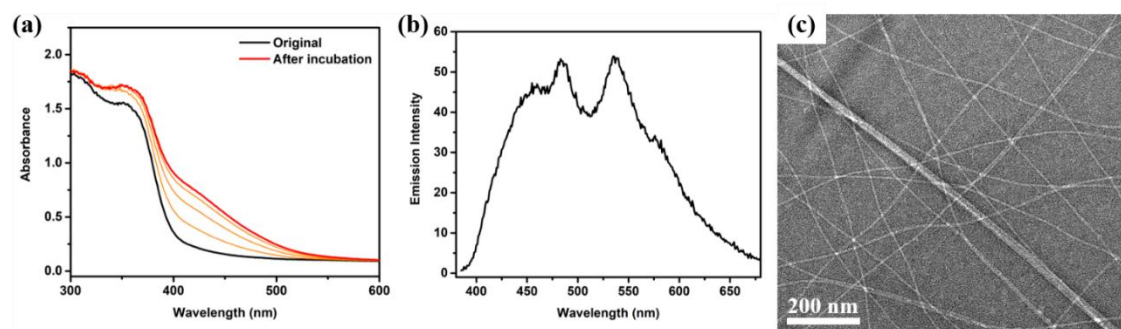
Figure 3.2 (a) UV-Vis absorption spectra of **GA 3.2** (400 μM) in DI water before (black-line) and after incubation, (red-line); **(b)** Emission spectrum of **GA 3.2** (1 mM) in DI water; (c) TEM image of thermal annealed solution of **GA 3.2** (2.28 mM).

Given that the (triisopropylsilyl)acetylene ligands would enrich the luminescent properties of cyclometalated gold(III) complexes,[69k] **GA 3.3** was synthesized using a similar procedure by incorporating (triisopropylsilyl)acetylene ligands into the GA precursor. However, the pure mono-alkynyl **GA 3.3** was not obtained even after the multiple column chromatography purification, resulting instead in a 1:5 mixture of mono-alkynyl **GA 3.3** and di-alkynyl **GA 3.3'** (Figure S3.8). The organic solution and aqueous solution of the mixture **GA 3.3** were studied by UV-Vis spectroscopy (Figure S3.9a and

Figure S3.9b respectively), which gave the absorption spectra same as that of **GA 3.1** (Figure 3.1a). Notably, the aqueous solution of the **GA 3.3** mixture (1.0 mM) exhibited minor light scattering, potentially attributable to the poor water solubility of di-alkynyl **GA 3.3'**. The higher proportion of di-alkynyl **GA 3.3'** in the mixture led to a significant enhancement in luminescence, with an emission band observed between 350 and 550 nm upon excitation at 420 nm. A similar increase in luminescence intensity was also observed for the organic solution of the **GA 3.3** mixture (1:1 DCM/MeOH, 1.0 mM) (Figure S3.9c). The critical aggregation concentration (CAC) of the **GA 3.3** mixture in aqueous solution was determined to be 20 mM (Figure S3.10). Transmission electron microscopy (TEM) analysis of the thermally annealed aqueous solution of the mixture **GA 3.3** (1.97 mM) revealed a mixture of nanosheet-like structures and solid particles with diameters of approximately 100 nm (Figure 3.3b). It is plausible that the nanosheet-like structures originated from **GA 3.3**, while the solid particles arose from the poorly soluble **GA 3.3'**. While the presence of both **GA 3.3** and **GA 3.3'** in the mixture complicated the investigation of supramolecular transformations, these findings suggested that the incorporation of strongly σ-donating alkynyl ligands can substantially enhanced the luminescent properties of cyclometalated gold(III) complexes.
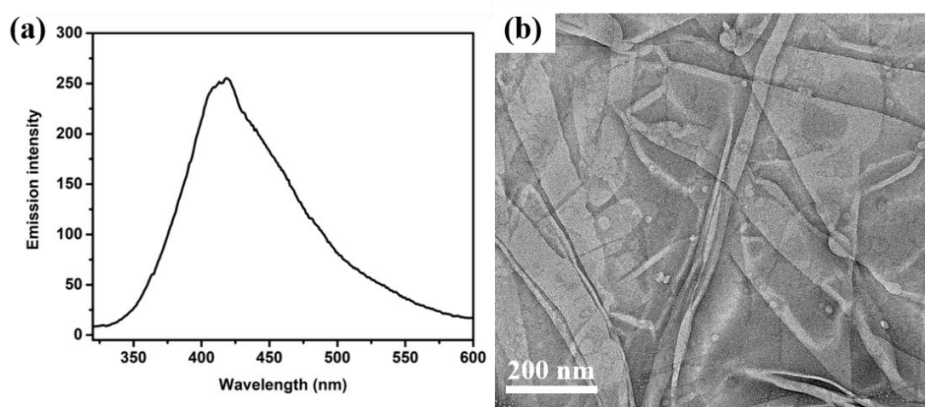
Figure 3.3 (a) Emission spectrum of **GA 3.3** (1 mM) in DI water; **(b)** TEM image of the

thermal annealed solution of **GA 3.3** (1.97 mM).

3.2.4 Cytocompatibility of GAs

To evaluate the cytocompatibility of the synthesized compounds, the thermally annealed aqueous solutions of GA precursor **S3.1**, **GA 3.1**, and **GA 3.2** were subjected to cytotoxicity studies. **GA 3.3**, due to its poor aqueous solubility, was excluded from these analyses. The impact of GA precursor **S3.1** on the viability of human bone marrow-derived mesenchymal stem cells (hBM-MSCs) was assessed using the MTS mitochondrial activity assay (Figure 3.4a). Exposure of hBM-MSCs to the GA precursor **S3.1** solution at concentrations ranging from 40 to 100 μM for 24 hours resulted in high cell viabilities (~90%), indicating minimal cytotoxicity. In contrast, both **GA 3.1** and GA **3.2** exhibited increased cytotoxicity towards hBM-MSCs at concentrations above 60 μM, as determined by the same MTS assay. Notably, **GA 3.1** displayed a more pronounced cytotoxic effect compared to **GA 3.2** (Figure 3.4b and 3.4c, respectively). Considering the same nanofiber structure conducted by GA precursor **S3.1** and **GA 3.2** showing lower cytotoxicity, while nanofibers of **GA 3.1** with larger diameter showing higher cytotoxicity, the cytotoxicity of GAs are possibly dependent on the nanostructures.
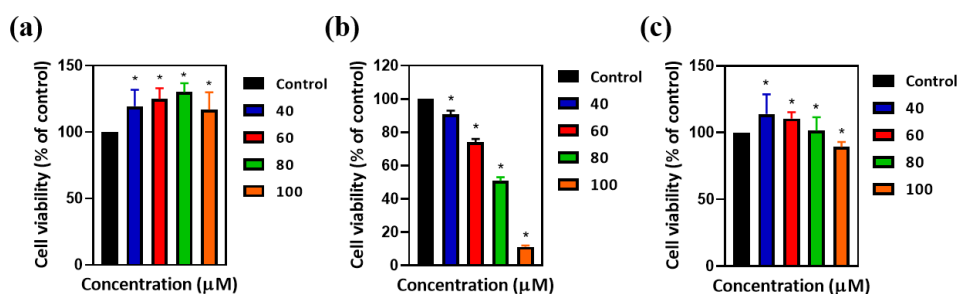
Figure 3.4 hBM-MSCs viability after incubated with **(a)** GA precursor **S3.1**, **(b) GA 3.1** and **(c) GA 3.2** gradient solutions for 24 h, respectively. All values are mean ± standard

deviation of n = 3. * denotes *P* < 0.05, which represents for statistically difference compared to the control group.

3.3 Conclusion

Gold(III) amphiphiles with the enhancement of luminescent properties by incorporating the strong σ-donating mono-alkynyl ligands in both organic and aqueous media were developed. The nanostructure of the thermal annealed aqueous solution of **GA 3.1** and **GA 3.2** was studied by TEM showing the nanofibers with different diameter. The CAC values were determined as 50 μM by DLS. The supramolecular assembly transformation of **GA 3.1** was studied upon the addition of sodium bromide for counterion exchange showing the transformation between nanofibers the nanotubes, which was reversible upon further addition of sodium tosylate. Cytocompatibilities of GA precursor **S3.1**, **GA 3.1** and **GA 3.2** showed their supramolecular assemblies with limited cytotoxicity to hBM-MSCs. This new strategy provides a valuable approach for the development of multifunctional supramolecular assemblies based on the amphiphilic gold(III) complexes.

3.4 Experimental Section

3.4.1 General Procedures

All reagents were acquired from commercial suppliers and utilized without further purification. Flash column chromatography was performed with silica gel 60 (230-400 mesh ASTM). Thin-layer chromatography employed on precoated silica gel 60 F254 plates. ^{1}H and ^{13}C NMR spectra were obtained on a Bruker DPX-400 or DPX-600 spectrometer with TMS serving as the internal standard. ^{1}H NMR data are presented as chemical shift (δ, ppm), multiplicity (s = singlet; brs = broad singlet; d = doublet; dd = double doublet; t = triplet; td = triple doublet; tt = triple triplet; q = quartet; qd = quadruple doublet, m = multiplet), coupling constant (Hz), integration. ^{13}C NMR data are presented as chemical shift (δ, ppm). High-resolution mass spectra (HR-MS) were acquired on an Agilent 6540 UHD Accurate-Mass Q-TOF LC/MS system employing ESI ionization. X-ray crystallographic analysis for small molecule structural determination was carried out using a Bruker D8 Venture single crystal X-ray diffractometer. Previously reported compounds were characterized by comparing their ^{1}H and/or ^{13}C NMR spectra to the published data.

3.4.2   UV-Vis Spectroscopy

The optical properties of the samples were analyzed using Agilent Cary 60 UV-Vis Spectrophotometer equipped with a Luma 40/8453 temperature-controlled cuvette holder. Measurements were conducted at 20°C using a quartz cuvette with a 1 cm path length.

3.4.3   Preparation of Aqueous Sample

A 1 wt.% solution of GAs in deionized water was prepared and subjected to a controlled heating and cooling process. The solution was initially heated to 50 °C for 5 minutes, followed by a gradual cooling to 20 °C at a rate of 1.0 °C/min. This annealing process aimed to facilitate the formation of assembled structures. For TEM analysis, the annealed solution was further diluted to 0.2 wt.%.

3.4.4   Transmission Electron Microscopy (TEM)

The morphology and size of the assembled structures were investigated using JEOL Model JEM-2010 Transmission Electron Microscope. Operating at 120 kV, the microscope was equipped with Gatan 794 CCD camera for image acquisition. Sample preparation involved depositing 5.0 μL of the sample solution onto a carbon-coated copper grid (Micro to Nano, EMR Carbon support film on copper, 400 square mesh). After blotting excess solution, the grid was stained with UranyLess EM stain solution (Electron Microscopy Science, 5.0 μL) for 20 seconds, followed by another blotting step to remove excess stain.

3.4.5 Dynamic Light Scattering (DLS)

Wyatt Technology DynaPro NanoStar was performed to determine Dynamic Light Scattering intensities of the samples. While acknowledging the anisotropic nature of the assembled structures, the scattering intensities were analyzed using models designed for spherical objects to provide an estimate of the assembly size. The critical aggregation concentration (CAC) of GA**s** was determined by measuring the scattering intensities of GAs solutions at various concentrations (1.0×10^{-3} to 1.0 mM) at 20°C, which followed the previously described procedures.[76a] The scattering rate was normalized by the solution concentration to obtain the molar scattering intensity (M Counts s^{-1} m^{-1}). Ten replicates were performed for each measurement, and the data were averaged to determine the mean molar scattering intensity and standard deviation.

3.4.6 Fluorescence

Fluorescence measurements were conducted at room temperature using an Agilent G9800AA Cary Eclipse fluorescence spectrophotometer. A 1 cm path length quartz cuvette was used for all measurements.

3.4.7 Cytotoxicity Test

The cytotoxicity of GAs was evaluated using 3-(4,5-dimethylthiazol-2-yl)-5-(3-carboxymethoxyphenyl)-2-(4-sulfophenyl)-2H-tetrazolium (MTS) assay, which measured cell viability. Human bone-marrow mesenchymal stem cells (hBM-MSCs) were seeded in a 96-well plate at a density of 3000 cells per well. After 12 h of incubation

in growth media including Minimum Essential Medium (MEM Alpha, no phenol red, Gibco, USA), 10% Fetal Bovine Serum (FBS, Gibco, USA) and 1% Antibiotic-Antimycotic (Gibco, USA), the cells were exposed to varying concentrations of GAs for further 24 h. Subsequently, MTS solution was added to each well, and the cells were incubated for an additional 2 h at 37°C in a 5% CO_2 atmosphere. The absorbance of each well was measured at 490 nm using a LEDETECT 96 microplate reader to determine cell viability.

3.4.8 Preparation of GAs
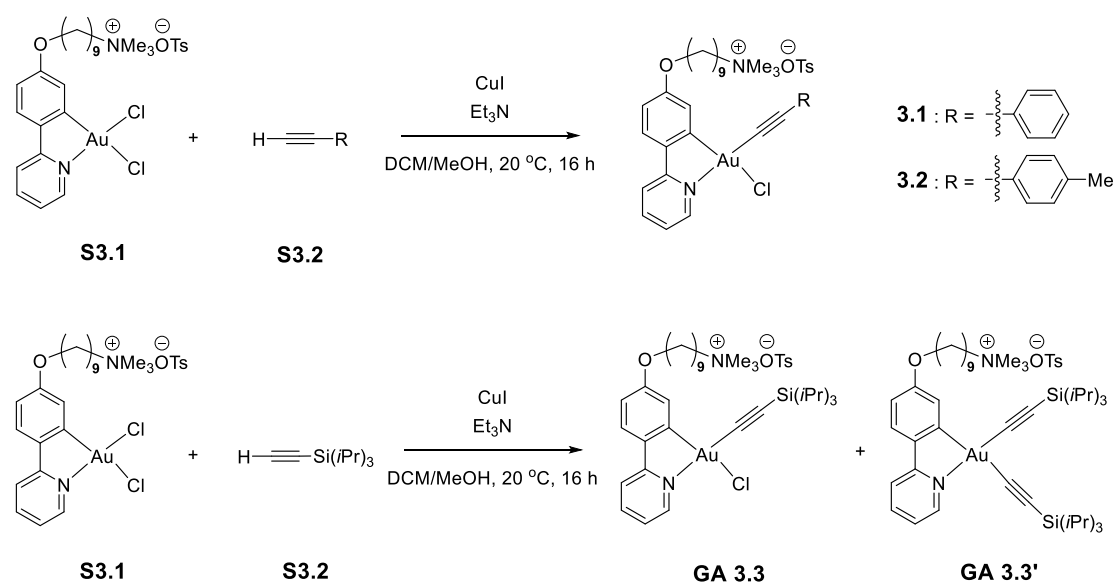
Scheme S3.1 Preparation of **GAs**.

Compound **3.1:** Synthesis according to our previous reported procedures.[57]

GAs: Gold(III) complex **S3.1** (20 mg, 0.025 mmol) was reacted with alkyne **S3.2** (0.126 mmol) in a DCM/MeOH mixture (10/1, 300 µL) with CuI (0.96 mg, 0.005 mmol) and triethylamine (2.55 mg, 3.5 µL). The reaction mixture was stirred for 16 h at room

temperature.[69k] After removing the solvent under reduced pressure, the crude product was purified by column chromatography to afford the desired gold(III) complexes **GA 3.1**, **GA 3.2**, and **GA 3.3** as pale-yellow solids.

3.4.9 Characterization Data
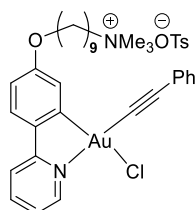
GA 3.1

46% yield.

^{1}H NMR (400 MHz, CDCl$_3$/CD$_3$OD) δ 9.26 (d, J = 5.9 Hz, 1H), 7.94 – 7.86 (m, 1H), 7.69 – 7.63 (m, 2H), 7.46 (d, J = 8.7 Hz, 1H), 7.40 (dd, J = 7.5, 2.1 Hz, 2H), 7.27 (t, J = 6.7 Hz, 1H), 7.16 (d, J = 1.5 Hz, 3H), 6.75 (dd, J = 8.6, 2.5 Hz, 1H), 3.89 (t, J = 6.5 Hz, 2H), 3.22 – 3.15 (m, 2H), 1.62 (td, J = 16.6, 15.2, 8.1 Hz, 4H), 1.26 (d, J = 7.2 Hz, 2H), 1.19 (d, J = 11.8 Hz, 8H).

^{13}C NMR (150 MHz, CDCl$_3$/CD$_3$OD) δ 163.99, 160.90, 148.20, 147.37, 142.00, 134.21, 131.82, 128.09, 127.59, 126.72, 125.12, 122.69, 120.17, 119.57, 115.00, 97.16, 84.83, 68.36, 66.95, 53.14, 29.11, 28.97, 28.92, 28.73, 26.05, 25.70, 23.01.

HRMS (ESI): [M – OTs]$^+$ Calcd. for [C$_{31}$H$_{39}$AuClN$_2$O]$^+$ 687.2416, found 687.2415.
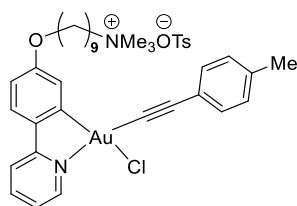
GA 3.2

32% yield.

¹H NMR (600 MHz, CD₃OD) δ 9.17 (d, J = 4.2 Hz, 1H), 8.09 – 8.04 (m, 1H), 7.87 (d, J = 7.8 Hz, 1H), 7.59 (d, J = 8.6 Hz, 1H), 7.54 (d, J = 2.5 Hz, 1H), 7.47 – 7.43 (m, 1H), 7.35 (d, J = 8.1 Hz, 2H), 7.14 (d, J = 8.1 Hz, 2H), 6.77 (dd, J = 8.6, 2.5 Hz, 1H), 3.96 (t, J = 6.9 Hz, 2H), 3.35 – 3.32 (m, 2H), 3.11 (s, 9H), 1.75 (dd, J = 14.5, 7.9, 6.9 Hz, 4H), 1.42 – 1.34 (m, 10H).

¹³C NMR (150 MHz, CDCl₃/ CD₃OD) δ 163.85, 160.64, 147.65, 146.61, 142.39, 137.50, 134.53, 131.32, 128.67, 127.01, 122.80, 122.30, 119.97, 119.53, 114.72, 96.66, 84.46, 68.14, 66.50, 53.41, 52.13, 28.97, 28.76, 28.70, 28.56, 25.93, 25.49, 22.57, 20.13.

HRMS (ESI): [M – OTs]⁺ Calcd. for [C₃₂H₄₁AuClN₂O]⁺ 701.2573, found 701.2573.

GA 3.3   **GA 3.3'**
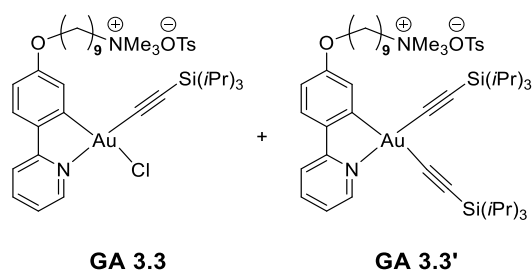
29% yield

¹H NMR (600 MHz, CD₃OD) δ 9.62 (d, J = 5.9 Hz, 5H), 9.35 (d, J = 6.1 Hz, 1H), 8.19 (d, J = 8.1 Hz, 1H), 8.18 – 8.14 (m, 5H), 8.07 (d, J = 8.7 Hz, 1H), 8.04 (d, J = 8.1 Hz, 5H), 7.87 – 7.84 (m, 2H), 7.83 (d, J = 8.7 Hz, 6H), 7.81 (d, J = 2.6 Hz, 5H), 7.75 (m, J = 9.2, 5.8, 3.3 Hz, 5H), 7.64 (td, J = 6.7, 6.2, 3.3 Hz, 5H), 7.55 (t, J = 6.2 Hz, 1H), 7.42 (t, J = 6.6 Hz, 5H), 6.99 – 6.96 (m, 1H), 6.88 (dd, J = 8.7, 2.6 Hz, 5H), 4.05 (t, J = 6.5 Hz, 12H), 3.37 – 3.34 (m, 12H), 3.14 (s, 55H), 1.84 – 1.79 (m, 29H), 1.54 (d, J = 6.5 Hz, 21H), 1.47 – 1.39 (m, 65H), 1.19 (dd, J = 12.1, 6.7 Hz, 234H).

HRMS (ESI): **GA 3.3** $[M - OTs]^+$ Calcd. for $[C_{34}H_{55}AuClN_2Osi]^+$ 767.3438, found 767.3437; **GA 3.3'** $[M - OTs]^+$ Calcd. for $[C_{45}H_{76}AuN_2OSi_2]^+$ 913.5162, found 913.5161.

3.4.10   Supporting Figures
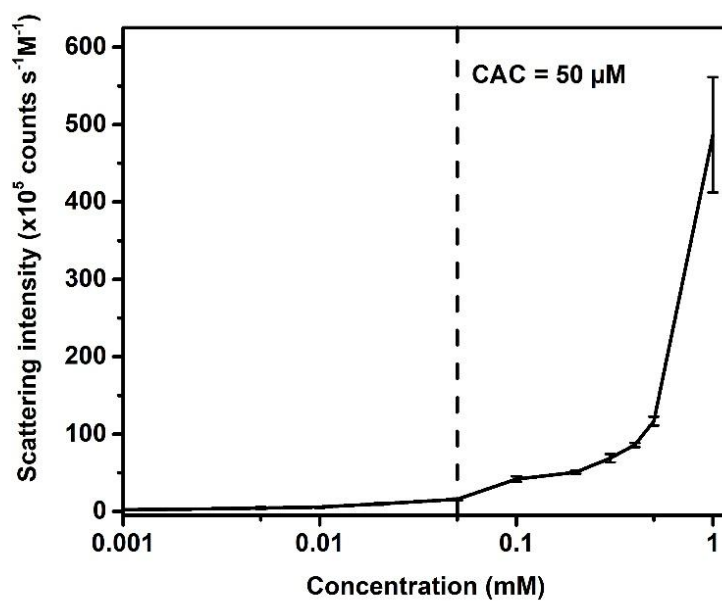
Figure S3.1 The critical aggregation concentration of aqueous solution of **GA 3.1**.
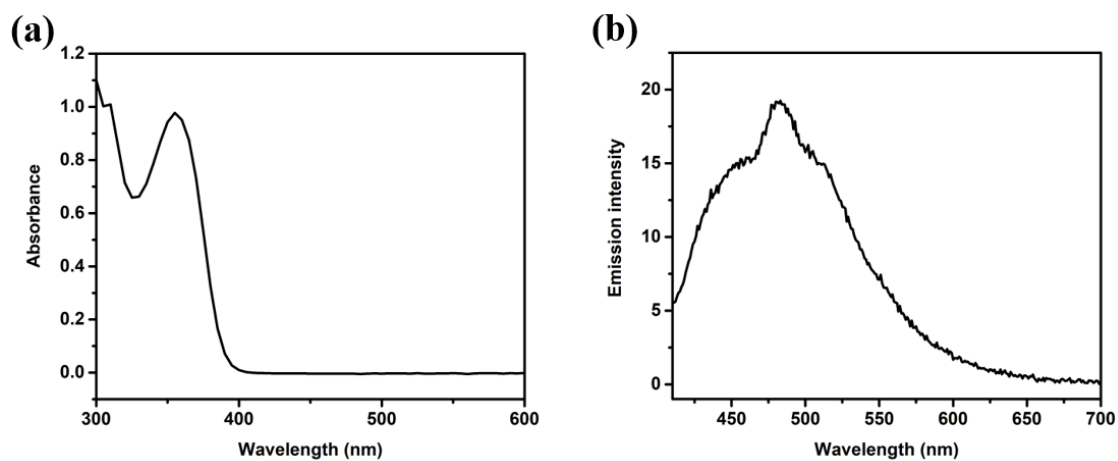
Figure S3.2 (a) UV-Vis absorption spectra of **GA 3.1** in DCM/MeOH 1:1 (400 µM);

(b) Emission spectra of **GA 3.1** in DCM/MeOH 1:1 (1 mM).
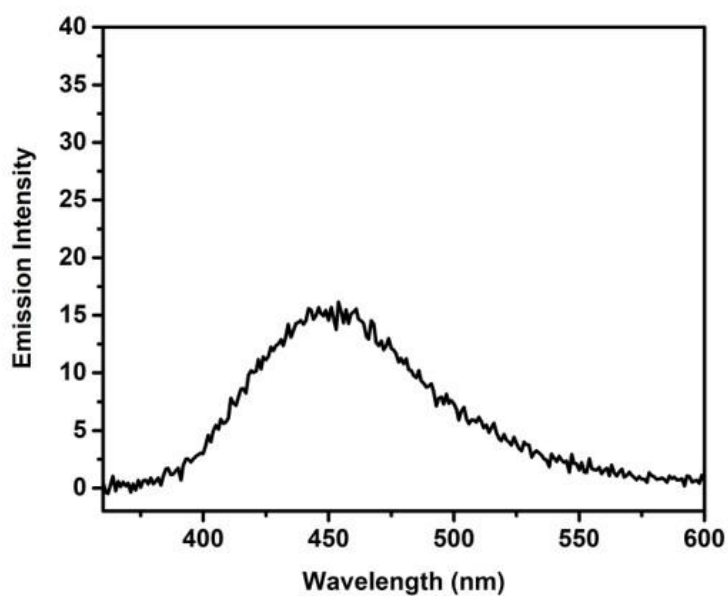
Figure S3.3 Emission spectrum of GA precursor **S3.1** in DI water (1 mM).
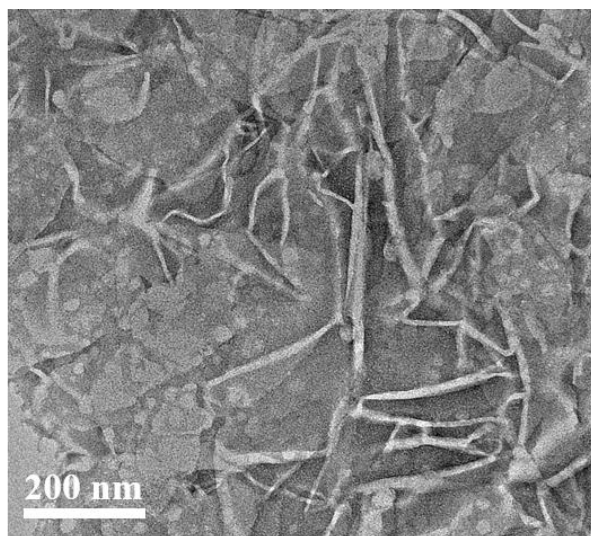
Figure S3.4 TEM image of the thermal annealed solution of **GA 3.1** after the addition

of sodium tosylate (2.0 equiv.) as further counterion exchange (2.32 mM).
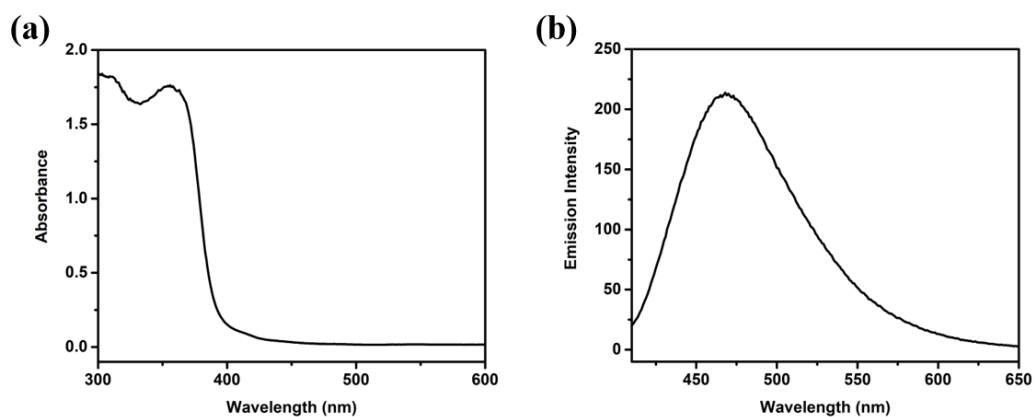
Figure S3.5 (a) UV-Vis absorption spectrum of **GA 3.2** in DCM/MeOH 1:1 (400 μM)

(b) Emission spectrum of **GA 3.2** in DCM/MeOH 1:1 (1 mM).
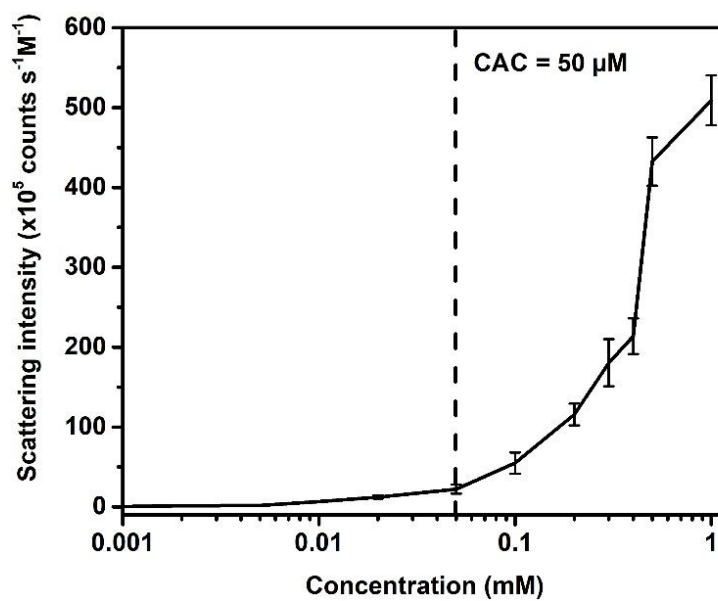
Figure S3.6 The critical aggregation concentration of aqueous solution of **GA 3.2**.
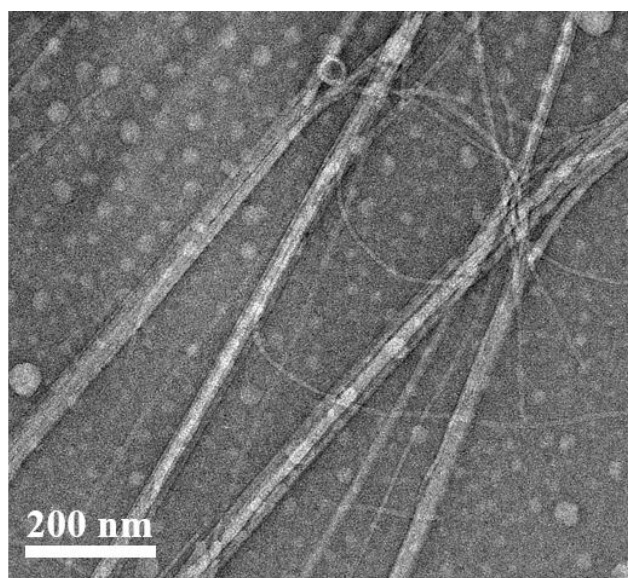
Figure S3.7 TEM image of the thermal annealed solution of **GA 3.2** after the addition

of sodium bromide for counterion exchange (2.28 mM).
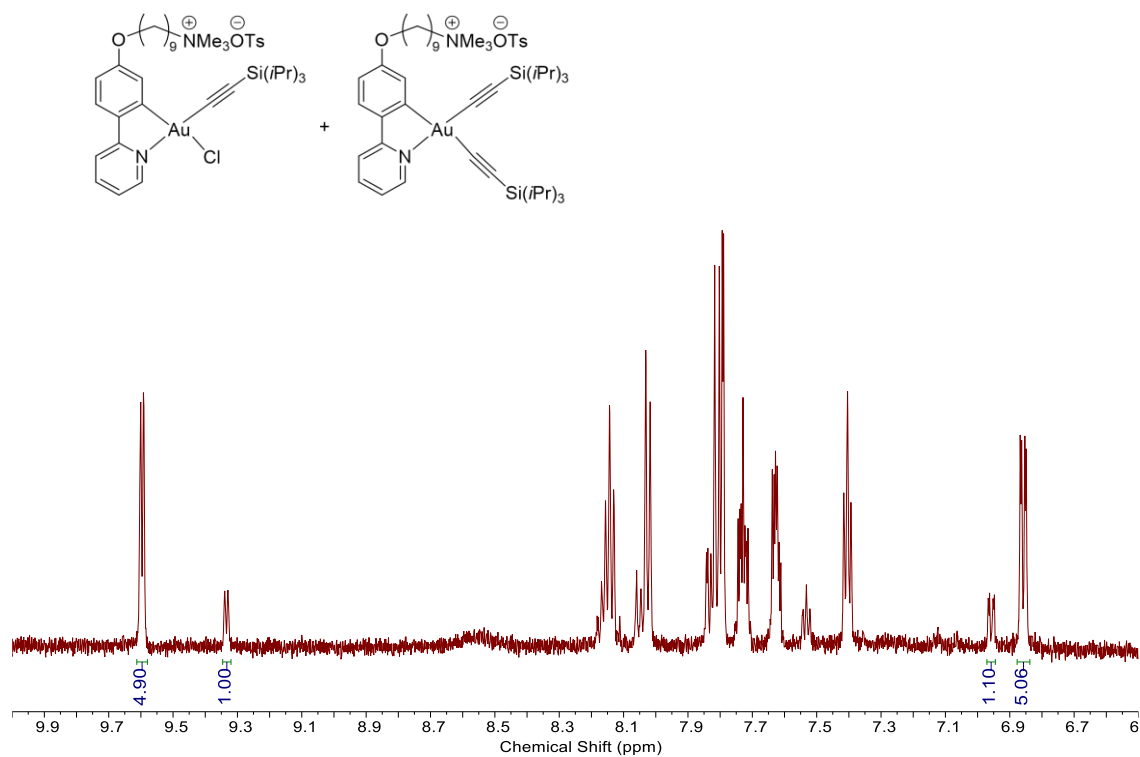
Figure S3.8 ^{1}H NMR spectrum (600 MHz, 6.5 – 10.0 ppm) of **GA 3.3** and **GA 3.3'** mixture, with relative integration of 1:5 corresponding to **GA 3.3** and **GA 3.3'**, respectively.
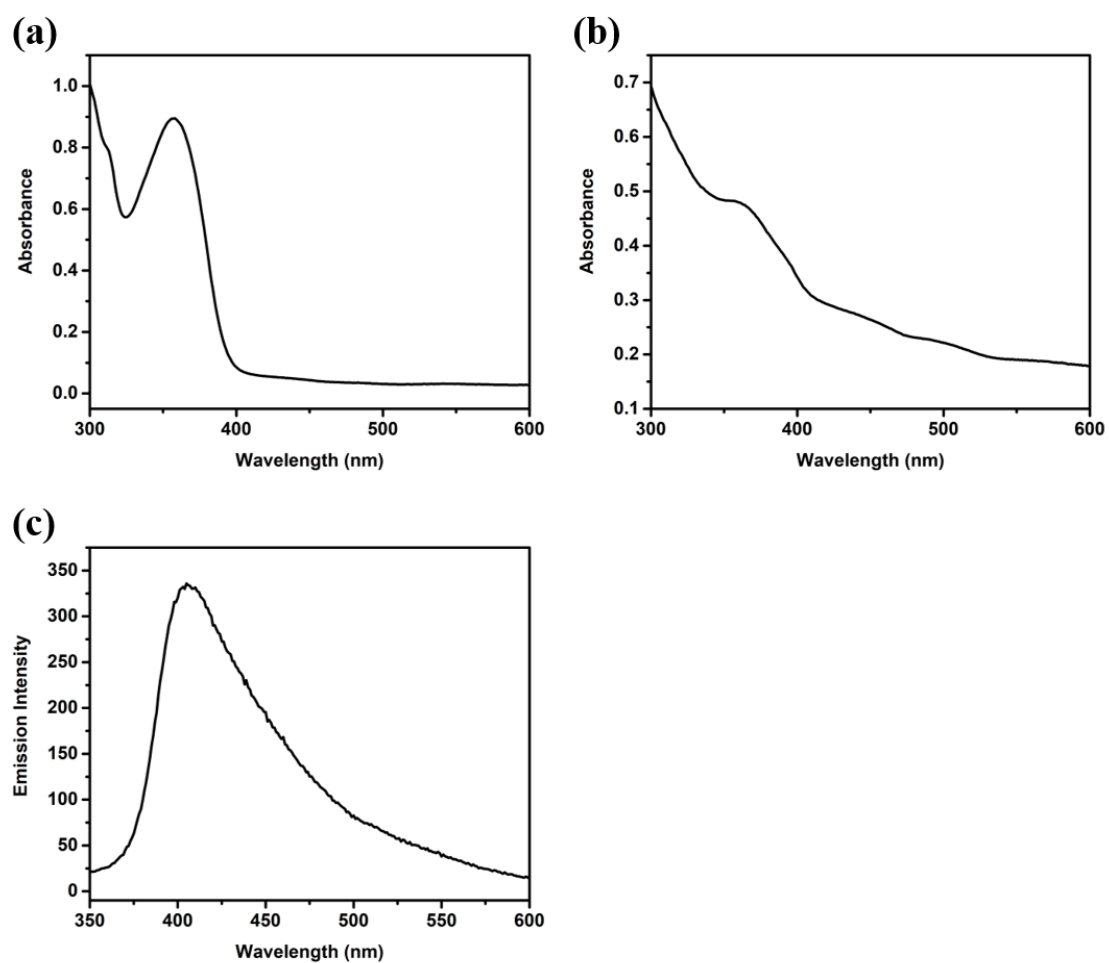
Figure S3.9 UV-Vis absorption spectra of **GA 3.3** in **(a)** DCM/MeOH 1:1 (400 µM) and

(b) DI water (1 mM); **(c)** Emission spectrum of **GA 3.3** in DCM/MeOH 1:1 (1 mM).
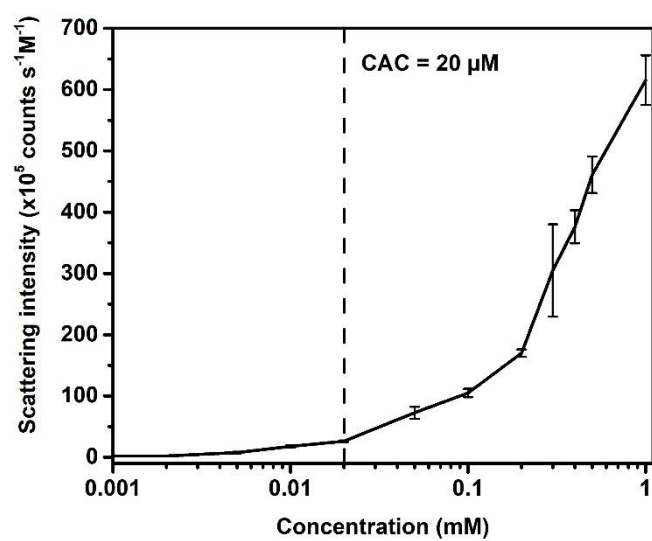
Figure S3.10 The critical aggregation concentration of aqueous solution of **GA 3.3**.

3.4.11 NMR Spectra

^{1}H NMR of GA 3.1 in CDCl$_3$/CD$_3$OD

^{13}C NMR of GA 3.1 in CDCl$_3$/CD$_3$OD

¹H NMR of GA 3.2 in CD₃OD
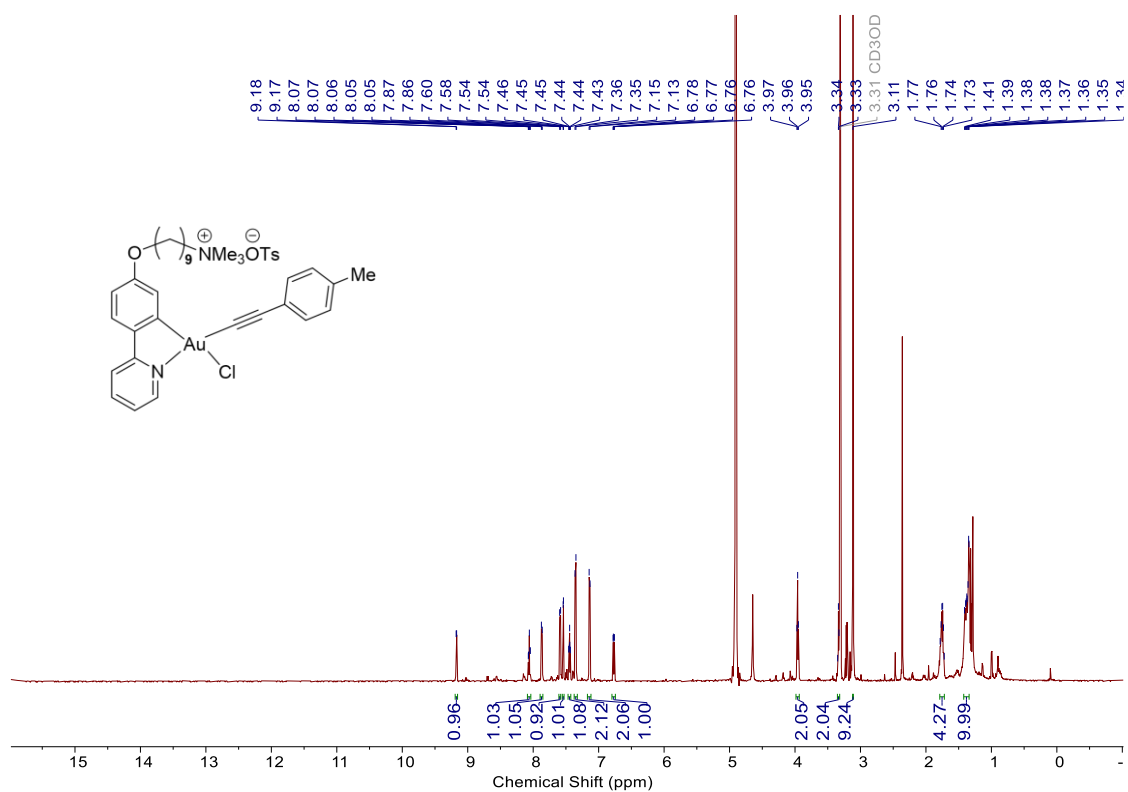
¹³C NMR of GA 3.2 in CD₃OD
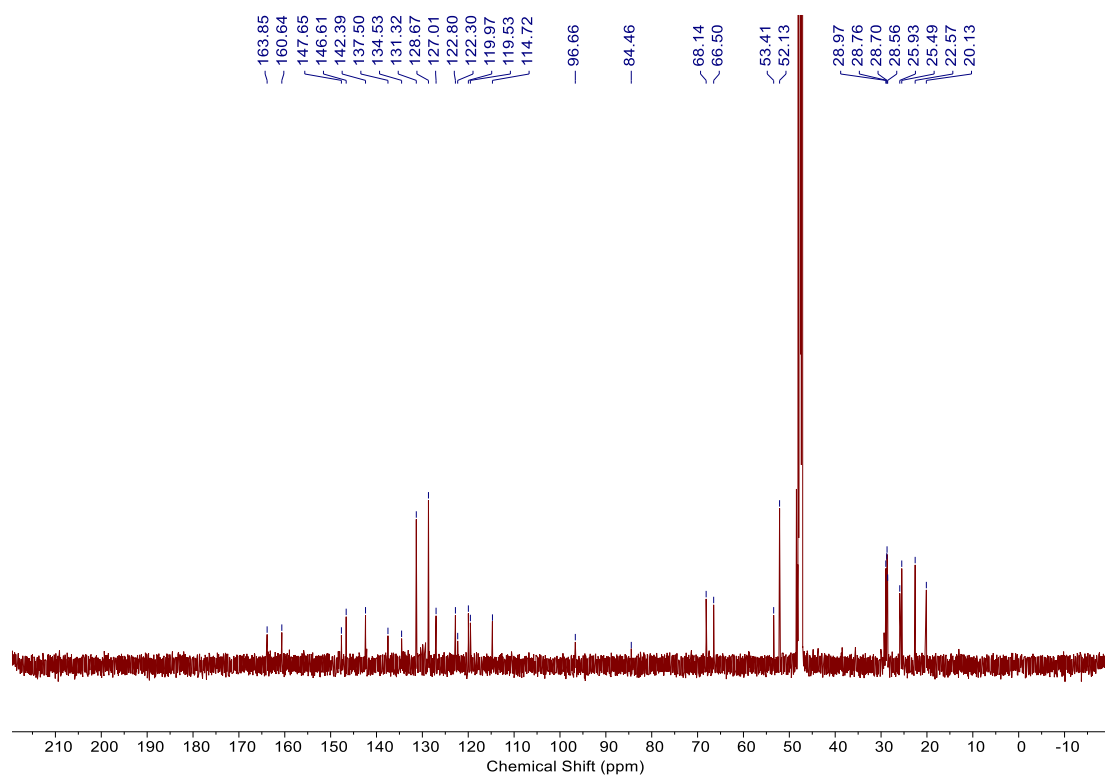
¹H NMR of GA 3.3 and GA 3.3' in CDCl₃/CD₃OD
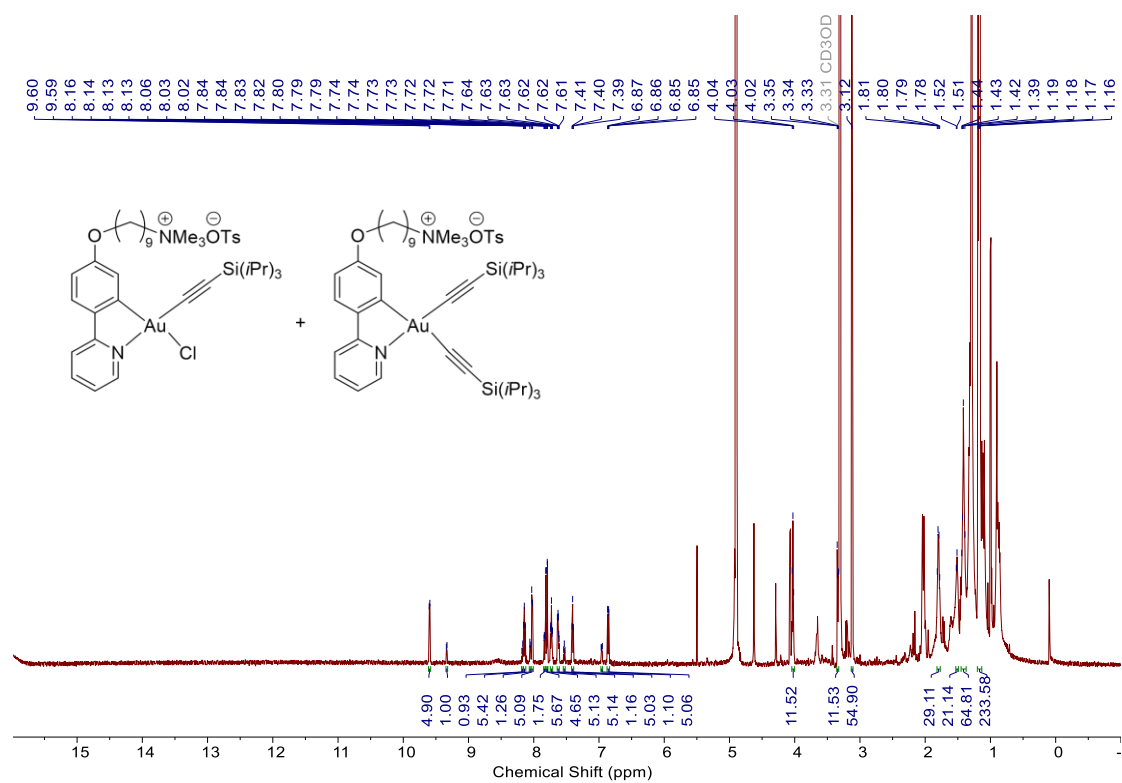
Chapter 4 Controlled Supramolecular Assemblies of Chiral Cyclometalated Gold(III) Amphiphiles in Aqueous Media

4.1 Introduction

Chiral organic amphiphiles were designed for self-assembly into supramolecular chiral hierarchical structures.[94] As an alternative strategy to organic amphiphiles, the chiral metal-ligand amphiphiles offer the structural diversity due to the variety of the chiral ligand design enabling the controls of supramolecular interactions and hierarchical structures of the corresponding supramolecular morphology.[87a, d] Despite numbers of reported cyclometalated gold(III) amphiphiles showing the high sensitivity to supramolecular transformations induced by slight changes in molecular structure,[57] the chiral supramolecular assembly of gold(III) amphiphile was largely unexplored.

Chiral cyclometalated oxazoline gold(III) complexes have shown with excellent performance in asymmetric catalysis showing high chirality transfer efficiency.[35] In this chapter, the first example of the chiral cyclometalated gold(III) amphiphile (GA) was demonstrated with supramolecular assembly in aqueous media. The amphiphilic nature of the oxazoline-based cyclometalated gold(III) complex arose from connecting the hydrophobic gold(III) core to a hydrophilic charged quaternary ammonium ion with an alkyl-linker which improved the aqueous solubility. The chirality was transferred from the chiral oxazoline moiety to the resulting supramolecular nanostructures. The counterion induced supramolecular transformations were demonstrated by the addition of D-, L-, or racemic-camphorsulfonates. Cytocompatibility of GA solution was shown with limited cytotoxicity.
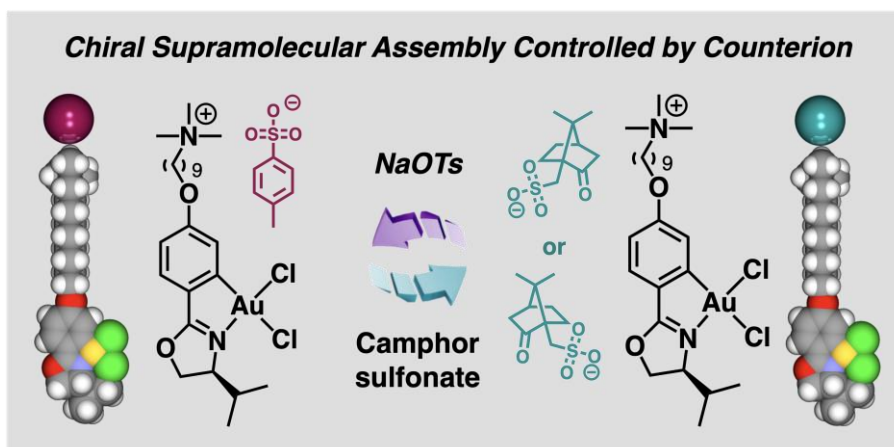
Scheme 4.1 Schematic illustration of the design of cyclometalated gold(III) amphiphiles.

4.2 Results and Discussion

4.2.1 Design and Synthesis of GA

GA 4.1 was designed as a chiral C^N-chelated oxazoline-based gold(III) complex exhibiting the amphiphilicity. The amphiphilic nature of **GA 4.1** was introduced by connecting a hydrophilic quaternary ammonium ion motif through an aliphatic nonyl-linker to the hydrophobic chiral oxazoline gold(III) core (Scheme 4.1). The synthetic procedure of **GA 4.1** began with using 2-bromo-4-hydroxybenzaldehyde as the starting material which attached to *tert*-butyldimethylsilyl ether group through an aliphatic nonyl-linker, affording compound **S4.2** (Scheme 4.2). The chirality of the ligand was first introduced by reacting the chiral amino alcohol to form the chiral oxazoline ligand **S4.3**. Continued with the bromide-mercury transmetalation, terminal silyl group modification, and the subsequent mercury-gold transmetalation methodologies, the gold(III) complex **S4.7** was obtained. Finally, the gold(III) amphiphile **GA 4.1** was afforded by the

nucleophilic substitution of the terminal tosylate group of compound **S4.7** using trimethylamine reagent. The newly synthesized chiral gold(III) amphiphile **GA 4.1** and its synthetic intermediates were characterized by ^{1}H NMR, ^{13}C NMR, and HRMS (see details in Experiment Section).
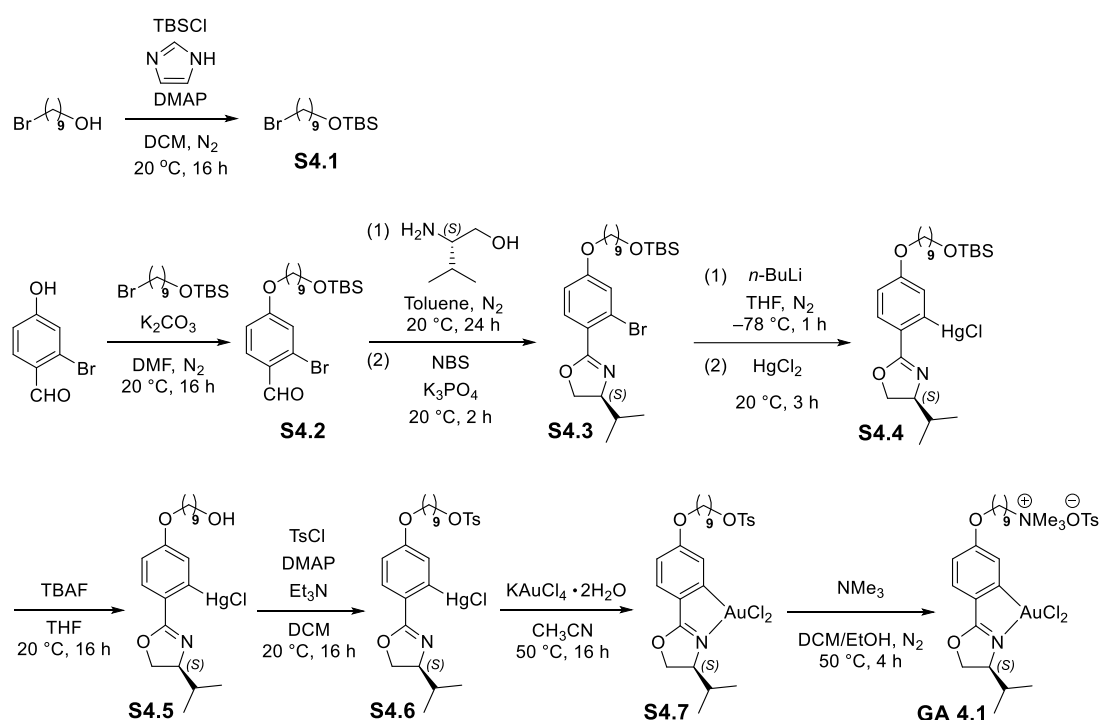
Scheme 4.2 Synthetic route of gold(III) amphiphile **GA 4.1**.

4.2.2 Aqueous Supramolecular Assembly and Cytocompatibility of GA

The optical properties of **GA 4.1** were investigated in both organic and aqueous media. UV-Vis spectroscopy of a 400 µM solution of **GA 4.1** in a 3:1 DCM/MeOH mixture revealed a prominent absorption band at 300 nm, accompanied by a shoulder band spanning 350-430 nm (Figure S4.1a). To assess the aggregation propensity in aqueous solution, a 1.0 wt.% (12.1 mM) solution of **GA 4.1** was prepared and subjected

to a thermal annealing process which involved heating the solution to 50°C followed by controlled cooling to 20°C at a rate of 1.0°C/min. Dynamic light scattering (DLS) analysis of the annealed solution of **GA 4.1** at various concentrations (0.01-1.0 mM) determined the critical aggregation concentration (CAC) to be 80 µM (Figure S4.1b). This low CAC value suggested a high propensity for **GA 4.1** to self-assemble into supramolecular structures in aqueous environments. The annealed solution of **GA 4.1** (400 µM) was also studied with UV-Vis absorption spectroscopy (Figure 4.1a), which showed the same spectrum (Figure 4.1a, black-line) as the organic solution of **GA 4.1**. The spectrum showed a slight hypsochromic shift and a decreased signal of the shoulder band at 350 nm – 430 nm during the thermal annealing process (Figure 4.1a, red-line). The solution was further studied by circular dichroism (CD) spectroscopy. In the CD spectrum (Figure 4.1b), the positive Cotton effect was first observed with decreasing wavelength from 370 nm to 250 nm, and the strong negative Cotton effect with decreasing wavelength from 250 nm to 210 nm. In contrast, the CD spectrum of the organic solution of **GA 4.1** (DCM/MeOH, 400 µM) showed lower intensity of Cotton effects (Figure S4.1c). This result possibly indicated the presence of the supramolecular helicity in the aqueous solution of **GA 4.1** leading to the increased signal in the CD spectrum. The morphology of self-assembled structures formed by **GA 4.1** in aqueous solution was investigated using transmission electron microscopy (TEM). Negative staining of a 0.2 wt.% (2.42 mM) thermally annealed aqueous solution of **GA 4.1** revealed the formation of lamellar nanostructures with irregular shapes and widths ranging from 200 nm to 1500 nm (Figure 4.1c). The cytocompatibility of **GA 4.1** was evaluated using the MTS assay, which measures mitochondrial activity as an indicator of cell viability. Human bone marrow-derived mesenchymal stem cells (hBM-MSCs) were exposed to a range of **GA 4.1**

concentrations (20-100 µM) prepared from a thermally annealed aqueous solution. The results, normalized to untreated cells, demonstrated minimal cytotoxicity over 24 h, with cell viabilities exceeding 90% for concentrations up to 80 µM (Figure 4.1d). A slight decrease in cell viability (over 80%) was observed at the highest concentration tested (100 µM, Figure 4.1d, blue bar). These findings suggest that **GA 4.1** exhibits good cytocompatibility towards hBM-MSCs within the concentration range studied.
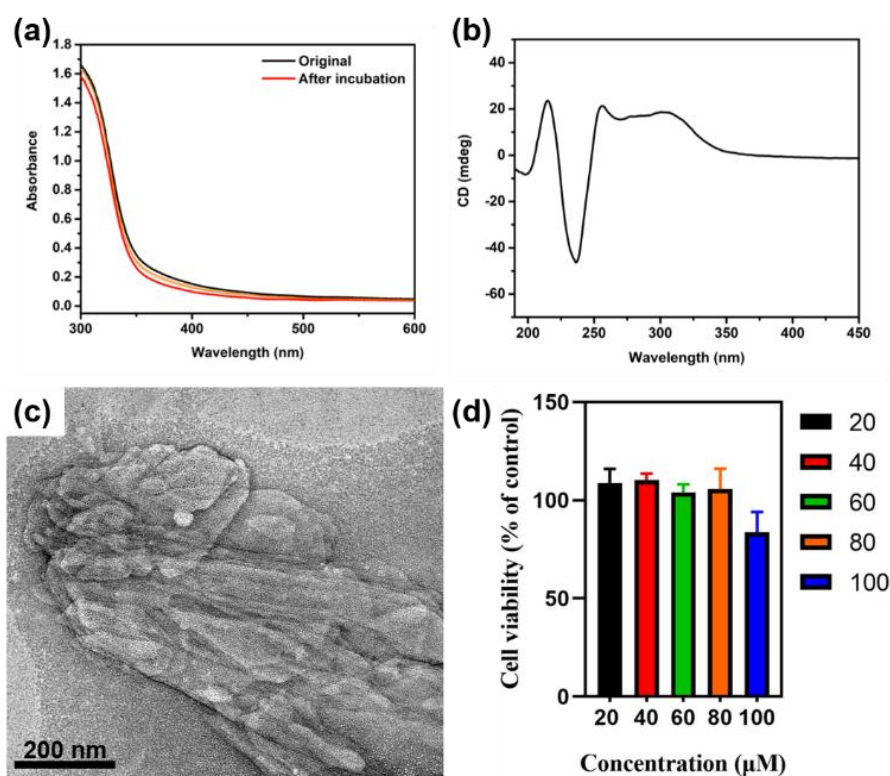
Figure 4.1 (a) UV-Vis absorption spectra of **GA 4.1** (400 µM) in DI water before (black-line) and after incubation (red-line); **(b)** CD spectrum of **GA 4.1** (400 µM) in DI water; **(c)** TEM image of the thermal annealed solution of **GA 4.1** (2.42 mM); **(d)** hBM-MSCs viability after incubated with **GA 4.1** gradient solutions for 24 h. All values are representing as mean ± standard deviation of n = 3. * denotes $P < 0.05$, which represents for statistically difference compared to the control group.

4.2.3 Counterion Controlled Chiral Supramolecular Assembly Transformations of GA

The influence of counterion exchange on the supramolecular assembly of **GA 4.1** was investigated using D- and L-camphorsulfonate as chiral counterions. To exchange the counterion to D-camphorsulfonate, the thermal annealed aqueous solution of **GA 4.1** (400 μM, final concentration) was treated with the addition of sodium D-camphorsulfonate solution (2.0 equiv.) followed by the same thermal annealing process, affording **GA 4.1D-Camphor**. UV-Vis absorption spectroscopy of the resulting solution of **GA 4.1D-Camphor** revealed an absorption maximum at 300 nm (Figure 4.2a), exhibiting a lower intensity compared to the original **GA 4.1** solution. Similarly, **GA 4.1L-Camphor** was synthesized using the same procedure, employing sodium L-camphorsulfonate as the counterion. UV-Vis absorption spectroscopy of **GA 4.1L-Camphor** (Figure 4.2b) displayed a spectrum nearly identical to that of **GA 4.1D-Camphor**. Moreover, the two thermal annealed aqueous solutions of **GA 4.1D-Camphor** and **GA 4.1L-Camphor** were prepared using the same thermal annealing process for CD measurements. In the CD spectrum of **GA 4.1D-Camphor**, stronger Cotton effect at 230 nm – 250 nm and weaker Cotton effect at 210 nm – 225 nm were observed (Figure 4.2c, black-line) as compared to the CD spectrum of the original **GA 4.1**. As reference, sodium D-camphorsulfonate solution (400 μM) gave only limited CD signal (Figure 4.2c, red-line). These results indicated that changing the counterion to chiral version would induce the supramolecular helicity transformation, resulting in the difference of the CD spectra between **GA 4.1D-Camphor** and original **GA 4.1**. Similarly, the CD spectrum of **GA 4.1L-Camphor** (Figure 4.2d, black-line) was almost the same as that of **GA 4.1D-Camphor**, which also indicated the presence of chiral counterion induced supramolecular helicity transformation. Furthermore, the thermal annealed

aqueous solution of **GA 4.1**_{D-Camphor} (3.86 mM, 0.2 wt.%) and **GA 4.1**_{L-Camphor} (3.86 mM, 0.2 wt.%) were studied by TEM to examine the supramolecular nanostructures. The supramolecular vesicles were observed in the TEM images of both **GA 4.1**_{D-Camphor} and **GA 4.1**_{L-Camphor} solutions with a diameter range of

~ 50 nm – 500 nm (Figures 4.2e and S4.2, Figures 4.2f and S4.3 respectively). As shown in TEM and CD results, the supramolecular transformations could be induced by the addition of chiral camphorsulfonates. However, the formation of supramolecular vesicles was possibly due to the incomplete counterion exchange process. Considering the similar binding affinities of camphorsulfonate and tosylate to tertiary ammonium ion, higher equivalent of chiral camphorsulfonate should be required for the complete counterion substitution.
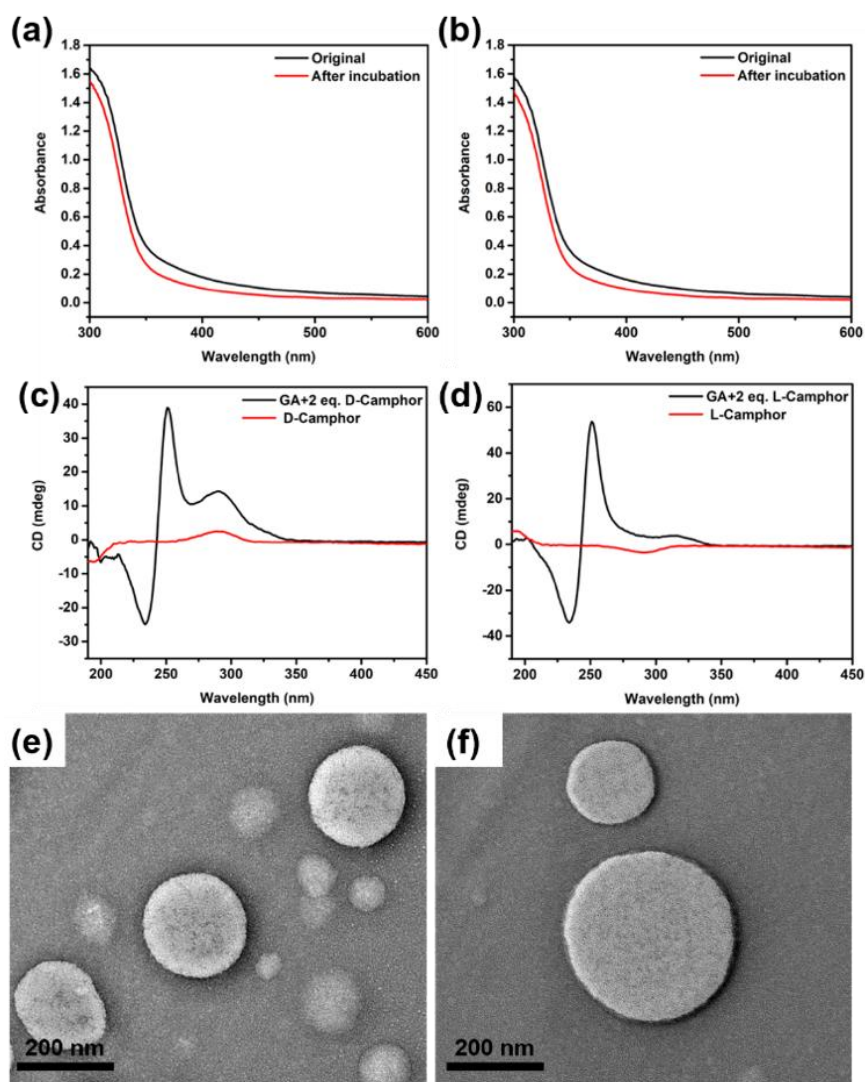
Figure 4.2 UV-Vis absorption spectra of **GA 4.1** (400 μM) in DI water before (black-line) and after incubation (red-line), after the addition of 2.0 equiv. of **(a)** sodium D-camphorsulfonate and **(b)** sodium L-camphorsulfonate; CD spectra of **GA 4.1** (400 μM) in DI water after the addition of 2.0 equiv. of **(c)** sodium D-camphorsulfonate and **(d)** sodium L-camphorsulfonate; TEM images of the thermal annealed solution of **GA 4.1** (3.86 mM) after the addition of 2.0 equiv. of **(e)** sodium D-camphorsulfonate and **(f)** sodium L-camphorsulfonate.

4.2.4　Counterion Ratio Influence on Chiral Supramolecular Assembly Transformations of GA

The different counterion ratios of **GA 4.1$_{\text{D-Camphor}}$** (400 μM) were prepared by the addition of sodium D-camphorsulfonate (4.0, 6.0, 8.0, and 10.0 equiv.) to the aqueous solution of **GA 4.1** followed by the thermal annealing process. In the CD measurements, these resulting solutions gave higher signal intensities of the Cotton effect in the spectra as compared to **GA 4.1$_{\text{D-Camphor}}$** with D-camphorsulfonate (2.0 equiv.) (Figure 4.3a). In addition, **GA 4.1$_{\text{D-Camphor}}$** with D-camphorsulfonate (4.0 equiv.) (3.22 mM, 0.2 wt.%) was first selected for TEM study. The supramolecular vesicles together with some large aspect ratio nanostructures were observed in the TEM image (Figures 4.3b and S4.4). Interestingly, increasing the D-camphorsulfonate ratio to 8.0 equiv. led to the formation of large aspect ratio supramolecular nanotubes (outer diameter ~ 50 nm – 200 nm, Figures 4.3c and S4.5). When the D-camphorsulfonate was further increased to 10.0 equiv., the nanotubes aggregated with vesicles were observed (Figure S4.6). These results implied that increasing the ratio of D-camphorsulfonate could enhance the supramolecular helicity.

Using the same preparation method, the different counterion ratios of **GA 4.1$_{\text{L-Camphor}}$** (400 μM) (4.0, 6.0, 8.0, and 10.0 equiv.) were prepared. In the CD measurements of **GA 4.1$_{\text{L-Camphor}}$** (Figure 4.3d), same observations were shown as **GA 4.1$_{\text{D-Camphor}}$** gave the increased intensities of the Cotton effect. Moreover, **GA 4.1$_{\text{L-Camphor}}$** with L-camphorsulfonate (4.0 equiv.) was first selected for TEM study. The nanofiber-like structures with large aspect ratios were observed in the TEM image (Figure 4.3e and S4.7). Increasing the L-camphorsulfonate ratio to 8.0 equiv. led to the formation of supramolecular nanotubes (outer diameter ~ 50 nm – 250 nm, Figure 4.3f and S4.8).

When the L-camphorsulfonate was further increased to 10.0 equiv., the nanotubes were partially disintegrated (Figure S4.9).

The similar TEM images and CD spectral shifts of **GA 4.1**$_{\text{D-Camphor}}$ and **GA 4.1**$_{\text{L-Camphor}}$ possibly indicated that although the counterion exchange process induced the supramolecular transformations, the intrinsic chirality of D- or L-camphorsulfonates was not transferred to the resulting nanostructures. In this concern, the racemic camphorsulfonate was used for counterion exchange instead of the enantiopure form. The aqueous solution of **GA 4.1** (400 μM) was added with the racemic mixture of camphorsulfonate (8.0 equiv.) followed by the thermal annealing process. In the CD measurements, same observations were shown as compared to the chiral counterion showing the increased intensities of the Cotton effect (Figure 4.4a). This result implied that the chirality of the camphorsulfonate did not affect the supramolecular transformation. In addition, the TEM image of this solution was obtained which showed that the supramolecular nanotubes (Figures 4.4b and S4.10) were same as that observed in chiral camphorsulfonates. From these results, the counterion induced supramolecular transformations were possibly due to the decreased packing parameter of **GA 4.1**.
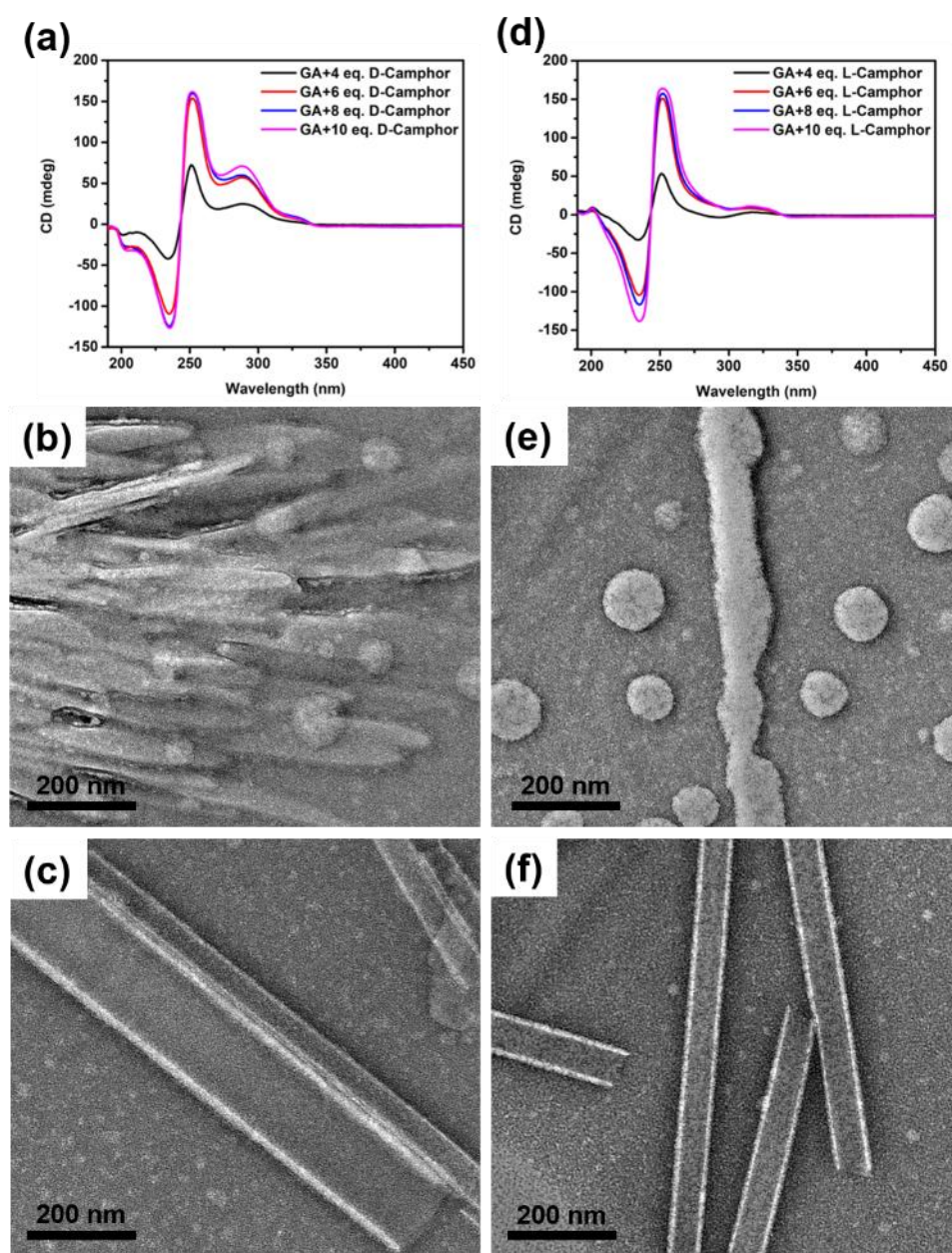
Figure 4.3 CD spectra of **GA 4.1** (400 μM) in DI water after the addition of **(a)** sodium D-camphorsulfonate (4.0, 6.0, 8.0, and 10.0 equiv.) and **(d)** sodium L-camphorsulfonate (4.0, 6.0, 8.0, and 10.0 equiv.); TEM images of the thermal annealed solution of **GA 4.1** (3.22 mM) after the addition of 4.0 equiv. of **(b)** sodium D-camphorsulfonate and **(e)** sodium L-camphorsulfonate; TEM images of the thermal annealed solution of **GA 4.1** (2.46 mM) after the addition of 8.0 equiv. of **(c)** sodium D-camphorsulfonate and **(f)** sodium L-camphorsulfonate.

To investigate the reversibility of the counterion-induced changes in the supramolecular assembly of **GA 4.1**, a solution of **GA 4.1**$_{\text{D-Camphor}}$ (containing 2.0 equiv. of sodium D-camphorsulfonate, 400 µM) was treated with 2.0 equiv. of sodium tosylate. The resulting mixture was then subjected to the standard thermal annealing process. This experiment aimed to assess whether the initial supramolecular organization of **GA 4.1** could be restored upon replacement of the D-camphorsulfonate counterions with tosylate ions. The TEM image showed the lamellar and nanosheet-like structures (Figures 4.4c and S4.11). This indicated that the vesicles were partially transformed back to lamellar structures. The resulting nanosheet-like structures was possibly the competitive supramolecular transformation pathway, arising from the excess amount of D-camphorsulfonate induced the complexities. For **GA 4.1**$_{\text{L-Camphor}}$ solution, similar supramolecular transformations were observed (Figure S4.12).
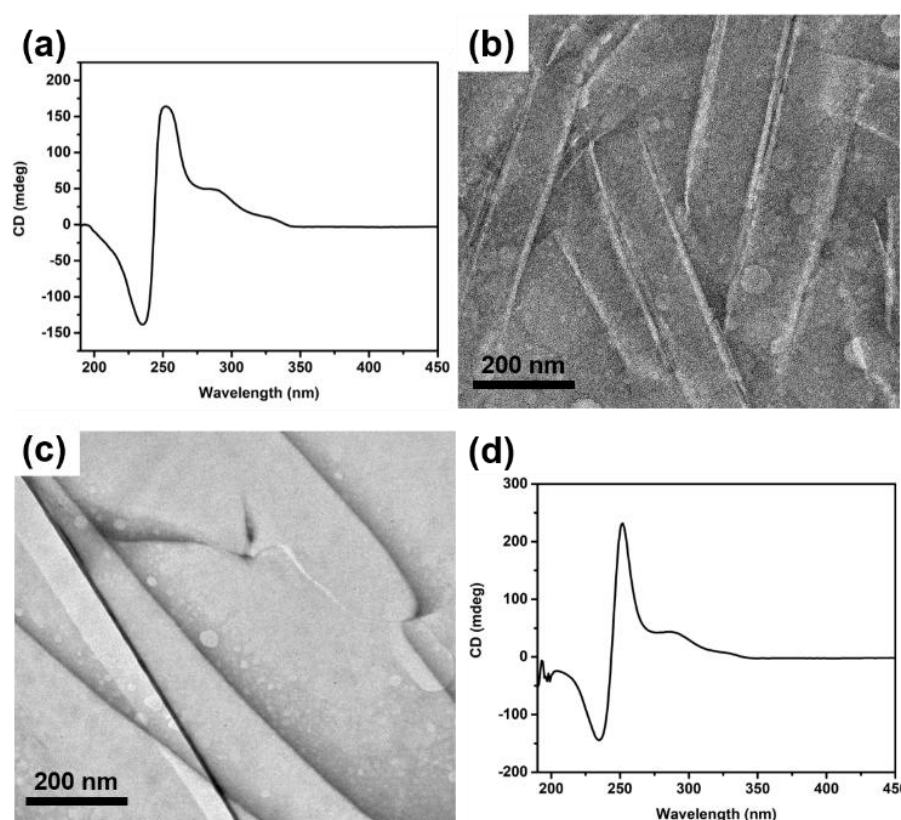
Figure 4.4 (a) CD spectra of **GA 4.1** (400 µM) in DI water and **(b)** TEM image of the

thermal annealed solution of **GA 4.1** (2.46 mM) after the addition of 8.0 equiv. of the racemic mixture of camphorsulfonate; **(c)** TEM image of the thermal annealed solution of **GA 4.1**_{D-Camphor} (3.26 mM) and **(d)** CD spectra of **GA 4.1**_{D-Camphor} (400 μM) in DI water after the addition of 2.0 equiv. of sodium tosylate.

4.3 Conclusion

The first example of chiral gold(III) amphiphile **GA 4.1** was synthesized, showing the enhanced supramolecular helicities in aqueous media. **GA 4.1** self-assembled to lamellar nanostructures in aqueous media as shown in the TEM image. D-, L-, or racemic-camphorsulfonates were separately added to the solution of **GA 4.1** for counterion exchanges. The ratios of the added camphorsulfonates determined the resulting supramolecular nanostructures, which transformed from lamellar structure to either vesicles or nanotubes. The counterion induced supramolecular transformations largely enhanced the supramolecular helicity, which was partially reversible upon further addition of sodium tosylate. The current gold(III) amphiphilic design was shown with good cytocompatibility that would be the foundation for the future development on controllable chiral counterion induced supramolecular *P*-, *M*-helicities of chiral gold(III) amphiphiles.

4.4　Experimental Section

4.4.1　General Procedures

All reagents were acquired from commercial suppliers and utilized without further purification. Flash column chromatography was performed with silica gel 60 (230-400 mesh ASTM). Thin-layer chromatography employed on precoated silica gel 60 F254 plates. ¹H and ¹³C NMR spectra were obtained on a Bruker DPX-400 or DPX-600 spectrometer with TMS serving as the internal standard. ¹H NMR data are presented as chemical shift (δ, ppm), multiplicity (s = singlet; brs = broad singlet; d = doublet; dd = double doublet; t = triplet; td = triple doublet; tt = triple triplet; q = quartet; qd = quadruple doublet, m = multiplet), coupling constant (Hz), integration. ¹³C NMR data are presented as chemical shift (δ, ppm). High-resolution mass spectra (HR-MS) were acquired on an Agilent 6540 UHD Accurate-Mass Q-TOF LC/MS system employing ESI ionization. X-ray crystallographic analysis for small molecule structural determination was carried out using a Bruker D8 Venture single crystal X-ray diffractometer. Previously reported compounds were characterized by comparing their ¹H and/or ¹³C NMR spectra to the published data.

4.4.2 Preparation of Aqueous Sample

A 1 wt.% solution of **GA** in deionized water was prepared and subjected to a controlled heating and cooling process. The solution was initially heated to 50°C for 5 minutes, followed by a gradual cooling to 20°C at a rate of 1.0°C/min. This annealing process aimed to facilitate the formation of assembled structures. For TEM analysis, the annealed solution was further diluted to 0.2 wt.%.

4.4.3 Incubation of GA with Sodium L-camphorsulfonate and Sodium D-camphorsulfonate for Counter Anion Controlled Supramolecular Transformation

A thermally annealed aqueous solution of **GA** (12.1 mM) was treated with increasing molar equivalents (2.0, 4.0, 6.0, 8.0, and 10.0) of either sodium L-camphorsulfonate or sodium D-camphorsulfonate. Following the addition of the counterion solution, each mixture was subjected to a controlled heating and cooling cycle, involving incubation at 50°C for 5 minutes followed by gradual cooling to 20°C at a rate of 1.0°C/min.

4.4.4 UV-Vis Spectroscopy

The optical properties of the samples were analyzed using Agilent Cary 60 UV-Vis Spectrophotometer equipped with a Luma 40/8453 temperature-controlled cuvette holder. Measurements were conducted at 20°C using a quartz cuvette with a 1 cm path length unless otherwise specified.

4.4.5 Circular Dichroism (CD) Spectroscopy

Circular dichroism (CD) spectra were acquired using a Jasco J-1500 CD spectrophotometer at ambient temperature. Measurements were conducted in a quartz cuvette with a path length of 1.0 mm.

4.4.6 Transmission Electron Microscopy (TEM)

The morphology and size of the assembled structures were investigated using JEOL Model JEM-2010 Transmission Electron Microscope. Operating at 120 kV, the microscope was equipped with Gatan 794 CCD camera for image acquisition. Sample preparation involved depositing 5.0 μL of the sample solution onto a carbon-coated copper grid (Micro to Nano, EMR Carbon support film on copper, 400 square mesh). After blotting excess solution, the grid was stained with UranyLess EM stain solution (Electron Microscopy Science, 5.0 μL) for 20 seconds, followed by another blotting step to remove excess stain.

4.4.7 Dynamic Light Scattering (DLS)

Wyatt Technology DynaPro NanoStar was performed to determine Dynamic Light Scattering intensities of the samples. While acknowledging the anisotropic nature of the assembled structures, the scattering intensities were analyzed using models designed for spherical objects to provide an estimate of the assembly size. The critical aggregation concentration (CAC) of **GA** was determined by measuring the scattering intensities of **GA** solutions at various concentrations (1.0×10^{-3} to 1.0 mM) at 20°C, which followed the previously described procedures.[76a] The scattering rate was normalized by the solution

concentration to obtain the molar scattering intensity (M Counts s^{-1} m^{-1}). Ten replicates were performed for each measurement, and the data were averaged to determine the mean molar scattering intensity and standard deviation.

4.4.8   Cytotoxicity Test

The cytotoxicity of GAs was evaluated using 3-(4,5-dimethylthiazol-2-yl)-5-(3-carboxymethoxyphenyl)-2-(4-sulfophenyl)-2H-tetrazolium (MTS) assay, which measured cell viability. Human bone-marrow mesenchymal stem cells (hBM-MSCs) were seeded in a 96-well plate at a density of 3000 cells per well. After 12 h of incubation in growth media including Minimum Essential Medium (MEM Alpha, no phenol red, Gibco, USA), 10% Fetal Bovine Serum (FBS, Gibco, USA) and 1% Antibiotic-Antimycotic (Gibco, USA), the cells were exposed to varying concentrations of **GA** for further 24 h. Subsequently, MTS solution was added to each well, and the cells were incubated for an additional 2 h at 37°C in a 5% CO_2 atmosphere. The absorbance of each well was measured

4.4.9 Preparation of GA
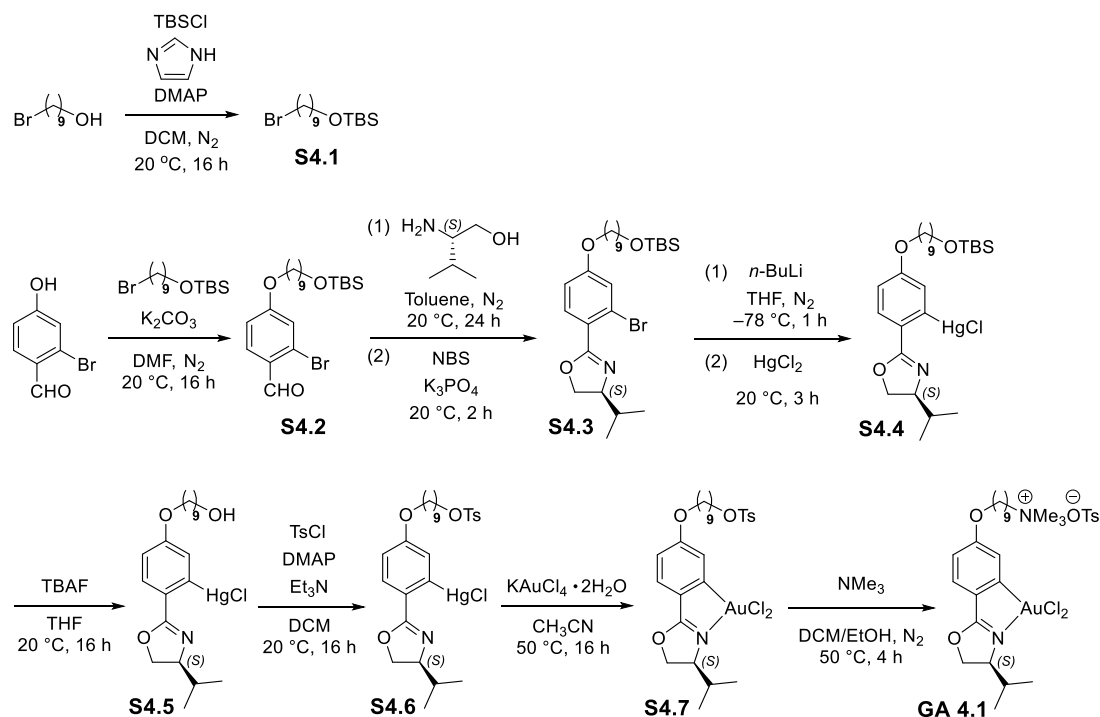
Scheme S4.1 Synthetic route of gold(III) amphiphiles **GA 4.1**.

Compound **S4.1**: 9-bromo-1-nonanol (4.46 g, 20 mmol) was added dropwise with tert-butyldimethylsilyl chloride (TBSCl, 3.92 g, 26 mmol) in the presence of imidazole (2.72 g, 40 mmol) and 4-dimethylaminopyridine (DMAP, 244 mg, 2 mmol) in 20 mL anhydrous DCM at room temperature and stirred for 16 h under nitrogen atmosphere. The resulting mixture was filtered, concentrated, and purified by column chromatography (hexane/EA) to afford compound **S4.1** as a colorless oil (6.07 g, 18.0 mmol, 90% yield).

Compound **S4.2**: Compound **S4.1** (2.0 g, 6.0 mmol) was reacted with 2-bromo-4-hydroxybenzaldehyde (1.0 g, 5.0 mmol) in the presence of potassium carbonate (K$_2$CO$_3$, 1.4 g, 10 mmol) in 10 mL anhydrous dimethylformamide at room temperature for 16 h

under nitrogen atmosphere. The resulting mixture was diluted by ethyl acetate (40 mL), washed by DI water (80 mL) for three times. The organic layer was dried with anhydrous $MgSO_4$, concentrated, and purified by column chromatography (hexane/EA) to afford compound **S4.2** as a pale-yellow oil (2.26 g, 4.95 mmol, 99% yield).

Compound S4.3: Compound **S4.2** (1.0 g, 2.2 mmol) was reacted with (*S*)-valinol (225 mg, 2.19 mmol) in 5 mL toluene at room temperature for 24 h under nitrogen atmosphere. Subsequently, potassium phosphate (K_3PO_4, 1.4 g, 6.6 mmol) and *N*-bromosuccinimide (NBS, 390 mg, 2.2 mmol) were added to the reaction mixture, and the reaction was stirred at room temperature for additional 2 h. After workup and purification by column chromatography, compound S4.3 was obtained as a colorless oil with a 46% yield. The resulting solution was washed by 5 mL sat. $NaHCO_3$ solution and 5 mL sat. $Na_2S_2O_3$ solution. The organic layer was dried with anhydrous $MgSO_4$, concentrated, and purified by column chromatography (hexane/EA) to afford compound **S4.3** as a colorless oil (549 mg, 1.0 mmol, 46% yield).

Compound S4.4: Compound **S4.3** (521 mg, 0.96 mmol) was treated with dropwise addition of *n*-butyllithium (2.5 M solution in hexane, 0.5 mL) at -78 °C in 10 mL anhydrous THF under nitrogen atmosphere. Subsequently, mercury(II) chloride ($HgCl_2$, 326 mg, 1.2 mmol) was added, and the reaction mixture was warmed to room temperature and stirred for further 3 h. The resulting solution was washed by 5 mL sat. NH_4Cl aqueous solution. The aqueous layer was extracted by DCM (20 mL × 2). The organic layer was combined, dried with anhydrous $MgSO_4$, concentrated, and purified by column

chromatography (hexane/EA) to afford compound **S4.4** as a colorless oil (492 mg, 0.71 mmol, 74% yield).

Compound S4.5: Compound **S4.4** (370 mg, 0.053 mmol) was treated with tetra-n-butylammonium fluoride (TBAF, 1.0 M solution in THF, 0.6 mL) in 2 mL THF at room temperature for 16 h. The resulting solution was concentrated, and purified by column chromatography (hexane/EA) to afford compound **S4.5** as a white solid (214 mg, 0.37 mmol, 69% yield).

Compound S4.6: Compound **S4.5** (214 mg, 0.37 mmol) was added in protion with *p*-toluenesulfonyl chloride (TsCl, 88 mg, 0.46 mmol) in the presence of DMAP (5 mg, 0.04 mmol) and triethylamine (Et$_3$N, 0.2 mL) in anhydrous dichloromethane at room temperature for 16 h. The resulting solution was concentrated and purified by column chromatography (hexane/EA) to afford compound **S4.6** as colorless oil (206 mg, 0.28 mmol, 76% yield).

Compound S4.7: Compound **S4.6** (135 mg, 0.14 mmol) was reacted with potassium tetrachloroaurate(III) dihydrate (KAuCl$_4$•2H$_2$O, 91 mg, 0.22 mmol) in acetonitrile at 50 °C for 16 h. The resulting solution was concentrated and suspended by DCM followed by the filtration through celite. The filtrate was concentrated and purified by column chromatography (DCM) to afford the crude product. Upon the recrystallization process (dichloromethane/methanol), compound **S4.7** was obtained as white solid (111 mg, 0.144 mmol, 79% yield).

GA 4.1: Compound **S4.7** (35 mg, 0.046 mmol) was reacted with a solution of trimethylamine in ethanol (20%) (1 mL) in the presence of 1 mL DCM in a sealed pressure tube at 50 °C under a nitrogen atmosphere for 4 h. The resulting solution was dried and redissolved in DCM/MeOH (10:1) and subject to column chromatography (dichloromethane/methanol), affording **GA 4.1** as white solid (12.5 mg, 0.015 mmol, 33% yield).

4.4.10 Characterization Data
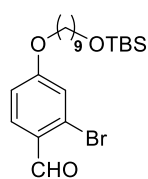
S4.2

^{1}H NMR (400 MHz, CDCl$_3$) δ 10.21 (s, 1H), 7.87 (d, J8.7 Hz, 1H), 7.12 (d, J = 2.4 Hz, 1H), 6.91 (dd, J = 8.4, 1.8 Hz, 1H), 4.01 (t, J = 6.5 Hz, 2H), 3.59 (t, J = 6.6 Hz, 2H), 1.84 – 1.74 (m, 2H), 1.50 (d, J = 6.7 Hz, 2H), 1.44 (q, J = 7.0 Hz, 2H), 1.31 (s, 8H), 0.89 (s, 9H), 0.04 (s, 6H).

^{13}C NMR (100 MHz, CDCl$_3$) δ 190.65, 164.22, 131.33, 128.78, 126.76, 118.97, 114.51, 68.83, 63.30, 32.86, 29.50, 29.35, 29.23, 28.93, 26.00, 25.88, 25.78, 18.39, -5.24.

HRMS (ESI): [M + H]$^+$ Calcd for [C$_{22}$H$_{37}$BrO$_3$Si]$^+$ 457.1768, found 457.1769.

S4.3
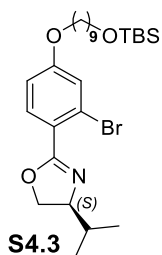
¹H NMR (600 MHz, CDCl₃) δ 7.63 (d, *J* = 8.7 Hz, 1H), 7.15 (d, *J* = 2.5 Hz, 1H), 6.83 (dd, *J* = 8.7, 2.4 Hz, 1H), 4.42 – 4.36 (m, 1H), 4.17 – 4.09 (m, 2H), 3.95 (t, *J* = 6.6 Hz, 2H), 3.59 (t, *J* = 6.7 Hz, 2H), 1.93 – 1.83 (m, 1H), 1.76 (p, *J* = 6.8 Hz, 2H), 1.51 (p, *J* = 6.8 Hz, 2H), 1.43 (p, *J* = 7.1 Hz, 2H), 1.37 – 1.28 (m, 9H), 1.04 (d, *J* = 6.8 Hz, 3H), 0.96 (d, *J* = 6.8 Hz, 3H), 0.89 (s, 9H), 0.04 (s, 6H).

¹³C NMR (150 MHz, CDCl₃) δ 162.66, 160.92, 132.33, 122.56, 121.78, 119.63, 113.51, 72.79, 70.03, 68.44, 63.32, 32.87, 32.73, 29.52, 29.36, 29.28, 29.02, 26.01, 25.92, 25.79, 18.82, 18.40, 18.18, -5.23.

HRMS (ESI): [M + H]⁺ Calcd for [C₂₇H₄₆BrNO₃Si]⁺ 540.2503, found 540.2527.

S4.4
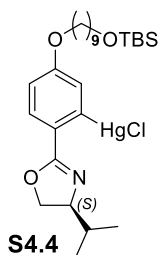
¹H NMR (400 MHz, CDCl₃) δ 7.81 (d, *J* = 8.7 Hz, 1H), 6.94 (d, *J* = 2.7 Hz, 1H), 6.80 (dd, *J* = 8.6, 2.6 Hz, 1H), 4.56 – 4.47 (m, 1H), 4.16 (t, *J* = 8.4 Hz, 1H), 4.03 – 3.92 (m, 3H), 3.60 (t, *J* = 6.6 Hz, 2H), 1.84-1.69 (m, 3H), 1.51 (t, *J* = 6.8 Hz, 2H), 1.48 – 1.40 (m, 2H), 1.31 (s, 8H), 1.05 (d, *J* = 6.7 Hz, 3H), 0.96 (d, *J* = 6.8 Hz, 3H), 0.89 (s, 9H), 0.04 (s, 6H).

¹³C NMR (100 MHz, CDCl₃) δ 167.81, 162.03, 129.70, 124.27, 123.11, 113.76, 72.46, 72.03, 68.28, 63.32, 33.10, 32.87, 29.54, 29.38, 29.32, 29.13, 26.01, 25.98, 25.80, 18.98, 18.40, -5.23.

HRMS (ESI): [M + H]⁺ Calcd for [C₂₇H₄₆ClHgNO₃Si]⁺ 689.2715, found 689.2720.

S4.5
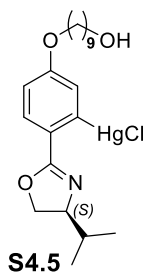
¹H NMR (600 MHz, CDCl₃) δ 7.81 (d, *J* = 8.6 Hz, 1H), 6.95 (d, *J* = 2.6 Hz, 1H), 6.81 (dd, *J* = 8.6, 2.6 Hz, 1H), 4.52 (dd, *J* = 9.7, 8.4 Hz, 1H), 4.16 (t, *J* = 8.5 Hz, 1H), 4.02 – 3.94 (m, 3H), 3.64 (h, *J* = 3.6 Hz, 2H), 1.57 (p, *J* = 6.5 Hz, 2H), 1.49 – 1.41 (m, 2H), 1.39 – 1.30 (m, 8H), 1.26 (t, *J* = 5.3 Hz, 1H), 1.05 (d, *J* = 6.7 Hz, 3H), 0.96 (d, *J* = 6.9 Hz, 3H).

¹³C NMR (150 MHz, CDCl₃) δ 167.80, 162.02, 129.70, 124.30, 123.12, 113.77, 72.48, 72.03, 68.26, 63.08, 33.11, 32.78, 29.50, 29.35, 29.28, 29.10, 25.97, 25.73, 19.00, 18.98.

HRMS (ESI): [M + H]⁺ Calcd for [C₂₁H₃₂ClHgNO₃]⁺ 584.1850, found 584.1846.

S4.6
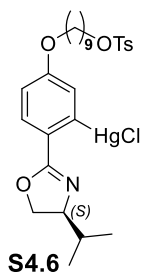
¹H NMR (600 MHz, CDCl₃) δ 7.81 (d, *J* = 8.6 Hz, 1H), 7.78 (d, *J* = 8.4 Hz, 2H), 7.34 (d, *J* = 8.4 Hz, 2H), 6.94 (d, *J* = 2.5 Hz, 1H), 6.80 (dd, *J* = 8.6, 2.6 Hz, 1H), 4.52 (dd, *J*

= 9.7, 8.3 Hz, 1H), 4.15 (t, J = 8.5 Hz, 1H), 4.01 (t, J = 6.5 Hz, 2H), 3.99 – 3.93 (m, 3H), 2.44 (s, 3H), 1.80 – 1.70 (m, 3H), 1.65 – 1.59 (m, 2H), 1.45 – 1.38 (m, 2H), 1.34 – 1.28 (m, 4H), 1.28 – 1.22 (m, 4H), 1.04 (d, J = 6.7 Hz, 3H), 0.95 (d, J = 6.7 Hz, 3H).

^{13}C NMR (150 MHz, CDCl₃) δ 167.79, 161.99, 152.46, 144.67, 133.19, 129.84, 129.71, 127.90, 124.30, 123.11, 113.74, 72.49, 72.03, 70.69, 68.21, 33.11, 29.30, 29.20, 29.09, 28.87, 28.81, 25.94, 25.33, 21.68, 19.02, 18.99.

HRMS (ESI): [M + H]$^+$ Calcd for [C$_{28}$H$_{38}$ClHgNO$_5$S]$^+$ 738.1938, found 738.1936.

S4.7
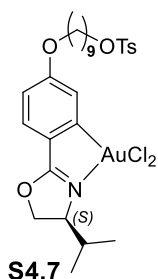
^{1}H NMR (600 MHz, CDCl₃) δ 7.78 (d, J = 8.3 Hz, 2H), 7.33 (dd, J = 10.2, 8.3 Hz, 3H), 7.29 (d, J = 2.3 Hz, 1H), 6.78 (dd, J = 8.5, 2.4 Hz, 1H), 4.94 (t, J = 9.3 Hz, 1H), 4.83 (dd, J = 9.0, 4.0 Hz, 1H), 4.67 (dt, J = 9.5, 3.7 Hz, 1H), 4.00 (t, J = 6.5 Hz, 2H), 4.00 – 3.93 (m, 2H), 2.85 – 2.72 (m, 1H), 2.44 (s, 3H), 1.76 (p, J = 6.5 Hz, 2H), 1.67 – 1.61 (m, 2H), 1.41 (p, J = 7.8, 7.3 Hz, 2H), 1.35 – 1.28 (m, 4H), 1.28 – 1.20 (m, 4H), 0.96 (d, J = 7.0 Hz, 3H), 0.79 (d, J = 7.0 Hz, 3H).

^{13}C NMR (150 MHz, CDCl₃) δ 180.13, 163.30, 149.58, 144.70, 133.14, 129.98, 129.85, 127.89, 116.84, 115.84, 114.82, 72.87, 70.71, 68.77, 66.57, 29.27, 29.15, 29.10, 28.90, 28.85, 28.81, 25.85, 25.33, 21.69, 18.43, 13.82.

HRMS (ESI): [M – Cl]$^+$ Calcd for [C$_{28}$H$_{38}$AuCl$_2$NO$_5$S]$^+$ 732.1819, found 732.1815.

GA 4.1
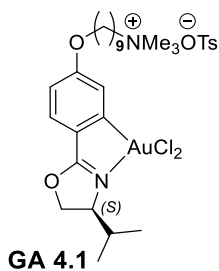
¹H NMR (600 MHz, CD₃OD) δ 7.71 (d, *J* = 8.2 Hz, 4H), 7.43 (d, *J* = 8.5 Hz, 1H), 7.29 (d, *J* = 2.4 Hz, 1H), 7.24 (d, *J* = 8.2 Hz, 4H), 6.93 (dd, *J* = 8.4, 2.4 Hz, 1H), 5.04 (dd, *J* = 9.3, 4.2 Hz, 1H), 4.98 (t, *J* = 9.3 Hz, 1H), 4.60 (dt, *J* = 9.4, 4.0 Hz, 1H), 4.07 (t, *J* = 6.5 Hz, 2H), 3.35 – 3.32 (m, 2H), 3.12 (s, 9H), 2.76 – 2.67 (m, 1H), 2.37 (s, 6H), 1.84 – 1.75 (m, 4H), 1.50 (p, *J* = 7.4 Hz, 2H), 1.44 – 1.36 (m, 8H), 0.98 (d, *J* = 7.1 Hz, 3H), 0.83 (d, *J* = 7.0 Hz, 3H).

¹³C NMR (150 MHz, CD₃OD) δ 180.24, 163.18, 148.57, 142.07, 140.34, 130.08, 128.44, 125.56, 117.18, 116.02, 114.06, 73.05, 68.58, 66.58, 66.46, 52.11, 29.19, 28.95, 28.79, 28.72, 28.47, 25.92, 25.51, 22.56, 19.93, 16.95, 12.49.

HRMS (ESI): [M – OTs]⁺ Calcd for [C₃₁H₄₇AuCl₂N₂O5S]⁺ 655.2127, found 655.2155.

4.4.11 Supporting Figures

(a)

(b)

(c)
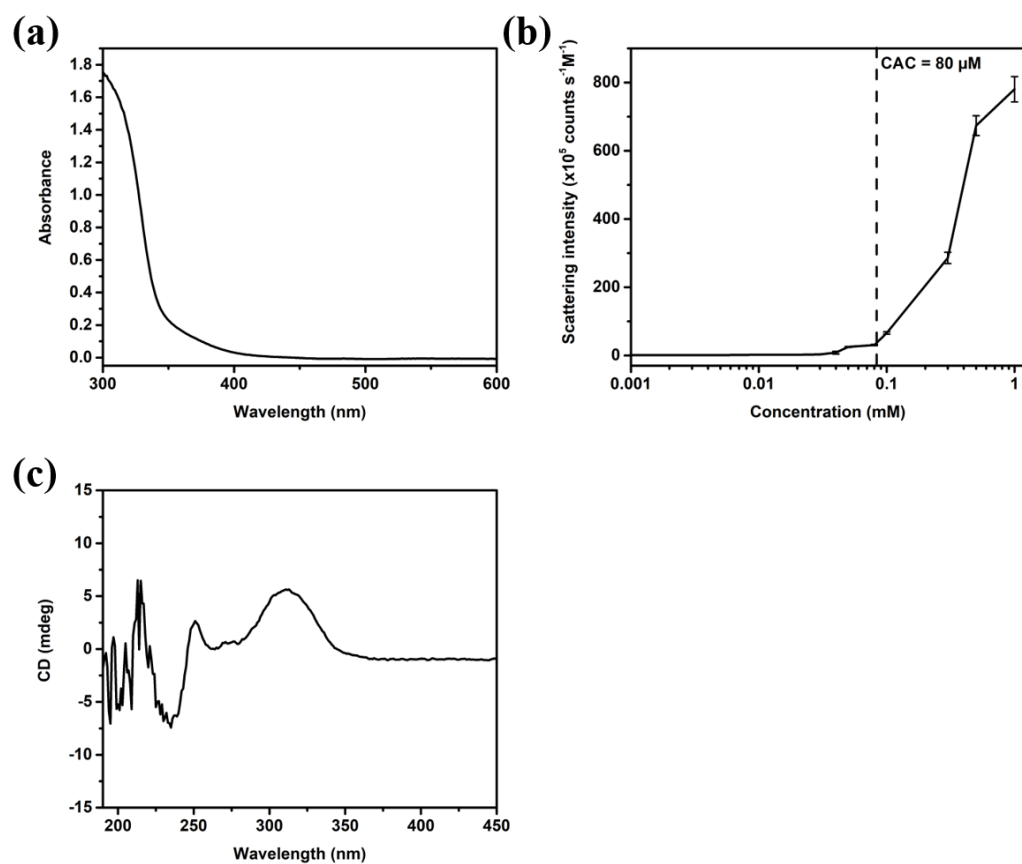
Figure S4.1 (a) UV-Vis absorption spectra of **GA 4.1** (400 µM) in DCM/MeOH 3:1; **(b)** The critical aggregation concentration of aqueous solution of **GA 4.1**; **(c)** CD spectra of **GA 4.1** (400 µM) in DCM/MeOH 3:1.
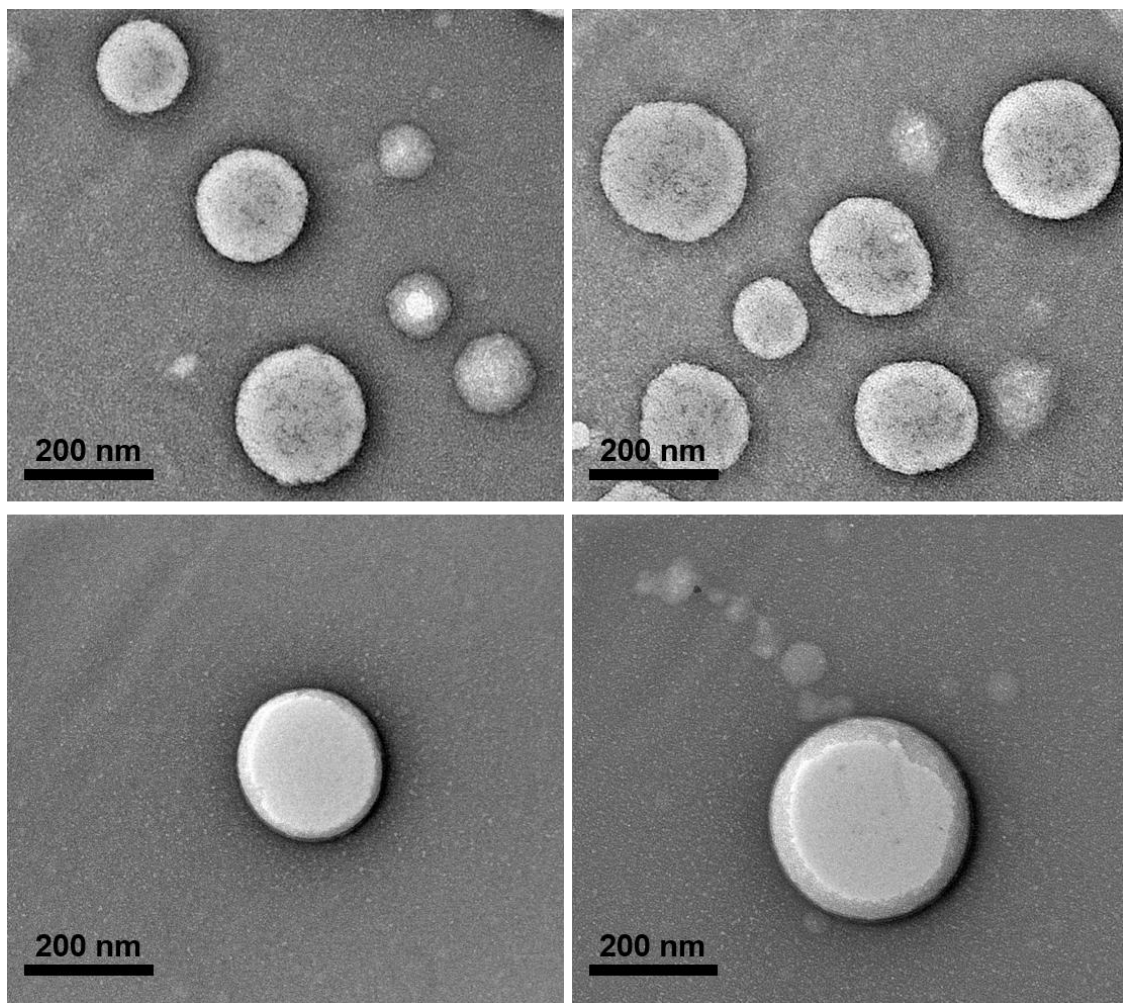
Figure S4.2 TEM images of the thermal annealed solution of **GA 4.1** (3.86 mM) after the addition of 2.0 equiv. of sodium D-camphorsulfonate.
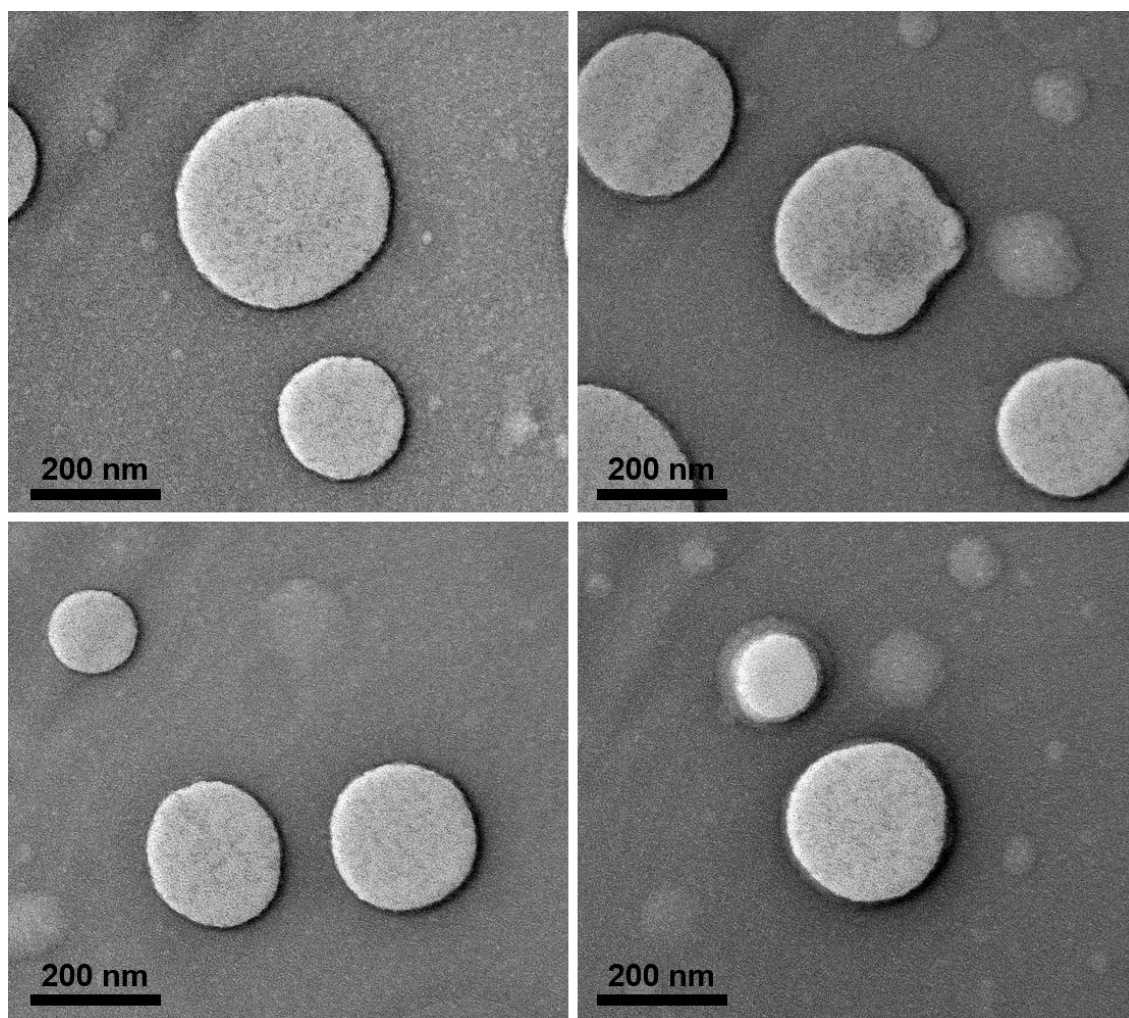
Figure S4.3 TEM images of the thermal annealed solution of **GA 4.1** (3.86 mM) after

the addition of 2.0 equiv. of sodium L-camphorsulfonate.
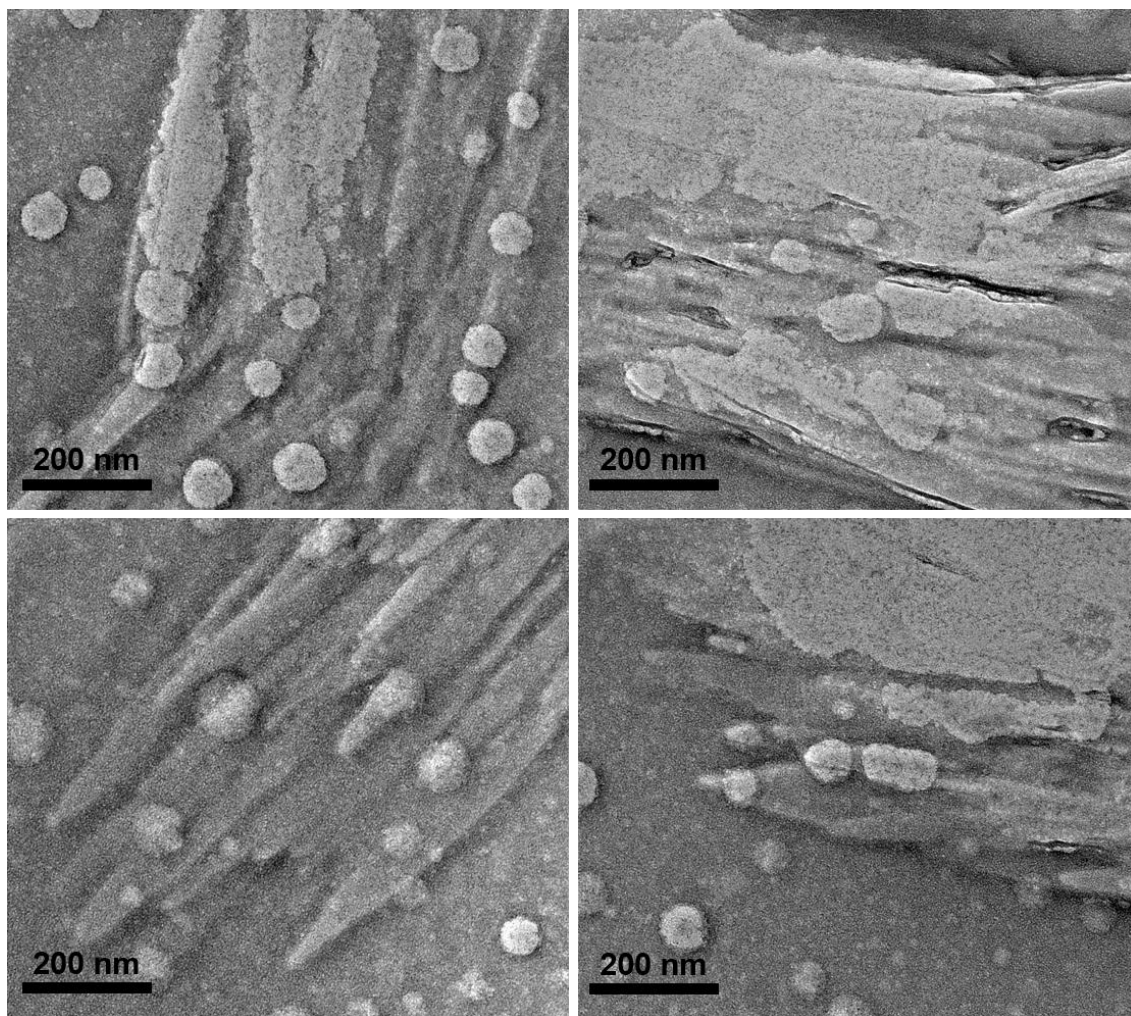
Figure S4.4 TEM images of the thermal annealed solution of **GA 4.1** (3.22 mM) after the addition of 4.0 equiv. of sodium D-camphorsulfonate.
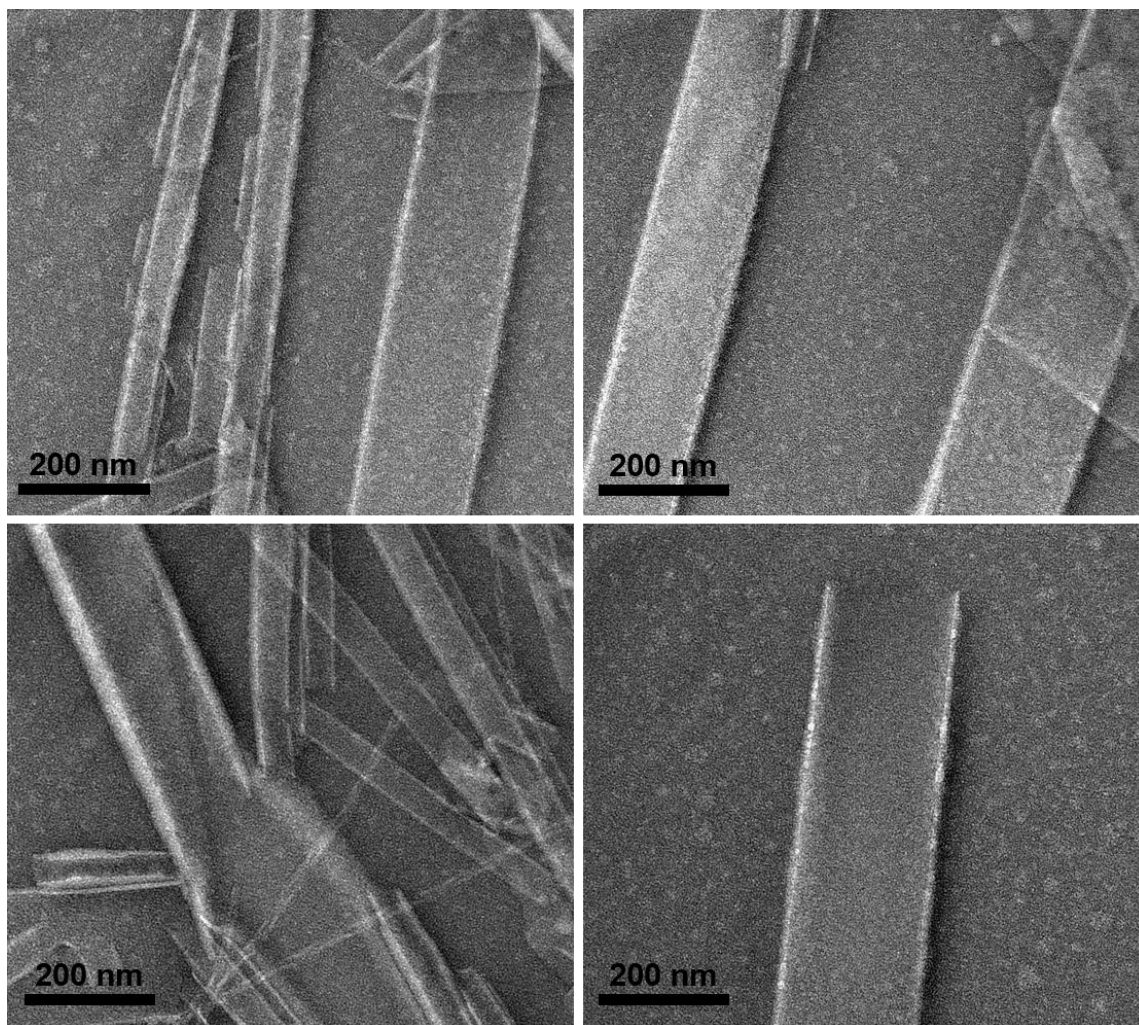
Figure S4.5 TEM images of the thermal annealed solution of **GA 4.1** (2.46 mM) after the addition of 8.0 equiv. of sodium D-camphorsulfonate.
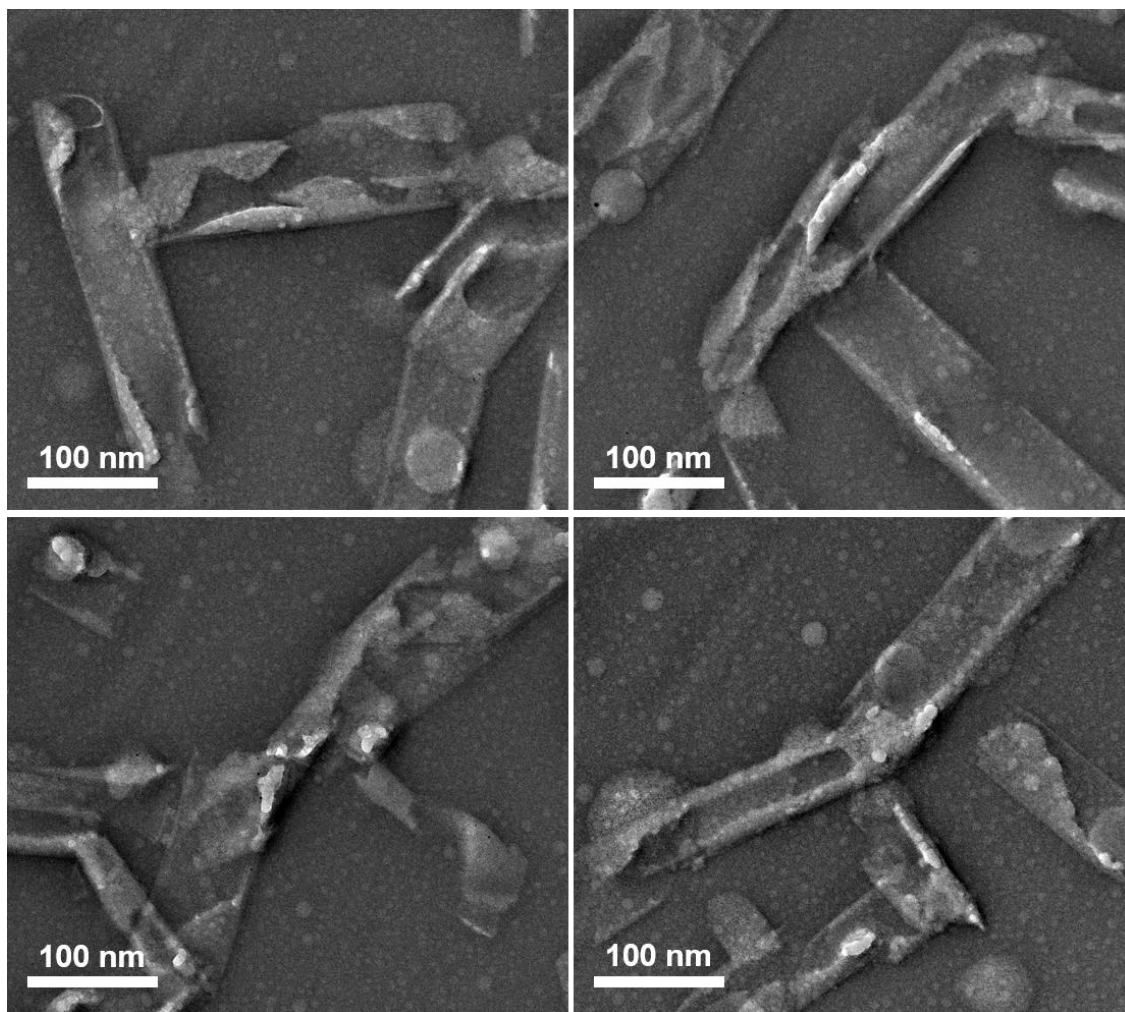
Figure S4.6 TEM images of the thermal annealed solution of **GA 4.1** (2.19 mM) after the addition of 10.0 equiv. of sodium D-camphorsulfonate.
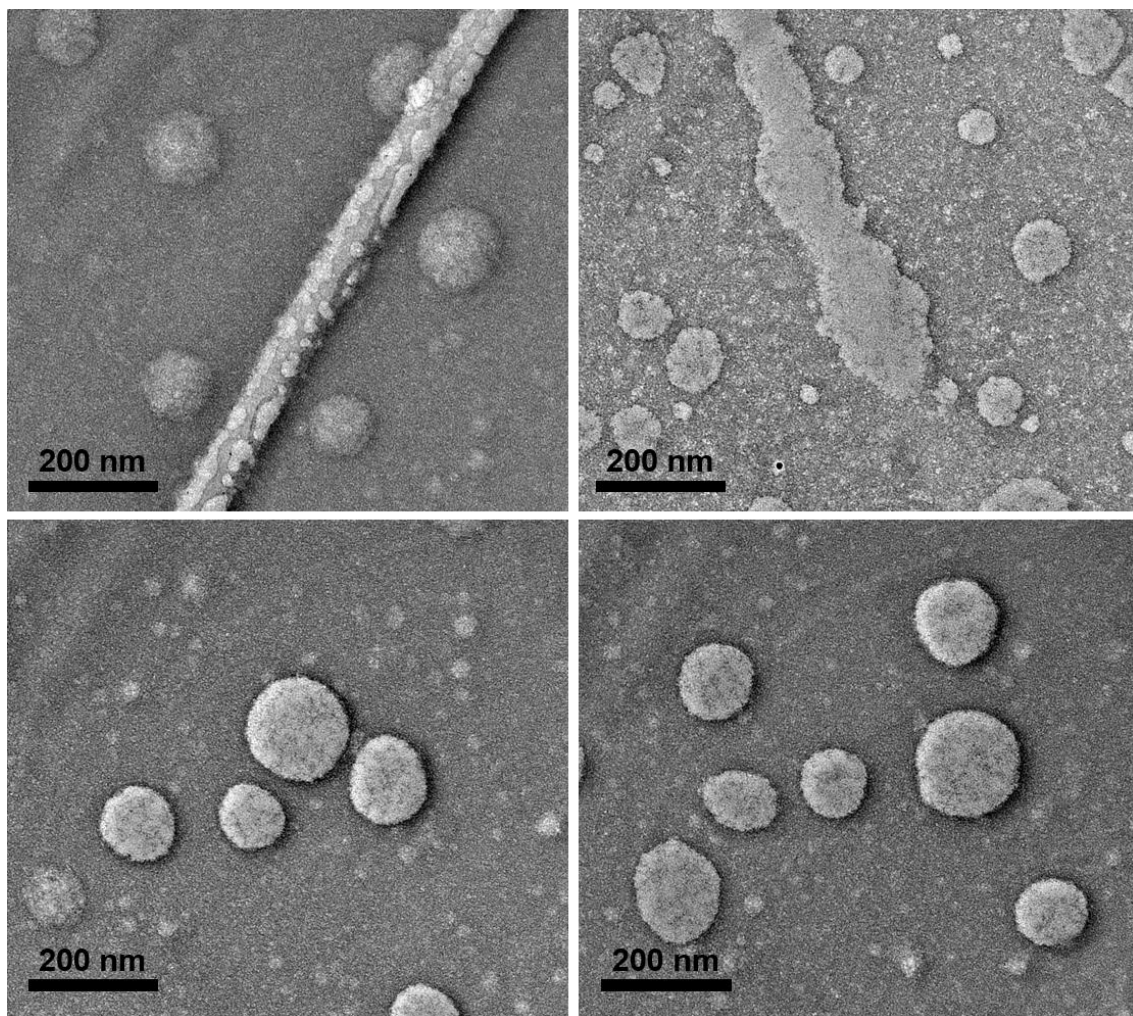
Figure S4.7 TEM images of the thermal annealed solution of **GA 4.1** (3.22 mM) after the addition of 4.0 equiv. of sodium L-camphorsulfonate.
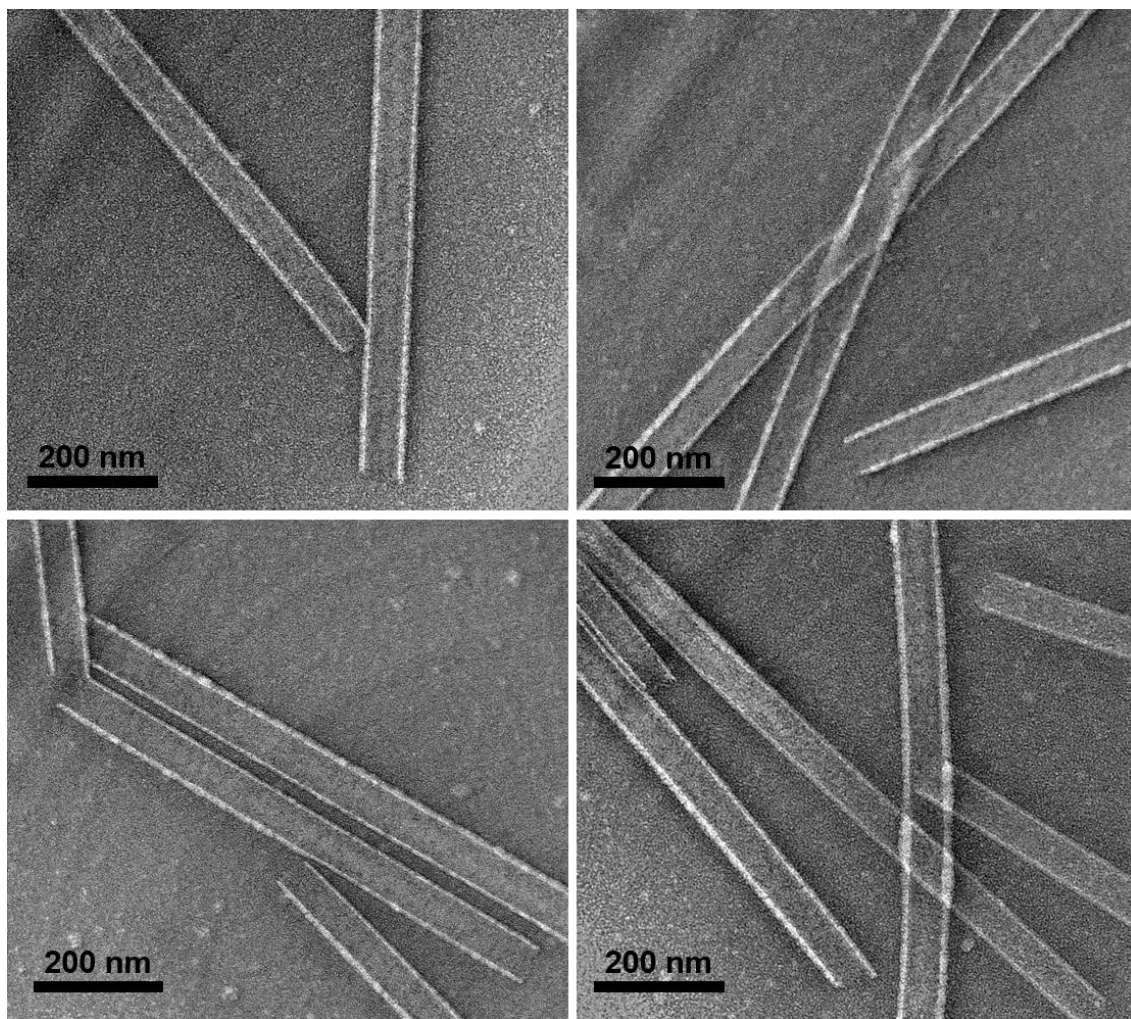
Figure S4.8 TEM images of the thermal annealed solution of **GA 4.1** (2.46 mM) after the addition of 8.0 equiv. of sodium L-camphorsulfonate.
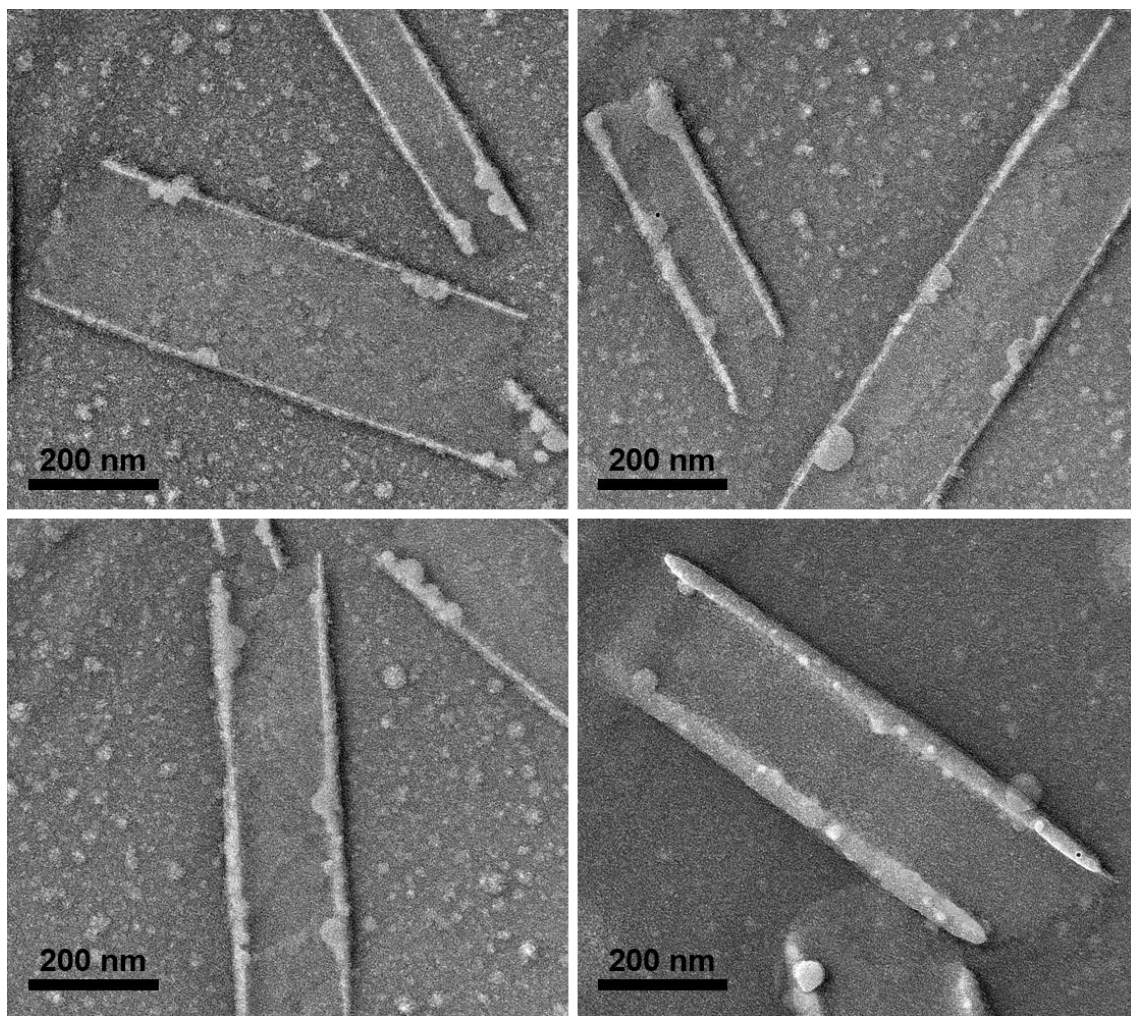
Figure S4.9 TEM images of the thermal annealed solution of **GA 4.1** (2.19 mM) after the addition of 10.0 equiv. of sodium L-camphorsulfonate.
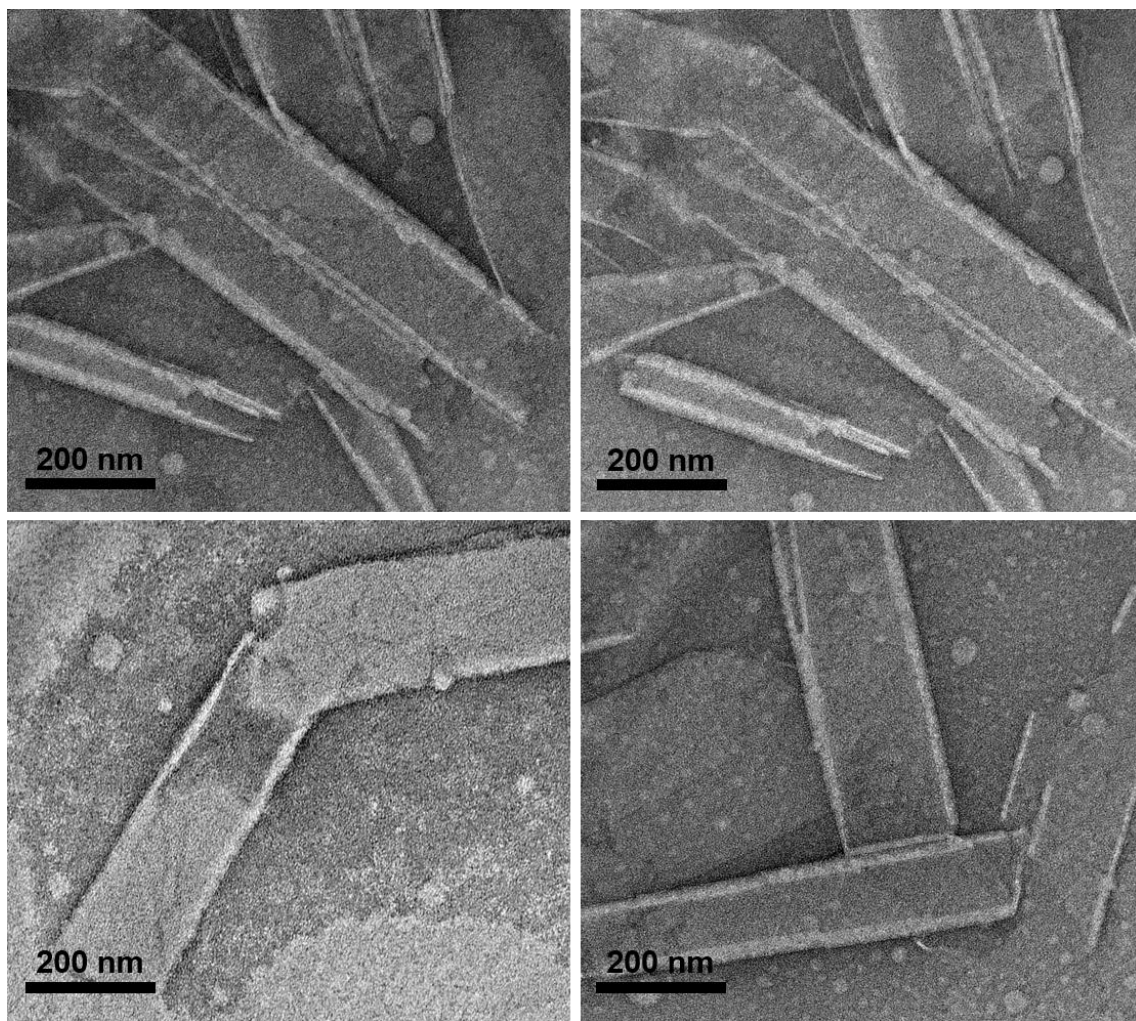
Figure S4.10 TEM images of the thermal annealed solution of **GA 4.1** (2.46 mM) after the addition of 8.0 equiv. of racemic mixture of camphorsulfonate.
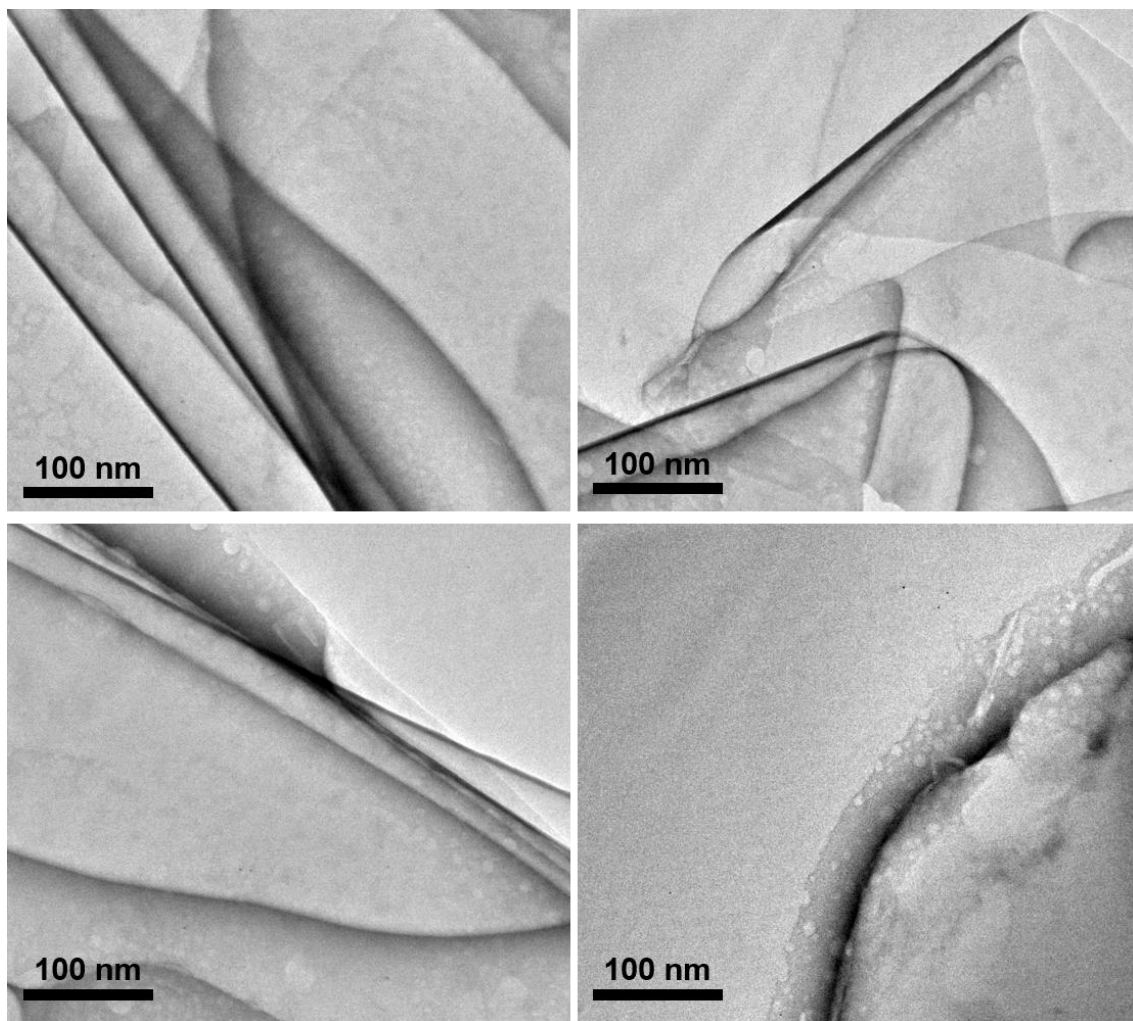
Figure S4.11 TEM images of the thermal annealed solution of **GA 4.1**D-Camphor (3.26 mM) after the addition of 2.0 equiv. of sodium tosylate.
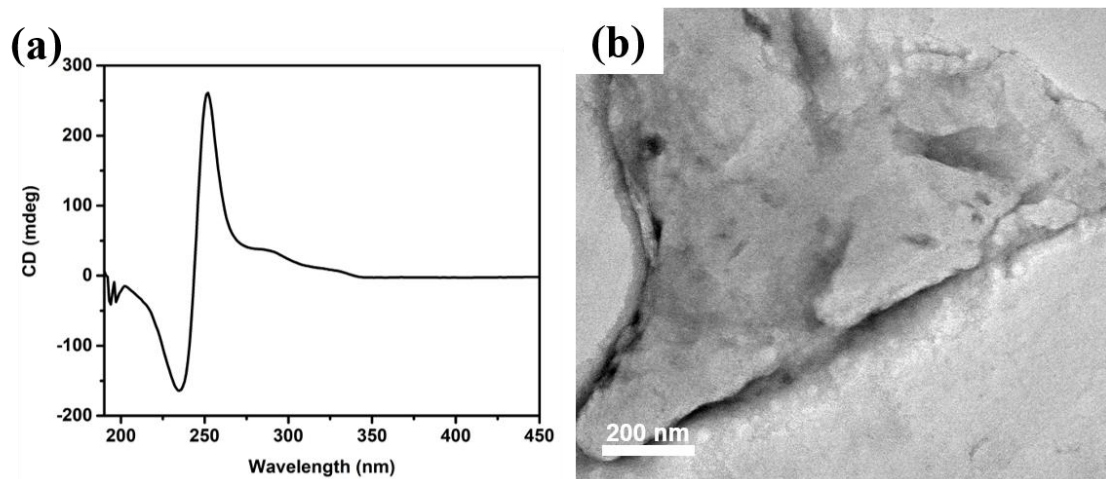
Figure S4.12 (a) CD spectrum of **GA 4.1L-Camphor** (400 µM) in DI water and **(b)** TEM image of the thermal annealed solution of **GA 4.1L-Camphor** (3.26 mM) after the addition of 2.0 equiv. of sodium tosylate.

4.4.12 NMR Spectra

^{1}H NMR of S4.2 in CDCl$_3$
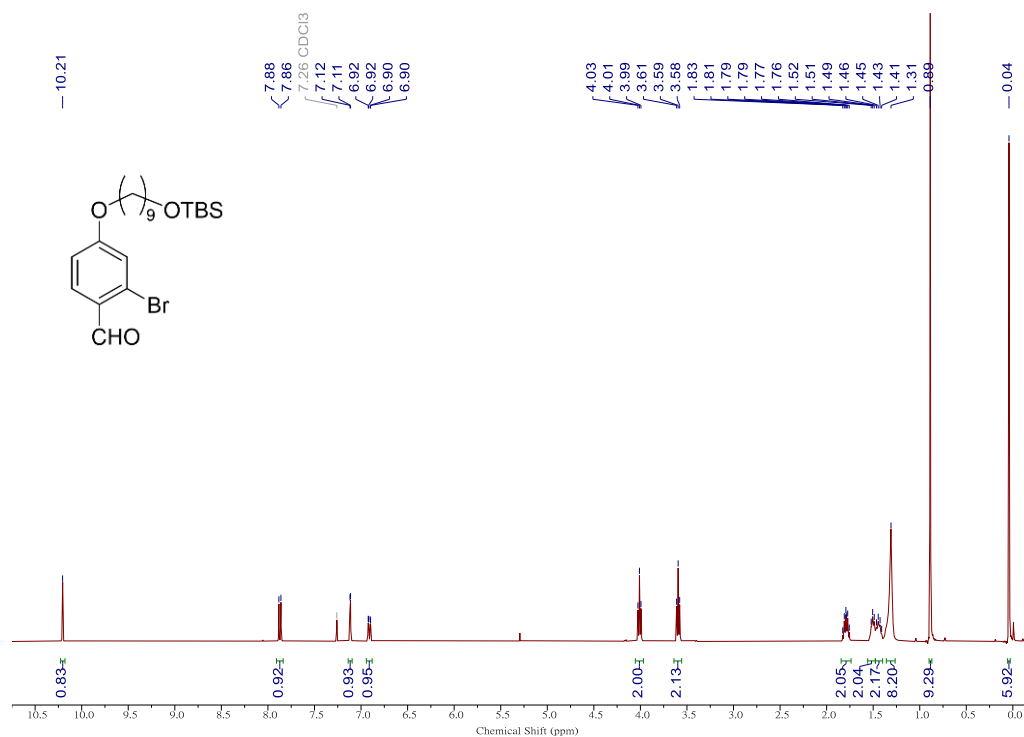
^{13}C NMR of S4.2 in CDCl$_3$
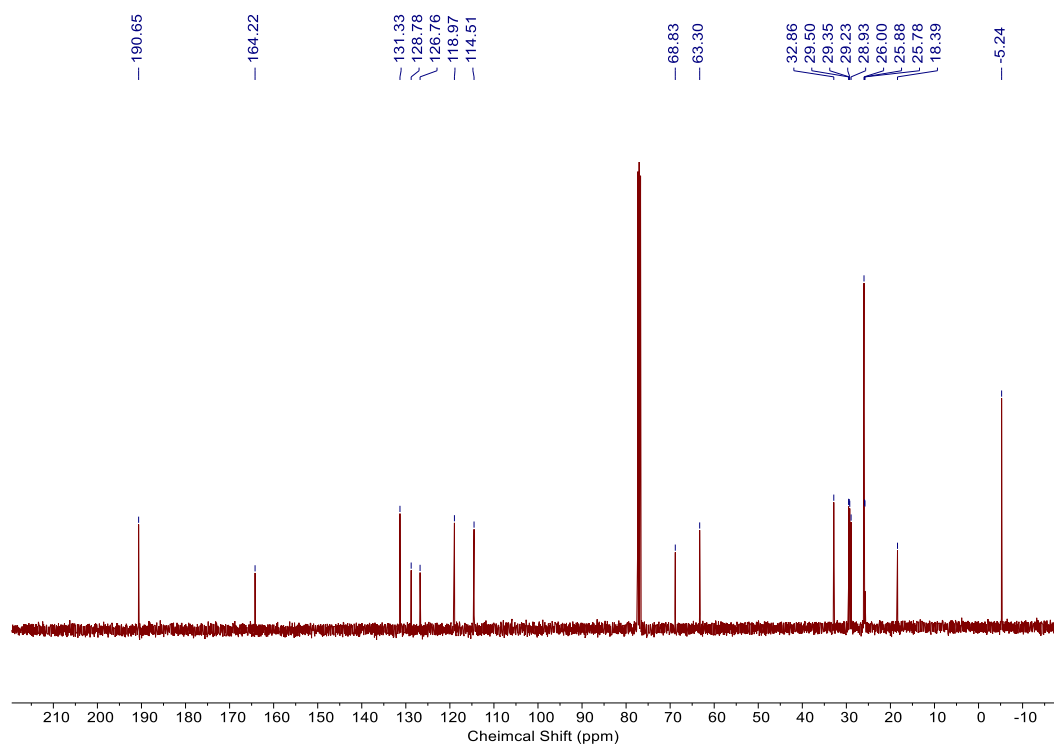
^{1}H NMR of S4.3 in CDCl$_3$

^{13}C NMR of S4.3 in CDCl$_3$

^{1}H NMR of S4.4 in CDCl$_3$

^{13}C NMR of S4.4 in CDCl$_3$

^{1}H NMR of S4.5 in CDCl$_3$

^{13}C NMR of S4.5 in CDCl$_3$

^{1}H NMR of S4.6 in CDCl$_3$

^{13}C NMR of S4.6 in CDCl$_3$

^{1}H NMR spectrum of S4.7 in CDCl$_3$

^{13}C NMR spectrum of S4.7 in CDCl$_3$

¹H NMR of GA 4.1 in CD₃OD

¹³C NMR of GA 4.1 in CD₃OD

References

1. Haruta, M. Gold rush. *Nature* **2005**, *437* (7062), 1098-1099.

2. (a) Hashmi, A. S. K. Homogeneous gold catalysts and alkynes: A successful liaison. *Gold Bulletin* **2003**, *36* (1), 3-9. (b) Hashmi, A. S.; Toste, D. F. *Modern gold catalyzed synthesis*; Wiley-VCH, 2012. (c) Toste, F. D.; Michelet, V. *Gold catalysis an homogeneous approach*; Imperial College Press, 2014.

3. Ito, Y.; Sawamura, M.; Hayashi, T. Catalytic asymmetric aldol reaction: reaction of aldehydes with isocyanoacetate catalyzed by a chiral ferrocenylphosphine-gold(I) complex. *Journal of the American Chemical Society* **1986**, *108* (20), 6405-6406.

4. (a) Fukuda, Y.; Utimoto, K. Effective transformation of unactivated alkynes into ketones or acetals with a gold(III) catalyst. *The Journal of Organic Chemistry* **1991**, *56* (11), 3729-3731. (b) Fukuda, Y.; Utimoto, K. Preparation of 2,3,4,5-Tetrahydropyridines from 5-Alkynylamines Under the Catalytic Action of Gold(III) Salts. *Synthesis* **1991**, *1991* (11), 975-978. (c) Fukuda, Y.; Utimoto, K. Efficient Transformation of Methyl Propargyl Ethers into α,β-Unsaturated Ketones. *Bulletin of the Chemical Society of Japan* **1991**, *64* (6), 2013-2015.

5. Teles, J. H.; Brode, S.; Chabanas, M. Cationic Gold(I) Complexes: Highly Efficient Catalysts for the Addition of Alcohols to Alkynes. *Angewandte Chemie International Edition* **1998**, *37* (10), 1415-1418.

6. Hashmi, A. S. K.; Schwarz, L.; Choi, J.-H.; Frost, T. M. A New Gold-Catalyzed C−C Bond Formation. *Angewandte Chemie International Edition* **2000**, *39* (13), 2285-2288.

7. Hashmi, A. S. K.; Frost, T. M.; Bats, J. W. Highly Selective Gold-Catalyzed Arene Synthesis. *Journal of the American Chemical Society* **2000**, *122* (46), 11553-11554.

8. Hashmi, A. S. K. The Catalysis Gold Rush: New Claims. *Angewandte Chemie International Edition* **2005**, *44* (43), 6990-6993.

9. (a) Hashmi, A. S. K. Gold-Catalyzed Organic Reactions. *Chemical Reviews* **2007**, *107* (7), 3180-3211. (b) Arcadi, A. Alternative Synthetic Methods through New Developments in Catalysis by Gold. *Chemical Reviews* **2008**, *108* (8), 3266-3325. (c) Gorin, D. J.; Sherry, B. D.; Toste, F. D. Ligand Effects in Homogeneous Au Catalysis. *Chemical Reviews* **2008**, *108* (8), 3351-3378. (d) Jiménez-Núñez, E.; Echavarren, A. M. Gold-Catalyzed Cycloisomerizations of Enynes: A Mechanistic Perspective. *Chemical Reviews* **2008**, *108* (8), 3326-3350. (e) Li, Z.; Brouwer, C.; He, C. Gold-Catalyzed Organic Transformations. *Chemical Reviews* **2008**, *108* (8), 3239-3265. (f) Corma, A.; Leyva-Pérez, A.; Sabater, M. J. Gold-Catalyzed Carbon−Heteroatom Bond-Forming Reactions. *Chemical Reviews* **2011**, *111* (3), 1657-1712. (g) Obradors, C.; Echavarren, A. M. Gold-Catalyzed Rearrangements and Beyond. *Accounts of Chemical Research* **2014**, *47* (3), 902-912. (h) Fensterbank, L.; Malacria, M. Molecular Complexity from Polyunsaturated Substrates: The Gold Catalysis Approach. *Accounts of Chemical Research* **2014**, *47* (3), 953-965. (i) Dorel, R.; Echavarren, A. M. Gold(I)-Catalyzed Activation of Alkynes for the Construction of Molecular Complexity. *Chemical Reviews* **2015**, *115* (17), 9028-9072. (j) Dorel, R.; Echavarren, A. M. Gold-Catalyzed Reactions via Cyclopropyl Gold Carbene-like Intermediates. *The Journal of Organic Chemistry* **2015**, *80* (15), 7321-7332. (k) Pflästerer, D.; Hashmi, A. S. K. Gold catalysis in total synthesis – recent achievements. *Chemical Society Reviews* **2016**, *45* (5), 1331-1367. (l) Asiri, A. M.; Hashmi, A. S. K. Gold-catalysed reactions of diynes. *Chemical Society Reviews* **2016**, *45* (16), 4471-4503. (m) Day, D. P.; Chan, P. W. H. Gold-Catalyzed Cycloisomerizations of 1,n-Diyne Carbonates and Esters. *Advanced Synthesis &*

Catalysis **2016**, *358* (9), 1368-1384. (n) Ma, B.; Liu, L.; Zhang, J. Gold-Catalyzed Site-Selective C−H Bond Functionalization with Diazo Compounds. *Asian Journal of Organic Chemistry* **2018**, *7* (10), 2015-2025. (o) Mato, M.; Franchino, A.; García-Morales, C.; Echavarren, A. M. Gold-Catalyzed Synthesis of Small Rings. *Chemical Reviews* **2021**, *121* (14), 8613-8684. (p) Chintawar, C. C.; Yadav, A. K.; Kumar, A.; Sancheti, S. P.; Patil, N. T. Divergent Gold Catalysis: Unlocking Molecular Diversity through Catalyst Control. *Chemical Reviews* **2021**, *121* (14), 8478-8558. (q) Hashmi, A. S. K. Introduction: Gold Chemistry. *Chemical Reviews* **2021**, *121* (14), 8309-8310. (r) Rocchigiani, L.; Bochmann, M. Recent Advances in Gold(III) Chemistry: Structure, Bonding, Reactivity, and Role in Homogeneous Catalysis. *Chemical Reviews* **2021**, *121* (14), 8364-8451.

10. (a) Fürstner, A. From Understanding to Prediction: Gold- and Platinum-Based π-Acid Catalysis for Target Oriented Synthesis. *Accounts of Chemical Research* **2014**, *47* (3), 925-938. (b) Zhang, Y.; Luo, T.; Yang, Z. Strategic innovation in the total synthesis of complex natural products using gold catalysis. *Natural Product Reports* **2014**, *31* (4), 489-503. (c) Lo, V. K.-Y.; Chan, A. O.-Y.; Che, C.-M. Gold and silver catalysis: from organic transformation to bioconjugation. *Organic & Biomolecular Chemistry* **2015**, *13* (24), 6667-6680. (d) Quach, R.; Furkert, D. P.; Brimble, M. A. Gold catalysis: synthesis of spiro, bridged, and fused ketal natural products. *Organic & Biomolecular Chemistry* **2017**, *15* (15), 3098-3104. (e) Pirovano, V. Gold-Catalyzed Functionalization Reactions of Indole. *European Journal of Organic Chemistry* **2018**, *2018* (17), 1925-1945. (f) Cheng, X.; Quintanilla, C. D.; Zhang, L. Total Synthesis and Structure Revision of Diplobifuranylone B. *The Journal of Organic Chemistry* **2019**, *84* (17), 11054-11060.

11. Gorin, D. J.; Toste, F. D. Relativistic effects in homogeneous gold catalysis. *Nature* **2007**, *446* (7134), 395-403.

12. Pyykkö, P. Relativity, Gold, Closed-Shell Interactions, and CsAu·NH₃. *Angewandte Chemie International Edition* **2002**, *41* (19), 3573-3578.

13. (a) Pyykkö, P. Theoretical Chemistry of Gold. *Angewandte Chemie International Edition* **2004**, *43* (34), 4412-4456. (b) Leyva-Pérez, A.; Corma, A. Similarities and Differences between the "Relativistic" Triad Gold, Platinum, and Mercury in Catalysis. *Angewandte Chemie International Edition* **2012**, *51* (3), 614-635.

14. Desclaux, J. P.; Pyykkö, P. Dirac-Fock one-centre calculations. The molecules CuH, AgH and AuH including p-type symmetry functions. *Chemical Physics Letters* **1976**, *39* (2), 300-303.

15. Schwarz, H. Relativistic Effects in Gas-Phase Ion Chemistry: An Experimentalist's View. *Angewandte Chemie International Edition* **2003**, *42* (37), 4442-4454.

16. (a) Schwerdtfeger, P.; Boyd, P. D. W.; Brienne, S.; Burrell, A. K. Relativistic effects in gold chemistry. 4. Gold(III) and gold(V) compounds. *Inorganic Chemistry* **1992**, *31* (16), 3411-3422. (b) Pérez-Bitrián, A.; Baya, M.; Casas, J. M.; Martín, A.; Menjón, B.; Orduna, J. An Organogold(III) Difluoride with a trans Arrangement. *Angewandte Chemie International Edition* **2018**, *57* (22), 6517-6521.

17. (a) Cao, L.; Jennings, M. C.; Puddephatt, R. J. Amine−Amide Equilibrium in Gold(III) Complexes and a Gold(III)−Gold(I) Aurophilic Bond. *Inorganic Chemistry* **2007**, *46* (4), 1361-1368. (b) Lu, W.; Chan, K. T.; Wu, S.-X.; Chen, Y.; Che, C.-M. Quest for an intermolecular Au(iii)···Au(iii) interaction between cyclometalated gold(iii) cations. *Chemical Science* **2012**, *3* (3), 752-755. (c) Chernyshev, A. N.; Chernysheva, M. V.; Hirva, P.; Kukushkin, V. Y.; Haukka, M. Weak aurophilic interactions in a series of Au(iii) double salts. *Dalton Transactions* **2015**, *44* (32), 14523-14531.

18. Nunes dos Santos Comprido, L.; Hashmi, A. S. K. Catalytic Oxidative Cyclisation Reactions of 1,6-Enynes: A Critical Comparison Between Gold and Palladium. *Israel Journal of Chemistry* **2013**, *53* (11-12), 883-891.

19. Bratsch, S. G. Standard Electrode Potentials and Temperature Coefficients in Water at 298.15 K. *Journal of Physical and Chemical Reference Data* **1989**, *18* (1), 1-21.

20. Kumar, R.; Nevado, C. Cyclometalated Gold(III) Complexes: Synthesis, Reactivity, and Physicochemical Properties. *Angewandte Chemie International Edition* **2017**, *56* (8), 1994-2015.

21. Harris, R. J.; Widenhoefer, R. A. Gold carbenes, gold-stabilized carbocations, and cationic intermediates relevant to gold-catalysed enyne cycloaddition. *Chemical Society Reviews* **2016**, *45* (16), 4533-4551.

22. (a) Hashmi, A. S. K. Homogeneous Gold Catalysis Beyond Assumptions and Proposals—Characterized Intermediates. *Angewandte Chemie International Edition* **2010**, *49* (31), 5232-5241. (b) Fürstner, A.; Davies, P. W. Catalytic Carbophilic Activation: Catalysis by Platinum and Gold π Acids. *Angewandte Chemie International Edition* **2007**, *46* (19), 3410-3449. (c) Gimeno, M. C.; Laguna, A. Three- and Four-Coordinate Gold(I) Complexes. *Chemical Reviews* **1997**, *97* (3), 511-522.

23. (a) Wang, Y.-M.; Lackner, A. D.; Toste, F. D. Development of Catalysts and Ligands for Enantioselective Gold Catalysis. *Accounts of Chemical Research* **2014**, *47* (3), 889-901. (b) Widenhoefer, R. A. Recent Developments in Enantioselective Gold(I) Catalysis. *Chemistry – A European Journal* **2008**, *14* (18), 5382-5391. (c) Bongers, N.; Krause, N. Golden Opportunities in Stereoselective Catalysis. *Angewandte Chemie International Edition* **2008**, *47* (12), 2178-2181. (d) Sengupta, S.; Shi, X. Recent Advances in Asymmetric Gold Catalysis. *ChemCatChem* **2010**, *2* (6), 609-619. (e) Pradal, A.; Toullec,

P. Y.; Michelet, V. Recent Developments in Asymmetric Catalysis in the Presence of Chiral Gold Complexes. *Synthesis* **2011**, *2011* (10), 1501-1514. (f) Cera, G.; Bandini, M. Enantioselective Gold(I) Catalysis with Chiral Monodentate Ligands. *Israel Journal of Chemistry* **2013**, *53* (11-12), 848-855. (g) Zi, W.; Dean Toste, F. Recent advances in enantioselective gold catalysis. *Chemical Society Reviews* **2016**, *45* (16), 4567-4589. (h) Li, Y.; Li, W.; Zhang, J. Gold-Catalyzed Enantioselective Annulations. *Chemistry – A European Journal* **2017**, *23* (3), 467-512. (i) Zuccarello, G.; Zanini, M.; Echavarren, A. M. Buchwald-Type Ligands on Gold(I) Catalysis. *Israel Journal of Chemistry* **2020**, *60* (3-4), 360-372. (j) Cheng, X.; Zhang, L. Designed Bifunctional Ligands in Cooperative Homogeneous Gold Catalysis. *CCS Chemistry* **2020**, *3* (1), 1989-2002. (k) Herrera, R. P.; Gimeno, M. C. Main Avenues in Gold Coordination Chemistry. *Chemical Reviews* **2021**, *121* (14), 8311-8363. (l) Das, A.; Patil, N. T. Enantioselective C−H Functionalization Reactions under Gold Catalysis. *Chemistry – A European Journal* **2022**, *28* (20), e202104371. (m) Hashmi, A. S. K. Raising the gold standard. *Nature* **2007**, *449* (7160), 292-293.

24. (a) Hamilton, G. L.; Kang, E. J.; Mba, M.; Toste, F. D. A Powerful Chiral Counterion Strategy for Asymmetric Transition Metal Catalysis. *Science* **2007**, *317* (5837), 496-499. (b) Hashmi, A. S. K.; Hubbert, C. Gold and Organocatalysis Combined. *Angewandte Chemie International Edition* **2010**, *49* (6), 1010-1012. (c) Phipps, R. J.; Hamilton, G. L.; Toste, F. D. The progression of chiral anions from concepts to applications in asymmetric catalysis. *Nature Chemistry* **2012**, *4* (8), 603-614. (d) Patil, N. T. Chirality Transfer and Memory of Chirality in Gold-Catalyzed Reactions. *Chemistry – An Asian Journal* **2012**, *7* (10), 2186-2194. (e) Loh, C. C. J.; Enders, D. Merging Organocatalysis and Gold Catalysis—A Critical Evaluation of the Underlying Concepts. *Chemistry – A European*

Journal **2012**, *18* (33), 10212-10225. (f) Inamdar, S. M.; Konala, A.; Patil, N. T. When gold meets chiral Brønsted acid catalysts: extending the boundaries of enantioselective gold catalysis. *Chemical Communications* **2014**, *50* (96), 15124-15135. (g) Chen, D.-F.; Han, Z.-Y.; Zhou, X.-L.; Gong, L.-Z. Asymmetric Organocatalysis Combined with Metal Catalysis: Concept, Proof of Concept, and Beyond. *Accounts of Chemical Research* **2014**, *47* (8), 2365-2377. (h) Ranieri, B.; Escofet, I.; Echavarren, A. M. Anatomy of gold catalysts: facts and myths. *Organic & Biomolecular Chemistry* **2015**, *13* (26), 7103-7118. (i) Jia, M.; Bandini, M. Counterion Effects in Homogeneous Gold Catalysis. *ACS Catalysis* **2015**, *5* (3), 1638-1652. (j) Wang, W.; Ji, C.-L.; Liu, K.; Zhao, C.-G.; Li, W.; Xie, J. Dinuclear gold catalysis. *Chemical Society Reviews* **2021**, *50* (3), 1874-1912. (k) Pegu, C.; Paroi, B.; Patil, N. T. Enantioselective merged gold/organocatalysis. *Chemical Communications* **2024**, *60* (27), 3607-3623.

25. (a) Alonso, I.; Trillo, B.; López, F.; Montserrat, S.; Ujaque, G.; Castedo, L.; Lledós, A.; Mascareñas, J. L. Gold-Catalyzed [4C+2C] Cycloadditions of Allenedienes, including an Enantioselective Version with New Phosphoramidite-Based Catalysts: Mechanistic Aspects of the Divergence between [4C+3C] and [4C+2C] Pathways. *Journal of the American Chemical Society* **2009**, *131* (36), 13020-13030. (b) Teller, H.; Flügge, S.; Goddard, R.; Fürstner, A. Enantioselective Gold Catalysis: Opportunities Provided by Monodentate Phosphoramidite Ligands with an Acyclic TADDOL Backbone. *Angewandte Chemie International Edition* **2010**, *49* (11), 1949-1953. (c) Yavari, K.; Aillard, P.; Zhang, Y.; Nuter, F.; Retailleau, P.; Voituriez, A.; Marinetti, A. Helicenes with Embedded Phosphole Units in Enantioselective Gold Catalysis. *Angewandte Chemie International Edition* **2014**, *53* (3), 861-865. (d) Zhang, Z.-M.; Chen, P.; Li, W.; Niu, Y.; Zhao, X.-L.; Zhang, J. A New Type of Chiral Sulfinamide

Monophosphine Ligands: Stereodivergent Synthesis and Application in Enantioselective Gold(I)-Catalyzed Cycloaddition Reactions. *Angewandte Chemie International Edition* **2014**, *53* (17), 4350-4354. (e) Zuccarello, G.; Mayans, J. G.; Escofet, I.; Scharnagel, D.; Kirillova, M. S.; Pérez-Jimeno, A. H.; Calleja, P.; Boothe, J. R.; Echavarren, A. M. Enantioselective Folding of Enynes by Gold(I) Catalysts with a Remote C2-Chiral Element. *Journal of the American Chemical Society* **2019**, *141* (30), 11858-11863.

26. (a) Jiang, J.-J.; Wong, M.-K. Recent Advances in the Development of Chiral Gold Complexes for Catalytic Asymmetric Catalysis. *Chemistry – An Asian Journal* **2021**, *16* (5), 364-377. (b) Zuccarello, G.; Escofet, I.; Caniparoli, U.; Echavarren, A. M. New-Generation Ligand Design for the Gold-Catalyzed Asymmetric Activation of Alkynes. *ChemPlusChem* **2021**, *86* (9), 1283-1296. (c) Mishra, S.; Urvashi; Patil, N. T. Chiral Ligands for Au(I), Au(III), and Au(I)/Au(III) Redox Catalysis. *Israel Journal of Chemistry* **2023**, *63* (9), e202200039. (d) Gade, A. B.; Urvashi; Patil, N. T. Asymmetric gold catalysis enabled by specially designed ligands. *Organic Chemistry Frontiers* **2024**, *11* (6), 1858-1895.

27. (a) Rodriguez, J.; Bourissou, D. Well-Defined Chiral Gold(III) Complexes: New Opportunities in Asymmetric Catalysis. *Angewandte Chemie International Edition* **2018**, *57* (2), 386-388. (b) Jouhannet, R.; Dagorne, S.; Blanc, A.; de Frémont, P. Chiral Gold(III) Complexes: Synthesis, Structure, and Potential Applications. *Chemistry – A European Journal* **2021**, *27* (36), 9218-9240. (c) Chintawar, C. C.; Patil, N. T. Enantioselective redox gold catalysis. *Gold Bulletin* **2022**, *55* (2), 161-168.

28. Michalak, M.; Kośnik, W. Chiral N-heterocyclic Carbene Gold Complexes: Synthesis and Applications in Catalysis. In *Catalysts*, 2019; Vol. 9.

29. Wu, C.-Y.; Horibe, T.; Jacobsen, C. B.; Toste, F. D. Stable gold(III) catalysts by oxidative addition of a carbon–carbon bond. *Nature* **2015**, *517* (7535), 449-454.

30. Bohan, P. T.; Toste, F. D. Well-Defined Chiral Gold(III) Complex Catalyzed Direct Enantioconvergent Kinetic Resolution of 1,5-Enynes. *Journal of the American Chemical Society* **2017**, *139* (32), 11016-11019.

31. Reid, J. P.; Hu, M.; Ito, S.; Huang, B.; Hong, C. M.; Xiang, H.; Sigman, M. S.; Toste, F. D. Strategies for remote enantiocontrol in chiral gold(iii) complexes applied to catalytic enantioselective γ,δ-Diels–Alder reactions. *Chemical Science* **2020**, *11* (25), 6450-6456.

32. Lo, V. K.-Y.; Kung, K. K.-Y.; Wong, M.-K.; Che, C.-M. Gold(III) (C^N) complex-catalyzed synthesis of propargylamines via a three-component coupling reaction of aldehydes, amines and alkynes. *Journal of Organometallic Chemistry* **2009**, *694* (4), 583-591.

33. Ko, H.-M.; Kung, K. K.-Y.; Cui, J.-F.; Wong, M.-K. Bis-cyclometallated gold(iii) complexes as efficient catalysts for synthesis of propargylamines and alkylated indoles. *Chemical Communications* **2013**, *49* (78), 8869-8871.

34. Cui, J.-F.; Ko, H.-M.; Shing, K.-P.; Deng, J.-R.; Lai, N. C.-H.; Wong, M.-K. C,O-Chelated BINOL/Gold(III) Complexes: Synthesis and Catalysis with Tunable Product Profiles. *Angewandte Chemie International Edition* **2017**, *56* (11), 3074-3079.

35. Jiang, J.-J.; Cui, J.-F.; Yang, B.; Ning, Y.; Lai, N. C.-H.; Wong, M.-K. Chiral Cyclometalated Oxazoline Gold(III) Complex-Catalyzed Asymmetric Carboalkoxylation of Alkynes. *Organic Letters* **2019**, *21* (16), 6289-6294.

36. Lehn, J.-M. Supramolecular polymer chemistry—scope and perspectives. *Polymer International* **2002**, *51* (10), 825-839.

37. Lehn, J. M. Cryptates: the chemistry of macropolycyclic inclusion complexes. *Accounts of Chemical Research* **1978**, *11* (2), 49-57.

38. Lehn, J.-M. Supramolecular chemistry: Where from? Where to? *Chemical Society Reviews* **2017**, *46* (9), 2378-2379.

39. (a) Alivisatos, P.; Barbara, P. F.; Castleman, A. W.; Chang, J.; Dixon, D. A.; Klein, M. L.; McLendon, G. L.; Miller, J. S.; Ratner, M. A.; Rossky, P. J.; et al. From Molecules to Materials: Current Trends and Future Directions. *Advanced Materials* **1998**, *10* (16), 1297-1336. (b) Li, X.; Liu, X.; Liu, X. Self-assembly of colloidal inorganic nanocrystals: nanoscale forces, emergent properties and applications. *Chemical Society Reviews* **2021**, *50* (3), 2074-2101.

40. Glotzer, S. C.; Solomon, M. J. Anisotropy of building blocks and their assembly into complex structures. *Nature Materials* **2007**, *6* (8), 557-562.

41. (a) Gompper, G.; Schick, M. *Self-assembling amphiphilic systems*; Academic Press, 1994. (b) Wang, C.; Wang, Z.; Zhang, X. Amphiphilic Building Blocks for Self-Assembly: From Amphiphiles to Supra-amphiphiles. *Accounts of Chemical Research* **2012**, *45* (4), 608-618.

42. Lombardo, D.; Kiselev, M. A.; Magazù, S.; Calandra, P. Amphiphiles Self-Assembly: Basic Concepts and Future Perspectives of Supramolecular Approaches. *Advances in Condensed Matter Physics* **2015**, *2015* (1), 151683.

43. (a) Holmberg; Jonsson; Kronberg; Lindman; Jonsson, B.; Kronberg, B.; Lindman, B. *Surfactants and Polymers in Aqueous Solution*; Wiley, 2002. (b) Rosen, M. J.; Kunjappu, J. T. *Surfactants and Interfacial Phenomena*; Wiley, 2012.

44. Dutta, B.; Barick, K. C.; Verma, G.; Choudhury, S.; Ganguly, R.; Hassan, P. A. Amphiphilic Self-Assembly in the Synthesis and Processing of Nanomaterials. In

Handbook on Synthesis Strategies for Advanced Materials: Volume-II: Processing and Functionalization of Materials, Tyagi, A. K., Ningthoujam, R. S. Eds.; Springer Nature Singapore, 2022; pp 475-514.

45. Israelachvili, J. N. *Intermolecular and surface forces*; Academic Press, 2011.

46. (a) Tanford, C. Thermodynamics of Micelle Formation: Prediction of Micelle Size and Size Distribution. *Proceedings of the National Academy of Sciences* **1974**, *71* (5), 1811-1815. (b) Wagay, T. A.; Askari, H.; Ismail, K. Synthesis, aggregation and adsorption behavior of benzyldimethylhexadecylammonium based double-chained metallosurfactants. *Journal of Molecular Liquids* **2020**, *299*, 112234.

47. Donner, A.; Trepka, B.; Theiss, S.; Immler, F.; Traber, J.; Polarz, S. NHC-Metallosurfactants as Active Polymerization Catalysts. *Langmuir* **2019**, *35* (50), 16514-16520.

48. Parera, E.; Marín-García, M.; Pons, R.; Comelles, F.; Suades, J.; Barnadas-Rodríguez, R. Supramolecular Arrangement of Molybdenum Carbonyl Metallosurfactants with CO-Releasing Properties. *Organometallics* **2016**, *35* (4), 484-493.

49. Lorenzetto, T.; Fabris, F.; Scarso, A. Recent metallosurfactants for sustainable catalysis in water. *Current Opinion in Colloid & Interface Science* **2023**, *64*, 101689.

50. A. Fallis, I.; C. Griffiths, P.; E. Hibbs, D.; B. Hursthouse, M.; L. Winnington, A. Solid state and solution behaviour of novel transition metal containing surfactants. *Chemical Communications* **1998**,   (6), 665-666.

51. (a) Zhang, J.; Meng, X.-G.; Zeng, X.-C.; Yu, X.-Q. Metallomicellar supramolecular systems and their applications in catalytic reactions. *Coordination Chemistry Reviews* **2009**, *253* (17), 2166-2177. (b) Bhattacharya, S.; Kumari, N. Metallomicelles as potent

catalysts for the ester hydrolysis reactions in water. *Coordination Chemistry Reviews* **2009**, *253* (17), 2133-2149.

52. Mauro, M.; De Paoli, G.; Otter, M.; Donghi, D.; D'Alfonso, G.; De Cola, L. Aggregation induced colour change for phosphorescent iridium(iii) complex-based anionic surfactants. *Dalton Transactions* **2011**, *40* (45), 12106-12116.

53. Gong, P.; Chen, Z.; Chen, Y.; Wang, W.; Wang, X.; Hu, A. High-relaxivity MRI contrast agents prepared from miniemulsion polymerization using gadolinium(iii)-based metallosurfactants. *Chemical Communications* **2011**, *47* (14), 4240-4242.

54. Kaur, R.; Mehta, S. K. Self aggregating metal surfactant complexes: Precursors for nanostructures. *Coordination Chemistry Reviews* **2014**, *262*, 37-54.

55. Wang, F.; Lan, M.; To, W.-P.; Li, K.; Lok, C.-N.; Wang, P.; Che, C.-M. A macromolecular cyclometalated gold(iii) amphiphile displays long-lived emissive excited state in water: self-assembly and in vitro photo-toxicity. *Chemical Communications* **2016**, *52* (90), 13273-13276.

56. Wan, Q.; Xia, J.; Lu, W.; Yang, J.; Che, C.-M. Kinetically Controlled Self-Assembly of Phosphorescent AuIII Aggregates and Ligand-to-Metal–Metal Charge Transfer Excited State: A Combined Spectroscopic and DFT/TDDFT Study. *Journal of the American Chemical Society* **2019**, *141* (29), 11572-11582.

57. Jiang, J.-J.; Chau, A. K.-H.; Wong, M.-K.; Leung, F. K.-C. Controlled Supramolecular Assembly of Gold (III) Amphiphiles in Aqueous Media. *European Journal of Inorganic Chemistry* **2022**, *2022* (24), e202200281.

58. (a) Williams, J. A. G. The coordination chemistry of dipyridylbenzene: N-deficient terpyridine or panacea for brightly luminescent metal complexes? *Chemical Society Reviews* **2009**, *38* (6), 1783-1801. (b) Baldo, M. A.; Thompson, M. E.; Forrest, S. R.

High-efficiency fluorescent organic light-emitting devices using a phosphorescent sensitizer. *Nature* **2000**, *403* (6771), 750-753.

59. (a) Balzani, V.; Campagna, S.; Accorsi, G. *Photochemistry and photophysics of coordination compounds*; Springer, 2007. (b) Yam, V. W.-W.; Wong, K. M.-C. Luminescent metal complexes of d6, d8 and d10 transition metal centres. *Chemical Communications* **2011**, *47* (42), 11579-11592.

60. Lee, L. C.-C.; Lo, K. K.-W. Luminescent and Photofunctional Transition Metal Complexes: From Molecular Design to Diagnostic and Therapeutic Applications. *Journal of the American Chemical Society* **2022**, *144* (32), 14420-14440.

61. (a) Yam, V. W.-W.; Cheng, E. C.-C. Highlights on the recent advances in gold chemistry—a photophysical perspective. *Chemical Society Reviews* **2008**, *37* (9), 1806-1813. (b) Bronner, C.; Wenger, O. S. Luminescent cyclometalated gold(iii) complexes. *Dalton Transactions* **2011**, *40* (46), 12409-12420.

62. (a) Würthner, F.; You, C.-C.; Saha-Möller, C. R. Metallosupramolecular squares: from structure to function. *Chemical Society Reviews* **2004**, *33* (3), 133-146. (b) Cooke, M. W.; Hanan, G. S. Luminescent polynuclear assemblies. *Chemical Society Reviews* **2007**, *36* (9), 1466-1476. (c) Cooke, M. W.; Chartrand, D.; Hanan, G. S. Self-assembly of discrete metallosupramolecular luminophores. *Coordination Chemistry Reviews* **2008**, *252* (8), 903-921. (d) Kumar, A.; Sun, S.-S.; Lees, A. J. Directed assembly metallocyclic supramolecular systems for molecular recognition and chemical sensing. *Coordination Chemistry Reviews* **2008**, *252* (8), 922-939. (e) Wing-Wah Yam, V.; Kam-Wing Lo, K. Luminescent polynuclear d10 metal complexes. *Chemical Society Reviews* **1999**, *28* (5), 323-334.

63. Yam, V. W.-W.; Au, V. K.-M.; Leung, S. Y.-L. Light-Emitting Self-Assembled Materials Based on d8 and d10 Transition Metal Complexes. *Chemical Reviews* **2015**, *115* (15), 7589-7728.

64. (a) Yeung, M. C.-L.; Yam, V. W.-W. Luminescent cation sensors: from host–guest chemistry, supramolecular chemistry to reaction-based mechanisms. *Chemical Society Reviews* **2015**, *44* (13), 4192-4202. (b) Yeung, M. C.-L.; Yam, V. W.-W. Molecular Design of Novel Classes of Luminescent Transition Metal Complexes and Their Use in Sensing, Biolabeling, and Cell Imaging. In *Luminescent and Photoactive Transition Metal Complexes as Biomolecular Probes and Cellular Reagents*, Lo, K. K.-W. Ed.; Springer Berlin Heidelberg, 2015; pp 109-129.

65. (a) Holder, E.; Langeveld, B. M. W.; Schubert, U. S. New Trends in the Use of Transition Metal–Ligand Complexes for Applications in Electroluminescent Devices. *Advanced Materials* **2005**, *17* (9), 1109-1121. (b) Wong, W.-Y.; Ho, C.-L. Heavy metal organometallic electrophosphors derived from multi-component chromophores. *Coordination Chemistry Reviews* **2009**, *253* (13), 1709-1758. (c) Chi, Y.; Chou, P.-T. Transition-metal phosphors with cyclometalating ligands: fundamentals and applications. *Chemical Society Reviews* **2010**, *39* (2), 638-655.

66. Zhang, C. X.; Lippard, S. J. New metal complexes as potential therapeutics. *Current Opinion in Chemical Biology* **2003**, *7* (4), 481-489.

67. Wing-Wah Yam, V.; Chung-Chin Cheng, E. Photochemistry and Photophysics of Coordination Compounds: Gold. In *Photochemistry and Photophysics of Coordination Compounds II*, Balzani, V., Campagna, S. Eds.; Springer Berlin Heidelberg, 2007; pp 269-309.

68. (a) Mendizabal, F.; Pyykkö, P. Aurophilic attraction in binuclear complexes with Au(i) and Au(iii). A theoretical study. *Physical Chemistry Chemical Physics* **2004**, *6* (5), 900-905. (b) Ortner, K.; Hilditch, L.; Zheng, Y.; Dilworth, J. R.; Abram, U. Gold Complexes with Potentially Tri- and Tetradentate Phosphinothiolate Ligands. *Inorganic Chemistry* **2000**, *39* (13), 2801-2806. (c) Klapötke, T. M.; Krumm, B.; Galvez-Ruiz, J.-C.; Nöth, H. Highly Sensitive Ammonium Tetraazidoaurates(III). *Inorganic Chemistry* **2005**, *44* (26), 9625-9627. (d) Hayoun, R.; Zhong, D. K.; Rheingold, A. L.; Doerrer, L. H. Gold(III) and Platinum(II) Polypyridyl Double Salts and a General Metathesis Route to Metallophilic Interactions. *Inorganic Chemistry* **2006**, *45* (16), 6120-6122. (e) Doerrer, L. H. METALLOPHILIC INTERACTIONS IN DOUBLE SALTS: TOWARD 1D METAL ATOM CHAINS. *Comments on Inorganic Chemistry* **2008**, *29* (3-4), 93-127.

69. (a) Yam, V. W.-W.; Choi, S. W.-K.; Lai, T.-F.; Lee, W.-K. Syntheses, crystal structures and photophysics of organogold(III) diimine complexes. *Journal of the Chemical Society, Dalton Transactions* **1993**, (6), 1001-1002. (b) Yam, V. W.-W.; Wong, K. M.-C.; Hung, L.-L.; Zhu, N. Luminescent Gold(III) Alkynyl Complexes: Synthesis, Structural Characterization, and Luminescence Properties. *Angewandte Chemie International Edition* **2005**, *44* (20), 3107-3110. (c) Wong, K. M.-C.; Hung, L.-L.; Lam, W. H.; Zhu, N.; Yam, V. W.-W. A Class of Luminescent Cyclometalated Alkynylgold(III) Complexes: Synthesis, Characterization, and Electrochemical, Photophysical, and Computational Studies of [Au(C∧N∧C)(C꞉CR)] (C∧N∧C = κ3C,N,C Bis-cyclometalated 2,6-Diphenylpyridyl). *Journal of the American Chemical Society* **2007**, *129* (14), 4350-4365. (d) Wong, K. M.-C.; Zhu, X.; Hung, L.-L.; Zhu, N.; Yam, V. W.-W.; Kwok, H.-S. A novel class of phosphorescent gold(iii) alkynyl-based organic light-emitting devices with tunable colour. *Chemical Communications* **2005**, (23),

2906-2908. (e) Au, V. K.-M.; Wong, K. M.-C.; Tsang, D. P.-K.; Chan, M.-Y.; Zhu, N.; Yam, V. W.-W. High-Efficiency Green Organic Light-Emitting Devices Utilizing Phosphorescent Bis-cyclometalated Alkynylgold(III) Complexes. *Journal of the American Chemical Society* **2010**, *132* (40), 14273-14278. (f) Tang, M.-C.; Tsang, D. P.-K.; Chan, M. M.-Y.; Wong, K. M.-C.; Yam, V. W.-W. Dendritic Luminescent Gold(III) Complexes for Highly Efficient Solution-Processable Organic Light-Emitting Devices. *Angewandte Chemie International Edition* **2013**, *52* (1), 446-449. (g) Tang, M.-C.; Chan, C. K.-M.; Tsang, D. P.-K.; Wong, Y.-C.; Chan, M. M.-Y.; Wong, K. M.-C.; Yam, V. W.-W. Saturated Red-Light-Emitting Gold(III) Triphenylamine Dendrimers for Solution-Processable Organic Light-Emitting Devices. *Chemistry – A European Journal* **2014**, *20* (46), 15233-15241. (h) Tang, M.-C.; Tsang, D. P.-K.; Wong, Y.-C.; Chan, M.-Y.; Wong, K. M.-C.; Yam, V. W.-W. Bipolar Gold(III) Complexes for Solution-Processable Organic Light-Emitting Devices with a Small Efficiency Roll-Off. *Journal of the American Chemical Society* **2014**, *136* (51), 17861-17868. (i) Au, V. K.-M.; Tsang, D. P.-K.; Wong, Y.-C.; Chan, M.-Y.; Yam, V. W.-W. Synthesis of alkynylgold(III) complexes with bis-cyclometalating ligand derived from ethyl 2,6-diphenylisonicotinate and their structural, electrochemical, photo- and electroluminescence studies. *Journal of Organometallic Chemistry* **2015**, *792*, 109-116. (j) Au, V. K.-M.; Wong, K. M.-C.; Zhu, N.; Yam, V. W.-W. Luminescent Cyclometalated Dialkynylgold(III) Complexes of 2-Phenylpyridine-Type Derivatives with Readily Tunable Emission Properties. *Chemistry – A European Journal* **2011**, *17* (1), 130-142. (k) Garg, J. A.; Blacque, O.; Venkatesan, K. Syntheses and Photophysical Properties of Luminescent Mono-cyclometalated Gold(III) cis-Dialkynyl Complexes. *Inorganic Chemistry* **2011**, *50* (12), 5430-5441. (l) Garg, J. A.; Blacque, O.; Fox, T.; Venkatesan, K. Stable and Tunable Phosphorescent Neutral

Cyclometalated Au(III) Diaryl Complexes. *Inorganic Chemistry* **2010**, *49* (24), 11463-11472. (m) Wong, K. M.-C.; Chan, M. M.-Y.; Yam, V. W.-W. Supramolecular Assembly of Metal-Ligand Chromophores for Sensing and Phosphorescent OLED Applications. *Advanced Materials* **2014**, *26* (31), 5558-5568.

70. Leung, M.-Y.; Leung, S. Y.-L.; Yim, K.-C.; Chan, A. K.-W.; Ng, M.; Yam, V. W.-W. Multiresponsive Luminescent Cationic Cyclometalated Gold(III) Amphiphiles and Their Supramolecular Assembly. *Journal of the American Chemical Society* **2019**, *141* (49), 19466-19478.

71. (a) Chen, Y.; Yekta, S.; Yudin, A. K. Modified BINOL Ligands in Asymmetric Catalysis. *Chemical Reviews* **2003**, *103* (8), 3155-3212. (b) Kočovský, P.; Vyskočil, Š.; Smrčina, M. Non-Symmetrically Substituted 1,1'-Binaphthyls in Enantioselective Catalysis. *Chemical Reviews* **2003**, *103* (8), 3213-3246. (c) Brunel, J. M. BINOL: A Versatile Chiral Reagent. *Chemical Reviews* **2005**, *105* (3), 857-898. (d) Han, Y.-Q.; Ding, Y.; Zhou, T.; Yan, S.-Y.; Song, H.; Shi, B.-F. Pd(II)-Catalyzed Enantioselective Alkynylation of Unbiased Methylene C(sp3)–H Bonds Using 3,3′-Fluorinated-BINOL as a Chiral Ligand. *Journal of the American Chemical Society* **2019**, *141* (11), 4558-4563.

72. (a) Aoyama, H.; Tokunaga, M.; Kiyosu, J.; Iwasawa, T.; Obora, Y.; Tsuji, Y. Kinetic Resolution of Axially Chiral 2,2'-Dihydroxy-1,1'-biaryls by Palladium-Catalyzed Alcoholysis. *Journal of the American Chemical Society* **2005**, *127* (30), 10474-10475. (b) Ma, G.; Deng, J.; Sibi, M. P. Fluxionally Chiral DMAP Catalysts: Kinetic Resolution of Axially Chiral Biaryl Compounds. *Angewandte Chemie International Edition* **2014**, *53* (44), 11818-11821. (c) Lu, S.; Poh, S. B.; Zhao, Y. Kinetic Resolution of 1,1′-Biaryl-2,2′-Diols and Amino Alcohols through NHC-Catalyzed Atroposelective Acylation. *Angewandte Chemie International Edition* **2014**, *53* (41), 11041-11045. (d) Ma, G.; Sibi,

M. P. Catalytic Kinetic Resolution of Biaryl Compounds. *Chemistry – A European Journal* **2015**, *21* (33), 11644-11657. (e) Jones, B. A.; Balan, T.; Jolliffe, J. D.; Campbell, C. D.; Smith, M. D. Practical and Scalable Kinetic Resolution of BINOLs Mediated by a Chiral Counterion. *Angewandte Chemie International Edition* **2019**, *58* (14), 4596-4600. (f) Qu, S.; Greenhalgh, M. D.; Smith, A. D. Isothiourea-Catalysed Regioselective Acylative Kinetic Resolution of Axially Chiral Biaryl Diols. *Chemistry – A European Journal* **2019**, *25* (11), 2816-2823. (g) Zhang, J.; Wang, K.; Zhu, C. Deracemization of Atropisomeric Biaryls Enabled by Copper Catalysis. *JACS Au* **2024**, *4* (2), 502-511. (h) Tanaka, K.; Okada, T.; Toda, F. Separation of the Enantiomers of 2,2′ -Dihydroxy-1, 1′ -binaphthyl and 10,10′ -Dihydroxy-9,9′ -biphenanthryl by Complexation with N-Alkylcinchonidinium Halides. *Angewandte Chemie International Edition in English* **1993**, *32* (8), 1147-1148. (i) Wang, Y.; Sun, J.; Ding, K. Practical Method and Novel Mechanism for Optical Resolution of BINOL by Molecular Complexation with N-Benzylcinchoninium Chloride. *Tetrahedron* **2000**, *56* (26), 4447-4451. (j) Lim, C. W.; Lee, S.-g. C2-Symmetric Bisphosphine Ligands Derived from 1,1′ -Binaphthyldiamines and Diphenylphosphinobenzoic Acid for Palladium Catalyzed Desymmetrizations. *Tetrahedron* **2000**, *56* (29), 5131-5136.

73. (a) Tayama, E.; Tanaka, H. An efficient optical resolution of nitrogen-centered chiral β-hydroxy-tetraalkylammonium salts via complexation with (R)-BINOL. *Tetrahedron Letters* **2007**, *48* (24), 4183-4185. (b) Tayama, E.; Otoyama, S.; Tanaka, H. Resolution of nitrogen-centered chiral tetraalkylammonium salts: application to [1,2] Stevens rearrangements with N-to-C chirality transmission. *Tetrahedron: Asymmetry* **2009**, *20* (22), 2600-2608. (c) Walsh, M. P.; Phelps, J. M.; Lennon, M. E.; Yufit, D. S.; Kitching, M. O. Enantioselective synthesis of ammonium cations. *Nature* **2021**, *597* (7874), 70-76.

74. Wang, Y.-B.; Tan, B. Construction of Axially Chiral Compounds via Asymmetric Organocatalysis. *Accounts of Chemical Research* **2018**, *51* (2), 534-547.

75. (a) Akiyama, T.; Mori, K. Stronger Brønsted Acids: Recent Progress. *Chemical Reviews* **2015**, *115* (17), 9277-9306. (b) da Silva, E. M.; Vidal, H. D.; Januário, M. A.; Corrêa, A. G. Advances in the Asymmetric Synthesis of BINOL Derivatives. *Molecules* **2023**, *28* (1), 12.

76. (a) Chau, M.-H.; Stuart, M. C. A.; Leung, F. K.-C. Red-light driven photoisomerisation and supramolecular transformation of indigo amphiphiles in aqueous media. *Colloids and Surfaces A: Physicochemical and Engineering Aspects* **2023**, *661*, 130939. (b) Wang, H. Recent advances in asymmetric oxidative coupling of 2-naphthol and its derivatives. *Chirality* **2010**, *22* (9), 827-837. (c) Wencel-Delord, J.; Panossian, A.; Leroux, F. R.; Colobert, F. Recent advances and new concepts for the synthesis of axially stereoenriched biaryls. *Chemical Society Reviews* **2015**, *44* (11), 3418-3430. (d) Tian, J.-M.; Wang, A.-F.; Yang, J.-S.; Zhao, X.-J.; Tu, Y.-Q.; Zhang, S.-Y.; Chen, Z.-M. Copper-Complex-Catalyzed Asymmetric Aerobic Oxidative Cross-Coupling of 2-Naphthols: Enantioselective Synthesis of 3,3′ -Substituted C1-Symmetric BINOLs. *Angewandte Chemie International Edition* **2019**, *58* (32), 11023-11027. (e) Horibe, T.; Nakagawa, K.; Hazeyama, T.; Takeda, K.; Ishihara, K. An enantioselective oxidative coupling reaction of 2-naphthol derivatives catalyzed by chiral diphosphine oxide–iron(ii) complexes. *Chemical Communications* **2019**, *55* (91), 13677-13680. (f) Yang, H.; Sun, J.; Gu, W.; Tang, W. Enantioselective Cross-Coupling for Axially Chiral Tetra-ortho-Substituted Biaryls and Asymmetric Synthesis of Gossypol. *Journal of the American Chemical Society* **2020**, *142* (17), 8036-8043. (g) Juárez-Hernandez, M.; Johnson, D. V.; Holland, H. L.; McNulty, J.; Capretta, A. Lipase-catalyzed stereoselective resolution and

desymmetrization of binaphthols. *Tetrahedron: Asymmetry* **2003**, *14* (3), 289-291. (h) Moustafa, G. A. I.; Oki, Y.; Akai, S. Lipase-Catalyzed Dynamic Kinetic Resolution of C1- and C2-Symmetric Racemic Axially Chiral 2,2′ -Dihydroxy-1,1′ -biaryls. *Angewandte Chemie International Edition* **2018**, *57* (32), 10278-10282. (i) Zhu, S.; Chen, Y.-H.; Wang, Y.-B.; Yu, P.; Li, S.-Y.; Xiang, S.-H.; Wang, J.-Q.; Xiao, J.; Tan, B. Organocatalytic atroposelective construction of axially chiral arylquinones. *Nature Communications* **2019**, *10* (1), 4268. (j) Yang, H.; Chen, J.; Zhou, L. Construction of Axially Chiral Compounds via Central-to-Axial Chirality Conversion. *Chemistry – An Asian Journal* **2020**, *15* (19), 2939-2951.

77. Guo, J.; Xiong, W.-B.; Ma, H.-R.; Fan, L.; Zhou, Y.-Y.; Wong, H. N. C.; Cui, J.-F. Optical resolution of 1,16-dihydroxytetraphenylene by chiral gold(iii) complexation and its applications as chiral ligands in asymmetric catalysis. *Chemical Science* **2022**, *13* (16), 4608-4615.

78. (a) Zi, W.; Toste, F. D. Gold(I)-Catalyzed Enantioselective Carboalkoxylation of Alkynes. *Journal of the American Chemical Society* **2013**, *135* (34), 12600-12603. (b) Mi, Y.; Zhou, T.; Wang, K.-P.; Lee, D.; Xia, Y. Mechanistic Understanding of the Divergent Cyclizations of o-Alkynylbenzaldehyde Acetals and Thioacetals Catalyzed by Metal Halides. *Chemistry – A European Journal* **2015**, *21* (48), 17256-17268.

79. Barrow, J. C.; Ngo, P. L.; Pellicore, J. M.; Selnick, H. G.; Nantermet, P. G. A facile three-step synthesis of 1,2-amino alcohols using the Ellman homochiral tert-butylsulfinamide. *Tetrahedron Letters* **2001**, *42* (11), 2051-2054.

80. (a) Dell'Acqua, M.; Facoetti, D.; Abbiati, G.; Rossi, E. Selective Base-Promoted Synthesis of Dihydroisobenzofurans by Domino Addition/Annulation Reactions of ortho-Alkynylbenzaldehydes. *Synthesis* **2010**, *2010* (14), 2367-2378. (b) Luo, H.; He, C.; Jiang,

H.; Zhu, S. Rapid Access to Oxabicyclo[2.2.2]octane Skeleton through Cu(I)-Catalyzed Generation and Trapping of Vinyl-o-quinodimethanes (Vinyl--QDMs)†. *Chinese Journal of Chemistry* **2020**, *38* (10), 1052-1056. (c) Ohta, Y.; Kubota, Y.; Watabe, T.; Chiba, H.; Oishi, S.; Fujii, N.; Ohno, H. Rapid Access to 3-(Aminomethyl)isoquinoline-Fused Polycyclic Compounds by Copper-Catalyzed Four-Component Coupling, Cascade Cyclization, and Oxidation. *The Journal of Organic Chemistry* **2009**, *74* (16), 6299-6302. (d) Kong, J.; Zhang, F.; Zhang, C.; Chang, W.; Liu, L.; Li, J. An efficient electrochemical oxidation of C(sp3)-H bond for the synthesis of arylketones. *Molecular Catalysis* **2022**, *530*, 112633. (e) Debrouwer, W.; Seigneur, R. A. J.; Heugebaert, T. S. A.; Stevens, C. V. Gold superacid-catalyzed preparation of benzo[c]thiophenes. *Chemical Communications* **2015**, *51* (4), 729-732. (f) He, G.; Wu, C.; Zhou, J.; Yang, Q.; Zhang, C.; Zhou, Y.; Zhang, H.; Liu, H. A Method for Synthesis of 3-Hydroxy-1-indanones via Cu-Catalyzed Intramolecular Annulation Reactions. *The Journal of Organic Chemistry* **2018**, *83* (21), 13356-13362. (g) Nejedlý, J.; Šámal, M.; Rybáček, J.; Sánchez, I. G.; Houska, V.; Warzecha, T.; Vacek, J.; Sieger, L.; Buděšínský, M.; Bednárová, L.; et al. Synthesis of Racemic, Diastereopure, and Enantiopure Carba- or Oxa[5]-, [6]-, [7]-, and -[19]helicene (Di)thiol Derivatives. *The Journal of Organic Chemistry* **2020**, *85* (1), 248-276. (h) Deng, J.-R.; Lai, N. C.-H.; Kung, K. K.-Y.; Yang, B.; Chung, S.-F.; Leung, A. S.-L.; Choi, M.-C.; Leung, Y.-C.; Wong, M.-K. N-Terminal selective modification of peptides and proteins using 2-ethynylbenzaldehydes. *Communications Chemistry* **2020**, *3* (1), 67. (i) Cao, Z.; Zhang, H.; Zhang, X.; Zhang, L.; Meng, X.; Chen, G.; Zhao, X.-E.; Sun, X.; You, J. Gold-catalyzed tandem cycloisomerization/Petasis–Ferrier rearrangement: a direct route to 3-alkoxyindanones from enynals and alcohols. *RSC Advances* **2015**, *5* (125), 103155-103158.

81. (a) Simmons, N. S.; Blout, E. R. The Structure of Tobacco Mosaic Virus and Its Components: Ultraviolet Optical Rotatory Dispersion. *Biophys J* **1960**, *1* (1), 55-62. (b) Lino, T. Assembly of salmonella flagellin in vitro and in vivo. *Journal of Supramolecular Structure* **1974**, *2* (2-4), 372-384. (c) Chapman, D. Phase transitions and fluidity characteristics of lipids and cell membranes. *Quarterly Reviews of Biophysics* **1975**, *8* (2), 185-235.

82. (a) Chen, S.; Costil, R.; Leung, F. K.-C.; Feringa, B. L. Self-Assembly of Photoresponsive Molecular Amphiphiles in Aqueous Media. *Angewandte Chemie International Edition* **2021**, *60* (21), 11604-11627. (b) Feringa, B. L. The Art of Building Small: From Molecular Switches to Motors (Nobel Lecture). *Angewandte Chemie International Edition* **2017**, *56* (37), 11060-11078. (c) Krieg, E.; Bastings, M. M. C.; Besenius, P.; Rybtchinski, B. Supramolecular Polymers in Aqueous Media. *Chemical Reviews* **2016**, *116* (4), 2414-2477. (d) Aida, T.; Meijer, E. W.; Stupp, S. I. Functional Supramolecular Polymers. *Science* **2012**, *335* (6070), 813-817.

83. (a) Dattler, D.; Fuks, G.; Heiser, J.; Moulin, E.; Perrot, A.; Yao, X.; Giuseppone, N. Design of Collective Motions from Synthetic Molecular Switches, Rotors, and Motors. *Chemical Reviews* **2020**, *120* (1), 310-433. (b) Baroncini, M.; Silvi, S.; Credi, A. Photo- and Redox-Driven Artificial Molecular Motors. *Chemical Reviews* **2020**, *120* (1), 200-268. (c) Shigemitsu, H.; Fujisaku, T.; Tanaka, W.; Kubota, R.; Minami, S.; Urayama, K.; Hamachi, I. An adaptive supramolecular hydrogel comprising self-sorting double nanofibre networks. *Nature Nanotechnology* **2018**, *13* (2), 165-172.

84. Volarić, J.; Szymanski, W.; Simeth, N. A.; Feringa, B. L. Molecular photoswitches in aqueous environments. *Chemical Society Reviews* **2021**, *50* (22), 12377-12449.

85. (a) Cheung, L.-H.; Kajitani, T.; Leung, F. K.-C. Visible-light controlled supramolecular transformations of donor-acceptor Stenhouse adducts amphiphiles at multiple length-scale. *Journal of Colloid and Interface Science* **2022**, *628*, 984-993. (b) Chau, A. K.-H.; Cheung, L.-H.; Leung, F. K.-C. Red-light controlled supramolecular co-assembly transformations of stiff stilbene and donor acceptor stenhouse adduct amphiphiles. *Dyes and Pigments* **2023**, *208*, 110807. (c) Kwan, K. S.-Y.; Lui, Y.-Y.; Kajitani, T.; Leung, F. K.-C. Aqueous Supramolecular Co-Assembly of Anionic and Cationic Photoresponsive Stiff-Stilbene Amphiphiles. *Macromolecular Rapid Communications* **2022**, *43* (21), 2200438.

86. Chau, A. K.-H.; Leung, F. K.-C. Exploration of molecular machines in supramolecular soft robotic systems. *Advances in Colloid and Interface Science* **2023**, *315*, 102892.

87. (a) Poon, J. K.-L.; Chen, Z.; Leung, S. Y.-L.; Leung, M.-Y.; Yam, V. W.-W. Geometrical manipulation of complex supramolecular tessellations by hierarchical assembly of amphiphilic platinum(II) complexes. *Proceedings of the National Academy of Sciences* **2021**, *118* (6), e2022829118. (b) Fu, H. L.-K.; Yam, V. W.-W. Supramolecular Metallogels of Platinum(II) and Gold(III) Complexes. *Chemistry Letters* **2018**, *47* (5), 605-610. (c) Owen, T.; Butler, A. Metallosurfactants of bioinorganic interest: Coordination-induced self assembly. *Coordination Chemistry Reviews* **2011**, *255* (7), 678-687. (d) Mayoral Muñoz, M. J.; Fernández, G. Metallosupramolecular amphiphilic π-systems. *Chemical Science* **2012**, *3* (5), 1395-1398.

88. (a) Destito, P.; Vidal, C.; López, F.; Mascareñas, J. L. Transition Metal-Promoted Reactions in Aqueous Media and Biological Settings. *Chemistry – A European Journal* **2021**, *27* (15), 4789-4816. (b) Thomas, S. R.; Casini, A. Gold compounds for catalysis

and metal-mediated transformations in biological systems. *Current Opinion in Chemical Biology* **2020**, *55*, 103-110. (c) Chang, T.-C.; Tanaka, K. In vivo organic synthesis by metal catalysts. *Bioorganic & Medicinal Chemistry* **2021**, *46*, 116353. (d) Sit, H.-Y.; Yang, B.; Ka-Yan Kung, K.; Siu-Lun Tam, J.; Wong, M.-K. Fluorescent Labelling of Glycans with FRET-Based Probes in a Gold(III)-Mediated Three-Component Coupling Reaction. *ChemPlusChem* **2019**, *84* (11), 1739-1743. (e) Kung, K. K.-Y.; Ko, H.-M.; Cui, J.-F.; Chong, H.-C.; Leung, Y.-C.; Wong, M.-K. Cyclometalated gold(iii) complexes for chemoselective cysteine modification via ligand controlled C–S bond-forming reductive elimination. *Chemical Communications* **2014**, *50* (80), 11899-11902. (f) Ko, H.-M.; Deng, J.-R.; Cui, J.-F.; Kung, K. K.-Y.; Leung, Y.-C.; Wong, M.-K. Selective modification of alkyne-linked peptides and proteins by cyclometalated gold(III) (C^N) complex-mediated alkynylation. *Bioorganic & Medicinal Chemistry* **2020**, *28* (7), 115375.

89. Yam, V. W.-W.; Chan, A. K.-W.; Hong, E. Y.-H. Charge-transfer processes in metal complexes enable luminescence and memory functions. *Nature Reviews Chemistry* **2020**, *4* (10), 528-541.

90. (a) Zhang, J.-J.; Lu , W.; Sun, R. W.-Y.; Che, C.-M. Organogold(III) Supramolecular Polymers for Anticancer Treatment. *Angewandte Chemie International Edition* **2012**, *51* (20), 4882-4886. (b) Au, V. K.-M.; Zhu, N.; Yam, V. W.-W. Luminescent Metallogels of Bis-Cyclometalated Alkynylgold(III) Complexes. *Inorganic Chemistry* **2013**, *52* (2), 558-567. (c) Yim, K.-C.; Au, V. K.-M.; Hung, L.-L.; Wong, K. M.-C.; Yam, V. W.-W. Luminescent Dinuclear Bis-Cyclometalated Gold(III) Alkynyls and Their Solvent-Dependent Morphologies through Supramolecular Self-Assembly. *Chemistry – A European Journal* **2016**, *22* (45), 16258-16270. (d) Siu, S. K.-L.; Po, C.; Yim, K.-C.; Au, V. K.-M.; Yam, V. W.-W. Synthesis, characterization and spectroscopic studies of

luminescent l-valine modified alkynyl-based cyclometalated gold(iii) complexes with gelation properties driven by π–π stacking, hydrogen bonding and hydrophobic–hydrophobic interactions. *CrystEngComm* **2015**, *17* (42), 8153-8162. (e) Yim, K.-C.; Lam, E. S.-H.; Wong, K. M.-C.; Au, V. K.-M.; Ko, C.-C.; Lam, W. H.; Yam, V. W.-W. Synthesis, Characterization, Self-Assembly, Gelation, Morphology and Computational Studies of Alkynylgold(III) Complexes of 2,6-Bis(benzimidazol-2′-yl)pyridine Derivatives. *Chemistry – A European Journal* **2014**, *20* (32), 9930-9939.

91. Lee, C.-H.; Tang, M.-C.; Kong, F. K.-W.; Cheung, W.-L.; Ng, M.; Chan, M.-Y.; Yam, V. W.-W. Isomeric Tetradentate Ligand-Containing Cyclometalated Gold(III) Complexes. *Journal of the American Chemical Society* **2020**, *142* (1), 520-529.

92. (a) Constable, E. C.; Leese, T. A. Metal exchange in organomercury complexes; a facile route to cyclometallated transition metal complexes. *Journal of Organometallic Chemistry* **1987**, *335* (3), 293-299. (b) Constable, E. C.; Leese, T. A. Cycloaurated derivatives of 2-phenylpyridine. *Journal of Organometallic Chemistry* **1989**, *363* (3), 419-424.

93. Shimizu, Y.; Azumi, T. Mechanism of external heavy atom effect on intersystem crossing in fluid solutions. Analysis based on fluorescence decay data. *The Journal of Physical Chemistry* **1982**, *86* (1), 22-26.

94. (a) Mateos-Timoneda, M. A.; Crego-Calama, M.; Reinhoudt, D. N. Supramolecular chirality of self-assembled systems in solution. *Chemical Society Reviews* **2004**, *33* (6), 363-372. (b) Liu, M.; Zhang, L.; Wang, T. Supramolecular Chirality in Self-Assembled Systems. *Chemical Reviews* **2015**, *115* (15), 7304-7397. (c) Ouyang, G.; Liu, M. Self-assembly of chiral supra-amphiphiles. *Materials Chemistry Frontiers* **2020**, *4* (1), 155-167.

95. Yam, V. W.-W.; Law, A. S.-Y. Recent advances in supramolecular self-assembly and biological applications of luminescent alkynylplatinum(II) polypyridine complexes. *Journal of the Chinese Chemical Society* **2020**, *67* (12), 2246-2252.